Metastable Microtubules: Dynamic Instability, Lattice Plasticity and Mechanosensing

Dissertation
zur Erlangung des Grades
des Doktors der Naturwissenschaften
der Naturwissenschaftlich-Technischen Fakultät
der Universität des Saarlandes

vorgelegt von
Shweta Nandakumar
Saarbrücken, 2025

UNIVERSITÄT
DES
SAARLANDES

Naturwissenschaftlich-Technische Fakultät

Metastable Microtubules: Dynamic Instability, Lattice Plasticity and Mechanosensing

Dissertation
zur Erlangung des Grades
des Doktors der Naturwissenschaften
der Naturwissenschaftlich-Technischen Fakultät
der Universität des Saarlandes
vorgelegt von
Shweta Nandakumar
Saarbrücken, 2025

Tag des Kolloquiums: 25.02.2026

Dekan: Prof. Dr.-Ing. Dirk Bähre

Berichterstatter: Prof. Dr. Laura Aradilla Zapata
Prof. Dr. Franziska Lautenschläger
Prof. Dr. David U. Mick

Vorsitz: Prof. Dr. Albrecht Ott

Akad. Mitglied: Dr. Carsten Alexander Baltes

Abstract

A multitude of cellular functions rely on active remodeling of the cytoskeleton and its components. Microtubules constitute the most rigid and dynamic component of the cytoskeleton. Their inherent metastability gives rise to their dynamic nature, and recent research shows that the microtubule lattice is also dynamic. This challenges the traditional view of microtubules as passive, load-bearing supports that bear compressive forces. Microtubule dynamicity is modulated by a variety of effectors - motor proteins, mechanical force, microtubule-associated proteins (MAPs), tubulin code, as well as microtubule-targeting drugs.

This dissertation combines *in vitro* reconstitution, cellular, and modelling approaches to investigate how microtubule metastability - manifested in both tip and lattice dynamics - aids their diverse functions.
By developing an *in vitro* assay that mimics intracellular mechanical stress, I study microtubule response to mechanical stress and how this is mediated in the presence of different effectors. I show that microtubule response is modulated by force, tubulin code, MAPs, and depolymerizing agents. This suggests that microtubules are not merely passive filaments but can actively undergo lattice remodeling in an effector-mediated manner. This work provides a framework for future studies on the regulation of microtubule response and offers insights into microtubule organization, pharmacology, and their emerging role as cellular mechanosensors.

Zusammenfassung

Eine Vielzahl zellulärer Funktionen hängt von der aktiven Umgestaltung des Zytoskeletts und seiner Komponenten ab. Mikrotubuli sind die steifsten und zugleich dynamischsten Komponenten des Zytoskeletts. Ihre inhärente dynamische Instabilität führt zu ihrer metastabilen Natur, und die aktuelle Forschung zeigt, dass auch der Schaft der Mikrotubuli dynamisch ist. Dies stellt die traditionelle Auffassung von Mikrotubuli als passive, strukturelle Stützen, die Druckkräfte aufnehmen, in Frage. Die Dynamik der Mikrotubuli wird durch eine Vielzahl von Effektoren moduliert – Motorproteine, mechanische Kräfte, Mikrotubuli-assoziierte Proteine (MAPs), Tubulin-Code sowie Mikrotubuli-aktive Wirkstoffe.

Unter Verwendung einer Kombination aus *In-vitro*-Rekonstitution, zellulären und Modellierungsansätzen untersucht diese Dissertation, wie die metastabile Natur von Mikrotubuli, die sich sowohl in der Spitzen- als auch Schaftdynamik manifestiert, die Funktion der Mikrotubuli unterstützt. Durch die Entwicklung eines In-vitro-Assays, das intrazellulären mechanischen Stress nachahmt, untersuchen wir die Reaktion der Mikrotubuli auf mechanischen Stress und wie diese in Gegenwart verschiedener Effektoren verändert wird. Wir zeigen, dass die Reaktion der Mikrotubuli durch Kraft, Tubulin-Code, MAPs und Depolymerisationsmittel moduliert wird. Dies deutet darauf hin, dass Mikrotubuli nicht nur passive Filamente sind, sondern aktiv zwischen strukturellen Zuständen innerhalb des Schafts wechseln können, und zwar auf effektorvermittelte Weise. Diese Arbeit liefert einen Rahmen für die weiterführende Erforschung der Regulation von Mikrotubuli und bietet Einblicke in die Organisation von Mikrotubuli, ihre Pharmakologie und ihre aufkommende Rolle als zelluläre Mechanosensoren.

"A song- an internal hum-and, equally, an external one: a message sent out from one being to another to signal interconnectedness and cooperativity. We can name cells, and even systems of cells, but we are yet to learn the songs of cell biology."

-Siddhartha Mukherjee

Table of Contents

List of abbreviations

ADP: Adenosine Diphosphate

AFM: Atomic Force Microscopy

ATP: Adenosine Triphosphate

BRB80: Brinkley Reassembly Buffer (80 mM PIPES)

BSA: Bovine Serum Albumin

CLASP: CLIP-Associating Protein

CRISPR: Clustered Regularly Spaced Palindromic Repeats

Cryo-EM: Cryo Electron Microscopy

Cryo-ET: Cryo-Electron Tomography

CTL: Cytotoxic T-Lymphocytes

CTT: C-terminal tails

DC: Dendritic cell

DMEM: Dulbecco's Modified Eagle Medium

DMSO: DiMethyl Sulfoxide

DTT: Dithiothreitol

EB: End Binding protein

EDTA: Ethylene diamine tetraacetic acid

EGTA: Ethylene glycol-bis(β-aminoethyl ether)-*N*,*N*,*N*',*N*'-tetraacetic acid

EML2: Echinoderm Microtubule Associated Protein Like 2

FBS: Fetal Bovine Serum

FLIC: Fluorescence Interference Contrast Microscopy

FWHM: Full Width Half Maximum

GDP: Guanine Diphosphate

GEF: Guanine nucleotide Exchange Factor

GFP: Green Fluorescent Protein

GTP: Guanine Triphosphate

HEK: Human Embryonic Kidney cells

HEPES: 4-(2-hydroxyethyl)-1-piperazineethanesulfonic acid

IRM: Interference Reflection Microscopy

KMC: Kinetic Monte Carlo modelling

Lp : Persistence length

k Da: Kilo-Dalton

M: Molar

MACF: Microtubule Actin Crosslinking Factor

MAP: Microtubule-Associated Protein

MIP: Microtubule Inner Protein

MST: Microscale Thermophoresis

MT: Microtubule

MTA: Microtubule Targeting Agents

MTBD: Microtubule Binding Domain

NHS-ester: N-Hydroxysuccinimide ester

PBS: Phosphate Buffered Saline

PDMS: Poly(DiMethylSiloxan)

PEG: Poly(ethylene) glycol

PF: Protofilament

PIPES: Piperazine-*N*,*N*'-bis(2-ethanesulphonic acid)

PT: Pretubulysin

PTMs: Post-translational modifications

ROS: Reactive Oxygen Species

RT: Room Temperature

SD: Standard deviation

SEM: Standard Error of Mean

SMPB: Single Molecule Photobleaching

STORM: Stochastic Optical Reconstruction Microscopy

TAZ: Transcriptional coactivator with a PDZ-binding motif

TIRF: Total Internal Reflection Fluorescence

TOG: Tumor Overexpressed Gene

TTL: Tubulin Tyrosine Ligase

WT: Wild Type

YAP : Yes Associated Protein

Declaration of generative AI and AI-assisted technologies in the writing process

During the preparation of this work, ChatGPT-5.2 (OpenAI) was used for language editing and stylistic refinement. After using this tool, I reviewed and edited the content as needed and I take full responsibility for the content of the published dissertation.

Glossary/List of terms

Anisotropy: structural property of a material that exhibits differences according to the direction of measurement. Microtubules are inherently anisotropic, with the longitudinal dimer-dimer bonds being stronger than the lateral.

Strain: normalized measure of deformation.

Stiffness: measure of rigidity of a material (polymer).

Stress: force per unit area (in Pa). Mathematical product of stiffness and strain.

Persistence length (L_p): measure of the stiffness of a polymer. Defined as the length over which correlations in the direction of the tangent are lost.

Microtubule GDP lattice: refers to the portion of the microtubule excluding the extremities. The lattice is composed of GDP-bound tubulin.

Defect: inherent structural irregularities in the microtubule lattice that occur spontaneously during microtubule growth.

(Microtubule) **bending:** deformation in shape caused by forces acting perpendicular to the microtubule.

Curvature: change of a curve's direction per unit distance along the curve. For a circle, the curvature is the reciprocal of the radius (r^{-1} or μm^{-1})

(Microtubule) **buckling**: deformation in shape caused by forces acting along the microtubule. Buckling occurs when microtubules are subjected to a force beyond the buckling threshold.

(Microtubule) **self-repair**: Incorporation of free GTP-tubulin into an existing lattice induced by tubulin loss occurring from damage/mechanical stress. Microtubule self-repair enables microtubules to preserve integrity against mechanical stress.

(Microtubule) **lattice dynamics**: process of tubulin loss and consequent tubulin incorporation. Refers to tubulin loss caused by both inherent defect mobility and damage due to stress.

Lattice plasticity: refers to the dynamic nature of the microtubule lattice that enables microtubules to adapt and remodel their lattice conformation.

Effector: a collective term to refer to factors (MAPs, motors, force) that can 'effect' microtubule lattice remodeling.

Run length of kinesin motors is the distance travelled by a single kinesin along the microtubule.

Dwell/interaction time: total duration over which a single kinesin motor is in association with the microtubule.

Gliding speed: velocity of microtubules gliding over a surface of kinesin motors.

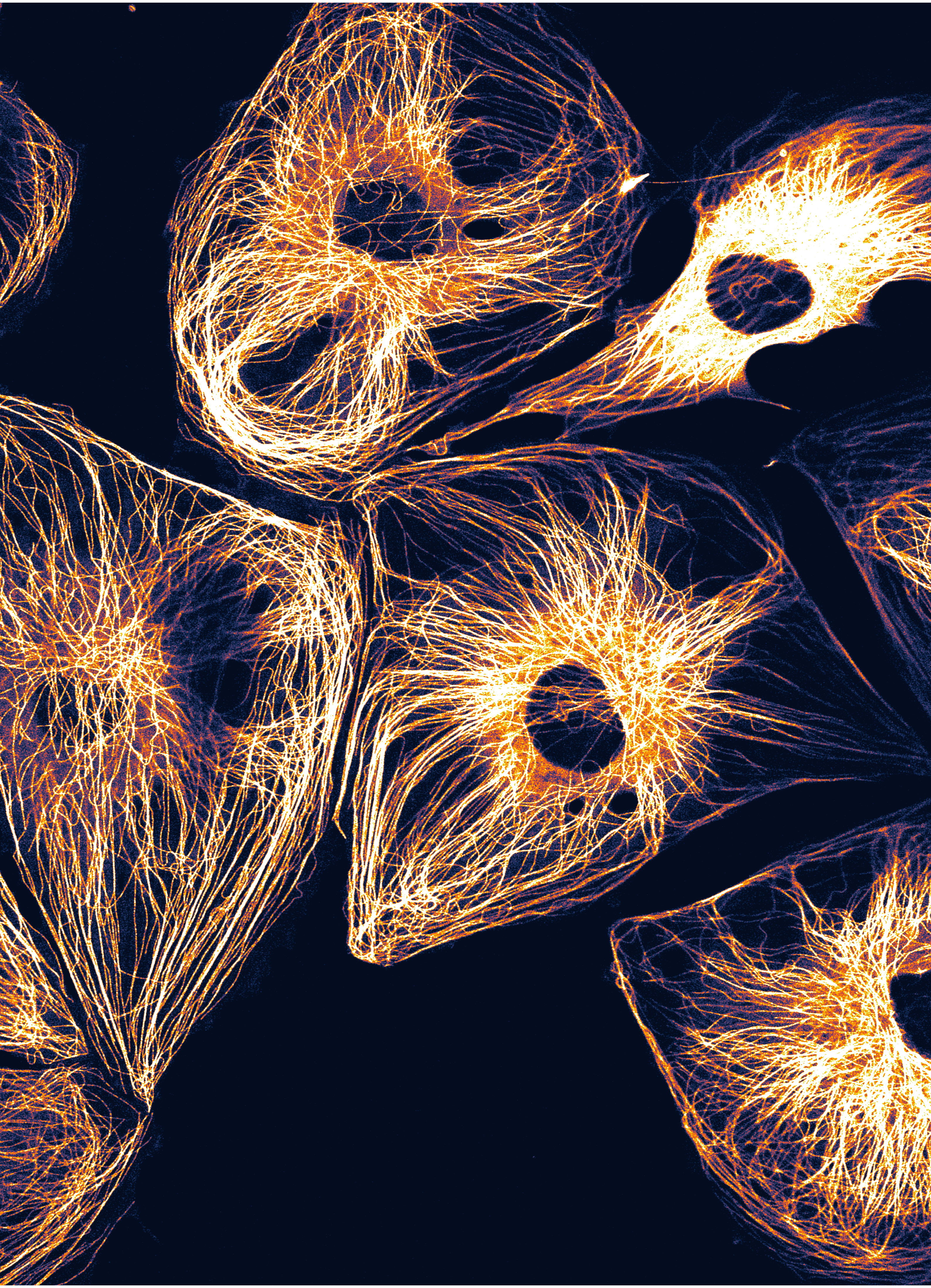

Introduction: The cytoskeleton and microtubules as metastable polymers

In this introductory chapter, I describe the emerging role of microtubules in cellular mechano-adaptation. I outline the structure, dynamicity of microtubules, and the heterogeneous nature of the microtubule lattice. By highlighting the emerging evidence on the metastable nature of the microtubule lattice and its implications in microtubule-based cellular processes, I hypothesize the role of microtubule metastability in regulating microtubule response and adaptation to stimuli.

0.1 The cytoskeleton

The cellular cytoskeleton is a dynamic network of interconnected biopolymers that provides structural support, shape, and mechanical adaptability to cells. It spans the expanse of the cell's interior, linking the nucleus and other organelles to the plasma membrane and the extracellular environment. It is comprised of three major filaments- actin microfilaments, intermediate filaments, microtubules (**Fig 0.1**). A fourth class of filaments called septins have been identified and characterized in the recent years.
The cytoskeleton is central to many cellular processes like cell migration, polarization, mitosis, and intracellular transport. It can actively remodel itself in response to mechanical cues, helping cells maintain their structural integrity, resist, and adapt to mechanical stimuli.

The three cytoskeletal filaments are distinct in their structure, mechanical properties and dynamics:

(i) Actin microfilaments (or F-actin) are helical, double-stranded polymers assembled from globular (G-actin) monomers with a diameter of ≈ 7-9 nm, via ATP hydrolysis (Cooper, 2000). They are semi-flexible in nature as characterized by their persistence length (L_p, bending stiffness).
(ii) Intermediate filaments are more heterogeneous and made up of different protein components depending on cell type. They are non-polar and flexible (Huber *et al.*, 2015).
(iii) Microtubules are hollow tubes having a diameter of 25 nm. They are made of α and β tubulin heterodimers and are the most rigid and dynamic of cytoskeletal filaments. Their dynamic nature is pivotal for mitosis, cell polarization and they serve as tracks for intracellular transport (Nikita & Mckintosh, 2021; Desai & Mitchison., 1997).

The focus on my dissertation was on microtubules and in the following sections, I describe their structure, dynamics, inherent heterogeneity and their emerging role as mediators of cellular mechanoadaptation to stimuli.

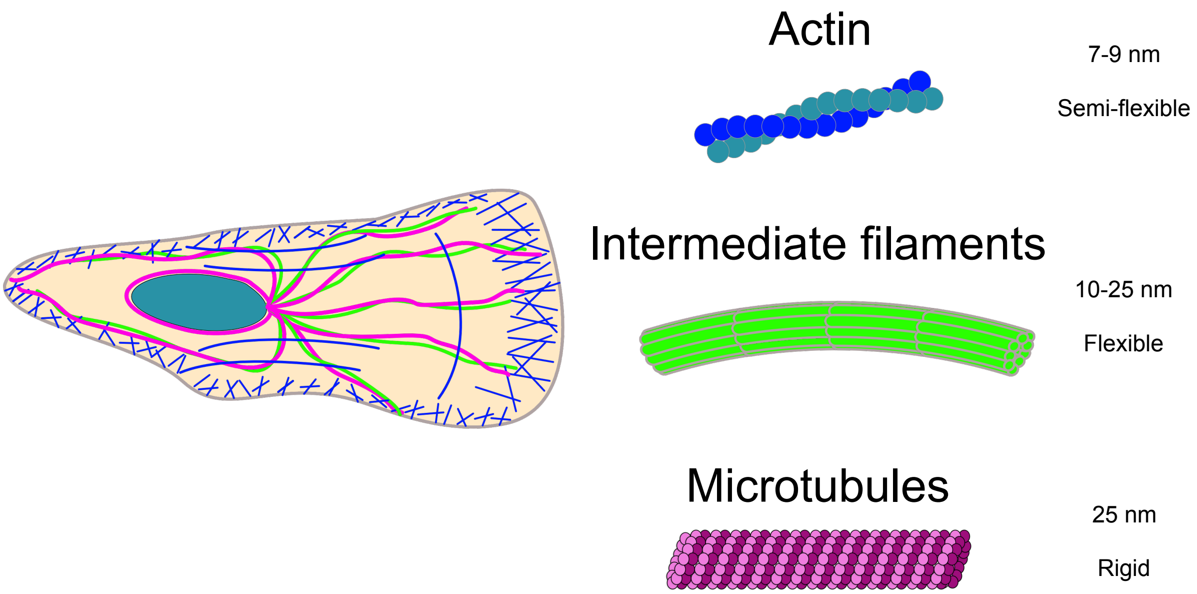

Fig 0.1: Overview of the three major cytoskeletal filaments. Microtubules are the most rigid of all three filaments.

0.2 Microtubules

Microtubules are rigid, hollow polymers composed of α and β-tubulin heterodimers. The dimers assemble longitudinally in the presence of the nucleotide GTP (Guanine Tri-phosphate) to form protofilaments that associate laterally to give microtubules their tubular form (**Fig 0.2a**).
Owing to the similarities in the periodic arrangement between the microtubule wall and crystal lattices, Grimstone and Klug, 1966 proposed the term 'lattice' to refer to the microtubule wall structure. During polymerization, GTP-tubulin is incorporated at the growing end and is hydrolysed over time to GDP. Thus, the microtubule lattice is predominantly composed of GDP (Guanine Di-phosphate)-tubulin.

Each tubulin subunit in the dimer can bind one GTP molecule. The GTP bound to the α-subunit is buried in the intradimer interface (called N-site) and therefore cannot be hydrolyzed. The GTP bound to the β-subunit (at the E-site) can be hydrolysed and is exchangeable (Brouhard & Nogales *et al.*, 1998). Thus, the nucleotide at the E-site of the β-subunit is exposed and during polymerization, the α-subunit of the incoming tubulin dimer interacts with the β-subunit at the growing or plus (+) end (Nogales, 2000; Mitchison, 1993). In solution, both GTP and GDP-bound tubulin dimers adopt a curved conformation (Nawrotek *et al.*, 2011). Upon incorporation into the growing end and GTP hydrolysis, the dimer undergoes structural changes that involve straightening of the dimer (Alushin *et al.*, 2014). Thus, part of the energy from GTP hydrolysis is used to deform the dimer, and this conformational strain is stored within the lattice, rendering it a metastable structure (Zhang *et al.*, 2015). This metastable nature gives rise to their highly dynamic nature and microtubules are the most dynamic of cytoskeletal components. This dynamicity is essential for a number of cellular functions and is core to the separation of chromosomes during mitosis (Inoue and Oldenbourg., 1998).

Tubulin constitutes about 2-3% of the total protein content in cell-extracts (Hiller and Weber, 1978). Both α and β-tubulin heterodimers possess three functional domains: (a) the N-terminal domain that consitutes the nucleotide binding domain, (b) intermediate domain and (c) the C-terminal tail (CTT) which is a hotspot for tubulin sequence variations as well as post-translational modifications (covered later in the section on the tubulin code). The CTTs of both α and β-tubulin heterodimers are also responsible for the interaction with Microtubule-Associated Proteins (MAPs) as well microtubule-based molecular motor proteins like kinesin and dynein that use microtubules as tracks for intracellular transport (Steinmetz and Prota, 2018; Nogales *et al.,* 1999, Nogales *et al.*, 1998).

Microtubule structure and stability is influenced by the interactions between the tubulin dimers in the microtubule lattice both in the lateral as well as longitudinal direction. The bonds between protofilaments in the microtubule lattice are anisotropic in nature (Nogales *et al.*, 1999; Huang *et al.*, 2008), with longitudinal bonds between tubulin dimers being stronger than lateral bonds. Depending on the lateral contacts formed, protofilaments can associate through homotypic (α-α or β-β subunits) or heterotypic (α-β) interactions, resulting in a B-lattice and A-lattice configuration, respectively (**Fig. 0.2b**). The configuration or lattice type influences microtubule stability, with emerging evidence suggesting that heterotypic (A-lattice) contacts are weaker than homotypic or B-lattice contacts (Katsuki *et al.*, 2014).

0.2.1 Mechanical properties of microtubules

Electron microscopy studies in the early 1990's showed that microtubules are highly rigid in nature with a bending stiffness or persistence length (L_p; resistance to bending) in the range of 1 mm with a young's modulus (E; measure of material stiffness) of 1.2 gigapascals (Hawkins *et al.*, 2010; Venier *et al.*, 1994; Gittes *et al.*, 1993). The stiffness of microtubules have been measured using a number of techniques over the last four decades, details of which can be found in Table 1, Chapter 1.

Microtubule stiffness is also influenced by growth conditions, specifically the growth concentration and presence of defects (Hawkins *et al.*, 2012). Microtubules grown in the presence of GMPCPP (guanylyl-(alpha, beta)-methylene-diphosphonate- a slowly hydrolyzable analog of GTP) were found to be 3-fold stiffer than those grown with GTP (Hyman *et al.*, 1995) whereas the stiffness of microtubules grown with GTPγS was found to be comparable to microtubules grown in the presence of GTP (Taviare *et al.*, 2013).

The presence and binding of Microtubule-Associated Proteins (MAPs) are also known to affect microtubule stiffness. Hawkins *et al.*, 2012 reported that small amounts (>1%) of MAPs can double the persistence length of microtubules as measured by thermal fluctuation experiments. Neuronal MAPs like Tau and MAP2 are reported to increase microtubule stiffness (Choi *et al.*, 2009; Mickey and Howard., 2005) whereas MAP-65-1 (a microtubule bundling protein in plants) enhances microtubule flexibility by a factor of four (Portran *et al.*, 2013). Post-translational modifications of tubulin, particularly acetylation has been found to also influence persistence length of microtubules, helping microtubules become more flexible and resistant to breakage (Xu *et al.*, 2017).

0.2.2 Dynamic instability

Microtubules, both in cells and *in vitro*, undergo characteristic transitions between growth and shrinkage in a phenomenon termed 'Dynamic instability' (Mitchison & Kirschner, 1984). This property enables microtubules to explore the cellular space and reorganize in response to cues. Microtubule dynamics is driven by GTP hydrolysis. As mentioned in the previous section, the strain stored in the microtubule lattice as a result of the conformational change associated with GTP-hydrolysis makes the microtubule lattice (that is composed to GDP-tubulin) unstable in nature. This metastable nature of the GDP-lattice makes it prone to depolymerization or shrinkage (Desai and Mitchison, 1997). The transition from growth to rapid shrinkage is termed as 'catastrophe' and vice versa, as 'rescue' (**Fig 0.2c**).

In cells, microtubule dynamics is regulated by the presence of a diverse set of microtubule-associated proteins (MAPs) that may either stabilize (eg: Tau superfamily, End binding proteins, CLIP-associated protein), destabilize (eg: EML2, kinesin-13), or sever (eg: katanin, spastin) microtubules. Further, emerging evidence suggests that the mechanics and dynamic properties of microtubules can be influenced by differences in tubulin composition as well as post-translational modifications, collectively termed as the 'Tubulin-code'.

For a long time, the lattice of the microtubules was thought to be a largely passive structure, but evidence in the last decade show that much like the tip, the microtubule lattice can also exchange tubulin subunits along its length, giving rise to lattice structure that is dynamic and can remodel or incorporate new tubulin subunits itself in response to tubulin loss from damage (a form of microtubule 'self-repair').

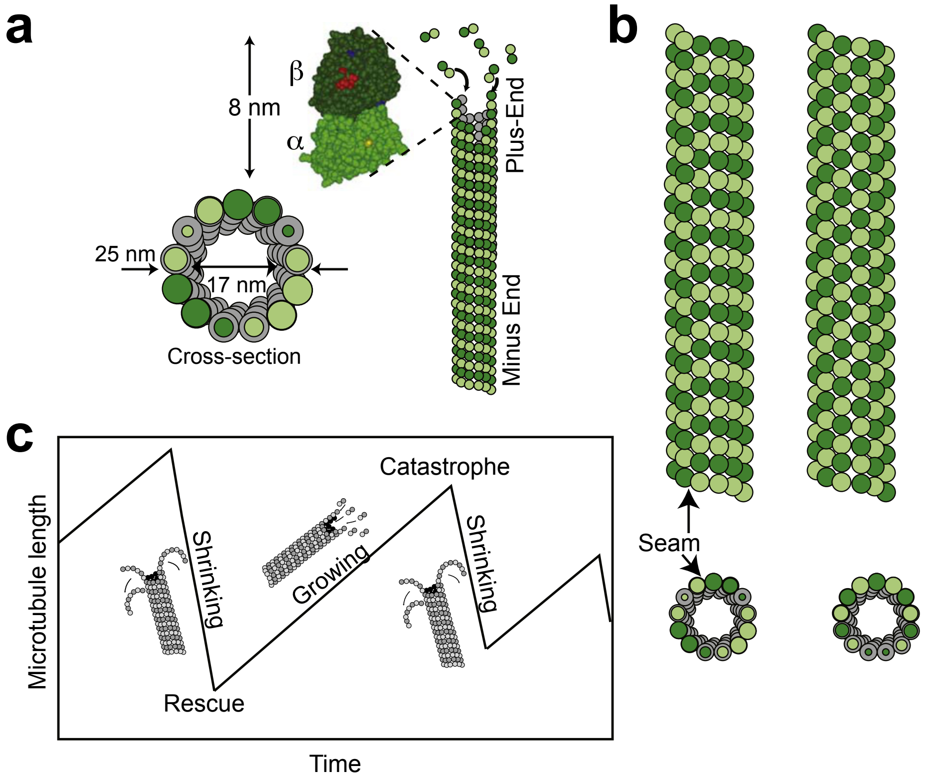

Fig: 0.2: Microtubule structure and dynamics (a) α & β tubulin heterodimers assemble longitudinally to form protofilaments that laterally associate to form the tubular form of microtubules. Microtubules have an outer diameter of 25 nm and an inner diameter of 17 nm. **(b)** (Left) Microtubule in a B (homotypic) lattice configuration with a single seam showing A (heterotypic) lattice contacts. (Right) Microtubule showing A-lattice configuration. There is no seam in an A-lattice. **(c)** Dynamic instability: microtubules grow and shrink by gain /loss of dimers. Stochastic transitions from shrinkage to growth are termed 'catastrophes' and vice versa, 'rescues' (Taken from Hawkins *et al.*, 2010).

0.2.3 Molecular motor proteins

Microtubule based motor proteins constitute a class of MAPs that associate with microtubules and via hydrolysis of ATP (Adenosine tri-phosphate), use microtubules as tracks for movement. These include the kinesin superfamily and cytoplasmic dyneins. Using the inherent polarity of microtubules, these motor proteins achieve directed transport of intracellular cargo. Dyneins move or walk towards the minus end of microtubules (Vale, 2003). Most members of the kinesin family are plus (or growing) end directed with some kinesins (Eg: kinesin-14) that are minus end directed. Besides their role in transport of cargoes, they can also crosslink microtubules and generate forces that slide and bend microtubules (Hirokawa *et al.*, 2010). Motor proteins are also active force generators and can exert stall forces upto 7 pN in the case of kinesin-1 (Blehm *et al.*, 2013). The bending and buckling action of microtubules in cells has been predominantly attributed to the action of motor proteins (Bicek *et al.*, 2009; Pallavacini *et al.*, 2017, Blob *et al.*, 2025). The kinesin superfamily comprises of 45 genes that constitute 14 distinct families (See **Fig 0.3**). Despite this diversity, all kinesins possess a motor domain that contains the microtubule binding domain as well as the nucleotide (ATP) binding domain, that is conserved across all families. The position of the motor domain dictates the direction of movement. Plus-end directed kinesins contain the motor domain at the N-terminal and are referred to as N-kinesins, whereas minus end directed kinesins contain the motor domain at the C-terminal and are referred to as C-kinesins (See **Fig 0.3**).

The experiments in this dissertation was performed using kinesin-1 which is an ubiquitous kinesin expressed across most cell types. It was the first kinesin motor identified by Ron Vale in 1985 (Vale *et al.*, 1985) and is plus-end directed. The structure of kinesin-1 (See **Fig 0.4**) consists of a dimer of heavy chains (KHC) bound to two light chains (KLC). In humans, there exists three isoforms of the KHC (KIF5A, KIF5B and KIF5C) and four for KLC (KLC1-4). KIF5B is ubiquitous, whereas KIF5C is specific for neurons (Kanai *et al.*, 2000). In addition to the motor domain, most kinesins have a flexible neck linker region and a stalk that is made up of coiled-coiled domains that is important for dimerizations. The stalk also connects the KHC to the KLC domains that bind to cargo and adaptor proteins (Kawaguchi *et al.*, 2013). Adaptor and scaffold proteins like TRAK1 link motors to organelles for transport (Hirokawa *et al.*, 2009).

Kinesins and dynein play a crucial role in the mitotic spindle and the depolymerizing activity of kinesin-13 (MCAK) is pivotal for regulating microtubule length in the spindle (McClung and Walczak, 2011). Furthermore, self-organization of the microtubule network by motor proteins is pivotal for symmetry-breaking and cell polarization. Kinesin-1 moves along microtubules by ATP hydrolysis and moves processively in 8 nm steps (size of tubulin heterodimer). The motile action of just unloaded motors was found to cause tubulin loss in the microtubule lattice (Triclin *et al.*, 2021, Carbo *et al.*, 2022). A recent study found that the force generated by 3 or more kinesin-1 motors is capable of triggering the loss of one tubulin dimer from the lattice, suggesting that motor proteins act as active force generators that may damage microtubule integrity in cells (Thery and Blanchoin, 2021). It thus becomes interesting to explore how microtubule integrity is maintained in cells where microtubules exist in association with motor proteins.

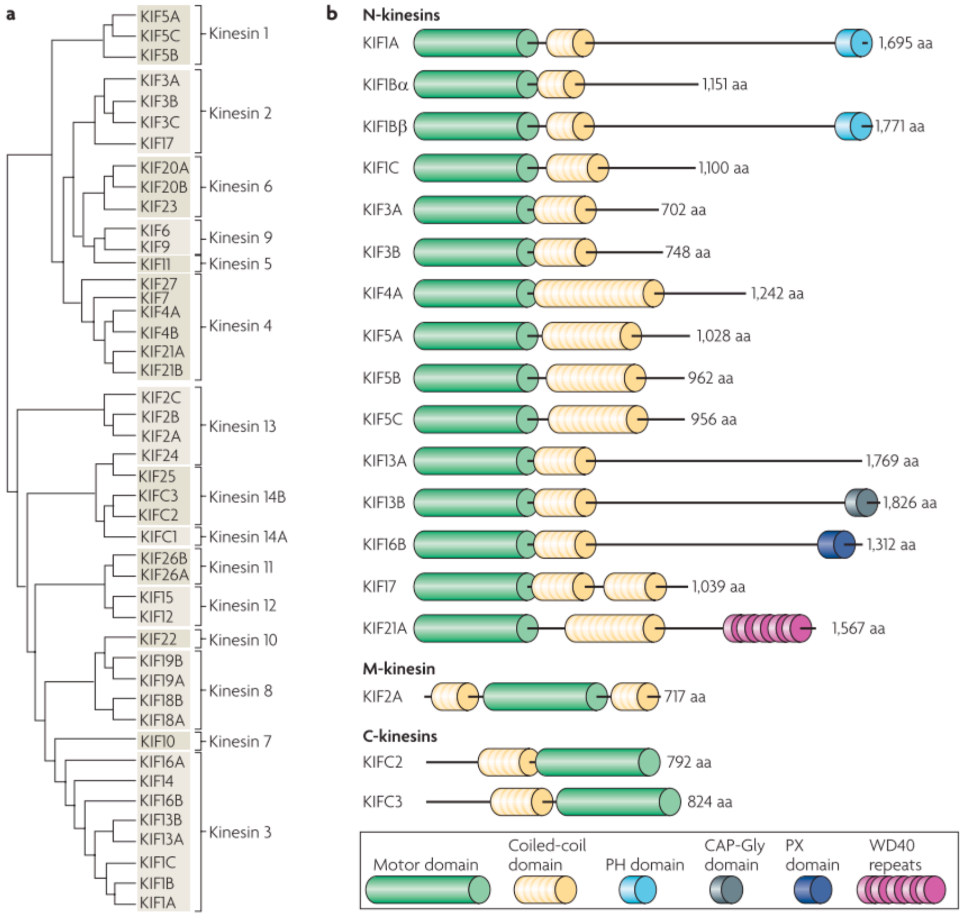

Fig 0.3: List of (a) kinesin families and (b) the different domains present in both N and C- kinesins (Taken from Hirokawa *et al.*, 2009).

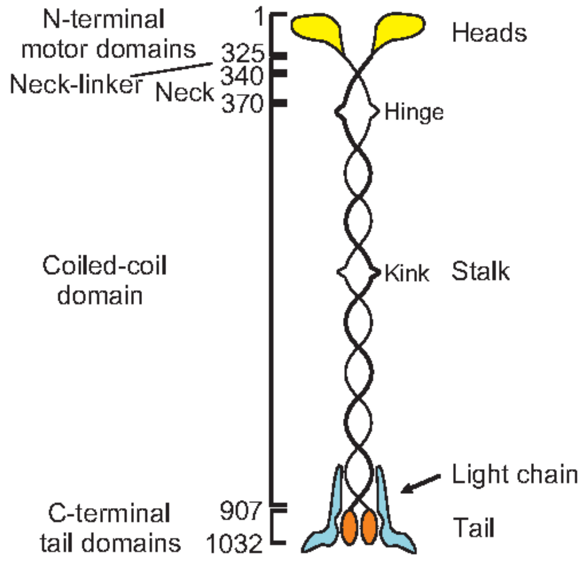

Fig 0.4: Structure of kinesin-1: Kinesin-1 exists as a dimer with a heavy chain (KHC) consisting of a N-terminal globular motor domain (340 aa), a neck linker region. A flexible hinge region connects the neck linker to the stalk with the coiled-coil domains that are important for dimerization. The stalk region also mediates interaction with the light chain (KLC) which is important for binding of cargo and adaptor proteins. (Taken from Kawaguchi *et al.*, 2013).

0.2.4 Microtubule network remodeling is critical to several cellular processes

Microtubules are indispensable for several cellular functions: They provide polarized tracks for intracellular transport by motor proteins like kinesin and dynein, enabling directed movement of vesicles and organelles. Their metastable nature is crucial for separation of chromosomes in the mitotic spindle. They are also critical for establishing and maintaining cell polarity (Ganguly *et al.*, 2012), particularly in polarized cells such as neurons, wherein along with MAPs they organize the architecture and morphology of axons and dendrites (Huang *et al.*, 2022). Beyond this, they form the structural core of diverse sub-cellular assemblies like the marginal band in platelets (van Deurs and Behnke, 1973), centrioles in centrosomes and the axonemal structures of cilia and flagella (Goodson and Jonasson, 2018). These diverse functions highlight their dual roles as stable structural elements as well as dynamically adaptable filaments.

Research in the past few decades has shown that cells can sense and respond to forces through active remodeling of the cellular cytoskeleton (Momotyuk *et al.*, 2025; Putra *et al.*, 2023; Poongkitwitton *et al.*, 2016; Fletcher and Mullins, 2010). Dynamic remodeling of the cellular microtubule network is pivotal for mitosis, cellular differentiation, and to establish polarity (Muroyama & Lechler, 2017; Ganguly *et al.*, 2012; Desai and Mitchison., 1997). Microtubules also serve as tracks for intracellular transport of cargoes by microtubule-based molecular motor proteins kinesin and dynein (Barlan & Gelfand, 2017). Microtubules are known to be sensitive to biochemical cues such as temperature, viscogens, and ions (Fernandes & Aumerier, 2024; Molines *et al.*, 2024; Fygenson *et al.*, 1994). They are also sensitive to mechanical cues- In plants, microtubules align with the axis of maximum tension (Hamant *et al.*, 2019). Microtubules bend and buckle under compressive forces (Brangwynne *et al.*, 2006) and orient along the direction of stress during morphogenesis to effect changes in cell shapes (Salbreux *et al.*, 2012). Refer to Chapter 1 for an overview of the origin and types of forces acting on microtubules.

The diversity of these functions raises fundamental questions: how are distinct microtubule subsets spatially organized and differentially regulated in cells? Given their high bending rigidity, how is microtubule integrity preserved under constant mechanical and biochemical stress in the intracellular environment?

Addressing these questions requires a deeper understanding of how the metastable nature of microtubules and cellular regulatory mechanisms converge to maintain both adaptability and mechanoresilience.

0.3 Heterogeneous nature of the microtubule lattice

Emerging evidence suggests that the microtubule lattice both *in vitro* and in cells is not uniform and is largely heterogeneous as a result of structural irregularities as well as the existence of different tubulin isotypes, as detailed below:

0.3.2 Lattice defects and irregularities

During polymerization, microtubules incur lattice irregularities or 'defects'. A lattice defect may be defined as a deviation from the regular protofilament arrangement. It was found that these structural defects are more likely to occur during fast growth conditions and when high tubulin concentrations were used for growth (Schaedel *et al.*, 2019; Kurachi *et al.*, 1995; Chretien *et al.*, 1992). Electron and atomic force microscopy have revealed the presence of different types of defects: Missing tubulin dimers ('point defects or dimer vacancies'), gaps between neighboring protofilaments, as well as protofilament mismatches (wherein there is a switch in the protofilament number) (Schaap *et al.*, 2004; Chrétien *et al.*, 1992), and seam-related vacancies. Refer to **Table 0.1** for an overview of types of defects. Microtubules polymerized in the presence of Taxol (microtubule-stabilizing drug) were also found to show a higher proportion of protofilament transitions (Arnal & Wade, 1995). Though Chrétien *et al.*, 1992 showed that protofilament transitions occur with an average separation of a few micrometers using *Xenopus* cell-free extracts, the frequency and types of defects that occur *in vivo* is largely unknown. Recent advances in cryo-ET techniques have helped identify the presence of lattice openings in cellular microtubules (Guyomar *et al.*, 2022; Chakraborty *et al.*, 2020; Atherton *et al.*, 2018). Guyomar *et al.*, (2022 showed that the seam number and location of defects are highly heterogeneous amongst microtubules. It is still under debate whether the microtubule seam constitutes a weak section of the lattice (Motta, Biswas *et al.*, 2023).

Type of defect	Description	Frequency/evidence	References
Protofilament transitions	Switch in no: of protofilaments (eg: 12 to 13; 14 to 15) along the same microtubule	Occurs approximately every few µms in microtubules grown *in vitro.* Frequencies range between 0.007 -0.04 µm^{-1} (*in vitro).*	Schaedel *et al.,* 2019*;* Atherton *et al.*, 2018; Arnal and Wade, 1995; Chrétian *et al.*, 1992
Variations in seam number	Presence of multiple seams (α–β lateral or heterotypic contacts). Potential weak sites. Result from monomer/dimer vacancies.	Heterogeneous in microtubules grown from *Xenopus* extracts. Frequent in microtubules grown *in vitro* (ranging from 0-5 seams).	Guyomar *et al.*, 2022; Howes *et al.*, 2017; Kikkawa *et al.*, 1994

Lattice-type transitions (Monomer/dimer vacancies)	Localized loss of a monomer or dimer within the lattice, appear as discontinuities between protofilaments. Lead to lattice- type transitions and formation of multiple seams.	Arise spontaneously *in vitro* especially under fast-growth conditions at high tubulin concentrations. Occur with a frequency of 3.69 μm^{-1} in *in vitro* and 0.1 μm^{-1} in microtubules constituted from *Xenopus* cell extracts.	Guyomar *et al.*, 2022.
Lattice openings/breaks	Discontinuities or openings in the microtubule wall	Observed in cellular microtubules	Guyomar *et al.*, 2022; Chakraborty *et al.*, 2020
Undefined defects	Combination of multiple defects leading to lattice heterogeneity	Observed in cryo-ET studies of *in situ* microtubules; frequency was shown to vary amongst cell types	Guyomar *et al.*, 2022; Chakraborty *et al.*, 2020

Table 0.1: Overview of the types of structural defects found in microtubules.

0.3.2 Tubulin code

Tubulin code refers to the emerging concept that different tubulin isotypes, together with post-translational modifications, modulate the composition of microtubules as well as have functional implications on microtubule stability and interactions (Janke & Magiera, 2020). The tubulin code offers cells biochemical tubulin diversity. In humans, there exist 9 isoforms of both α and β-tubulin with α1A (TUBA1A) and βI (TUBB) being expressed ubiquitously across most cell types (See **Fig 0.5**). Tubulin isotypes can indirectly influence the mechanics of microtubules by influencing microtubule structure in terms of regulating the protofilament number as well as affecting polymerization dynamics (Vemu *et* al., 2017; Pamula *et* al., 2016; Panda *et al.*, 1994). In cells, microtubules exist as mosaic structures of different tubulin isotypes. A recent *in vitro* study showed that copolymerization of different tubulin isotypes resulted in sectioned microtubules that showed differences in protofilament number as well as affinity to certain MAPs (Prakash *et al.*, 2025). Additionally, the mechanical properties of microtubules are also further diversified with distinct post-translational modifications (PTMs) that predominantly modify the CTTs of both α and β-tubulin (See **Fig 0.5**). Table 0.2 shows a list of the predominant PTMs, their occurrence and the enzymes that carry out the modifications.

For a detailed review on the role of the tubulin code in regulating microtubule mechanics, refer to Chapter 1.

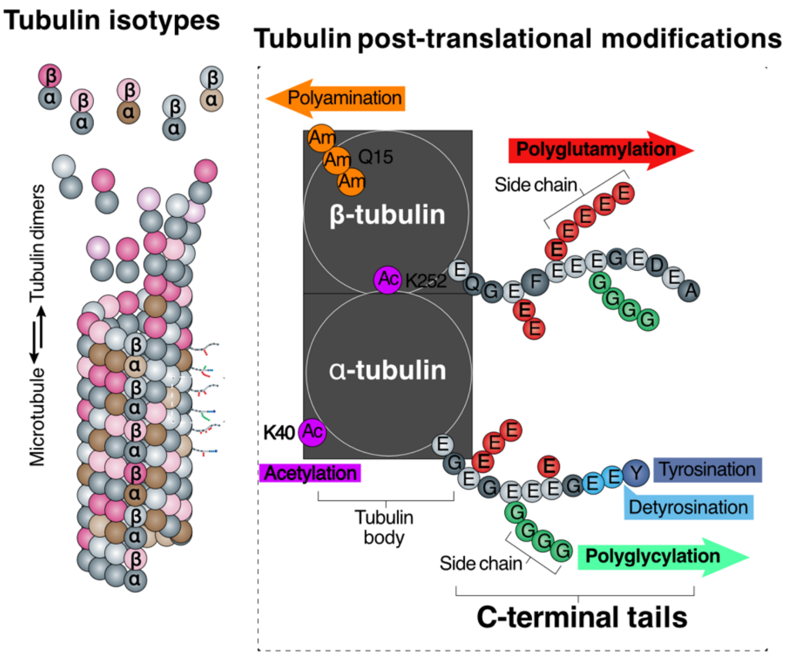

Figure 0.5: Tubulin code adds an additional layer of heterogeneity to microtubule composition. Microtubules can be composed of different tubulin isotypes and can further undergo modifications at the CTT of both α and β-tubulin by a variety of PTMs (Adapted from Janke and Magiera., 2020).

Post-translation modification	Occurs on	Modifications	Mediated by the enzymes
Acetylation	Lysine 40 residue on α- tubulin. Occurs in the lumen.	Addition of acetyl groups	αTAT-1 (α- tubulin-N-acetyltransferase-1)
Detyrosination	C-terminal tail of α- tubulin	Removal of tyrosine residue	VASH-1/2- SVBP (Vasohibin 1/2 with Small Vasohibin Binding Protein) complex
Tyrosination	C-terminal tail of α- tubulin	Addition of tyrosine residue	TTL (Tubulin Tyrosine Ligase)
Polyglutamylation	C-terminal of both α and β tubulin	Addition of glutamate residues	TTLLs (Tubulin Tyrosine Ligase-Like enzymes)
Polyglycination	C-terminal of both α and β tubulin	Addition of glycine residues	TTLLs (Tubulin Tyrosine Ligase-Like enzymes)
Phosphorylation	Mostly β tubulin	Addition of phosphate groups	Various Kinases (CDKs-Cyclin Dependent Kinases)

Table 0.2: Overview of the types of PTMs found in microtubules (Roll Mecak., 2020; Janke and Magiera, 2020).

0.4 Lattice dynamics and ability to self-repair

Structural imperfections and non-uniformity in the lattice serve as local hotspots that can influence the stability, dynamics, and response of microtubules to external factors like force and MAPs. Lattice defects induced by Taxol (a microtubule targeting drug) was shown to influence growth rate, catastrophe, and rescue rates at the microtubule tip using *in vitro* reconstitution studies with purified tubulin and minimal components (Rai *et al.*, 2021). Emerging evidence also suggests that these discontinuities are pivotal for the incorporation of new tubulin dimers into the lattice of existing microtubules, thus promoting localized tubulin turnover and enhancing microtubule stability (Motta, Biswas *et al.*, 2023; Cross, 2019; Schaedel *et al.*, 2019). Microtubules exposed to stress by orthogonal fluid flow (Schaedel *et al.*, 2015) and motor forces (Triclin *et al.*, 2021) exhibited localized tubulin turnover along the lattice, indicating that this process of tubulin turnover also serves as a process by which microtubules can self-repair against lattice damage.

In addition, cellular microtubules may be constituted from tubulin of different isotypes and post-translational modifications that contribute to further diversity and heterogeneity in terms of microtubule lattice conformations (Janke *et al.*, 2020). Recent studies also show that binding of certain MAPs like End-Binding (EB proteins) and kinesin-1 motors (Chew *et al.*, 2025; Peet *et al.*, 2018; Loeffelholz *et al.*, 2017) can modulate lattice conformations. Together, these findings tell us that far from being a passive structure, the metastable lattice is dynamic, much like the microtubule tip. Microtubule lattice remodeling can thus be influenced by 'effectors' like MAPs, motors, Microtubule Targeting Agents (MTAs) and force. This intrinsic lattice plasticity, in combination with their mechanical properties enable microtubules to serve as a heterogenic interface that can sense mechanical stimuli and translate them into biochemical cues via lattice remodeling, thus effecting cellular level mechanoadaptation. For a detailed review on how the different effectors modulate lattice remodeling and contribute to microtubule-based mechanoadaptation, see Chapter 1.

0.5 Traditional view vs emerging paradigm

The tensegrity model of cell mechanics, proposed by Donald Ingber in the 1980s, conceptualizes the cellular cytoskeleton as a pre-stressed structure. According to this model, cellular shape and mechanical stability are maintained as a balance between tension and localized compression. In this framework, microtubules are described as rigid struts that resist compression whilst actin and intermediate filaments bear tensile forces (Ingber, 1993; Ingber 2003). Early studies provided substantial support to this model- disruption of the microtubule network resulted in an increase in cell contractility (Wang *et al.*, 2001) and live-cell imaging showed that microtubules in cells buckle under compression (Brangwynne *et al.*, 2006).

However, emerging evidence shows that microtubules are dynamic, display constant tubulin turnover and self-repair in response to force (Schaedel *et al.*, 2015) as well as the action of motor proteins (Geng *et al.*, 2025; Tsitov *et al.*, 2022; Triclin *et al.*, 2021). These findings indicate that microtubules are mechanoadaptive and capable of remodeling their lattice in real time rather than functioning as static load-bearing elements. Rheological and modelling studies also show that the cytoskeletal force landscape constitutes cytoskeletal crosstalk amongst the different filaments, active force generation by molecular motor proteins, and the viscous cytosol (Yang *et al.*, 2024; Wu *et al.*, 2022).

At the actin-rich cortex and at focal adhesion sites, tethered microtubules were found to exist under tensile stress using laser ablation experiments (Colin *et al.*, 2018), challenging one of the core assumptions of the tensegrity model. This suggests that microtubules act as dynamic modulators that are force-sensitive, can remodel and integrate mechanical and biochemical feedback to achieve cellular mechanoadaptation (refer to **Fig 0.3**).

Contemporary perspectives thus favour an updated view of the tensegrity model that accounts for the dynamic and adaptive nature of the filaments, interactions between the different filament networks and crosslinkers, as well as the effect of the viscoelastic cytoplasm along the lines of the biochemomechanical tensegrity model proposed by Sun *et al.*, 2023. In this framework, cellular shape and mechanical stability are maintained as a result of dynamic, feedback-driven interaction amongst cytoskeletal filament networks, crosslinkers, and the viscoelastic cytoplasm.

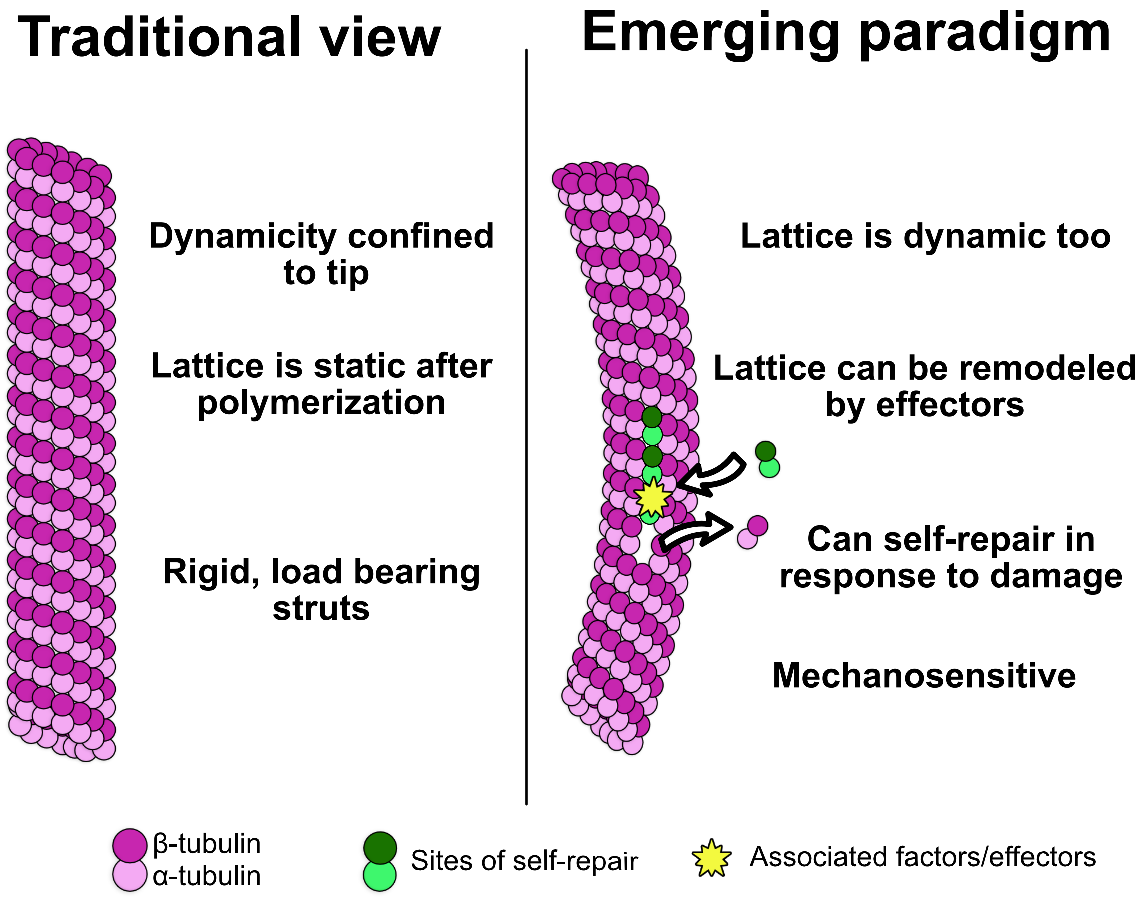

Fig 0.6: Traditional view vs emerging paradigm on the nature and role of microtubules.

In this emerging perspective (See **Fig 0.6**) fortified by recent evidence, microtubules are increasingly being viewed as dynamic filaments that exchange tubulin subunits along its entire length and can remodel or repair tubulin loss resulting from damage. Thus, moving away from their role as passive struts that can bear mechanical force, recent evidence show that microtubules can actively sense and adapt to forces. This calls for studies that explore how the material properties of microtubules along with their metastable nature enable microtubules to sense and adapt to stimuli. In this context, it is also interesting to explore how this adaptation is mediated and since in cells, microtubules exist in association with a repertoire of diverse proteins and PTMs, how this adaptation is mediated by factors separate from inherent metastability.

0.6 Research questions addressed

As outlined above, microtubules are inherently metastable polymers, with their metastable nature being reflected in both tip and lattice dynamics. While dynamic instability at the tip governs growth and shrinkage, lattice dynamics enables microtubules to be adaptable in response to external factors as well as damage.

Considering that microtubules are central to several cellular functions like intracellular transport, mitosis, polarization during cell migration, an essential question arises: how is the intrinsic metastable nature of microtubules regulated in cells to (re)organize, modulate and maintain functionally distinct microtubule subsets?

Despite their high rigidity, microtubules must navigate a crowded challenging intracellular environment. They are seen to frequently adopt curved shapes in cells, indicating that they experience substantial forces in the intracellular environment. Understanding **how microtubule integrity is preserved under stress is fundamental to understand how microtubule function is regulated in cells.**

This dissertation addresses the overarching question:
How does the metastable nature of microtubules govern their response and adaptation to stress?

To answer this, in the first part of my work, I investigate **how microtubule damage as well as self-repair mechanisms are influenced by mechanical stress that mimics intracellular force regimes.** Previous studies show that microtubules can sense and adapt to mechanical stimuli. Microtubules can self-repair in response to bending by orthogonal fluid flow (Schaedel *et al.*, 2015) and the action of molecular motor proteins (Triclin *et al.*, 2021). These studies suggest that lattice dynamics constitute an intrinsic adaptive response to damage induced by mechanical stress.

However, it is unclear **whether inherent microtubule self-repair mechanisms are sufficient to preserve microtubule integrity against forces that act on them in the cellular environment**. To address this gap, I developed *in vitro* assays that recapitulate microtubule bending and buckling as seen in cells and consequently perform a quantitative analysis of microtubule self-repair and survival under the influence of different components that may contribute to this mechanical stress.

In cells, microtubules exist in association with intracellular factors, MAPs and are also diverse in composition due to the tubulin code. This raises the second key question: **how do intracellular factors, MAPs, and the tubulin code influence microtubule lattice remodeling and**

microtubule stability under mechanical load? This work further examines how these factors influence microtubule dynamics and survival under mechanical stress.

In addition to mechanical stimuli, **microtubules serve as targets for a variety of therapeutic strategies, that predominantly use microtubule targeting chemical agents or drugs to perturb microtubule dynamics and thus disrupt cell division. Hence, in the latter part of this dissertation, I investigate how chemical perturbations to microtubules by drugs affect microtubule dynamicity and how this translates to cellular-level implications.**
Together, these studies aim to elucidate how microtubule metastability underlies their mechanoadaptive nature and are thus crucial for microtubule-based cellular functions.

0.7 Aim and Objectives

The primary research question of this dissertation as stated above focusses on investigating microtubule response to stress (both mechanical and chemical in nature) in an attempt to elucidate the mechanisms that regulate microtubule integrity, metastability and survival within the challenging intracellular environment.
This is addressed through five inter-related studies, each of which explores a distinct aspect of microtubule response under stress:
Study 1 investigates how microtubules withstand damage and undergo corresponding self-repair when subjected to bending and buckling forces. With an emphasis on subjecting microtubules to mechanical stress similar to what they face in the intracellular environment, I develop *in vitro* assays that recapitulate intracellular mechanical stress.

Objective 1.1: To standardize and optimize a protocol for the preparation of capped GDP-microtubules free of stabilizing agents.
Though previous *in vitro* studies have explored self-repair in the presence of motor proteins, these studies have been performed on Taxol-stabilized microtubules. The presence of Taxol has been shown to soften and stabilize microtubules (Hawkins *et al.*, 2013; Lopez and Valentine, 2014). Closer to physiological conditions, we aimed to use GDP microtubules in our assays.

Objective 1.2: To establish an *in vitro* assay setup that mimics intracellular bending and buckling stress.
Observing microtubule bending shapes in live cells (refer to Chapter 2) reveals that microtubules display dynamic bending events (characterized by frequent change in curvature) and tend to persist in bent conformations for long periods of time. Therefore, we sought to:

Specific objective 1.2.1: Assess microtubule self-repair in microtubules maintained in static bent conformations.

Specific objective 1.2.2: To develop an *in vitro* assay setup to subject microtubules to buckling action mediated by motor proteins, as in the intracellular environment.

Specific objective 1.2.3: To evaluate microtubule self-repair and survival under motor-induced buckling.

Objective 1.3: To perform kinesin-driven microtubule buckling assays in the presence of HEK293 cell lysates to investigate the role of intracellular factors in microtubule survival.

Study 2 examines the temporal evolution of lattice dynamics using multi-cycle tubulin incorporation assays.

Study 3 explores the relationship between microtubule lattice dynamics and how tubulin loss is accelerated with increasing microtubule curvature.

Study 4 investigates how variations in the tubulin code influence microtubule response to mechanical stress, exploring how cells may integrate biochemical regulation with microtubule mechanics and resilience.

Study 5 characterizes the microtubule depolymerization potential of a lesser known depolymerizing drug – Pretubulysin. Further, I investigate how perturbations to the dynamic instability at the microtubule ends impact microtubule behaviour both at the filament and cellular level.

Together, these studies provide a comprehensive framework to explore how the metastable nature of microtubules enable them to sense, adapt in the face of stress that is mechanical and chemical in nature.

0.8 Outline of Thesis

The chapters of this thesis are organised as follows:

Chapter 1 provides a comprehensive review of existing literature on the type and origin of forces acting on microtubules in cells and describes the unique mechano-adaptive properties of microtubules that enable them to sense, adapt, and respond to mechanical stimuli. The chapter highlights recent studies on the role of effectors- MAPs, motor proteins, and the tubulin code- in aiding microtubule function and discusses the emerging role of microtubules as cellular mechanosensors.

Chapter 2 details the core findings of my PhD dissertation, wherein I investigate the limits of inherent microtubule self-repair mechanisms in preserving microtubule integrity under mechanical stress **(Study 1)**. By establishing an *in vitro* assay setup that mimics intracellular bending and buckling, the study reports the limits of microtubule self-repair. Complementing experimental observations with simulation data as well as cellular approaches, the work analyzes the relationship between curvature and motor-force-induced microtubule damage. I demonstrate that the presence of intracellular factors enhances microtubule survival, underscoring the importance of additional cellular-based regulatory mechanisms in preserving microtubule integrity.

Microtubule lattice dynamics is inherent to the metastable nature of microtubules and their function. **Chapter 3** explores the nature of microtubule lattice dynamics, investigating the nature of defect propagation using tubulin incorporation as a readout **(Study 2)**. I also take a closer look at the relationship between microtubule lattice dynamics and bending stress (static curvature). I show how microtubule lattice dynamics can be modulated by curvature **(Study 3)**.

In **Chapter 4**, I investigate the possible role of microtubule post-translational modifications (PTMs) and tubulin isotypes in modulating microtubule response to mechanical force **(Study 4)**. I compare the trends of survival under mechanical stress, of microtubules grown from tubulin purified from bovine brain (rich in PTMs) vs from tubulin purified from HeLa cells (lacking certain PTMs and tubulin isotypes).

In **Chapter 5**, along with immune-cell based studies with collaborators, I show how microtubule destabilizing agents interfere with microtubule dynamics using the case study of a new microtubule depolymerizing drug - Pretubulysin. The study showcases how perturbations in microtubule dynamics and mass have cellular-level implications **(Study 5)**.

0.9 References

1. Blehm, B. H., Schroer, T. A., Trybus, K. M., Chemla, Y. R., & Selvin, P. R. (2013). In vivo optical trapping indicates kinesin's stall force is reduced by dynein during intracellular transport. Proceedings of the National Academy of Sciences of the United States of America, 110(9), 3381–3386.
2. Brangwynne, C. P., MacKintosh, F. C., & Weitz, D. A. (2006). Force fluctuations and polymerization dynamics of intracellular microtubules. Journal of Cell Biology, 173(5), 733–741.
3. Colin, A., Singaravelu, P., Théry, M., & Blanchoin, L. (2018). Actin–microtubule cross-talk in cell mechanics and motility. Nature Reviews Molecular Cell Biology, 19(12), 733–745.
4. Desai, A., Mitchison, T.J. (1997). Microtubule polymerization dynamics. Annu. Rev. Cell Dev. Biol, 13, 83-117.
5. Ems-McClung, S. C., & Walczak, C. E. (2010). Kinesin-13s in mitosis: Key players in the spatial and temporal organization of spindle microtubules. *Seminars in cell & developmental biology*, *21*(3), 276–282.
6. Florian Huber et al. (2015). Cytoskeletal crosstalk: when three different personalities team up. Current Opinion in Cell Biology 32, pp. 39–47.
7. Ganguly, A., Yang, H., Sharma, R., Patel, K. D., & Cabral, F. (2012). The role of microtubules and their dynamics in cell migration. The Journal of biological chemistry, 287(52), 43359–43369.
8. Geng Q, Bonilla A, Sandwith SN, Verhey KJ. (2025) Multi-kinesin clusters impart mechanical stress that reveals mechanisms of microtubule breakage in cells. J Cell Biol. 2025 Oct 6;224(10):e202501070. Doi: 10.1083/jcb.202501070. Epub 2025 Aug 11.
9. Geoffrey M. Cooper. (2000). Actin, Myosin, and Cell Movement. The Cell: A Molecular Approach. 2nd edition. Sinauer Associates, 2000.
10. Goodson, H. V., & Jonasson, E. M. (2018). Microtubules and Microtubule-Associated Proteins. Cold Spring Harbor perspectives in biology, 10(6), a022608.
11. Grimstone, A. V., & Klug, A. (1966). Observations on the substructure of flagellar fibres. Journal of cell science, 1(3), 351–362.
12. Hiller, G., & Weber, K. (1978). Radioimmunoassay for tubulin: a quantitative comparison of the tubulin content of different established tissue culture cells and tissues. Cell, 14(4), 795–804.
13. Hirokawa, N., Noda, Y., Tanaka, Y., & Niwa, S. (2009). Kinesin superfamily motor proteins and intracellular transport. Nature reviews. Molecular cell biology, 10(10), 682–696. https://doi.org/10.1038/nrm2774

14. Huang, L., Peng, Y., Tao, X., Ding, X., Li, R., Jiang, Y., & Zuo, W. (2022). Microtubule Organization Is Essential for Maintaining Cellular Morphology and Function. Oxidative medicine and cellular longevity, 2022, 1623181.
15. Ingber, D. E. (1993). Cellular tensegrity: Defining new rules of biological design that govern the cytoskeleton. Journal of Cell Science, 104(3), 613–627. https://doi.org/10.1242/jcs.104.3.613
16. Ingber, D. E. (2003). Tensegrity I. Cell structure and hierarchical systems biology. Journal of Cell Science, 116(7), 1157–1173. https://doi.org/10.1242/jcs.00359
17. Inoué, S., & Oldenbourg, R. (1998). Microtubule dynamics in mitotic spindle displayed by polarized light microscopy. Molecular biology of the cell, 9(7), 1603–1607. https://doi.org/10.1091/mbc.9.7.1603
18. Janke, C., & Magiera, M. M. (2020). The tubulin code and its role in controlling microtubule properties and functions. Nature reviews. Molecular cell biology, 21(6), 307–326. https://doi.org/10.1038/s41580-020-0214-3
19. Kanai, Y., Okada, Y., Tanaka, Y., Harada, A., Terada, S., & Hirokawa, N. (2000). KIF5C, a novel neuronal kinesin enriched in motor neurons. *The Journal of neuroscience : the official journal of the Society for Neuroscience*, *20*(17), 6374–6384.
20. Kawaguchi K. (2013). Role of kinesin-1 in the pathogenesis of SPG10, a rare form of hereditary spastic paraplegia. *The Neuroscientist : a review journal bringing neurobiology, neurology and psychiatry*, *19*(4), 336–344.
21. Mitchison, T, Kirscher, M. (1984). Dynamic instability of microtubule growth. Nature. 312, 237-242.
22. Mitchitson, T.J. (1993). Localization of an exchangeable GTP binding site at the plus end of microtubules. Science. 261, 1044-1047.
23. Nawrotek, A., Knossow, M., & Gigant, B. (2011). The determinants that Govern microtubule assembly from the atomic structure of GTP-tubulin. Journal of Molecular Biology, 412(1), 35–42.
24. Nikita B. Gudimchuk and J. Richard McIntosh. (2021). Regulation of microtubule dynamics, mechanics and function through the growing tip. In: Nature Reviews Molecular Cell Biology 22, pp. 777–795
25. Nogales, E. (2000). Structural insights into microtubule function. Annu. Rev. Biochem. 69, 277-302.
26. Nogales, E., Whittaker, M., Milligan, R. A., & Downing, K. H. (1999). High-resolution model of the microtubule. Cell, 96(1), 79–88.
27. Nogales, E., Wolf, S. G., & Downing, K. H. (1998). Structure of the alpha beta tubulin dimer by electron crystallography. Nature, 391(6663), 199–203.
28. Pamula, M. C., Ti, S. C., & Kapoor, T. M. (2016). The structured core of human β tubulin confers isotype-specific polymerization properties. The Journal of cell biology, 213(4), 425–433.
29. Panda, D., Miller, H. P., Banerjee, A., Ludueña, R. F., & Wilson, L. (1994). Microtubule dynamics in vitro are regulated by the tubulin isotype composition. Proceedings of the National Academy of Sciences of the United States of America, 91(24), 11358–11362.
30. Roll-Mecak A. (2020). The Tubulin Code in Microtubule Dynamics and Information Encoding. Developmental cell, 54(1), 7–20.
31. Schaedel, L., John, K., Gaillard, J., Nachury, M. V., Blanchoin, L., & Théry, M. (2015). Microtubules self-repair in response to mechanical stress. Nature Materials, 14(11), 1156–1163.
32. Sun S, Zhang L, Chen X, Feng X. (2023) Biochemomechanical tensegrity model of cytoskeleton. J.Mechanics and physics of solids, 175, 105288.
33. Triclin, S., Inoue, D., Gaillard, J., Htet, Z. M., DeSantis, M. E., Portran, D., Derivery, E., Aumeier, C., Schaedel, L., John, K., Leterrier, C., Reck-Peterson, S. L., Blanchoin, L., & Théry, M. (2021). Self-repair protects microtubules from destruction by molecular motors. Nature materials, 20(6), 883–891.
34. Tsitkov S, Rodriguez JB 3rd, Bassir Kazeruni NM, Sweet M, Nitta T, Hess H. (2022). The rate of microtubule breaking increases exponentially with curvature. Sci Rep. 12(1):20899.
35. Vale, R. D., Reese, T. S., & Sheetz, M. P. (1985). Identification of a novel force-generating protein, kinesin, involved in microtubule-based motility. *Cell*, *42*(1), 39–50.
36. Vale, R.D. (2003). The molecular motor toolbox for intracellular transport. Cell 112, 467-480.
37. van Deurs, B., Behnke, O. (1973). The microtubule marginal band of mammalian red blood cells. Z. Anat. Entwickl. Gesch. 143, 43–47.
38. Vemu, A., Atherton, J., Spector, J. O., Moores, C. A., & Roll-Mecak, A. (2017). Tubulin isoform composition tunes microtubule dynamics. Molecular biology of the cell, 28(25), 3564–3572.
39. Wang, N., Naruse, K., Stamenović, D., Fredberg, J. J., Mijailovich, S. M., Tolić-Nørrelykke, I. M., … & Ingber, D. E. (2001). Mechanical behavior in living cells consistent with the tensegrity model. Journal of Cell Science, 114(20), 3771–3781.
40. Yang, H., Henzel, T., Stewart, E. M., Anand, L., & Guo, M. (2023). An interpenetrating-network theory of cytoplasm. ArXiv, arXiv:2306.07256v1.

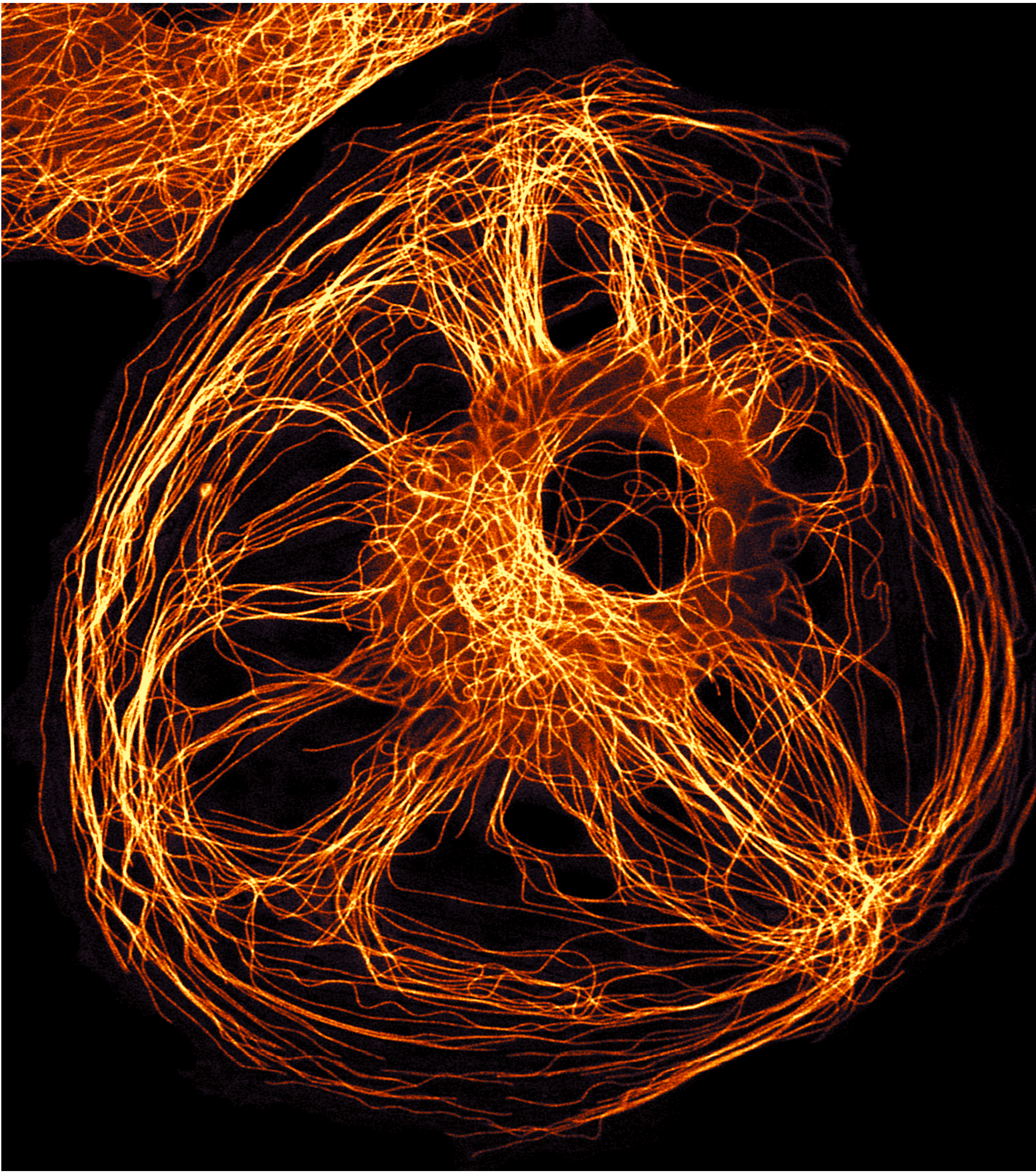

Chapter 1

The force-sensitive nature of microtubules and their role in cellular mechanosensing

In the review article below, we outline the force-sensitive nature of microtubules, trace the origin and nature of forces acting on microtubules and the properties of microtubules that facilitate their mechano-adaptive nature.

Faculty NT
Cumulative form of the dissertation
Confirmation of the contribution of co-authors

Title of the dissertation:

Metastable Microtubules: dynamic instability, lattice plasticity and mechanosensing

Title of the publication with all necessary bibliographic information:

The mechanoadaptive cytoskeleton: emerging role of microtubules

Quality of the publication, e.g. review article, conference contribution, research article, etc.:

Review article

Review process or publication status (in preparation, submitted, accepted):

In preparation. Invited review for AIP Biophysics Reviews

Explanation of the contributions of the co-authors:

Laura Aradilla Zapata (née Schaedel): conceptualization and supervision. Conceptualized and provided the initial draft of Figure 5.

Shweta Nandakumar: conceptualization, curated and reviewed literature, wrote the following sections:

(a) Abstract
(b) Introduction
(c) Sections I, II, III, IV a-d, IV f-g
(d) Conclusion

Curated the information displayed in Table 1 and 2. Conceptualized and designed figures 1, 2, 3.

Dyuthi Sreekumar: conceptualization, curated and reviewed literature, wrote the following sections:

(a) Section IV c, IV e
(b) Section V
(c) Conclusion

Conceptualized the design of Figures 1-4. Conceptualized and designed figure 4. Adapted and improved the design of Figure 5.

Signature of the doctoral candidate:

Shweta. N

Shweta Nandakumar

Signature of the **co-authors:**
(or, if applicable, the supervisor for **individual** co-authors - only in the event that these co-authors cannot be reached or do not have up-to-date contact details)

Name	Signature
Laura Aradilla Zapata (née Schaedel)	L. Aradilla
Dyuthi Sreekumar	

The mechanoadaptive cytoskeleton: emerging role of microtubules

Shweta Nandakumar [1*], Dyuthi Sreekumar [1*], Laura Schaedel [1,2*]

Affiliations:
[1] Experimental Physics and Center for Biophysics, Saarland University, 66123 Saarbrücken, Germany
[2] PharmaScienceHub (PSH), 66123 Saarbrücken, Germany
* Both authors contributed equally
* Corresponding author (laura.aradillazapata@uni-saarland.de)

Abstract

Microtubules are the most rigid and dynamic of cytoskeletal filaments. They are central to several cellular processes, including mitosis, cell polarization, and act as tracks for intracellular transport. Their inherent dynamic instability gives rise to their metastable nature and as shown recently, the microtubule lattice is also capable of incorporating free tubulin dimers, implying that much like the microtubule tip, the lattice is also dynamic in nature.

Owing to their rigid and hollow structure, microtubules have been conventionally regarded as rigid, passive scaffolds that can bear compressive forces exerted on them, without much change in their internal structure and dynamics. Research over the last decade challenges this notion- indicating that microtubules are sensitive to forces and can adapt themselves to stimuli by active remodeling of the lattice, recruitment of microtubule-associated proteins and other associated factors, thus triggering downstream mechanosignalling pathways. In this manner, microtubules not only play a pivotal role in structuring cellular response but act as a core mechanosensing element of the cellular cytoskeleton.

In this review, we explore the role of microtubules in cellular mechanosensing and mechanoadaptation. We first outline the biophysical properties of microtubules, the type and origin of forces acting on microtubules, and then present evidence on how microtubules respond to mechanical force. We highlight the unique properties of microtubules that facilitate their mechanoadaptive behaviour and review recent findings implicating their involvement in the cellular mechanotransduction pathways. Finally, we discuss open questions and future directions for exploring the emerging role of microtubules as dynamic, mechanosensitive elements of the cellular cytoskeleton.

Introduction

The cellular cytoskeleton consists of an interconnected network of biopolymers, namely actin, intermediate filaments and microtubules, that gives cells their shape and size. The transmission and adaptive response to external force, as well as those generated in the intracellular environment, is critical for cellular function. Cells can sense and respond to forces through active remodeling of the cellular cytoskeleton

(Momotyuk *et al*., 2025; Putra *et al*., 2023; Poongkitwitton *et al*., 2016; Fletcher and Mullins, 2010).

Microtubules are stiff, hollow biopolymers (having a diameter of 25 nm) made up of α and β-tubulin heterodimers (Mandelkow *et al*.,1986; Brouhard & Rice., 2008) that polymerize in the presence of guanosine triphosphate (GTP). Microtubules constitute the most dynamic component of the cytoskeleton and stochastically switch between phases of growth and shrinkage in a phenomenon termed 'Dynamic instability' (Cassimeris *et al*., 1988; Walker *et al*., 1988; Mitchison & Kirschener., 1984). Dynamic remodeling of the cellular microtubule network is pivotal for mitosis, cellular differentiation and to establish polarity (Muroyama & Lechler, 2017; Ganguly *et al*., 2012; Desai and Mitchison., 1997). Microtubules also serve as tracks for intracellular transport of cargoes by microtubule-based molecular motor proteins like kinesin and dynein (Barlan & Gelfand, 2017). Microtubules are known to be sensitive to biochemical cues like temperature, viscogens and ions (Fernandes & Aumerier., 2024; Molines *et al*., 2024 and Fygenson *et al*., 1994). Microtubule dynamicity is also modulated by force (Janson *et al*., 2003; Dogterom & Yurke, 1997). Force generation as a result of microtubule network dynamics has been implicated to play an important role in cell shortening during gastrulation, morphogenesis and tissue remodeling (Matis, 2020).

Microtubules are sensitive to mechanical cues

Research from the early 1970s on the behavior of microtubules in cells implicated that microtubules possess the ability to translate mechanical cues to cellular responses. Early models on microtubule-related thermodynamics predicted that axial compression of microtubules may promote microtubule assembly (Buxbaum and Heidemann, 1992). This was further correlated by Zheng *et al*.,1993 in a study wherein they found tension-induced microtubule polymerization during neurite initiation in fibroblasts as well as chick sensory neurons (Zheng *et al*., 1993). It was also reported that microtubule disassembly induced the expression of NF-κB transcription factor in endothelial cells (Rosette and Karin., 1995).

In plants, microtubules align with the axis of maximum tension (**Fig 1a)** (Hamant *et al*., 2019). Microtubules bend and buckle under compressive forces (Brangwynne *et al*., 2006) and orient along the direction of stress during morphogenesis to effect changes in cell shapes (Salbreux *et al*., 2012). Disruption of the cellular microtubule network using drugs like nocodazole (that inhibit microtubule dynamics) reduced cell stiffness and resistance (Wang *et al*., 2001). In epithelial cells, microtubule disruption caused loss of polarity (Sumigray *et al*., 2018).

Studies particularly focused on plant response to stimuli have also reported rearrangement of the plant microtubule cytoskeleton (Komis *et al*., 2002; Lü *et al*., 2007). In the last two decades, there has been increasing evidence on the influence of microtubule dynamics on actomyosin contractility as well as the essential role of microtubules in cellular mechanical response. Atomic force microscopy-based indentation studies showed that microtubules can withstand up to 15% lateral deformation before collapse (Schaap., 2006), suggesting that microtubules are inherently adaptable to mechanical stimuli.

As the most dynamic of cytoskeletal filaments, it is interesting to investigate how microtubules sense, adapt and respond to mechanical signals as a network. Also, is there a physiological relevance to how microtubules are sensitive to perturbations in the cellular environment, or is it a price that the cell must pay to be adaptable in a dynamic environment?

This review attempts to provide a comprehensive overview of the origin and type of forces that act on microtubules in the cellular environment, their influence on microtubule mechanics and the mechanisms that enable microtubules to resist these forces. We also highlight the unique properties of microtubules that help them serve as mechanoadaptive elements of the cellular cytoskeleton.

Understanding the impact of these different forces (in the cellular context) on microtubule mechanics and the consequent response of microtubules may augment our knowledge on how the dynamically adaptable and mechanosensitive nature of microtubules is central to cellular physiology.

I. The metastable nature of microtubules makes them dynamically adaptable

During polymerization, α and β-tubulin heterodimers come together in the presence of Mg^{2+}-GTP in a head-to-tail fashion to form protofilaments that then interact laterally to form ‘tubes’. Owing to the similarities in the periodic and regular arrangement of the microtubule wall and crystal lattices, Grimstone and Klug., 1966 proposed the term ‘lattice’ to refer to the microtubule wall structure.

Structural studies on the strength and stability of the lateral and longitudinal bonds between tubulin dimers in the microtubule lattice revealed that there exists an inherent anisotropy: lateral bonds between adjacent protofilaments are weaker than longitudinal bonds (Huang *et al*., 2008; Nogales *et al*., 1999).

During polymerization, microtubules incur lattice irregularities or ‘defects’. It was found that these structural defects are more likely to occur during fast growth conditions and when high tubulin concentrations were used for growth (Schaedel *et al*., 2019; Kurachi *et al*., 1995; Chretien *et al*., 1992). Electron and atomic force microscopy have revealed the presence of different types of defects: Missing tubulin dimers (‘point defects or dimer vacancies’), gaps between neighboring protofilaments as well as protofilament mismatches (wherein there is a switch in the protofilament number) (Schaap *et al*., 2004; Chrétien *et al*., 1992) and seam-related vacancies. Microtubules polymerized in the presence of Taxol (microtubule stabilizing drug) were also found to show a higher proportion of protofilament transitions (Arnal & Wade, 1995). Though Chrétien *et al*., 1992 showed that protofilament transitions occur with an average separation of a few micrometers using *Xenopus* cell-free extracts, the frequency and types of defects that occur *in vivo* are largely unknown. Recent advances in cryo-ET techniques have helped identify the presence of lattice openings in cellular microtubules (Guyomar *et al*., 2022; Chakraborty *et al*., 2020; Atherton *et al*., 2018). Guyomar *et al*., 2022 showed that the seam number and location of defects is highly heterogeneous amongst microtubules. It is still under debate whether the microtubule seam constitutes a weak section of the lattice (Motta, Biswas *et al*., 2023).

These imperfections in the lattice serve as local hotspots that can influence the stability, dynamic nature and response of microtubules to external factors like force and Microtubule Associated Proteins (MAPs). Lattice defects induced by Taxol was shown to influence growth rate, catastrophe and rescue rates at the microtubule tip using *in vitro* reconstitution studies with purified tubulin and minimal components (Rai *et al*., 2021). Emerging evidence also suggests that these discontinuities are pivotal for incorporation of new tubulin dimers into existing microtubules, thus promoting localized tubulin turnover and enhancing microtubule stability (Motta, Biswas *et al*., 2023; Cross, 2019; Schaedel *et al*., 2019). Microtubules exposed to stress by orthogonal fluid flow (Schaedel *et al*., 2015) and motor forces (Triclin *et al*., 2021) exhibited localized tubulin turnover along the lattice, indicating that this process of tubulin turnover helps microtubules self-repair against lattice damage.

In addition, cellular microtubules may be constituted from tubulin of different isotypes and post-translational modifications that contribute to further diversity and heterogeneity (Janke *et al*., 2020). Recent studies also show that binding of certain MAPs like End-Binding (EB proteins) and kinesin-1 motors (Chew *et al*., 2025; Peet *et al*., 2018; Loeffelholz *et al*., 2017) can modulate lattice conformations.

These findings tell us that far from being a passive structure, the metastable lattice is dynamic much like the microtubule tip. This lattice plasticity in combination with their mechanical properties enable microtubules to serve as an allosteric interface that can sense mechanical stimuli and translate them into biochemical cues via lattice remodeling, recruitment of associated factors, thus effecting cellular level mechanoadaptation.

II. Mechanical properties of microtubules

Electron microscopy *in vitro* studies in the early 1990's established microtubules as the most rigid of cytoskeletal filaments (Venier *et al*., 1994). Their flexural rigidity or bending stiffness (resistance to bending) is comparable to that of carbon nanotubes (Hawkins *et al*., 2010).

Owing to the difficulty in estimating the mechanical properties of microtubules in cells, most of the existing knowledge comes from *in vitro* studies. Over the years, numerous groups have quantified microtubule rigidity using different experimental approaches, resulting in substantial variability with estimates ranging from 0.03 mm to 46.8 mm (Hawkins *et al*., 2010). This variability likely arises from the measurement technique, the polymerization conditions as well as the presence/absence of microtubule stabilizing drugs.

Thermal fluctuations can serve as an indirect, yet powerful probe to assess microtubule stiffness, by analyzing the slight bending of microtubule filaments (predominantly longer microtubules) by thermal forces. The first quantitative estimation of the flexural rigidity of microtubules from thermal fluctuations using dark-field and video enhanced microscopy revealed that microtubules had a persistence length (L_p) of 1mm with a Young's modulus (E) of 1.2 gigapascals (Gittes *et al*., 1993). The study also reported that the persistence length increased to 5.2 mm for Taxol-stabilized microtubules, whilst more recent studies report a increase in microtubule flexibility with taxol, implicating that Microtubule Targeting Agents (MTAs) might also influence the stiffness of microtubules (Mitra & Sept. 2008; Arnal & Wade., 1995; Dye *et al*., 1993). Others have used approaches that directly exert external force: either by hydrodynamic flow, optical tweezers, atomic force microscopy or assays using immobilized kinesin (Hawkins *et al*., 2010; van Mameren *et al*., 2009; Kikumoto *et al*., 2006; Janson & Dogterom., 2004; Cassimeris *et al*., 2001; Kurachi *et al*., 1995; Felgner *et al*.,1996; Venier *et al*., 1994). By exerting osmotic pressure on microtubule bundles in the presence of a depletant, Needlemen *et al*., 2005, showed that microtubules buckle beyond a critical osmotic pressure (600 Pa) and are laterally deformed, thus indicating the flexible nature of the lateral tubulin bonds. Refer to **Table 1** for estimates of microtubule persistence length using different approaches.

It is challenging to directly measure microtubule persistence length in cells owing to the complex and heterogeneous cellular environment making it difficult to interpret the properties of a singular element often leading to contradictory results. Much of the existing data on mechanical properties of cellular microtubules is derived from studies on cilia. Bending rigidity of microtubule doublets in cilia was found to be 2- 4 x 10^{-24} Nm^2 with a persistence length of 0.5-1 mm (Battle *et al*., 2015). In a separate study on microtubules in the pillar cells of the inner ear, Tolmeo *et al*., 1997 reported a persistence length of 16 mm. The stiffness of microtubules was found to be largely also dependent on length- with shorter filaments being more flexible than longer ones

(Pampaloni *et al*., 2006; Taute *et al*., 2008). This behavior could stem from the anisotropy of tubulin bonds-owing to which microtubules exhibit high lateral deformability and longitudinal stiffness (Sim *et al*., 2013; Huber *et al*., 2013; Sui *et al*., 2010).

Microtubule stiffness is also influenced by growth conditions, specifically the growth concentration and presence of defects (Hawkins *et al*., 2012). Microtubules grown at higher concentrations of tubulin, tend to have more structural defects and this may result in them being more flexible (Kurachi *et al*., 1995; Janson and Dogterom., 2004). Microtubules grown in the presence of GMPCPP (guanylyl-(alpha, beta)-methylene-diphosphonate- a slowly hydrolyzable analog of GTP) were found to be 3-fold stiffer than those grown with GTP (Hyman *et al*., 1995) whereas the stiffness of microtubules grown with GTPγS was found to be comparable to microtubules polymerized in the presence of GTP (Taviare *et al*., 2013).

The presence and binding of MAPs are also known to affect microtubule stiffness. Hawkins *et al*., 2012 reported that small amounts (>1%) of MAPs can double the persistence length of microtubules as measured by thermal fluctuation experiments. Neuronal MAPs like Tau and MAP2 are reported to increase microtubule stiffness (Choi *et al*., 2009; Mickey and Howard., 2005) whereas MAP-65-1 (a microtubule bundling protein in plants) enhances microtubule flexibility by a factor of four (Portran *et al*., 2013). Post-translational modifications, particularly acetylation has been found to also influence persistence length of microtubules, helping microtubules become more flexible and resistant to breakage (Xu *et al*., 2017).

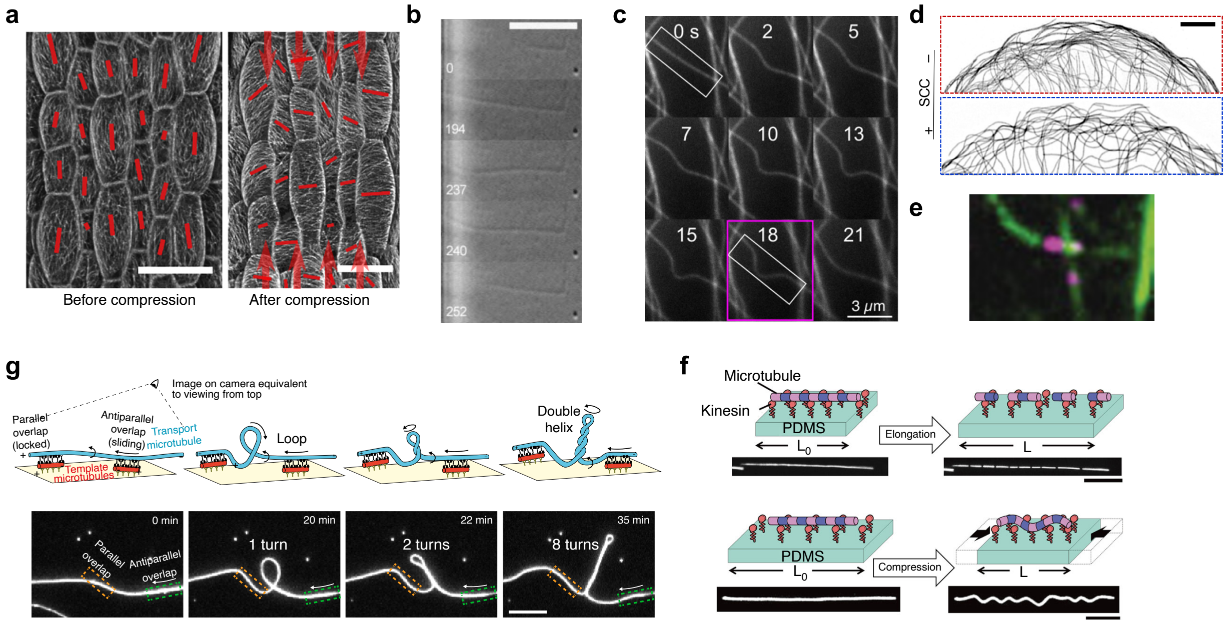

Fig 1: Microtubules are force sensitive. **(a)** Cortical microtubules before (left) and after (right) compression along the axis of the *Arabidopsis* hypocotyl (Robinson & Kuhlmeier, 2018). Scale bars: 50 μm **(b)** Time-lapse (in s) sequence of microtubules polymerizing and buckling. Scale bar: 5 μm (Janson *et al*., 2004). **(c)** Dynamic microtubule bending in LLC-PK1 cells. Scale bar: 3 μm (Bicek *et al*., 2009).

(d) Microtubules adopt buckled conformations after being subjected to stretch-compression cycles. Scale bar: 5 µm (Li *et al.*, 2023). **(e)** Self-repair (magenta) at microtubule crossover sites (green) in cells (Aumerier, Schaedel *et al.*, 2016). **(f)** Buckling of microtubules on kinesin-coated surfaces exposed to compressive forces (Kabir *et al.*, 2020). Scale bar: 10 µm **(g)** 2-D motility assay showing twisting and looping of transport microtubules sliding on template microtubules induced by the sliding action of kinesin-14 motors. Scale bar: 10 µm (Mitra *et al.*, 2020).

Study and approach	Value reported	Reference
Thermal fluctuations of Taxol stabilized microtubules	5.2 mm	Gittes *et al.*, 1993
Vesicle deformation studies using GDP-tubulin	6.3 ± 2.4 mm	Elbaum *et al.*, 1996
Thermal fluctuations of short Taxol stabilized microtubules (2.6 µm)	0.11 ± 0.05 mm	Pampaloni *et al.*, 2006
Thermal fluctuations of long Taxol stabilized microtubules (47.5 µm)	5.035 ± 0.8 mm	Pampaloni *et al.*, 2006
Optical trap buckling of Taxol stabilized microtubules	6.1 ± 1.3 mm	Van Mameren *et al.*,2009
Thermal fluctuations of microtubules with 18% Tau	2.2 ± 0.3 mm	Hawkins *et al.*, 2012
Microtubule doublets in cilia	0.5-1 mm	Battle *et al.*, 2015
Acetylated microtubules of GDP microtubules using microfluidics based bending assays	2 mm	Xu *et al.*, 2017
Taxol stabilized microtubules gliding over motors	0.1-0.5 mm	Sweet *et al.*, 2022
Curvature analysis of GDP microtubules immobilized to rigor kinesin coated surfaces	0.3 ± 0.09 mm	Wisanpitayakorn *et al.*, 2022.
Cellular cryo-ET studies measuring apparent persistence length by tracing microtubule shapes in interphase HeLa cells	45.6 µm	Chakraborty *et al.*, 2020

Table 1: Overview of microtubule persistence length measurements using different approaches.

III. Origin and impact of forces on microtubules

In cells, microtubules produce forces that shape their microenvironment, whilst also being subjected to forces that influence their behavior, resulting in a force-feedback mechanism that facilitates self-regulation. In this section, we detail how microtubule-based based force-balance effects the establishment of microtubule arrays and network (re)organization, essential for mitotic spindle formation, centrosome positioning and polarization. This force balance exists as a dynamic equilibrium between microtubule dynamicity, active forces generated by molecular motors and passive forces like friction.

In this section, we will focus on the different forces that act on microtubules, their magnitude as well as the physiological contexts in which these forces play a role:

a. Pushing and pulling forces generated by microtubule polymerization and depolymerization:

Early studies in the late 1980’s on microtubule dynamics revealed that microtubule polymerization and depolymerization serve as direct ways of force production by microtubules, but there remained a lack of quantitative studies on the magnitude of these forces (Fygenson *et al*., 1997; Elbaum *et al*.,1996; Inoue & Salmon, 1995; Waterman-Storer *et al*., 1995; Hotani & Miyamoto., 1990).

Janson *et al*., 2003, studied how dynamic instability of microtubules is regulated by force. Building upon earlier *in vitro* studies wherein they observed a decrease in microtubule growth velocity (from 1.2 μm/min to 0.2 μm/min) at opposing forces of 3-4 pN, the authors quantified the elastic response of a single, polymerizing microtubule pushing against a 2 μm-high microfabricated glass barrier (**Fig 1b)**. Estimating the force component along the growing end of the microtubule, they reported that the growth velocity decreased with increasing force and that contact with a rigid barrier resulted in stalled polymerization or catastrophe (Dogterom *et al*., 2002; Dogterom & Yurke., 1997). They hypothesized that the pushing force generated, changes the rate of tubulin incorporation at the microtubule growing end in concurrence with the Brownian ratchet model of force-velocity relation in growing microtubules. In these assays, they also reported events of microtubule sliding along the barrier and buckling under force (Janson *et al*., 2003).

In a recent study, Gelin *et al*., 2023, showed that forces generated by polymerizing microtubules are sufficient to penetrate through dense, cross-linked actin networks (as those found in the cell cortex) and that the frequency of these breaching events increased in the presence of the neuronal MAP- Tau. Thus, the force of a growing microtubule pushing against a rigid barrier like the cell cortex or an organelle may enhance microtubule catastrophe. This effect also explains how the cell achieves dynamic spatial microtubule organization wherein the microtubule catastrophe rate is higher at the cell periphery, thus limiting microtubule growth at the cellular boundaries as reported in (Mimori-Kiyosue *et al*, 2005; Komarova *et al*, 2002).

In contrast, pulling forces are generated on objects that are coupled to the other end (minus end) of a depolymerizing microtubule. During depolymerization, the elastic energy stored in the microtubule lattice as a result of GTP hydrolysis is released, generated substantial pulling force that can move organelles and kinetochores. Early *in vitro* studies reported a microtubule depolymerization driven movement of kinetochores required forces in the range of 3-5 pN (Koshland *et al*., 1988; Grishchuk *et al*., 2005; Mcintosh *et al*., 2008). Subsequent studies involving optical traps showed that depolymerizing microtubules can generate forces ranging from 30–65 pN. In the mitotic spindle, pulling forces are exerted by shrinking microtubule on the kinetochore-chromosome complex. It has been shown that the resulting tensile stress on microtubule helps stabilize the kinetochore-microtubule attachment (Volkov *et al*., 2013, Akiyoshi *et al*., 2010).

Pulling and pushing forces generated by microtubule plus end - cell cortex interaction has also been found to play a central role in centrosome and organelle positioning in yeast, but its role in centrosome positioning in mammals is still unclear (Tolic., 2008). A recent study by Schaeffer *et al*., 2024 showed that centrosome positioning occurs independent of microtubule forces in PtK2 epithelial cells and microtubules only play a role in remodeling the cytoskeleton following centrosome positioning.

Thus, pulling/pushing force-induced microtubule spatial organization plays a central role in mitotic spindle positioning, chromosome segregation, and nuclear (re)organization, thus offering the cell a route to regulate microtubule dynamicity in response to force or cell geometry (Gelin *et al*., 2023; Akiyoshi *et al*., 2010).

b. Effect of active forces arising from action of molecular motors

(i) Bending and buckling of microtubules

Despite being the stiffest of cytoskeletal filaments, microtubules in cells are often found to adopt bent and buckled forms with short wavelengths in the order of a few microns and with an average curvature of 0.3 μm^{-1} (Odde *et al*., 1999). Early studies reported that these bent microtubule shapes appear to be dynamic and change in the order of seconds (**Fig 1c)** (Miki-Noumara and Kamiya., 1976,1979; Schulze & Kirschner., 1988). It was also observed that microtubule in flagella adopted stable bent and helical shapes (Costello *et al*., 1973; Amos, 1978; Amos and Amos., 1991).

Though both microtubule bending and buckling in cells occur in tandem, it is important to distinguish the two phenomena. Bending occurs as a result of forces acting perpendicular to the microtubule, whereas buckling results when a force (beyond the buckling threshold) acts along the microtubule in a parallel direction.

Bending and buckling of microtubules result from microtubules being subjected to compressive forces. A recent study showed that microtubules adopted buckled forms in cells following stretch-compression cycles (**Fig 1d)** (Li *et al.*, 2023). Bending of microtubules (both *in vitro* and in cells) can result from the action of thermal fluctuations, polymerization forces, actomyosin contractility or due to the action of microtubule-based motor proteins. Considering the timescales over which microtubules persisted in the bent shape, the contribution of thermal fluctuations was deemed to be negligible (Wang *et al.*, 2001). Studies quantifying local microtubule curvature in response to thermal fluctuations found an apparent persistence length of 20 µm, much lower than the value reported from *in vitro* studies (Bragwynne *et al.*, 2007; Pallavicini *et al.*, 2014). Bicek *et al.*, 2009, studied microtubule bending in LLC-PK1 epithelial cells and observed curvatures higher than those expected from thermal forces alone.

The effect of pushing forces (3-4 pN) generated during microtubule polymerization against a barrier can bend and buckle microtubules (refer section above). Bicek *et al.*, 2009, found that though growing microtubule ends bend and buckle, buckling microtubules were also seen to bend more during depolymerization. The authors also further observed dynamic microtubule bending and buckling events following microtubule depolymerization by subjecting the cells to Nocodazole (microtubule depolymerizing drug), indicating that polymerization forces played a minor role in bending and buckling of microtubules.

In the cytoskeleton, myosin motors act in association with actin filaments and exert contractile forces (Waterman-Storer and Salmon., 1997). Forces generated by actomyosin contractility were hypothesized to cause microtubule bending and buckling (Brangwynne *et al.*, 2006; Gupton *et al.*, 2002; Waterman-Storer and Salmon., 1997). Bicek *et al.*, 2009, reported that microtubules continued to appear bent and buckled in cells even when treated with Blebbistatin (myosin inhibiting drug) and concluded that actin based retrograde flow occurred at time scales that were slow in comparison to the bending and buckling dynamics. They also observed that in most buckling events, the proximal regions of the buckling microtubules appear to be transported anterogradely against a stationary tip.

By tracking the dynamics of buckling microtubules in cells as well as reconstituting microtubule buckling *in vitro* using microtubule gliding assays in the presence of motor protein kinesin (wherein microtubules are transported on a surface of immobilized kinesin motors), the authors found that the microtubule curvatures as well as relaxation times following buckling were comparable to those found *in vivo*. These studies help us conclude that the major source of forces that bend and buckle microtubules in cells would arise from the action of microtubule-based motor proteins. Later studies by inhibiting dynein in cells (by overexpression of CC1 p150 dynactin binding domain) reduced microtubule bend formation as well as directed microtubule transport, fortifying the conclusions by Bicek *et al* (Kent *et al*., 2016).

Though a large proportion of microtubules in cells appear to bend and buckle, occurrences of microtubule breakage in cells are rare (Gupton *et al*., 2002; Odde *et al*., 1999; Waterman-Storer & Salmon, 1997). Odde *et al*., 1999 reported that microtubules that broke were often highly curved, and there exists a correlation between high microtubule curvature and breakage (Odde *et al*., 1999). In a recent study, Tsitkov *et al*., 2022 quantified the curvature of Taxol-stabilized microtubules that were seen to break in gliding assays with kinesin and concluded that the rate of microtubule breaking increases exponentially with increasing curvature as a consequence of motor activity (Tsitkov *et al*., 2022). In gliding assays, microtubules were also seen to bend as well as loop (usually when one end of the microtubule is stuck to an immobile motor protein) and seen to display curvatures of 0.4-2 rad/µm (Liu *et al*., 2011; Bourdieu *et al*., 1995).

The forces generated by the action of microtubule-based motors have been shown to cause microtubule damage**.** Kuo *et al*., 2022 estimated the forces required to pull a tubulin dimer out of the microtubule lattice to be 30 pN. Using optical tweezers and conjugated kinesin molecules bound to microtubule, they also report that the force generated by 3 kinesin-1 motors is sufficient to remove tubulin dimers from the lattice (Kuo *et al*., 2022). *In vitro* gliding assays wherein microtubules are transported on a surface of immobilized kinesin motors showed molecular wear of microtubules over time owing to the loss of dimers from microtubule ends due to friction between motors and microtubule (Dumont *et al*., 2015). This was confirmed in a later study by Triclin *et al*., 2021 wherein gliding GDP (non-stabilized) microtubules were found to depolymerize in the absence of free tubulin in the systems in assays with kinesin and dynein. The authors show that just the walking action motors on microtubules can uncap the stable ends of GDP-microtubules and trigger microtubule depolymerization. Inducing buckling of stabilized microtubules bound to kinesins on the surface using stretch-compression cycles revealed that buckling microtubules break at 2.5% strain (**Fig 1f)** and that this frequency is dependent on microtubule-motor interaction and motor concentration (Kabir *et al*., 2020).

(ii) Motor-induced helical and rotational forces in the mitotic spindle

Mitotic spindle orientation is important for morphogenesis and early studies have postulated that the chiral nature of the spindle arises from rotational forces of microtubule bundles.

In addition to stepping and sliding microtubules, motor proteins can also sidestep along the different protofilaments, thereby inducing helical motion of microtubules. In cells, this is observed as the helical motion of endocytic vesicles (Lee *et al*., 2019) as well as in *in vitro* 3D stepping assays. In these assays, a 'Template microtubule' is suspended onto a microstructure/ridge and short 'Transport' microtubules are added (**Fig 1g)**, in presence of crosslinking motors like kinesin-5 or kinesin-14 (Mitra *et al*., 2020; Meißner & Diez, 2024).

Kinesin-14 is a microtubule minus-end directed, non-processive motor that crosslinks anti-parallel microtubules. Using 3D stepping assays, Mitra *et al*., 2020 showed that kinesin-14 induced right-handed, helical motion of antiparallel microtubules with a median helical pitch of 1.6 µm. In contrast, kinesin-5 (Eg5 in Humans and Ncd in *Drosophila*) is a plus- end directed motor that induces right-handed helical motion of anti-parallel microtubules with a mean pitch of 1.5 µm. In addition, it is also reported to cause transport microtubules to orbit around fixed template microtubules without any forward movement (Meißner *et al*., 2024).

In the spindle midzone, kinesin-5 and kinesin-14 motors act antagonistically but the torque generated by both motors may add up to induce twisting/coiling of microtubules (Mitra *et al*., 2019). Similarly, kinesin-8 is a processive, dimeric motor that depolymerizes microtubule plus ends and induces left-handed rotation of microtubules with a pitch of 1 µm (Bormuth *et al*., 2012).

This helical motion of microtubules occurs as a result of the off-axis component to motor forces resulting in torque generation and helical motion (Ramaiya *et al*., 2017). A study by Brunnbauer *et al*., 2012 used laser trap assays to show that the neck linker region of kinesin motor proteins is essential for generation of torque. Torque forces on microtubule bundles in the mitotic spindle help maintain its chirality (Novak *et al*., 2018). For a detailed overview of the helical motion of different kinesin and dynein motors, please refer to Meißner & Diez., 2024.

Rotational/ looping motion of gliding microtubules caused by motor proteins is typically observed in gliding assays where one end of the microtubule is immobilized to the surface (either via a substrate or due to an inactive motor) and the other end experiences pushing forces by motor proteins resulting in an off-axis component to motor stepping causing the microtubule to buckle, rotate or loop (Meißner *et al*.,2024; Mitra *et al*., 2019; Mimori & Miki-Noumura.,1995). Cytoplasmic dynein was also reported to rotate/coil microtubules (Can *et al*., 2015; Vale & Toyoshima., 1988) indicating the presence of an off-axis component to the stepping force. In comparison to kinesin, dynein was reported to rotate microtubules in both directions with a bias to the right-handed rotation in the absence of any load (Ferro *et al*., 2019; Mitra *et al*., 2015).

Torque generation by crosslinking motors and consequent helical and rotational microtubule movement is postulated to help in balance of forces in the mitotic spindle in association with other mitotic spindle proteins like PRC-1 (microtubule crosslinking MAP) and augmin (microtubule nucleator) (Trupinic *et al.*, 2022). The presence of off-axis stepping may also serve as a potential avenue for sidestepping mechanisms for motor proteins to navigate across MAP condensates/complexes (obstacles on the microtubule that may potentially hinder motor processivity) (Mitra *et al.*, 2019).

(iii) Distribution, cooperativity and regulation of microtubule motor protein activity in the cell

The forces and action of motor proteins is crucial for many microtubule-based cellular functions. Therefore, it is natural to ponder on the localization of different motor proteins in the cell, their recruitment as well as regulation. Early studies using quantitative immunoblotting of different cellular fractions from fibroblasts showed that 68% of cellular kinesin is in the soluble form, 32% is found in association with organelles/membranes whereas negligible amounts were detectable in the cytoskeletal fractions (Hollenbeck.,1989).

Further studies revealed that most of the cytoplasmic dynein and kinesin exists in the auto-inhibited form in the cellular cytoplasm. Kinesin-1 adopts a folded, inactive state that involves the kinesin light chain (KLC). The KLC domain consists of a conserved motif (QIAKPIRP) that binds to the switch I helix in the kinesin motor domain thus preventing the release of ADP. Autoinhibition has been best studied in the case of kinesin-1 but was also found to occur for kinesin-2, kinesin-3 and kinesin-7. Release of kinesin from its autoinhibited state is shown to occur by cargo binding to its tail domain, binding of Zygin-1 and JIP1 proteins (Jun N-terminal Kinase-interacting protein) in the case of kinesin-1 as well as through phosphorylation (in the case of kinesin-5 and kinesin-7) (Cai *et al.*,2007; Espeut *et al.*, 2008). Cargo-binding also helps kinesin-5 switch between diffusive to processive motion (Kapitein *et al.*, 2008).

Dynein activation and function is regulated by dynactin that forms the dynein-dynactin complex and via a diverse range of adaptor proteins like Lis1 (Lissencephaly 1) and Nudel (Nuclear Distribution protein nudE) (Gill *et al.*,1991; Schroer *et al.*, 1991). In addition to activating and regulating dynein function, adaptor proteins also regulate cargo specificity (Reck-Peterson *et al.*, 2018). For a detailed review of dynein adaptor proteins and cargos, refer to Reck-Peterson *et al.*, 2018.

Recent studies report the cooperative nature of motor binding and transport, wherein binding of motor proteins to a microtubule changes the state of the microtubule lattice (binding of kinesin expands the microtubule lattice) and further induces the binding of more kinesin motors (Peet *et al*., 2018; Shima *et al*., 2018; Wijeratne *et al*., 2022; Xie *et al*., 2024).

A recent *in vitro* study showed how motors of opposite polarity (kinesin-1 and kinesin-14) segregated microtubules into different domains and arrangements depending on the concentration of the individual motors present (Utzschneider *et al*., 2024). Bidirectional transport of cargo is achieved by the action of antagonistic motor teams of kinesin and Dynein (Soppina *et al*., 2009). The direction of transport and force balance is then determined by the concentration and number of the individual motors ('Tug-of-war' mechanism) and by the presence of roadblocks on the microtubule lattice that affect the binding affinities of either motor protein (Utzschneider *et al*., 2024; D'Souza *et al*., 2023; Monzon *et al*., 2020).

c. Effect of frictional forces in crosslinked, bundled and sliding microtubules

In many cellular processes, microtubules exist in crosslinked and bundled conformations, together with crosslinking MAPs/ motor proteins, such as in the mitotic spindle and as microtubule bundles that span neurons. In these assemblies, microtubule filaments are in close contact with each other and with the cytoplasm, leading to frictional forces.
The frictional forces that arise from filament-filament interaction determine the mechanics of microtubule assemblies as well as their integrity. Microtubule bundles are known to resist bending and buckling forces better than single microtubule filaments (Soheilypour *et al*., 2015). Studies on sliding friction in microtubule bundles indicate that these forces are dominated by hydrodynamic interactions possibly stemming from the charged, disordered amino acid domains (or 'e-hooks') that span the microtubule surface. It is hypothesized that these domains form a polyelectrolyte brush of sorts that lowers sliding friction (Ward *et al*., 2015).

In addition to bending and buckling microtubules, molecular motor proteins also exert frictional forces on microtubules. Bormuth *et al*., 2009 showed that kinesin-8 (Kip3p) exerts friction forces of the order of several piconewton using optical tweezer experiments. They postulated that the friction arises from breaking of the motor-microtubule bonds and that the frictional force generated influences motor motility.

Sliding between microtubule filaments drives anaphase and flagellar movement. In the mitotic spindle, sliding of microtubules by motor proteins is primarily achieved through their strong cross-linking action. Kinesin-5 (Eg5 in humans cross-links and bundles microtubules via its pair of motor domains as well as a C-terminal microtubule binding domain (Weinger *et al*., 2011). It was found that Eg5 displays diffusive motion (that doesn't require ATP hydrolysis) on single microtubules, but when in a crosslinked state, switches to ATP dependent directional motion, wherein it slides antiparallel microtubules with a speed of 30 nm/s (Kapitein *et al*., 2005; 2008). Sliding of microtubule filaments by the motor protein kinesin-5 is pivotal for mitotic spindle positioning.

In comparison, the minus-end directed kinesin-14 (Ncd in *Drosophila*; Klp2p in *S.Pombe* crosslinks microtubules using one pair of motor domains, and one pair of diffusible microtubule binding tail domains located at opposite ends (Fink *et al*., 2009). Kinesin-14 slides microtubules at a speed of 80 nm/s (Furuta & Toyoshima., 2008). *In vitro* studies have implicated that dynein also crosslinks and slides anti-parallel microtubules in microtubule overlaps through its two motor domains. Interestingly, Chakraborty *et al*., 2020 also reported that the processivity of dynein motors was found to be more enhanced in microtubule bundles. In the spindle, inward microtubule sliding by dynein counteracts the outward microtubule sliding by kinesin-5 (Tanenbaum *et al*., 2013; Chakraborty *et al*., 2020). The dynein-dynactin complex helps recruit the microtubule crosslinker- NuMA (Nuclear Mitotic Apparatus) to the spindle poles- a process important for spindle orientation (Seldin *et al*., 2016).

The mitotic spindle also constitutes an ensemble of non-motor, diffusible crosslinking MAPs of the PRC-1 family (Ase1 in yeast and MAP-65 in plants), as well as End-binding (EB family) proteins that track the growing microtubule ends.

Frictional forces that arise from bundling MAPs are known to slow down microtubule sliding caused by action of motor proteins. Ase1 that binds to anti-parallel microtubules slows down sliding caused by kinesin-14 through an 'adaptive braking' mechanism wherein compaction of the Ase1 domains leads to stabilization of microtubule overlaps and decreases sliding velocity (Krattenmacher *et al*., 2024; Braun *et al*., 2012; Janson *et al*., 2007; Kapitein *et al*., 2008). Interestingly, PRC1 complexes with kinesin-4 (KIF4) and localizes to growing microtubule ends wherein kinesin-4 suppresses further growth (Bieling *et al*., 2010; Kurasawa *et al*., 2004)

The role of cross-linking proteins in stabilizing microtubule overlaps and consequent force generation in the piconewton range has been well-documented. It is hypothesized that passive crosslinkers (eg, the PRC1/Ase1/MAP65 family) generate entropic forces arising from their diffusive motion in microtubule overlaps in addition to frictional forces (Lansky *et al*., 2015). The magnitude of the frictional forces generated by crosslinkers increases with crosslinker density.

In vitro reconstitution assays focusing on crosslinking MAPs involved in the mitotic spindle revealed that the diffusive movement of MAPs and their directionality may be governed by asymmetric nature of frictional force between the MAP and the microtubule. Forth *et al*., 2014 performed optical trap experiments wherein they estimated the force response of MAP coated beads on microtubules being oscillated and found that the diffusive movement of MAPs is asymmetric in the case of NuMA and EB1 and is mediated by frictional forces and microtubule filament polarity. They also found that the frictional resistance that is generated in the case of NuMA and PRC1 is in the sub-pN range (Forth *et al*., 2014).

Thus, binding and diffusible motion of crosslinking MAPs as well as motor proteins help mediate the forces that position the mitotic spindle. Beyond the spindle, sliding forces generated by cytoplasmic motor proteins like kinesin-1 has been shown to play a pivotal role in oocyte streaming in early development in *Drosophila* (Lu *et al*., 2016), neurite growth and in formation of cellular protrusions consisting of parallel microtubule bundles (Jolly *et al*., 2010). In neurons, MAPs like Tau and MAP-2 crosslink microtubules and form bundles that contribute to axonal growth (Myers & Baas, 2007).

Type of force acting on microtubules	**Magnitude of force**
Pushing force due to polymerization against a barrier	3-4 pN
Force generated by depolymerization	30-65 pN
Maximum stall force exerted by motor proteins	4-8 pN
Sliding/frictional force of motors	1-3 pN
Maximum rotational force exerted by motor proteins	5 pN
Max torque generated by motor proteins	1,650 pN nm
Force required to pull tubulin dimer from the lattice	30 pN
Crosslinker mediated frictional resistance (NumA, PRC1)	sub-pN range

Table 2: List of types and magnitude of forces acting on microtubules.

Frictional forces have been reported to damage microtubules and trigger microtubule self-repair mechanisms. A recent *in vitro* study on assessing tubulin turnover in the lattice by immobilizing microtubules on micropillars reported lesser damage and self-repair, relative to assays performed on surface treated cover-glasses. This implies that just the contact of microtubule with the passivated coverglass surface causes significant microtubule damage

(Alexandrova *et al*., 2022). Microtubule damage and consequent self-repair have been reported at microtubule crossover sites (**Fig 1e, Fig 2b)** in cells (Aumerier, Schaedel *et al*., 2016; Forges *et al*., 2016; Gazzola *et al*., 2023). It has also been shown that these crossover sites may be hotspots for the severing action of MAPs (eg. katanin). Further studies hypothesize that this localization of katanin at microtubule crossovers may be facilitated by katanin recognizing lattice irregularities stemming from damage from frictional forces generated at these crossover sites (Eng *et al*., 2021).

A summary of the type and magnitude of forces acting on microtubules is listed in **Table 2**.

IV. The unique mechano-adaptive properties of microtubules

Below, we list the different mechano-adaptive properties of microtubules that facilitate their role as cellular mechanosensors:

a. Modulation of microtubule dynamics/length

In cells, microtubules display persistent growth at the cell interior but asymmetric transitions at the cell edge. This serves as a mechanism in which microtubules can rapidly sense changes at the cell periphery and accommodate the changing cell shape.

During interphase, the minus ends of microtubules are positioned near the nucleus at the overlap zones whereas the dynamic plus ends grow and shrink between the nucleus and the cellular poles. Localization of pushing/compressive forces that cause an enhanced catastrophe of growing microtubule ends at the cortex during interphase, help in positioning the nucleus in the opposite direction as indicated in experimental as well as computational studies using fission yeast (*S.Pombe)* as a model. Regulating microtubule length is essential as longer microtubule pushing at the cell cortex may bend and buckle. Studies report kinesin-8 and kinesin-13 (MCAK) mediated microtubule depolymerization controls microtubule length to ensure spindle length regulation as well as (re)centering of the nucleus (Gardner *et al*, 2008; Stumpff *et al*, 2008).

Although instances of microtubule breakage in cells are rare and are usually seen in the case of highly curved microtubules. Such curvature-induced microtubule breakage and subsequent depolymerization can increase the free tubulin pool in the cytoplasm, leading to new microtubule growth. Thus, bending of microtubules in response to force can induce microtubule breakage and microtubule network remodeling and help the cell accommodate new shapes

(Guppton *et al*., 2002; Odde *et al*., 1999). Microtubule breakage helps in axonal branching and transport in neurons (Baas *et al*., 2006).

b. Self-repair in response to mechanical stress

Microtubules are also capable of self-repair in response to mechanical stress by incorporating new tubulin dimers at sites of localized stress. Early *in* vitro experiments by Dye et al.,1992 showed that breakage of end-stabilized microtubules can be prevented by introducing buffer with free tubulin, implicating that dimer loss and incorporation are pivotal for microtubule stability. This notion was further strengthened by the observations of Schaedel *et al*., 2015 wherein microtubules exposed to orthogonal fluid-flow recovered their stiffness when allowed to recover in a solution with free tubulin. This property of self-repair and incorporation of free tubulin into spots of dimer loss can be visualized by using free tubulin (**Fig 2a**) tagged with a different fluorescent dye (Schaedel *et al*., 2015). Microinjection and photo-conversion experiments in PtK2 cells also showed that tubulin turnover occurs in cells and is much more accelerated and prominent in bundled and curved microtubules (**Fig 2b**), crossover sites (**Fig 1e**) and zones of lateral fluctuations (Gazzola *et al*., 2023; Aumerier, Schaedel *et al*., 2016).

Subsequent studies showed that this was an inherent, spontaneous process that occurred even in the absence of force induced damage and was dependent on the presence of defects (Schaedel *et al*., 2019). It was also found that self-repair helps enhance microtubule survival against the gliding action of molecular motors (Triclin *et al*., 2021). These studies were pivotal to causing a paradigm shift in the way microtubule dynamics was perceived and that the dynamic nature of microtubules extends beyond the tip, prompting the use of the term ‘lattice dynamics or plasticity’ over ‘self-repair’ (Motta, Biswas *et al*., 2023; Cross *et al*., 2019).
Tubulin turnover may also create localized stretches of GTP-tubulin or ‘GTP islands’ that may promote rescue events (Aher *et al*., 2022; Aumerier *et al*., 2016; de Forges *et al*., 2016). MAPs like EB and CLIP-170 have been shown to recognize GTP-like lattice states and may be preferentially recruited to sites of self-repair (de Forges *et al*., 2016).

This interplay suggests that lattice repair is indeed a dynamic process that is a crucial part of the microtubule-based mechano-responsive feedback loop that links mechanical stimuli, lattice conformation, and MAP recruitment. Thus, lattice plasticity may be the key property that endows microtubules to act as a mechanical interface that is sensitive and adaptive to stimuli. Several open questions remain, the most prominent of them being whether this ability to self-repair in response to damage is sufficient to preserve microtubule integrity and stability in the cellular environment, or is this process dependent on other factors?

Another interesting avenue to explore would be the factors that regulate inherent tubulin turnover. A combination of cryo-ET, *in vitro* reconstitution and modelling studies may help us uncover the mechanism that regulates tubulin turnover in the lattice.

c. Modulation of microtubule dynamics by MAPs

MAPs enable microtubules to participate in a variety of cellular processes such as neuronal development, assembly of mitotic and meiotic spindles, and the formation of the ciliary axoneme. Among these, structural MAPs are known to affect their stability and polymerization. MAP1 proteins have been associated with a stabilization function, among which MAP1B plays a major role in regulating microtubule stability and catastrophe depending on its phosphorylation state. MAP4 enhances tubulin polymerization and stability by sterically blocking disassembly. Apart from these, Tau, a neuronal MAP has been shown to promote axonal microtubule stabilization. Single molecule studies by Tan *et al*., 2019 also showed that Tau self-association is reversible and is regulated by the microtubule lattice, which results in dynamic, localized condensation of tau molecules on the microtubule surface. Complementary to this study, Siahaan *et al*., 2019, have demonstrated that tau on microtubules can form cohesive tau islands when it coexists in two kinetically distinct phases. Tau also play an important role in buckling of microtubule bundles during compression (Soyheliypour *et al*., 2015).

Certain MAPs like MAP-7 and MAP-9 are known to enhance motor motility. It was recently shown that following the release of autoinhibition by cargo-binding, MAP-7 helps enhances the landing of active kinesin-1 motors to microtubule tracks by 25-fold revealing a synergistic relation between MAP-7 and kinesin-1 recruitment (Monroy *et al*., 2018; Chiba *et al*., 2022).

End - binding or +TIP-tracking proteins like EB1 and Mal3 (yeast analog of EB1) have also been shown to mediate microtubule plus-end cortex interaction. Varying the expression levels of EB proteins may serve as a possible mechanism by which cells regulate pushing forces (Busch *et al*., 2004). Furthermore, microtubule plus ends have a limited load-bearing capacity required for their direct mechanical function since they are susceptible to compression-induced catastrophes (Janson *et al*., 2003). Therefore, it was suggested that the catastrophe rescue factors, which encourage assembly, could improve microtubule plus ends' stability at load-bearing microtubule sites (Noordsta I & Akhmanova A, 2017, van der Vaart B *et al*., 2009). TOG-domain proteins like cytoplasmic linker proteins (CLIPs) and CLIP-associated proteins (CLASPs) increase microtubule polymerization rates and promote rescues. End-binding proteins (EBs) form a tip-tracking complex that promotes microtubule dynamics and growth. In a similar manner, catastrophe is inhibited by kinesin-4 family (Akhmanova A *et al*., 2015) and a newly discovered +TIP protein SLAIN2 (van der Vaart B *et al*., 2011). In addition to this, XMAP215 (another TOG domain protein) has been shown to assist in microtubule polymerization under tensile stress by dynamically linking to growing and shrinking ends of the microtubules (Trushko *et al*., 2013). Furthermore, MAPs and other cellular factors inhibit motor processivity (Telley I A *et al*., 2009).

MAPs have been shown to play a crucial role in translating mechanical cues into structural and organizational changes within the plant cytoskeleton. The molecular mechanisms that allow cortical microtubules to be mechanically sensitive include the localization of many MAPs known to influence microtubule stability and dynamics. Katanin (severing MAP) generates new microtubule ends that align with the stress axis, thus allowing rapid reorganization of the microtubule network (Uyttewaal *et al*., 2012). Plants lacking katanin have disorganized microtubule networks and altered patterns of growth anisotropy, demonstrating the necessity of katanin in mechanical adaptation. Like katanin, CLASP proteins are important for stabilizing microtubule ends at the cell cortex and are necessary for the maintenance of ordered arrays of microtubules when subjected to mechanical stress (Ambrose *et al*., 2011). The MAP65 family also contributes significantly to mechanical adaptation by cross-linking antiparallel microtubules and creating stable bundles that are resistant to depolymerization (Lucas *et al*., 2011). Thus, localization and MAP-mediated microtubule bundling effects mechano-adaptation.

Whilst inherent lattice plasticity allows for spontaneous tubulin turnover, emerging evidence show that this process can be modulated by MAPs. It was shown recently that Tau can mediate the dynamic remodeling of the microtubule lattice and enhance tubulin turnover by promoting the elimination of lattice defects (Biswas *et al*., 2025). In this way, MAPs might promote lattice remodeling by modulating the inherent lattice anisotropy.

MAPs are also known to recognize and be recruited to sites of mechanical stress. Severing MAPs like katanin and spastin were shown to localize and sever sites of mechanical stress. It is postulated that the severed fragments might serve as a template for microtubule regrowth (Vemu *et al*., 2018). Li *et al*., 2023 showed that CLASP and EB1 relocated to sites along the microtubule lattice in cells exposed to stretch-compression cycles (**Fig 2c**). This fortified previous reports of Aher *et al*., 2020 who showed that CLASP localized to sites of damage on microtubules. A recent study also showed the recruitment of MAP-65 to bent microtubules both *in vitro* and in *Arabidopsis* stems (**Fig 2d)** (Motta *et al*., 2025). In this study, the authors also show that MAP-65 recruits free tubulin to sites of damage/defects, guiding lattice-templated nucleation of new microtubules and thus promoting the formation of microtubule bundles.

Like MAPs, microtubule-based motor proteins are also sensitive to mechanical cues. A recent *in vitro* reconstitution study showed that dynein-based cargo transport was enhanced when microtubules were subjected to tensile stress up to 2.5% strain (Nasrin *et al*., 2024). These findings strongly suggest that MAPs are able to read/recognize the state of the microtubule lattice or subtle changes in conformation that may be triggered by force or defects. It would be interesting to explore if the recruitment or binding of these MAPs occurs in a cooperative manner. Multiple MAPs can effect changes in the microtubule by acting competitively or in a synergistic manner. An open question in this direction is whether MAPs localize to sites of damage/defects by recognizing lattice conformation or rather through recognition of GTP-tubulin incorporation at these sites. Deciphering the direct role of MAP-microtubule interaction in cell mechanics will require an understanding of the full extent of their interaction with microtubules. Thus, microtubule damage and consequent self-repair may recruit signaling proteins, intracellular factors as well as MAPs. Through local regulation of the concentration of crosslinkers, MAPs and motors, the cell can direct the transport of specific cargo as well as signaling molecules, thus effecting an adaptive response of the cell to mechanical stress.

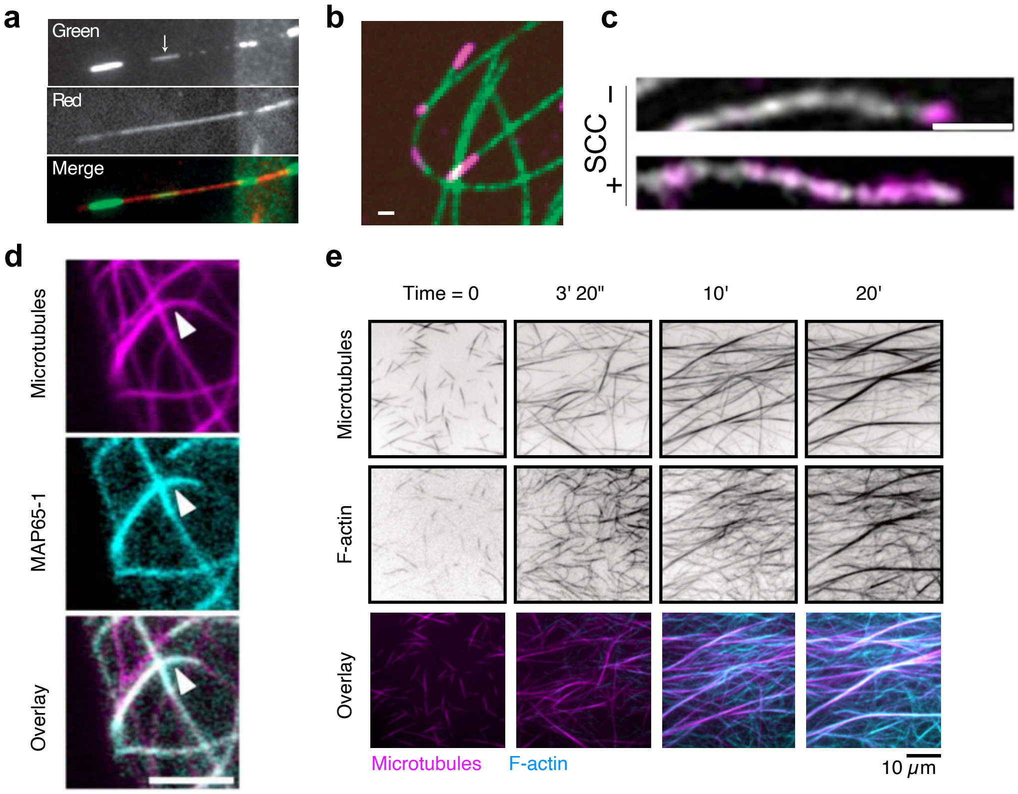

Fig 2: Microtubule response to mechanical stimuli. **(a)** Microtubule (in red) showing incorporation of green tubulin (self-repair) from solution following bending by orthogonal fluid flow (Schaedel *et al*., 2015). **(b)** Incorporations (in magenta) in curved microtubule sections (green) in Ptk2 cells microinjected with tubulin (magenta) (Gazzola *et al*., 2023). Scale bar: 1 µm. **(c)** CLASP2 comets relocate from tips to the lattice when microtubules are subjected to

stretch-compression cycles. Scale bar: 2 µm (Li *et al*., 2023). **(d)** MAP-65 (cyan) localizes to bent microtubules (magenta) in *Arabidopsis* stems. Scale bar: 5 µm (Motta *et al*., 2025). **(e)** Self-organization in actin (cyan)-microtubule (magenta) composites (Kucera *et al*., 2022).

d. Link between microtubule mechanics, MAP localization and the tubulin code

Tubulin expression in cells is tightly regulated and complex, with cell-specific expression of different tubulin isoforms as well as conserved Post Translational Modifications (PTMs) in what is now popularly termed as the 'Tubulin code'. For a comprehensive overview of the tubulin code, please refer Gadadhar *et al*., 2017; Mecak *et al*., 2020; Janke and Magiera., 2020.

In humans, there exist 9 isoforms of both α and β tubulin with α1A (TUBA1A) and βI (TUBB) being expressed ubiquitously across all cell types. Tubulin isotypes can indirectly influence the mechanics of microtubules by influencing microtubule structure in terms of regulating the protofilament number as well as affecting polymerization dynamics. Microtubule polymerized from α1B/β2B-tubulin dimers were shown to be more resistant to depolymerization (Pamula *et al*., 2016; Ti *et al*., 2018).

The mechanical properties of microtubules are also further diversified with distinct PTMs- acetylation, phosphorylation, polyamination, glutamylation, glycination of both α and β tubulin as well as methylation, detyrosination and palmitoylation of α-tubulin. Certain types of PTMs (like acetylation) are known to stabilize a subset of microtubules in the cell. Long-lived microtubules were found to be predominantly acetylated (by the action of tubulin acetyltransferase α-TAT1 in humans and MEC-17 in *C. elegans*) at the lysine 40 residue of α-tubulin in the lumen of Microtubule (L'Hernault & Rosenbaum.,1985; Akella *et al.,* 2010). Reports suggest that this modification facilitates protofilament sliding by reducing inter-protofilament interaction, increasing microtubule lattice plasticity/flexibility and protecting microtubules from breakage and mechanical aging (Ye *et al*., 2025; Xu *et al*., 2017). Polyglutamylation of tubulin by glutamylases of the TTL-like family (Kimura *et al*., 2010) is reported to enhance the action of severing enzymes like spastin and katanin (Valenstein and Roll-Mecak., 2016; Lacroix *et al*., 2010), thus controlling microtubule density.

PTMs can also influence the binding of MAPs and molecular motors to microtubules. This could serve as a mechanical/polarization cue to direct microtubule transport. Early studies reported a change in kinesin-1 transport in response to changes in microtubule acetylation, implying a correlation between tubulin acetylation and kinesin-1 localization (Reed *et al*., 2006). A recent study by Andreu-Carbo *et al*., 2024, contradicts this finding and showed that kinesin-1 doesn't directly increase microtubule acetylation and that the activity of α-TAT1 is dependent on the presence of damage sites that may be caused by kinesin-1 activity. Recent studies also show that elevated levels of ROS (Reactive Oxygen Species) can modulate the expression levels of α-TAT-1, suggesting that tubulin acetylation may serve as a critical integrator of redox signals and regulate cellular oxidative stress response (Carmona *et al*., 2025). Ikegami *et al*., 2007 also showed that polyglutamylation was essential in the transport of presynaptic vesicles by kinesin-3. Polyglutamylation was also shown to influence the binding of Tau, MAP1 as well as regulate kinesin-1 mediated transport of postsynaptic cargos (Bonnet *et al*., 2001; Maas *et al*., 2009).

In neurons, the binding of kinesin-1 to detyrosinated microtubules in axons facilitates kinesin mediated axonal transport (Kaul *et al*.,2014; Dunn *et al*., 2008). Kinesin-1 is also reported to mediate the interaction between detyrosinated microtubules and vimentin intermediate filaments in fibroblasts (Liao & Gundersen., 1998; Kreitzer *et al*.,1999). Detyrosination of microtubules is also known to facilitate binding of CLIP-170 (Nirschl *et al*., 2016; Peris *et al*., 2006) as well as prevent the depolymerizing action of kinesin-13, thus contributing to microtubule stability (Peris *et al*., 2009).

In this way, cells can combine the diversity offered by both the tubulin and the MAP code to regulate microtubule-based interactions and processes in a selective and specific manner.

Recent evidence on mechano-dependent mediation of the tubulin code

The repertoire of tubulin isotypes and PTMs serves as a great resource for the cell to regulate and (re)organize the intracellular microtubule network locally as an adaptive response to external mechanical stimuli. Modulating the expression of specific tubulin isotypes or PTMs changes the microtubule dynamics and microtubule-associated interaction pathways, thus aiding microtubules in mechanosensing.

In this direction, Torrino *et al*., 2021 showed that the stiffness of the cell's Extracellular matrix (ECM) modulates glutamylation of microtubules by suppressing microtubule dynamics, promoting microtubule stability, thus influencing changes in cell shape and mechanics. The authors also showed that overexpression of tubulin mutants lacking glutamylation sites decreased microtubule stability and hampered cancer progression. Thus, cells may harness the diversity offered by the tubulin code and post-translational modifications to modulate cellular metabolism and the mechanical properties of microtubules. Detyrosination of microtubules and its role in kinesin-1-mediated transport of APC (Adenomatous Polyposis Coli) was reported to be crucial for symmetry breaking and cell migration (Lavrsen *et al*., 2023).

The RNA binding protein-Muscleblind-1(MBL-1) was found to interact and enhance the expression of mec-7, mec-12 mRNA that encode tubulin subunits MEC-7 (β-tubulin) and MEC-12 (α-tubulin) in *C.elegans* touch neurons. The interaction was found to be important for touch-sensation as well as synapse formation in neurites (Puri *et al*., 2023).

Recently Viar *et al*., 2024 used a combination of immunolabeling and Cryo-ET (Cryo-Electron Tomography) studies to show that glycylation and polyglutamylation PTMs in motile cilia give rise to a protofilament-specific pattern (that they term ‘Tubulin nano-code’) which may directly influence interaction with dynein, and contribute to ciliary beating as well as ciliary function (Viar *et al*., 2024).

e. Cytoskeletal crosstalk and lateral reinforcement against mechanical stress

Studies over the last decades have shown mechanical coupling of microtubules to the surrounding elastic cytoskeleton significantly increased the critical buckling force when subjected to compressive forces (Bragwaynne *et al*., 2006). Therefore, the surrounding cytoskeleton's mechanical reinforcement may offer a structural foundation for the microtubule network to support the heavy loads needed to stabilize the entire cytoskeleton (Stamenovic *et al*., 2002; Bragwaynne *et al*., 2006). Earlier studies have shown that at lower stresses, vimentin and microtubules are highly strained; however, when the strain is removed, neither filament retained their original state, instead exhibiting unrecoverable strain characteristics of the viscous flow (Janmay *et al*., 1991). Through the interactions with other cytoskeletal systems like Vimentin Intermediate Filaments (VIF) can enhance the mechanical strength and deformations by slowing down the viscoelastic relaxations. Furthermore, by propagating local strain and stress into the cell, VIFs can deform microtubules and actin that interact and interpenetrate within the network (Gan *et al*, 2016; Costigliola *et al*, 2017; Huber *et al*., 2015).

Vimentin intermediate filaments were found to modulate cellular stress responses by facilitating actomyosin-mediated force transmission as well as via reinforcement of microtubule networks under compression (Alisafaei F *et al*., 2024).

The mechanism of finite elasticity, viscoelastic relaxation, damage, and healing in the mechanical response of the interpenetrating network in eukaryotic cytoplasm is explained by the proposed interpenetrating-network model, which also demonstrates the coupling between interpenetrating cytoskeletal components. While F-actin and microtubules can relax, break, and reform under large deformations, it is observed that intermediate filaments can nonlinearly stiffen. Cell survival under severe mechanical deformations may depend on the energy dissipation that the cytoskeletal polymer networks' reorganization provides. Researchers have observed a wide range of behaviors in cells when subjected to large deformations. Some cells show stiffening in response to force-displacement, while others show softening. It is also unclear how the cytoskeletal networks combine to produce the bulk mechanical properties of the cytoplasm (Yang H *et al*, 2023).

Cytoskeletal crosstalk between the filaments may be mediated by crosslinking proteins like MACF (Microtubule Actin Crosslinking factor), plectin, MAPs, motors or other cytolinkers. Actin-microtubule crosstalk is pivotal for many cellular processes. Lopez *et al*., 2014 showed how an engineered crosslinker (TipAct) associated with EB proteins and linked the growing ends of microtubules to actin filaments. Active remodeling of microtubules occurs during migration and microtubule depolymerization in the periphery of migrating dendritic cells has been shown to trigger actomyosin-mediated cellular retraction events. Numerous recent studies reveal the link between microtubule catastrophes and actomyosin activity via the RhoA GEF-H1 (Guanine Exchange Factor). Upon microtubule depolymerization, GEF-H1 is released, is targeted to membrane-associated sites and triggers actomyosin contraction via RhoA-ROCK pathway (Kopf *et al*., 2020; Azotei *et al*., 2019).

Emergence of structural memory in cytoskeletal composites

Observing the dynamic and behavior of microtubules in cells indicates that microtubules also grow along tracks/paths previously occupied by other microtubules (Schulze & Kirschner., 1988). Together with molecular motor proteins, microtubules also associate and self-organize with actin and intermediate filaments to form dynamic composites.

Rheological and strain-stiffening studies on entangled as well as crosslinked microtubule networks have revealed that these networks behave similar to soft, elastic solids that showed compression when forces upto 30 pN were applied (Yang *et al*., 2012). Cellular studies on cytoskeletal crosstalk between the three cytoskeletal biopolymers implicate the occurrence of remodeling based on guided templation-wherein one filament network serves as a template for the growth of another. Evidence from recent research shows growth of microtubules along vimentin intermediate filaments (Gan *et al*., 2016) and alongside actin bundles in neurons (Sanchez-Huertas *et al*., 2020; Biswas *et al*., 2018).

Study on actin-microtubule-crosslinker composites using optical tweezer-microrheology showed that the mechanics of the composite can be controlled by modulating the concentration of actin, microtubules and crosslinking protein/agent (Lopez *et al*., 2014). Increasing microtubule density , prevented bending of actin filaments and displayed an elastic response, whereas increasing actin concentration, reinforced microtubules against buckling (Ricketts *et al*., 2018). In a follow-up study, Sheung *et al*., 2021 quantified linear force response in actin-myosin- microtubule composites and found that microtubules act as a scaffold, increasing actin-actin interaction, improving myosin contractility, resulting in a composite with a degree of strain memory (termed ‘mechano- or structural memory’) or time-delayed response that remains even after the cessation of force.

Kucera *et al.*, 2022 performed studies on actin-microtubule composites in the presence of the motor protein kinesin-1 and revealed that in addition to alignment of both filament networks, actin filaments can act as a memory scaffold to guide and template the reorganization/assembly of microtubules thus demonstrating architectural stability and dynamic plasticity (**Fig 2e)**. They also found that this composite assembly was sensitive to external stimuli and postulated that generation of structural memory in active composites together with crosslinkers, could serve as an autoregulatory mechanism, by which cells can sense and adapt to mechano-chemical changes (Kucera *et al.*, 2022).

f. Sensitivity of microtubule dynamics to the physico-chemical cytoplasmic environment:

Early studies indicate that the mitotic spindle and cellular microtubules were sensitive to high hydrostatic pressure of tens of MPa (Salmon, 1975; Bourns *et al.*, 1988). Microtubules are one of the most pressure-sensitive of cytoskeletal components with pressure-labile disintegration of longitudinal dimer-dimer contacts observed at pressures of 100-150 MPa (Gao *et al.*, 2018). The study also found that macromolecular crowding increases the stability of microtubules by 15-45 MPa and that the presence of MAPs like MAP2c helps assist microtubule nucleation and growth under high pressure.

The cellular cytoplasm is dense and about 40% of the cytoplasmic volume constitutes lipids, sugars and proteins (Fulton., 1982). Macromolecular crowding (or the crowding of macromolecules in the cellular cytoplasm) is key to cytoplasmic viscosity, protein function and interaction as most protein-protein interactions are diffusion-limited at the mesoscale. In this fashion, cells can sense, adapt and modulate protein interactions according to their intracellular cytoplasmic environment (Holt and Delarue., 2023; Alric *et al.*, 2022).
Assemblies of microtubules and crosslinker proteins (including motor proteins) also show fluid-like behavior (nematic behavior) with the ability to sense and adapt to confinement/boundaries (Suzuki *et al.*, 2017). Molecular crowding can induce microtubule bundling as well as affect reaction kinetics (Ellis., 2001; Hosek and Tang., 2004). It was found that the rate of tubulin addition to growing ends increased by 10-fold in viscous environments (Molines *et al.*, 2022; Wieczorek *et al.*, 2013). Microtubule depolymerization was also found to be inhibited in the presence of osmolytes like PEG (Polyethylene Glycol) and TMAO (trimethylamine-*N*-oxide), implicating the role of cytoplasmic osmolality on microtubule dynamics (Molines *et al.*, 2024; Bachand *et al.*, 2018). Molines *et al.*, 2022 further observed similar change in microtubule

dynamics with osmolality in both PtK2 epithelial cells and well as in *in vitro* systems using a viscous buffer. The sensitivity of microtubule dynamics to different viscogens is dependent on the molecular nature of the viscogen (Molines *et al*., 2024). A recent study by Molines *et al*., 2024 tested the influence of glycerol, Bovine Serum Albumin (BSA) and trehalose on microtubule dynamics and found that glycerol effectively slows down microtubule shrinkage as well as the threshold for nucleation. The authors also hypothesize that regulation of bio-viscogen concentrations and microtubule dynamics might function as a form of visco-adaptation to stress and external cues (Molines *et al*., 2024). Thus, in the physiological context, the physical properties of the cytoplasm determine the rate of microtubule polymerization and depolymerization.

g. Long-range communication along the microtubule lattice:

Research in the last decade increasingly implicates that conformational changes of individual tubulin heterodimers in the microtubule lattice is tightly coupled to microtubule mechanics and that there may exist allostery-based-mechanical coupling in the microtubule lattice- wherein a localized effect is transmitted along the entire microtubule.

Brouhard and Rice., 2018 postulate that conformational changes of one tubulin heterodimer may propagate beyond the neighboring tubulin dimers (long-range mechanical coupling) thereby modifying the conformations of dimers situated farther away in the microtubule lattice. *In vitro* microfluidics-based bending studies show that both bending-induced damage and consequent self-repair appear to be extended over the microtubule rather than showing a localized pattern, pointing towards possible lattice rearrangement over long distances (Schaedel *et al*., 2015).

Atomistic models on microtubule dynamic instability conclude that GTP hydrolysis enhances short- and long-range cooperativity between protofilaments and that microtubule instability is driven by strain propagation in both lateral and longitudinal directions (Igaev & Grubmüller., 2020). In a separate study, Rai *et al*., found that microtubules grown in the presence of different microtubule-binding drugs (and thus possessing drug-induced lattice defects) displayed higher and more frequent catastrophes, implying that the effect of defects in the lattice can propagate and influence the conformation as well as mechanics of the microtubule end (Rai *et al*., 2021). Long-range coupling may also explain synergistic binding of different MAPs along the same microtubule, as shown by Zanic *et al*., 2013. In this study, it was found that the polymerase activity of XMAP215 was enhanced in the presence of EB1. The concept of allosteric regulation was found to be central to the function of polymer-based interconnected cellular networks (Mathy and Kortemme., 2023). Molecular modelling and dynamic network analysis conclude that this mediation of mechanical information is achieved through β-tubulin subunits thus fortifying previous reports of β-tubulin controlling microtubule architecture (Cannariato *et al*., 2023; Chaaban & Brouhard., 2017; Ti *et al*., 2018).

Fig 3 summarizes the diverse aspects of the mechanoadaptive properties of microtubules.

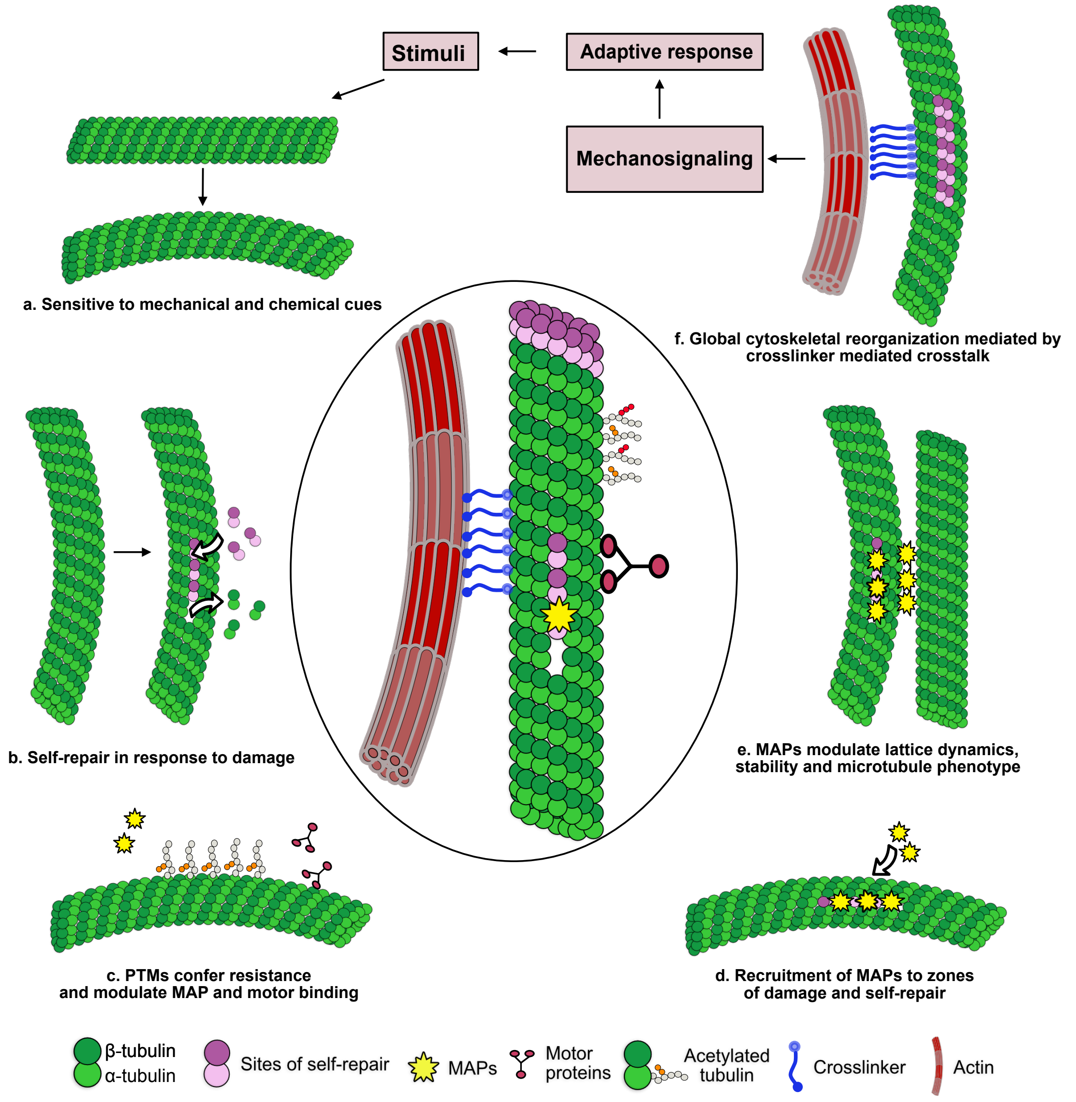

Fig 3: Unique mechano-adaptive properties of microtubules: a) The force-sensitive nature of microtubules makes them sensitive to mechanical and biochemical stimuli. **b)** Microtubules can self-repair by incorporating free tubulin along the lattice at points of defects and damage. **c)** PTMs (acetylation is depicted here) may confer resistance by enhancing microtubule flexibilty and can modulate the lattice conformation to influence binding of MAPs and motor proteins. **d)** MAPs may directly be recruited to sites of damage and self-repair. **e)** MAPs modulate lattice dynamics by accelerating/preventing tubulin turnover, thus influencing stabiliy. MAPs might also change microtubule phenotype (bundling, nucleation, severing etc). **f)** Microtubule response may be translated to global cytoskeletal reorganization via crosslinkers and crosstalk with other cytoskeletal filaments. In this way, microtubules integrate stimuli with inherent lattice plasticity to formulate an adaptive response.

V. Role of microtubules in other facets of the cellular mechanobiology pathway:

Microtubule mediated mechanotransduction:

Mechanotransduction is a process by which cells sense the mechanical properties of their surrounding microenvironment and coordinate to perform cellular functions such as migration, adhesion and differentiation. Mechanically generated signals (e.g., tension, pressure, and substrate rigidity) are converted to biochemical signals that can induce changes in cell movement, adhesion, proliferation and differentiation. For many years, it was known that actin filaments and intermediate filaments were important in mechanically transmitting signals to cells. However, the role of microtubules, especially in the transmission of mechanical signals within cells, has become increasingly recognized as an important regulatory mechanism.

The interaction between microtubules and focal adhesions (FAs) is essential for understanding the process of mechanotransduction and cell migration. Focal adhesions are large multiprotein complexes that connect the actin cytoskeleton to the ECM via integrins. These act as mechanical linkages for the transduction of mechanical signals received from the ECM to the intracellular environment. Early studies using live cell microscopy have shown that microtubules facilitate the rapid assembly and disassembly of focal adhesions that are necessary for directional migration and cell polarity (Kaverina *et al*., 1998; Ezratty *et al*., 2005).

Using plus-end tracking proteins including CLASPs, EB1 and regulatory enzymes such as focal adhesion kinases (FAK) and dynamin, microtubules selectively target focal adhesions (Stehbens and Wittmann, 2012). By dynamically extending toward focal adhesions and delivering proteins and other molecules required for the regulation of adhesion and endocytic processes, microtubules allow for the spatiotemporal control of adhesion disassembly. Depolymerizing or stabilizing microtubules impairs the disassembly of adhesions and results in the aberrant persistence of adhesions and reduced migration rates (Small and Kaverina, 2003; Stehbens *et al*., 2014).

The coordination of microtubules with actin and intermediate filaments regulates the mechanosensitivity of focal adhesions. Microtubules interact with actomyosin networks at the leading edge of migrating cells to maintain a balance of protrusive and contractile forces (Dogterom and Koenderink, 2019). Targeting microtubules to FAs causes localized actin depolymerization and FA disassembly, whereas microtubule depolymerization releases GEF-H1 and promotes RhoA-driven actomyosin contractility, enhancing adhesion site stability (Seetharaman *et al*., 2022; Kaverina *et al*., 1998; Efimov *et al*., 2008). In addition to this, kinesin-1 motors allow the delivery of integrin-containing vesicles to newly formed adhesions. This, in turn facilitates adhesion turnover and directional migration (Theisen *et al*., 2012). In this way, microtubules function as a "mechanostat" that maintains cell integrity under mechanical stress (Ju *et al*., 2024). Additionally, microtubule-mediated proprioception i.e., the ability to sense the internal mechanical state has been observed in amoeboid cells, where microtubules regulate shape and coherence by controlling actomyosin contractility (Kopf *et al*., 2020).

Plant morphogenesis is influenced by mechanical forces and is responsible for various aspects of cellular and tissue development. Mechanically induced responses of plant cells are largely due to sensing mechanical stimuli via the cytoskeleton, especially the cortical microtubule network, which acts as both a sensor and effector in the plant's mechanotransduction apparatus (Hamant & Traas, 2010; Uyttewaal *et al*., 2012).

Cortical microtubules are found directly beneath the plasma membrane and are oriented parallel to the main stress axes of the cell wall. Orientation of microtubules, therefore, determines the orientation of cellulose synthase complex (CSC) deposition and consequently directs the anisotropic expansion of cells (Paredez *et al*., 2006; Sampathkumar *et al*., 2014). Cells undergoing mechanical stress, such as compression, bending, or fluctuations in turgor pressure, rapidly reorient their cortical microtubule networks along new axes of stress. Therefore, the feedback loop between mechanical stress and microtubule organization ensures that plant cells grow in accordance with both internal and external mechanical constraints (Hamant *et al*., 2008; Landrein & Hamant, 2013).

Mechanotransduction also occurs through communication between the microtubule cytoskeleton and the plasma membrane. Activation of mechanosensitive ion channels, such as members of the MSL (MscS-Like) and PIEZO families, caused by mechanical stress can lead to localized increases in cytosolic Ca^{2+} concentrations and subsequently cause changes in microtubule dynamics (Nakagawa *et al*., 2007; Haswell & Verslues, 2015). Elevated levels of Ca^{2+} in the cytosol can modify the activity of certain MAPs or induce microtubule catastrophe, thus acting as a biochemical amplifier of mechanical signals. Additionally, proteins connecting microtubules to CSCs such as CSI1 and POM2 allow physical connections that facilitate feedback between wall mechanics and microtubule organization (Gu *et al*., 2010; Bringmann *et al*., 2012). These protein-protein interactions enable the cell to detect changes in the wall tension and accordingly adjust the orientation of microtubules. Similarly, mechanical constraints guide the establishment of circumferential microtubule arrays in developing roots and hypocotyls by determining the direction of elongation as well as the organ shape (Hejnowicz *et al*., 2000; Sampathkumar *et al*., 2014).

In conclusion, microtubules act as dynamic regulators of cellular mechanotransduction that couple the mechanical signals received from the extracellular matrix, membrane and focal adhesions, with cytoskeletal remodeling and biochemical signaling. The structural properties of microtubules, their PTMs, and their coordination with FAs and actomyosin networks allow for cells to detect and process mechanical stimuli and adapt to changing environmental mechanical stresses. Therefore, deciphering these mechanisms will be essential for understanding how the crosstalk of the cytoskeleton controls cell migration, tissue organization, and adaptation to mechanical stress.

Microtubules and the nucleus:

Mechanical forces are transduced to nuclear responses via linkers of the nucleoskeleton and the cytoskeleton complex (LINC), which couples the cytoskeleton to the nuclear lamina and associated chromatin. Change in nuclear size upon perturbation of actomyosin and microtubules affirmed their roles in exerting tensile and compressive forces, respectively on the nucleus, correlating with their functions in the cellular context (Towbin BD *et al*, 2009; Ingber DE *et al* 2008; Mazumdar A, Shivashankar GV, 2010). It has also been reported that a balance of forces between intermediate filaments and microtubules is required to maintain the genome organization and nuclear structure of the cardiomyocyte (Heffler J *et al*, 2020). p53 has been shown to associate with microtubule-based motor protein dynein, which indicates that p53 may use dynein to translocate from the cytoplasm to the nucleus (Paraskevi Giannakakou *et al*., 2000). Nucleocytoplasmic transport plays essential roles in the organization of cytoplasmic microtubules during interphase. However, the molecular mechanisms of how the microtubule organization is coordinated by the nucleocytoplasmic transport remain to be known (Kume Kazinori *et al*., 2018). Furthermore, Taiber *et al*., 2022 have provided evidence in favor of a microtubule cargo model that relies on the interaction of kinesin-1 and Nesprin-4 to demonstrate the nuclear positioning in outer hair cells (OHC).

Several studies have delineated the physiological significance of linking the nucleus and microtubules. Biedzinski *et al*., 2020 have shown the mechanism that drives myeloid differentiation. In this study, microtubule bundles were shown to squeeze the nucleus of HSPCs and form large invaginations, thus causing changes in chromatin organization. These microtubule-induced nuclear shape changes result in gene expression profiles that favor myeloid differentiation. This provides fresh insights into how early commitment to the myeloid lineage is affected by forces generated by microtubules. Findings of a recent study suggest that spreading nuclei during myotube differentiation is facilitated by microtubule nucleation at the surface of the nuclear envelope (Gimpel P *et al*., 2017). Apart from this, microtubules present within the nucleus have been shown to mediate DNA repair and mediate nonlinear motion of damaged chromatin (Oshidari R *et al*., 2018). Recent evidence has shown that SUN1, a LINC protein, regulates cell-cell junctions from the nucleus via LINC complex-microtubule interactions. This long-range regulation is crucial for blood vessel sprouting and junction integrity since it affects peripheral microtubule dynamics and Rho-regulated contractility (Buglak D B *et al*., 2023).

Furthermore, a few studies have also explored the microtubule-nuclear connections in other cell types. In plant epidermal cells, it has been shown that nucleus-associated microtubules determine the cell division plane (Flanders J D *et al*., 1990). In yeasts, microtubules emerging from the spindle pole body elongate to form stable microtubule bundles that drive the cells towards quiescence (Laporte and Sagot, 2014).

These studies collectively highlight the multiple ways that microtubules support the maintenance of nuclear structure, position, and function. In addition to providing a scaffold for intracellular movement and a means by which to move vesicles along the cytoskeleton, microtubules function dynamically as both regulators of nuclear stiffness/mechanics and gene expression. Through interaction with the LINC complex and its associated motors, microtubules provide a link between the physical forces present within the cytoplasm and the organization of chromatin. As a result, this enables the cell to adjust its nuclear shape, position, and transcriptional activities based on physiological and mechanical stimuli. The coordination of biochemical and mechanical signals between the cytoplasm and the nucleus is essential for developmental processes, including differentiation and tissue morphogenesis, and for genome stability. Thus, future research focused on identifying how microtubule post-translational modifications and nucleocytoplasmic transport influence the interactions described above will be necessary to understand the mechanisms by which cellular forces are integrated at the nuclear level during development and disease progression.

Microtubules in mechanosignaling:

Microtubules provide an essential link for mechanical signals that are generated by the extracellular environment to be transmitted to intracellular mechanisms that control the behaviour of a cell through the action of numerous molecular motors and protein kinases. Motor proteins (dynein, kinesin) that bind to microtubules at the cell cortex sense and produce mechanical forces on the microtubule, resulting in changes in the rate and extent of microtubule polymerization and stability, thereby influencing the localized activation of signaling pathways involved in cell movement, attachment, and differentiation (Kaverina *et al*., 1998; Waterman-Storer *et al*., 1999; Ligon and Holzbaur, 2007; Stehbens and Wittmann, 2012).

Mechanoreceptor pathways have also been associated with the stabilization of microtubules; Xang *et al*. (2023), for instance, showed that stabilizing microtubules in nucleus pulposus cells resulted in activation of the Hippo signaling pathway, which suppresses YAP activity, while it increases levels of Col2 and Sox9, both of which are the most important transcription factors involved in maintaining cartilage homeostasis. Re-organization of the microtubule network in response to mechanical stress results in degradation of AMOT proteins that sequester YAP/TAZ. AMOT proteins may thus serve as a link between microtubule remodeling and the YAP/TAZ mechanosignaling pathway (Vanni *et al*., 2025). Microtubules may further influence the Rho/ROCK signaling pathway by forming a complex with the cytoplasmic tail of an integrin receptor and subsequently modulating the assembly of myosin IIA filament and force of contraction via modulating actin-myosin contractile units (Rafiq *et al*., 2019). Changes in microtubule lattice conformation may also influence Rho/ROCK signaling via the microtubule-GEF H1- RhoA contractility axis. A recent structural study on GEF-H1 indicates that the C1-domain of GEF-H1 mediates its interaction with microtubules, with the binding localized to both the intra-dimer interface and inter-protofilament contacts on the microtubule outer surface (Choi *et al.*, 2025). This characteristic binding of GEF-H1 to microtubules may be pivotal to the release/further recruitment of GEF-H1 in response to changes in the microtubule lattice mediated by MAPs, motors or mechanical stress. The study also identified C1 domains in other key signaling proteins central to other signaling pathways like AKAP13 (another RhoGEF), RASSF1A (Hippo pathway), RAF1A (MAPK pathway).

These studies collectively illustrate the role of microtubules as molecular transducers of mechanical signals generated by deformation at the plasma membrane, relaying them to downstream metabolic pathways that regulate cell morphology and contractility. **Fig 4** shows the involvement of microtubules in different steps of the cellular mechanobiology pathway.

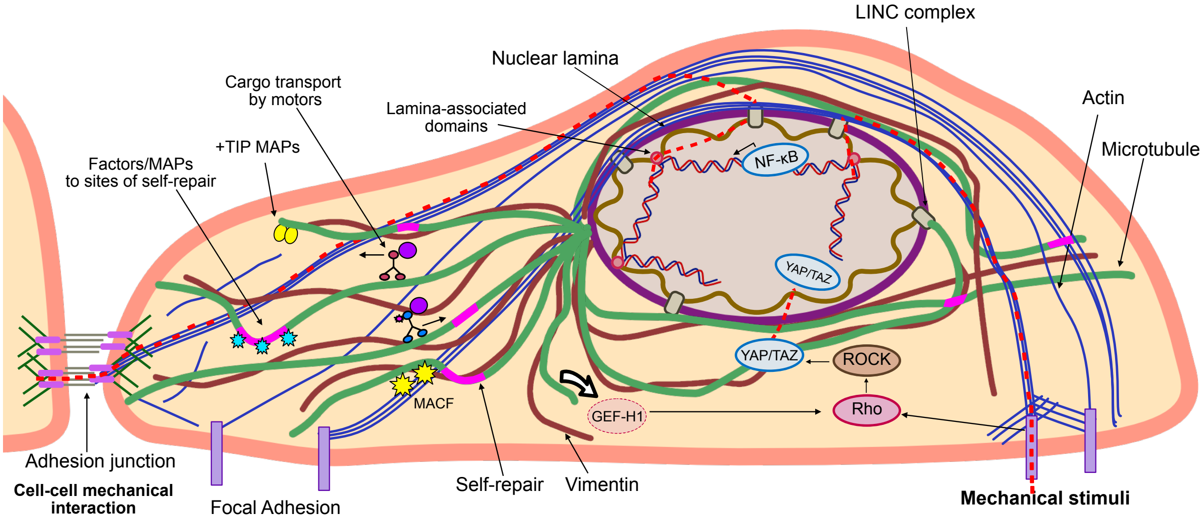

Fig 4: Mechanosensing: Microtubules sense mechanical stimuli from focal adhesions located along the cell membrane. **Mechanoadaptation:** Microtubules undergo self-repair and recruit intracellular factors, MAPs, and cyto-linkers (like MACF) to respond and adapt to stimuli, thus transducing biochemical signals across the cytoskeletal landscape. **Mechanotransduction:** Microtubule remodeling or deformation is directly transduced to the nucleus via LINC complexes on the nuclear membrane interface. **Mechanosignaling:** GEF-H1 released from depolymerizing microtubules triggers the release of YAP/TAZ via the Rho-ROCK pathway. Stabilization of microtubules can suppress YAP/TAZ.

Conclusion:

Microtubules are unique in both their extreme stiffness and their ability to reorganize rapidly. Far from acting as rigid, passive struts, microtubules play a central role in mechanosensation and mechanotransduction pathways. Recent studies increasingly indicate that the force-sensitive nature of the microtubule cytoskeleton helps microtubules serve as a mechanostat for the cell. The dynamic adaptability of the microtubule lattice allows them to translate small mechanical stimuli into biochemical signals that effect cytoskeletal (re)organization and gene expression. This is primarily mediated through a series of changes in microtubule network mechanics, recruitment of MAPs, cytolinkers, crosstalk with other cytoskeletal filaments, thus triggering secondary changes in actomyosin contractility, mechano-signaling, and subsequent cellular mechano-response (**Fig 5**). In this way, microtubules effectively orchestrate cellular adaptation to mechanical cues and coordinate important cellular functions. Exploring the molecular mechanisms and force thresholds that trigger lattice remodeling and microtubule-mediated mechanosignaling will be crucial for revealing how cells sense and adapt to mechanical stimuli. Insights in this direction may open new research avenues for targeting microtubule mechanosensitivity for treating cancer and other neurodegenerative diseases.

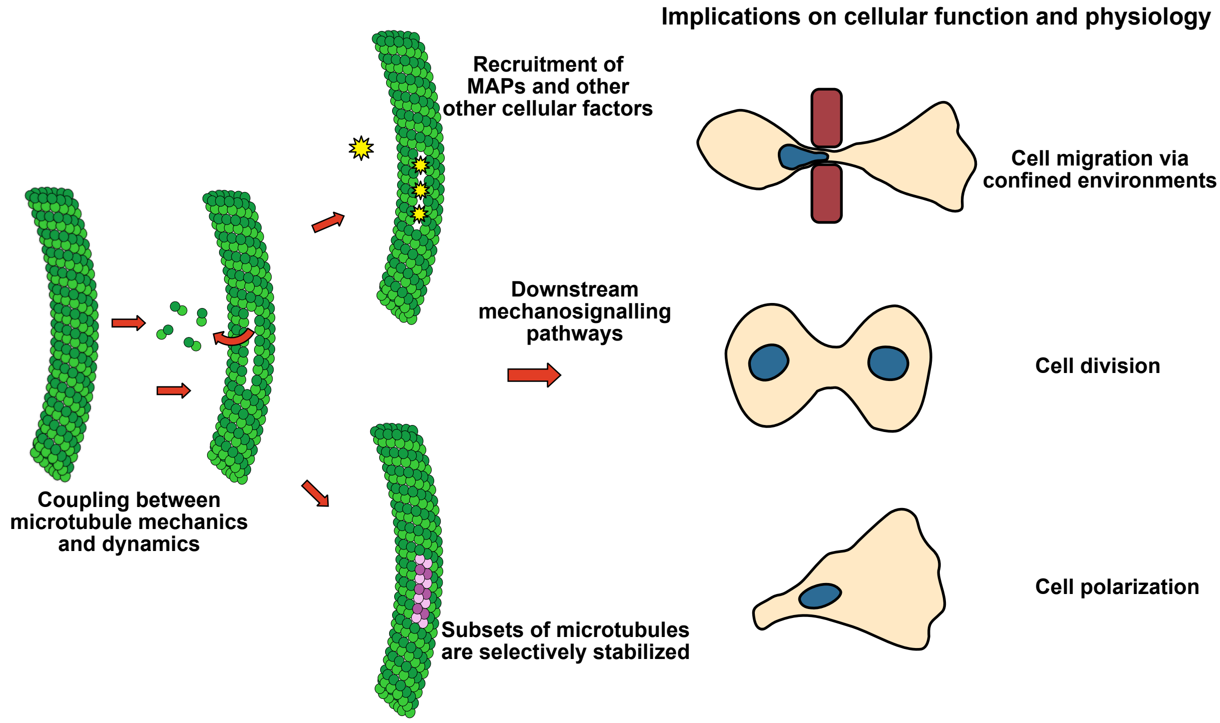

Fig 5: Conceptual model of role of microtubules as cellular mechanosensors. The force sensitive nature and dynamically adaptable nature of microtubules make them sensitive to stimuli. Microtubules respond to stimuli through self-repair, recruitment of MAPs and lattice remodeling that triggers downstream signaling pathways thus serving as an allosteric interface for integration of mechanical and biochemical signals.

References:

1. Aher A, Rai D, Schaedel L, Gaillard J, John K, Liu Q, Altelaar M, Blanchoin L, Thery M, Akhmanova A. (2020). CLASP Mediates Microtubule Repair by Restricting Lattice Damage and Regulating Tubulin Incorporation. Curr Biol. 30(11):2175-2183.e6.
2. Ahmad, R., Kleineberg, C., Nasirimarekani, V., Su, Y. J., Goli Pozveh, S., Bae, A., Sundmacher, K., Bodenschatz, E., Guido, I., Vidaković-Koch, T., & Gholami, A. (2021). Light-Powered Reactivation of Flagella and Contraction of Microtubule Networks: Toward Building an Artificial Cell. ACS synthetic biology, 10(6), 1490–1504.

3. Akhmanova, A., & Steinmetz, M. O. (2015). Control of microtubule organization and dynamics: two ends in the limelight. Nature reviews. Molecular cell biology, 16(12), 711–726. https://doi.org/10.1038/nrm4084

4. Akiyoshi, B. *et al*. (2010).Tension directly stabilizes reconstituted kinetochore-microtubule attachments. Nature 468, 576–579.

5. Alric, B., Formosa-Dague, C., Dague, E., Holt, L. J., & Delarue, M. (2022). Macromolecular crowding limits growth under pressure. Nature physics, 18(4), 411–416. https://doi.org/10.1038/s41567-022-01506-1

6. Ambrose, C., Allard, J., Cytrynbaum, E. *et al*. (2011). A CLASP-modulated cell edge barrier mechanism drives cell-wide cortical microtubule organization in Arabidopsis. Nat Commun 2, 430.

7. Andreu-Carbó, M., Egoldt, C., Velluz, MC. *et al*. (2024). Microtubule damage shapes the acetylation gradient. Nat Commun 15, 2029. https://doi.org/10.1038/s41467-024-46379-5

8. Asakawa, K., Toya, M., Sato, M., Kanai, M., Kume, K., Goshima, T., Garcia, M. A., Hirata, D., & Toda, T. (2005). Mal3, the fission yeast EB1 homologue, cooperates with Bub1 spindle checkpoint to prevent monopolar attachment. EMBO reports, 6(12), 1194–1200. https://doi.org/10.1038/sj.embor.7400540

9. Azoitei, M. L., Noh, J., Marston, D. J., Roudot, P., Marshall, C. B., Daugird, T. A., Lisanza, S. L., Sandí, M. J., Ikura, M., Sondek, J., Rottapel, R., Hahn, K. M., & Danuser, G. (2019). Spatiotemporal dynamics of GEF-H1 activation controlled by microtubule- and Src-mediated pathways. The Journal of cell biology, 218(9), 3077–3097.

10. Bachand, G. D., Jain, R., Ko, R., Bouxsein, N. F., & VanDelinder, V. (2018). Inhibition of microtubule depolymerization by osmolytes. Biomacromolecules, 19(7), 2401-2408.

11. Barlan, K., & Gelfand, V. I. (2017). Microtubule-Based Transport and the Distribution, Tethering, and Organization of Organelles. Cold Spring Harbor perspectives in biology, 9(5), a025817.

12. Biedzinski, S., Agsu, G., Vianay, B., Delord, M., Blanchoin, L., Larghero, J., Faivre, L., Théry, M., & Brunet, S. (2020). Microtubules control nuclear shape and gene expression during early stages of hematopoietic differentiation. The EMBO journal, 39(23), e103957. https://doi.org/10.15252/embj.2019103957

13. Bieling P, Telley IA, Surrey T. (2010). A minimal midzone protein module controls formation and length of antiparallel microtubule overlaps. Cell, 142:420–432.

14. Biswas S., Kalil K. (2018). The microtubule-associated protein tau mediates the organization of microtubules and their dynamic exploration of actin-rich lamellipodia and filopodia of cortical growth cones. J. Neurosci. 38, 291–307.

15. Biswas, S., Grover, R., Reuther, C., Poojari, C.S., Shaebani, R, **Nandakumar, S**., Grünewald, M., Zablotsky, A., Hub, J.S., Diez, S., John, K., Schaedel, L. (2025). Tau accelerates tubulin exchange in the microtubule lattice. Nat. Phys. 21, 1616–1628.

16. Bonnet, C., Boucher, D., Lazereg, S., Pedrotti, B., Islam, K., Denoulet, P. and Larcher, J. C. (2001). Differential binding regulation of microtubule-associated proteins MAP1A, MAP1B, and MAP2 by tubulin polyglutamylation. J. Biol. Chem. 276, 12839-12848.

17. Bormuth V, Nitzsche B, Ruhnow F, Mitra A, Storch M, Rammner B, Howard J, Diez S. (2012). The highly processive kinesin 8, Kip3, switches microtubule protofilaments with a bias toward the left. Biophys J, 103:L4–L6.

18. Bormuth, V., Varga, V., Howard, J., & Schäffer, E. (2009). Protein Friction Limits Diffusive and Directed Movements of Kinesin Motors on Microtubules. Science, 325(5942), 870–873. https://doi.org/10.1126/science.1174923

19. Bormuth, V., Varga, V., Howard, J., & Schäffer, E. (2010). Breaking of bonds between a kinesin motor and microtubules causes protein friction. Optical Trapping and Optical Micromanipulation VII, 7762, 36–42. https://doi.org/10.1117/12.863545

20. Bourns, B., Franklin, S., E. D. Salmon. (1988). High hydrostatic pressure effects in vivo: changes in cell morphology, microtubule assembly, and actin organization. Cell Motil. Cytoskeleton. 10:380–390.

21. Braun, M., Lansky, Z., Fink, G., Ruhnow, F., Diez, S., & Janson, M. E. (2011). Adaptive braking by Ase1 prevents overlapping microtubules from sliding completely apart. Nature Cell Biology, 13(10), 1259–1264. https://doi.org/10.1038/ncb2323

22. Bringmann, M., Landrein, B., Schudoma, C., Hamant, O., Hauser, M. T., & Persson, S. (2012). Cracking the elusive alignment hypothesis: the microtubule-cellulose synthase nexus unraveled. Trends in plant science, 17(11), 666–674. https://doi.org/10.1016/j.tplants.2012.06.003

23. Buglak, D. B., Bougaran, P., Kulikauskas, M. R., Liu, Z., Monaghan-Benson, E., Gold, A. L., Marvin, A. P., Burciu, A., Tanke, N. T., Oatley, M., Ricketts, S. N., Kinghorn, K., Johnson, B. N., Shiau, C. E., Rogers, S., Guilluy, C., & Bautch, V. L. (2023). Nuclear SUN1 stabilizes endothelial cell junctions via microtubules to regulate blood vessel formation. eLife, 12, e83652. https://doi.org/10.7554/eLife.83652

24. Busch, K. E., & Brunner, D. (2004). The microtubule plus end-tracking proteins mal3p and tip1p cooperate for cell-end targeting of interphase microtubules. Current Biology, 14(7), 548-559.

25. Cai, D., Hoppe, A. D., Swanson, J. A. & Verhey, K. J. (2007). Kinesin-1 structural organization and conformational changes revealed by FRET stoichiometry in live cells. J. Cell Biol. 176, 51–63.

26. Can S, Dewitt MA, Yildiz A. (2014). Bidirectional helical motility of cytoplasmic dynein around microtubules. Elife, 3.

27. Carmona, B., L. S. Delgado, I., Nolasco, S., Marques, R., Gonçalves, J., Soares, H. (2025). Tubulin Acetylation and the Cellular Mechanosensing and Stress Response. In: Halasa, M., Wawruszak, A. (eds) Histone and Non-Histone Reversible Acetylation in Development, Aging and Disease. Results and Problems in Cell Differentiation, vol 75. Springer, Cham. https://doi.org/10.1007/978-3-031-91459-1_5

28. Cassimeris L, Pryer NK, Salmon ED. (1988). Real-time observations of microtubule dynamic instability in living cells. J Cell Biol.107(6 Pt 1):2223-31. Doi: 10.1083/jcb.107.6.2223. PMID: 3198684; PMCID: PMC2115680.

29. Chakraborty M, Toleikis A, Siddiqui N *et al* (2020) Activation of cytoplasmic dynein through microtubule crossbridging. BioRxiv 038950. https://doi.org/10.1101/2020.04.13.038950

30. Chiba, K., Ori-McKenney, K. M., Niwa, S., & McKenney, R. J. (2022). Synergistic autoinhibition and activation mechanisms control kinesin-1 motor activity. Cell reports, 39(9), 110900. https://doi.org/10.1016/j.celrep.2022.110900

31. Coleman, A. K., Joca, H. C., Shi, G., Lederer, W. J., & Ward, C. W. (2021). Tubulin acetylation increases cytoskeletal stiffness to regulate mechanotransduction in striated muscle. The Journal of general physiology, 153(7), e202012743. https://doi.org/10.1085/jgp.202012743

32. Colin A, Kotila T, Guérin C, Orhant-Prioux M, Vianay B, Mogilner A, Lappalainen P, Théry M, Blanchoin L.(2023). Recycling of the actin monomer pool limits the lifetime of network turnover. EMBO J, 42(9):e112717.

33. D J Flanders, D J Rawlins, P J Shaw, C W Lloyd. (1990). Nucleus-associated microtubules help determine the division plane of plant epidermal cells: avoidance of four-way junctions and the role of cell geometry.. J Cell Biol, 110 (4): 1111–1122.

34. D'Souza, A.I., Grover, R., Monzon, G.A. *et al*. (2023). Vesicles driven by dynein and kinesin exhibit directional reversals without regulators. Nat Commun 14, 7532. https://doi.org/10.1038/s41467-023-42605-8

35. Dogterom *et al* (2002)., Force generation by polymerizing microtubules, Appl Phy A

36. Dogterom M, Yurke B. (1997).Measurement of the force-velocity relation for growing microtubules. Science, 278(5339):856-60.

37. Dogterom, M., & Koenderink, G. H. (2019). Actin-microtubule crosstalk in cell biology. Nature reviews. Molecular cell biology, 20(1), 38–54. https://doi.org/10.1038/s41580-018-0067-1

38. Dunn, S., Morrison, E. E., Liverpool, T. B., Molina-Paris, C., Cross, R. A., Alonso, M. C. and Peckham, M. (2008). Differential trafficking of Kif5c on tyrosinated and detyrosinated microtubules in live cells. J. Cell Sci. 121, 1085-1095.

39. Efimov, A., Schiefermeier, N., Grigoriev, I., Ohi, R., Brown, M. C., Turner, C. E., Small, J. V., & Kaverina, I. (2008). Paxillin-dependent stimulation of microtubule catastrophes at focal adhesion sites. Journal of cell science, 121(Pt 2), 196–204. https://doi.org/10.1242/jcs.012666

40. Elbaum, M., Fygenson, D.K, Libchaber, A. (1997). Mechanics of microtubule-based membrane extension. Phys. Rev. Lett. 76, 4078.

41. Eng RC, Schneider R, Matz TW, Carter R, Ehrhardt DW, Jönsson H, Nikoloski Z, Sampathkumar A. (2021). KATANIN and CLASP function at different spatial scales to mediate microtubule response to mechanical stress in Arabidopsis cotyledons. Curr Biol, 31(15):3262-3274.e6.

42. Espeut, J. *et al*. (2008). Phosphorylation relieves autoinhibition of the kinetochore motor Cenp-E. Mol. Cell 29, 637–643.

43. Ezratty, E. J., Partridge, M. A., & Gundersen, G. G. (2005). Microtubule-induced focal adhesion disassembly is mediated by dynamin and focal adhesion kinase. Nature cell biology, 7(6), 581–590. https://doi.org/10.1038/ncb1262

44. Ferro LS, Can S, Turner MA, ElShenawy MM, Yildiz A. (2019). Kinesin and dynein use distinct mechanisms to bypass obstacles. Elife, 8:1–20.

45. Fletcher, D., Mullins, R. (2010) Cell mechanics and the cytoskeleton. Nature 463, 485–492. https://doi.org/10.1038/nature08908

46. Forth, S., Hsia, K.-C., Shimamoto, Y., & Kapoor, T. M. (2014). Asymmetric Friction of Nonmotor MAPs Can Lead to Their Directional Motion in Active Microtubule Networks. Cell, 157(2), 420–432. https://doi.org/10.1016/j.cell.2014.02.018

47. Furuta, K., & Toyoshima, Y. Y. (2008). Minus-end-directed motor Ncd exhibits processive movement that is enhanced by microtubule bundling in vitro. Current biology: CB, 18(2), 152–157. https://doi.org/10.1016/j.cub.2007.12.056

48. Ga, M., L, S., A, Ds., V, H., L, S., & S, D. (2020). Stable tug-of-war between kinesin-1 and cytoplasmic dynein upon different ATP and roadblock concentrations. Journal of Cell Science, 133(22). https://doi.org/10.1242/jcs.249938

49. Gadadhar, S., Bodakuntla, S., Natarajan, K., & Janke, C. (2017). The tubulin code at a glance. Journal of Cell Science, 130(8), 1347–1353. https://doi.org/10.1242/jcs.199471

50. Ganguly, A., Yang, H., Sharma, R., Patel, K. D., & Cabral, F. (2012). The role of microtubules and their dynamics in cell migration. The Journal of biological chemistry, 287(52), 43359–43369.

51. Gao, M., Berghaus, M., Möbitz, S., Schuabb, V., Erwin, N., Herzog, M., Julius, K., Sternemann, C., & Winter, R. (2018). On the Origin of Microtubules' High-Pressure Sensitivity. Biophysical journal, 114(5), 1080–1090. https://doi.org/10.1016/j.bpj.2018.01.021

52. Gélin, M., Schaeffer, A., Gaillard, J., Guérin, C., Vianay, B., Orhant-Prioux, M., Braun, M., Leterrier, C., Blanchoin, L., & Théry, M. (2023). Microtubules under mechanical pressure can breach dense actin networks. Journal of Cell Science, 136(22), jcs261667. https://doi.org/10.1242/jcs.261667

53. Gimpel, P., Lee, Y. L., Sobota, R. M., Calvi, A., Koullourou, V., Patel, R., Mamchaoui, K., Nédélec, F., Shackleton, S., Schmoranzer, J., Burke, B., Cadot, B., & Gomes, E. R. (2017). Nesprin-1α-Dependent Microtubule Nucleation from the Nuclear Envelope via Akap450 Is Necessary for Nuclear Positioning in Muscle Cells. Current biology : CB, 27(19), 2999–3009.e9. https://doi.org/10.1016/j.cub.2017.08.031

54. Hamant O, Inoue D, Bouchez D, Dumais J, Mjolsness E (2019) Are microtubules tension sensors? Nat Commun 10:2360

55. Hamant, O., Heisler, M. G., Jönsson, H., Krupinski, P., Uyttewaal, M., Bokov, P., Corson, F., Sahlin, P., Boudaoud, A., Meyerowitz, E. M., Couder, Y., & Traas, J. (2008). Developmental patterning by mechanical signals in Arabidopsis. Science (New York, N.Y.), 322(5908), 1650–1655. https://doi.org/10.1126/science.1165594

56. Hamant, O., Traas, J., & Boudaoud, A. (2010). Regulation of shape and patterning in plant development. Current opinion in genetics & development, 20(4), 454–459. https://doi.org/10.1016/j.gde.2010.04.009

57. Haswell, E. S., & Verslues, P. E. (2015). The ongoing search for the molecular basis of plant osmosensing. The Journal of general physiology, 145(5), 389–394. https://doi.org/10.1085/jgp.201411295

58. Heffler, J., Shah, P. P., Robison, P., Phyo, S., Veliz, K., Uchida, K., Bogush, A., Rhoades, J., Jain, R., & Prosser, B. L. (2020). A Balance Between Intermediate Filaments and Microtubules Maintains Nuclear Architecture in the Cardiomyocyte. Circulation research, 126(3), e10–e26. https://doi.org/10.1161/CIRCRESAHA.119.315582

59. Hejnowicz, Z., Rusin, A., & Rusin, T. (2000). Tensile Tissue Stress Affects the Orientation of Cortical Microtubules in the Epidermis of Sunflower Hypocotyl. Journal of plant growth regulation, 19(1), 31–44. https://doi.org/10.1007/s003440000005

60. Hollenbeck, P. J. (1989). The distribution, abundance and subcellular localization of kinesin. Journal of Cell Biology, 108(6), 2335–2342. https://doi.org/10.1083/jcb.108.6.2335

61. Holt, L. J., & Delarue, M. (2023). Macromolecular crowding: Sensing without a sensor. Current opinion in cell biology, 85, 102269. https://doi.org/10.1016/j.ceb.2023.102269

62. Hotani, H and Miyamoto, H. (1990). Dynamic features of microtubules as visualized by dark-field microscopy. Adv. Biophys. 26, 135-156.

63. Huber F, Boire A, López MP, Koenderink GH. (2015). Cytoskeletal crosstalk: when three different personalities team up. Curr Opin Cell Biol, 32:39-47.

64. Ikegami, K. *et al*. (2007). Loss of α-tubulin polyglutamylation in ROSA22 mice is associated with abnormal targeting of KIF1A and modulated synaptic function. Proc. Natl Acad. Sci. USA 104, 3213–8.

65. Ingber D. E. (2008). Tensegrity-based mechanosensing from macro to micro. Progress in biophysics and molecular biology, 97(2-3), 163–179. https://doi.org/10.1016/j.pbiomolbio.2008.02.005

66. Inoué, S., & Salmon, E. D. (1995). Force Generation by Microtubule Assembly/Disassembly in Mitosis and Related Movements. Molecular Biology of the Cell, 6(12), 1619–1640. https://doi.org/10.1091/mbc.6.12.1619

67. Janet Y. Sheung, Daisy H. Achiriloaie, Christopher Currie, Karthik Peddireddy, Aaron Xie, Jessalyn Simon-Parker, Gloria Lee, Michael J. Rust, Moumita Das, Jennifer L. Ross, and Rae M. (2021). Robertson-Anderson. Motor driven restructuring of Cytoskeleton Composites Leads to Tunable Time-Varying Elasticity ACS Macro Letters,10 (9), 1151-1158

68. Janke, C., & Magiera, M. M. (2020). The tubulin code and its role in controlling microtubule properties and functions. Nature Reviews. Molecular Cell Biology, 21(6), 307–326. https://doi.org/10.1038/s41580-020-0214-3

69. Janson, M. E., de Dood, M. E., & Dogterom, M. (2003). Dynamic instability of microtubules is regulated by force. Journal of Cell Biology, 161(6), 1029–1034. https://doi.org/10.1083/jcb.200301147

70. Janson, M. E., Loughlin, R., Loïodice, I., Fu, C., Brunner, D., Nédélec, F. J., & Tran, P. T. (2007). Crosslinkers and motors organize dynamic microtubules to form stable bipolar arrays in fission yeast. Cell, 128(2), 357–368. https://doi.org/10.1016/j.cell.2006.12.030

71. Jolly, A. L., Kim, H., Srinivasan, D., Lakonishok, M., Larson, A. G., & Gelfand, V. I. (2010). Kinesin-1 heavy chain mediates microtubule sliding to drive changes in cell shape. Proceedings of the National Academy of Sciences, 107(27), 12151–12156. https://doi.org/10.1073/pnas.1004736107

72. Ju, R. J., Falconer, A. D., Schmidt, C. J., Enriquez Martinez, M. A., Dean, K. M., Fiolka, R. P., Sester, D. P., Nobis, M., Timpson, P., Lomakin, A. J., Danuser, G., White, M. D., Haass, N. K., Oelz, D. B., & Stehbens, S. J. (2024). Compression-dependent microtubule reinforcement enables cells to navigate confined environments. Nature cell biology, 26(9), 1520–1534. https://doi.org/10.1038/s41556-024-01476-x

73. Kapitein, L. C., Peterman, E. J., Kwok, B. H., Kim, J. H., Kapoor, T. M., & Schmidt, C. F. (2005). The bipolar mitotic kinesin Eg5 moves on both microtubules that it crosslinks. Nature, 435(7038), 114–118. https://doi.org/10.1038/nature03503

74. Kapitein, L.C., B.H. Kwok, J.S. Weinger, C.F. Schmidt, T.M. Kapoor, and E.J.G. Peterman. (2008). Microtubule cross-linking triggers the directional motility of kinesin-5. J. Cell Biol. 182:421–428).

75. Kaverina, I., Krylyshkina, O., & Small, J. V. (1998). Microtubule targeting of substrate contacts promotes their relaxation and dissociation. Journal of Cell Biology, 142(6), 181–190. https://doi.org/10.1083/jcb.142.6.181

76. Kaverina, I., Rottner, K., & Small, J. V. (1998). Targeting, capture, and stabilization of microtubules at early focal adhesions. The Journal of cell biology, 142(1), 181–190. https://doi.org/10.1083/jcb.142.1.181

77. Kerr, J. P., Robison, P., Shi, G., Bogush, A. I., Kempema, A. M., Hexum, J. K., Becerra, N., Harki, D. A., Martin, S. S., Raiteri, R. *et al*. (2015). Detyrosinated microtubules modulate mechanotransduction in heart and skeletal muscle. Nat. Commun. 6, 8526.

78. Kimura, Y., Kurabe, N., Ikegami, K., Tsutsumi, K., Konishi, Y., Kaplan, O. I., Kunitomo, H., Iino, Y., Blacque, O. E. and Setou, M. (2010). Identification of tubulin deglutamylase among Caenorhabditis elegans and mammalian cytosolic carboxypeptidases (CCPs). J. Biol. Chem. 285, 22936-22941.

79. Komarova YA, Akhmanova AS, Kojima S, Galjart N, Borisy GG. (2002) Cytoplasmic linker proteins promote microtubule rescue in vivo. J Cell Biol,159(4):589-99.

80. Konishi, Y. and Setou, M. (2009). Tubulin tyrosination navigates the kinesin-1 motor domain to axons. Nat. Neurosci. 12, 559-567.

81. Kopf, A., Renkawitz, J., Hauschild, R., Girkontaite, I., Tedford, K., Merrin, J., Thorn-Seshold, O., Trauner, D., Häcker, H., Fischer, K. D., Kiermaier, E., & Sixt, M. (2020). Microtubules control cellular shape and coherence in amoeboid migrating cells. The Journal of cell biology, 219(6), e201907154.

82. Koshland, D. E., Mitchison, T. J., & Kirschner, M. W. (1988). Polewards chromosome movement driven by microtubule depolymerization in vitro. Nature, 331, 499–504.

83. Krattenmacher, J., Lera-Ramirez, M., Beber, A., Herynek, S., Grycova, L., Liu, X., Neuzil, P., Nedelec, F., Diez, S., Braun, M., & Lansky, Z. (2024). Ase1 selectively increases the lifetime of antiparallel microtubule overlaps. Current biology: CB, S0960-9822(24)00994-1. Advance online publication. https://doi.org/10.1016/j.cub.2024.07.055

84. Kreitzer, G., Liao, G. and Gundersen, G. G. (1999). Detyrosination of tubulin regulates the interaction of intermediate filaments with microtubules in vivo via a kinesin-dependent mechanism. Mol. Biol. Cell 10, 1105-1118.

85. Kučera, O., Gaillard, J., Guérin, C., Théry, M., & Blanchoin, L. (2022). Actin-microtubule dynamic composite forms responsive active matter with memory. Proceedings of the National Academy of Sciences of the United States of America, 119(31), e2209522119. https://doi.org/10.1073/pnas.2209522119

86. Kume, K., Kaneko, S., Nishikawa, K., Mizunuma, M., & Hirata, D. (2018). Role of nucleocytoplasmic transport in interphase microtubule organization in fission yeast. Biochemical and biophysical research communications, 503(2), 1160–1167. https://doi.org/10.1016/j.bbrc.2018.06.135

87. Kurasawa, Y., Earnshaw, W. C., Mochizuki, Y., Dohmae, N., & Todokoro, K. (2004). Essential roles of KIF4 and its binding partner PRC1 in organized central spindle midzone formation. The EMBO Journal, 23(16), 3237–3248. https://doi.org/10.1038/sj.emboj.7600347

88. Lacroix, B., van Dijk, J., Gold, N. D., Guizetti, J., Aldrian-Herrada, G., Rogowski, K., Gerlich, D. W. and Janke, C. (2010). Tubulin polyglutamylation stimulates spastin-mediated microtubule severing. J. Cell Biol. 189, 945-954.

89. Landrein, B., & Hamant, O. (2013). How mechanical stress controls microtubule behavior and morphogenesis in plants: history, experiments and revisited theories. The Plant journal: for cell and molecular biology, 75(2), 324–338. https://doi.org/10.1111/tpj.12188

90. Lansky, Z., Braun, M., Lüdecke, A., Schlierf, M., ten Wolde, P. R., Janson, M. E., & Diez, S. (2015). Diffusible crosslinkers generate directed forces in microtubule networks. Cell, 160(6), 1159–1168. https://doi.org/10.1016/j.cell.2015.01.051

91. Laporte, D., & Sagot, I. (2014). Microtubules move the nucleus to quiescence. Nucleus (Austin, Tex.), 5(2), 113–118. https://doi.org/10.4161/nucl.28538

92. Laura Meißner, Lukas Niese, Stefan Diez. (2024). Helical motion and torque generation by microtubule motors, Current Opinion in Cell Biology, Volume 88, 102367, ISSN 0955-0674.

93. Lavrsen, Kirstine, Girish Rajendraprasad, Marcin Leda, Susana Eibes, Elisa Vitiello, Vasileios Katopodis, Andrew B. Goryachev, and Marin Barisic. (2023). Microtubule detyrosination drives symmetry breaking to polarize cells for directed cell migration. Proceedings of the National Academy of Sciences 120, no. 22, e2300322120.

94. Lecompte, W. & John, K. (2023). Molecular motors enhance microtubule lattice plasticity. APS. 1, 013012.

95. Lee, S., & Higuchi, H. (2019). 3D rotational motion of an endocytic vesicle on a complex microtubule network in a living cell. Biomedical optics express, 10(12), 6611-6624.

96. Lei, L., Li, S., & Gu, Y. (2012). Cellulose synthase interactive protein 1 (CSI1) mediates the intimate relationship between cellulose microfibrils and cortical microtubules. Plant signaling & behavior, 7(7), 714–718. https://doi.org/10.4161/psb.20338

97. Liao, G. and Gundersen, G. G. (1998). Kinesin is a candidate for cross-bridging microtubules and intermediate filaments. Selective binding of kinesin to detyrosinated tubulin and vimentin. J. Biol. Chem. 273, 9797-9803.

98. Ligon, L. A., & Holzbaur, E. L. (2007). Microtubules tethered at epithelial cell junctions by dynein facilitate efficient junction assembly. Traffic (Copenhagen, Denmark), 8(7), 808–819. https://doi.org/10.1111/j.1600-0854.2007.00574.x

99. Lindsey Seldin,Andrew Muroyama, Terry Lechler. (2016) NuMA-microtubule interactions are critical for spindle orientation and the morphogenesis of diverse epidermal structures eLife 5:e12504.

100. Lu, W., Lakonishok, M., & Gelfand, V. I. (2015). Kinesin-1–powered microtubule sliding initiates axonal regeneration in Drosophila cultured neurons. Molecular Biology of the Cell, 26(7), 1296–1307. https://doi.org/10.1091/mbc.E14-10-1423

101. Lucas, J. R., Courtney, S., Hassfurder, M., Dhingra, S., Bryant, A., & Shaw, S. L. (2011). Microtubule-associated proteins MAP65-1 and MAP65-2 positively regulate axial cell growth in etiolated Arabidopsis hypocotyls. The Plant cell, 23(5), 1889–1903.

102. Maas, C., Belgardt, D., Lee, H. K., Heisler, F. F., Lappe-Siefke, C., Magiera, M. M., van Dijk, J., Hausrat, T. J., Janke, C. and Kneussel, M. (2009). Synaptic activation modifies microtubules underlying transport of postsynaptic cargo. Proc. Natl. Acad. Sci. USA 106, 8731-8736.

103. Matis M. (2020). The Mechanical Role of Microtubules in Tissue Remodeling. Bioessays.42(5):e1900244. doi: 10.1002/bies.201900244. Epub 2020 Apr 6. PMID: 32249455.

104. Mazumder, A., & Shivashankar, G. V. (2010). Emergence of a prestressed eukaryotic nucleus during cellular differentiation and development. Journal of the Royal Society, Interface, 7 Suppl 3(Suppl 3), S321–S330.

105. McIntosh, J. R., Volkov, V., Ataullakhanov, F. I., & Grishchuk, E. L. (2008). Tubulin depolymerization may be an ancient biological motor. Journal of Cell Science, 123(20), 3425–3434.

106. Grishchuk, E. L. (2017). Biophysics of microtubule end coupling at the kinetochore. Progress in Molecular and Subcellular Biology, 56, 397–428.

107. Meißner, L., Niese, L., Schüring, I., Mitra, A., & Diez, S. (2024). Human kinesin-5 KIF11 drives the helical motion of anti-parallel and parallel microtubules around each other. The EMBO Journal, 43(7), 1244–1256. https://doi.org/10.1038/s44318-024-00048-x

108. Mimori Y, Miki-Noumura T. (1995). Extrusion of rotating microtubules on the dynein-track from a microtubule-dynein g-complex. Cell Motil Cytoskeleton, 30:17–25.

109. Mitra A, Ruhnow F, Nitzsche B, Diez S. (2015) Impact-free measurement of microtubule rotations on kinesin and cytoplasmic dynein coated surfaces. PloS One, 10, e0136920.

110. Mitra, A., Meißner, L., Gandhimathi, R., Renger, R., Ruhnow, F., & Diez, S. (2020). Kinesin-14 motors drive a right-handed helical motion of antiparallel microtubules around each other. Nature Communications, 11(1), 2565. https://doi.org/10.1038/s41467-020-16328-z

111. Molines, A. T., Lemière, J., Gazzola, M., Steinmark, I. E., Edrington, C. H., Hsu, C. T., Real-Calderon, P., Suhling, K., Goshima, G., Holt, L. J., Thery, M., Brouhard, G. J., & Chang, F. (2022). Physical properties of the cytoplasm modulate the rates of microtubule polymerization and depolymerization. Developmental cell, 57(4), 466–479.e6. https://doi.org/10.1016/j.devcel.2022.02.001

112. Monroy BY, Sawyer DL, Ackermann BE, Borden MM, Tan TC, and Ori-McKenney KM (2018). Competition between microtubule-associated proteins directs motor transport. Nat Commun 9, 1487.

113. Monroy, B. Y., Tan, T. C., Oclaman, J. M., Han, J. S., Simó, S., Niwa, S., Nowakowski, D. W., McKenney, R. J., & Ori-McKenney, K. M. (2020). A Combinatorial MAP Code Dictates Polarized Microtubule Transport. Developmental Cell, 53(1), 60-72.e4. https://doi.org/10.1016/j.devcel.2020.01.029

114. Motta, M.R., Biswas, S., Schaedel, L. (2023). Beyond uniformity: Exploring the heterogeneous and dynamic nature of the microtubule lattice. European journal of cell biology. 102(4), 151370.

115. Motta, M.R., Grisam, C., Grünewald, M., König, B., Meißner, L., Niese, L., Diez, S., Hamant, O., Schaedel, L. (2025). MAP65-1/PRC1 reinforces microtubules through nucleation. BioRxiv preprint. Doi.org/10.1101/2025.09.14.676082

116. Muroyama, A., & Lechler, T. (2017). Microtubule organization, dynamics and functions in differentiated cells. Development (Cambridge, England), 144(17), 3012–3021.

117. Myers, K. A., & Baas, P. W. (2007). Kinesin-5 regulates the growth of the axon by acting as a brake on its microtubule array. The Journal of cell biology, 178(6), 1081–1091. https://doi.org/10.1083/jcb.200702074

118. Nakagawa, T., Kurose, T., Hino, T., Tanaka, K., Kawamukai, M., Niwa, Y., Toyooka, K., Matsuoka, K., Jinbo, T., & Kimura, T. (2007). Development of series of gateway binary vectors, pGWBs, for realizing efficient construction of fusion genes for plant transformation. Journal of bioscience and bioengineering, 104(1), 34–41. https://doi.org/10.1263/jbb.104.34

119. Nasrin, S.R., Bassir Kazeruni, N.M., Rodriguez, J.B. *et al*. (2024). Mechanical fatigue in microtubules. Sci Rep 14, 26336. https://doi.org/10.1038/s41598-024-76409

120. Nirschl, J. J., Magiera, M. M., Lazarus, J. E., Janke, C. and Holzbaur, E. L. F. (2016). Alpha-tubulin tyrosination and CLIP-170 phosphorylation regulate the initiation of dynein-driven transport in neurons. Cell Rep 14, 2637-2652.

121. Noordstra, I., & Akhmanova, A. (2017). Linking cortical microtubule attachment and exocytosis. F1000Research, 6, 469. https://doi.org/10.12688/f1000research.10729.1

122. Novak, M., Polak, B., Simunić, J. *et al*. (2018). The mitotic spindle is chiral due to torques within microtubule bundles. Nat Commun 9, 3571.

123. Novosedlik, S., Reichel, F., van Veldhuisen, T. *et al*. (2025). Cytoskeleton-functionalized synthetic cells with life-like mechanical features and regulated membrane dynamicity. Nat. Chem. 17, 356–364.

124. Oshidari, R., Strecker, J., Chung, D.K.C. *et al*. (2018). Nuclear microtubule filaments mediate non-linear directional motion of chromatin and promote DNA repair. Nat Commun 9, 2567. https://doi.org/10.1038/s41467-018-05009-7

125. Pamula, M.C., Ti, S.-C. & Kapoor, T.M. (2016). The structured core of human beta tubulin 1278 confers isotype-specific polymerization properties. J Cell Biol 213, 425-433.

126. Paraskevi Giannakakou, Dan Sackett, Tito Fojo. (2000). Tubulin/Microtubules: Still a Promising Target for New Chemotherapeutic Agents, JNCI: Journal of the National Cancer Institute, Volume 92, Issue 3, 182–183, https://doi.org/10.1093/jnci/92.3.182

127. Paredez, A. R., Somerville, C. R., & Ehrhardt, D. W. (2006). Visualization of cellulose synthase demonstrates functional association with microtubules. Science (New York, N.Y.), 312(5779), 1491–1495. https://doi.org/10.1126/science.1126551

128. Peet, D. R., Burroughs, N. J., & Cross, R. A. (2018). Kinesin expands and stabilizes the GDP-microtubule lattice. Nature nanotechnology, 13(5), 386–391. https://doi.org/10.1038/s41565-018-0084-4

129. Peris, L., Thery, M., Fauré, J., Saoudi, Y., Lafanechè re, L., Chilton, J. K., Gordon-Weeks, P., Galjart, N., Bornens, M., Wordeman, L. *et al*. (2006). Tubulin tyrosination is a major factor affecting the recruitment of CAP-Gly proteins at microtubule plus ends. J. Cell Biol. 174, 839-849.

130. Peris, L., Wagenbach, M., Lafanechè re, L., Brocard, J., Moore, A. T., Kozielski, F., Job, D., Wordeman, L. and Andrieux, A. (2009). Motor-dependent microtubule disassembly driven by tubulin tyrosination. J. Cell Biol. 185, 1159-1166.

131. Pongkitwitoon, S., Uzer, G., Rubin, J. & Judex, S. (2016). Cytoskeletal configuration modulates mechanically induced changes in mesenchymal stem cell osteogenesis, morphology, and stiffness. Sci. Rep. 6, 34791.

132. Preciado López M, Huber F, Grigoriev I, Steinmetz MO, Akhmanova A, Dogterom M, Koenderink GH. (2014). In vitro reconstitution of dynamic microtubules interacting with actin filament networks. Methods Enzymol. 540:301-20.

133. Preciado López, M., Huber, F., Grigoriev, I., Steinmetz, M. O., Akhmanova, A., Koenderink, G. H., & Dogterom, M. (2014). Actin-microtubule coordination at growing microtubule ends. Nature communications, 5, 4778.

134. Puri D, Sharma S, Samaddar S, Ravivarma S, Banerjee S, Ghosh-Roy A. (2023). Muscleblind-1 interacts with tubulin mRNAs to regulate the microtubule cytoskeleton in C. elegans mechanosensory neurons. PloS Genet 19(8): e1010885. https://doi.org/10.1371/journal.pgen.1010885.

135. Putra, V.D.L., Kilian, K.A. & Knothe Tate, M.L. (2023). Biomechanical, biophysical and biochemical modulators of cytoskeletal remodeling and emergent stem cell lineage commitment. Commun Biol 6, 75. https://doi.org/10.1038/s42003-022-04320-w

136. Rafiq, N. B. M., Nishimura, Y., Plotnikov, S. V., Thiagarajan, V., Zhang, Z., Shi, S., Natarajan, M., Viasnoff, V., Kanchanawong, P., Jones, G. E., & Bershadsky, A. D. (2019). A mechano-signalling network linking microtubules, myosin IIA filaments and integrin-based adhesions. Nature materials, 18(6), 638–649. https://doi.org/10.1038/s41563-019-0371-y

137. Rai A, Liu T, Katrukha EA, Estévez-Gallego J, Manka SW, Paterson I, Díaz JF, Kapitein LC, Moores CA, Akhmanova A. (2021). Lattice defects induced by microtubule-stabilizing agents exert a long-range effect on microtubule growth by promoting catastrophes. Proc Natl Acad Sci U S A. 118(51):e2112261118.

138. Reed, N. A., Cai, D., Blasius, T. L., Jih, G. T., Meyhofer, E., Gaertig, J. and Verhey, K. J. (2006). Microtubule acetylation promotes Kinesin-1 binding and transport. Curr. Biol. 16, 2166-2172.

139. Ricketts, S.N., Francis, M.L., Farhadi, L. Rust, MJ. Das, M. Ross, J.L and Roberson-Anderson, RM. (2019). Varying crosslinking motifs drive the mesoscale mechanics of actin-microtubule composites. Sci Rep 9, 12831. https://doi.org/10.1038/s41598-019-49236-4

140. Robinson, S. & Kuhlemeier, C. (2018). Global compression reorients cortical microtubules in 78pprox.78sis hypocotyl epidermis and promotes growth. Curr. Biol 28, 1794–1802.e2 (2018).

141. Robison, P., Caporizzo, M. A., Ahmadzadeh, H., Bogush, A. I., Chen, C. Y., Margulies, K. B., Shenoy, V. B., & Prosser, B. L. (2016). Detyrosinated microtubules buckle and bear load in contracting cardiomyocytes. Science (New York, N.Y.), 352(6284), aaf0659. https://doi.org/10.1126/science.aaf0659

142. Roll-Mecak, A. (2020). The Tubulin Code in Microtubule Dynamics and Information Encoding. Developmental Cell, 54(1), 7–20.https://doi.org/10.1016/j.devcel.2020.06.008

143. Salbreux, G., Charras, G., & Paluch, E. (2012). Actin cortex mechanics and cellular morphogenesis. Annual Review of Cell and Developmental Biology, 28, 111–132. https://doi.org/10.1146/annurev-cellbio-101011-155718

144. Salmon ED. (1975). Pressure-induced depolymerization of spindle microtubules. I. Changes in birefringence and spindle length. J Cell Biol. 65(3):603-14.

145. Sampathkumar, A., Krupinski, P., Wightman, R., Milani, P., Berquand, A., Boudaoud, A., Hamant, O., Jönsson, H., & Meyerowitz, E. M. (2014). Subcellular and supracellular mechanical stress prescribes cytoskeleton behavior in Arabidopsis cotyledon pavement cells. eLife, 3, e01967. https://doi.org/10.7554/eLife.01967

146. Sánchez-Huertas C., *et al*. (2020). The +TIP Navigator-1 is an actin-microtubule crosslinker that regulates axonal growth cone motility. J. Cell Biol. 219, e201905199.

147. Schulze, E., & Kirschner, M. (1988). New features of microtubule behaviour observed in vivo. Nature, 334(6180), 356–359. https://doi.org/10.1038/334356a0

148. Seetharaman, S., Vianay, B., Roca, V., Farrugia, A. J., De Pascalis, C., Boëda, B., Dingli, F., Loew, D., Vassilopoulos, S., Bershadsky, A., Théry, M., & Etienne-Manneville, S. (2022). Microtubules tune mechanosensitive cell responses. Nature materials, 21(3), 366–377. https://doi.org/10.1038/s41563-021-01108-x

149. Shima, T., Morikawa, M., Kaneshiro, J., Kambara, T., Kamimura, S., Yagi, T., Iwamoto, H., Uemura, S., Shigematsu, H., Shirouzu, M., Ichimura, T., Watanabe, T. M., Nitta, R., Okada, Y., & Hirokawa, N. (2018). Kinesin-binding-triggered conformation switching of microtubules contributes to polarized transport. The Journal of cell biology, 217(12), 4164–4183. https://doi.org/10.1083/jcb.201711178

150. Siahaan, V., Krattenmacher, J., Hyman, A. A., Diez, S., Hernández-Vega, A., Lansky, Z., & Braun, M. (2019). Kinetically distinct phases of tau on microtubules regulate kinesin motors and severing enzymes. Nature cell biology, 21(9), 1086–1092. https://doi.org/10.1038/s41556-019-0374-6

151. Small, J. V., & Kaverina, I. (2003). Microtubules meet substrate adhesions to arrange cell polarity. Current opinion in cell biology, 15(1), 40–47. https://doi.org/10.1016/s0955-0674(02)00008-x

152. Soheilypour, M., Peyro, M., Peter, S. J., & Mofrad, M. R. K. (2015). Buckling behavior of individual and bundled microtubules. Biophysical journal, 108(7), 1718–1726. https://doi.org/10.1016/j.bpj.2015.01.030

153. Soppina, V., Rai, A. K., Ramaiya, A. J., Barak, P., & Mallik, R. (2009). Tug-of-war between dissimilar teams of microtubule motors regulates transport and fission of endosomes. Proceedings of the National Academy of Sciences of the United States of America, 106(46), 19381–19386. https://doi.org/10.1073/pnas.0906524106

154. Stehbens, S. J., Paszek, M., Pemble, H., Ettinger, A., Gierke, S., & Wittmann, T. (2014). CLASPs link focal-adhesion-associated microtubule capture to localized exocytosis and adhesion site turnover. Nature cell biology, 16(6), 561–573. https://doi.org/10.1038/ncb2975

155. Stehbens, S., & Wittmann, T. (2012). Targeting and transport: how microtubules control focal adhesion dynamics. The Journal of cell biology, 198(4), 481–489. https://doi.org/10.1083/jcb.201206050

156. Sumigray, K. D., Chen, H., & Lechler, T. (2018). The LINC complex regulates epidermal morphogenesis by coupling tissue-tension to microtubule organization. Nature Cell Biology, 20(4), 447–455. https://doi.org/10.1038/s41556-018-0064-8

157. Taiber, S., Gozlan, O., Cohen, R., Andrade, L. R., Gregory, E. F., Starr, D. A., Moran, Y., Hipp, R., Kelley, M. W., Manor, U., Sprinzak, D., & Avraham, K. B. (2022). A Nesprin-4/kinesin-1 cargo model for nuclear positioning in cochlear outer hair cells. Frontiers in cell and developmental biology, 10, 974168. https://doi.org/10.3389/fcell.2022.974168

158. Tan, R., Lam, A. J., Tan, T., Han, J., Nowakowski, D. W., Vershinin, M., Simó, S., Ori-McKenney, K. M., & McKenney, R. J. (2019). Microtubules gate tau condensation to spatially regulate microtubule functions. Nature cell biology, 21(9), 1078–1085. https://doi.org/10.1038/s41556-019-0375-5

159. Tanenbaum, M.E, Vale, R.D., McKenney, R.J. (2013) Cytoplasmic dynein crosslinks and slides anti-parallel microtubules using its two motor domains eLife 2:e00943

160. Telley, I. A., Bieling, P., & Surrey, T. (2009). Obstacles on the microtubule reduce the processivity of Kinesin-1 in a minimal in vitro system and in cell extract. Biophysical journal, 96(8), 3341–3353. https://doi.org/10.1016/j.bpj.2009.01.015

161. Theisen, U., Straube, E., & Straube, A. (2012). Directional persistence of migrating cells requires Kif1C-mediated stabilization of trailing adhesions. Developmental cell, 23(6), 1153–1166. https://doi.org/10.1016/j.devcel.2012.11.005

162. Ti, S.-C., Alushin, G.M. & Kapoor, T.M. (2018). Human beta-Tubulin Isotypes Can Regulate Microtubule Protofilament Number and Stability. Dev Cell 47, 175-190 e175.

163. Tolić-Nørrelykke IM. (2008).Push-me-pull-you: how microtubules organize the cell interior. Eur Biophys J., 37(7):1271-8.

164. Torrino, S., Grasset, E. M., Audebert, S., Belhadj, I., Lacoux, C., Haynes, M., Pisano, S., Abélanet, S., Brau, F., Chan, S. Y., Mari, B., Oldham, W. M., Ewald, A. J., & Bertero, T. (2021). Mechano-induced cell metabolism promotes microtubule glutamylation to force metastasis. Cell Metabolism, 33(7), 1342-1357.e10. https://doi.org/10.1016/j.cmet.2021.05.009

165. Towbin, B. D., González-Aguilera, C., Sack, R., Gaidatzis, D., Kalck, V., Meister, P., Askjaer, P., & Gasser, S. M. (2012). Step-wise methylation of histone H3K9 positions heterochromatin at the nuclear periphery. Cell, 150(5), 934–947. https://doi.org/10.1016/j.cell.2012.06.051

166. Trupinić M, Kokanović B, Ponjavić I, Barišić I, Šegvić S, Ivec A, Tolić IM (2022) The chirality of the mitotic spindle provides a mechanical response to forces and depends on microtubule motors and augmin. Curr Biol 32:2480–2493

167. Trushko, E. Schäffer, & J. Howard. (2013). The growth speed of microtubules with XMAP215-coated beads coupled to their ends is increased by tensile force, Proc. Natl. Acad. Sci. U.S.A. 110 (36) 14670-14675, https://doi.org/10.1073/pnas.1218053110.

168. Utzschneider C, Suresh B, Sciortino A, Gaillard J, Schaeffer A, Pattanayak S, Joanny JF, Blanchoin L, Théry M. (2024). Force balance of opposing diffusive motors generates polarity-sorted microtubule patterns. Proc Natl Acad Sci U S A. 121(49):e2406985121

169. Uyttewaal, M., Burian, A., Alim, K., Landrein, B., Borowska-Wykręt, D., Dedieu, A., Peaucelle, A., Ludynia, M., Traas, J., Boudaoud, A., Kwiatkowska, D., & Hamant, O. (2012). Mechanical stress acts via katanin to amplify differences in growth rate between adjacent cells in Arabidopsis. Cell, 149(2), 439–451. https://doi.org/10.1016/j.cell.2012.02.048

170. Vale RD, Yano Toyoshima Y. (1988). Rotation and translocation of microtubules in vitro induced by dyneins from Tetrahymena cilia. Cell, 52:459–469.

171. Valenstein, M. L. and Roll-Mecak, A. (2016). Graded control of microtubule severing by tubulin glutamylation. Cell 164, 911-921.

172. van der Vaart, B., Akhmanova, A., & Straube, A. (2009). Regulation of microtubule dynamic instability. Biochemical Society transactions, 37(Pt 5), 1007–1013. https://doi.org/10.1042/BST0371007

173. van der Vaart, B., Manatschal, C., Grigoriev, I., Olieric, V., Gouveia, S. M., Bjelic, S., Demmers, J., Vorobjev, I., Hoogenraad, C. C., Steinmetz, M. O., & Akhmanova, A. (2011). SLAIN2 links microtubule plus end-tracking proteins and controls microtubule growth in interphase. The Journal of cell biology, 193(6), 1083–1099. https://doi.org/10.1083/jcb.201012179

174. Vemu, A., Szczesna, E., Zehr, E. A., Spector, J. O., Grigorieff, N., Deaconescu, A. M., & Roll-Mecak, A. (2018). Severing enzymes amplify microtubule arrays through lattice GTP-tubulin incorporation. Science (New York, N.Y.), 361(6404), eaau1504. https://doi.org/10.1126/science.aau1504

175. Verhey, K. J., & Hammond, J. W. (2009). Traffic control: Regulation of kinesin motors. Nature Reviews Molecular Cell Biology, 10(11), 765–777. https://doi.org/10.1038/nrm2782

176. Volkov, V. A., Zaytsev, A. V., Gudimchuk, N. B., Grissom, P. M., Kirkland, K. A., McIntosh, J. R., & Grishchuk, E. L. (2013). Long tethers provide high-force coupling of the Dam1 ring to shortening microtubules. PNAS, 110, 7708–7713.

177. Walker, R. A., O'brien, E. T., Pryer, N. K., Soboeiro, M. F., Voter, W. A., Erickson, H. P., & Salmon, E. D. (1988). Dynamic instability of individual microtubules analyzed by video light microscopy: rate constants and transition frequencies. The Journal of cell biology, 107(4), 1437-1448

178. Wang, N., Naruse, K., Stamenović, D., Fredberg, J. J., Mijailovich, S. M., Tolić-Nørrelykke, I. M., … & Ingber, D. E. (2001). Mechanical behavior in living cells consistent with the tensegrity model. Journal of Cell Science, 114(20), 3771–3781. https://doi.org/10.1242/jcs.114.20.3771

179. Ward, A., Hilitski, F., Schwenger, W., Welch, D., Lau, A. W. C., Vitelli, V., Mahadevan, L., & Dogic, Z. (2015). Solid friction between soft filaments. Nature Materials, 14(6), 583–588. https://doi.org/10.1038/nmat4222

180. Waterman-Storer, C. M., & Salmon, E. (1999). Positive feedback interactions between microtubule and actin dynamics during cell motility. Current opinion in cell biology, 11(1), 61–67. https://doi.org/10.1016/s0955-0674(99)80008-8

181. Waterman-Storer, C.M, Gregory, J, S. F. Parsons, E. D. Salmon, J. (1995). Membrane/microtubule tip attachment complexes (TACs) allow the assembly dynamics of plus ends to push and pull membranes into tubulovesicular networks in interphase Xenopus egg extracts. Cell Biol. 130(5), 1161-1169.

182. Weinger, J. S., Qiu, M., Yang, G., & Kapoor, T. M. (2011). A Nonmotor Microtubule Binding Site in Kinesin-5 Is Required for Filament Crosslinking and Sliding. Current Biology, 21(2), 154–160. https://doi.org/10.1016/j.cub.2010.12.038

183. Wieczorek, M., Chaaban, S., & Brouhard, G. J. (2013). Macromolecular crowding pushes catalyzed microtubule growth to near the theoretical limit. Cellular and Molecular Bioengineering, 6, 383-392.

184. Wijeratne, S. S., Fiorenza, S. A., Neary, A. E., Subramanian, R., & Betterton, M. D. (2022). Motor guidance by long-range communication on the microtubule highway. Proceedings of the National Academy of Sciences of the United States of America, 119(28), e2120193119. https://doi.org/10.1073/pnas.2120193119

185. Yang, Y., Lin, J., Kaytanli, B., Saleh, O.A., Valentine, M.T. (2012). Direct correlation between creep compliance and deformation in entangled and sparsely crosslinked microtubule networks, Soft Matter 8, 1776–1784.

186. Ye, Y., Hao, Z., Luo, J. *et al.* (2025) Tubulin isotypes of C. elegans harness the mechanosensitivity of the lattice for microtubule luminal accessibility. Nat. Phys. 21, 1420–1430. https://doi.org/10.1038/s41567-025-02983-w

187. Zhang, X., Shu, S., Feng, Z., Qiu, Y., Bao, H., & Zhu, Z. (2023). Microtubule stabilization promotes the synthesis of type 2 collagen in nucleus pulposus cell by activating hippo-yap pathway. Frontiers in pharmacology, 14, 1102318. https://doi.org/10.3389/fphar.2023.1102318

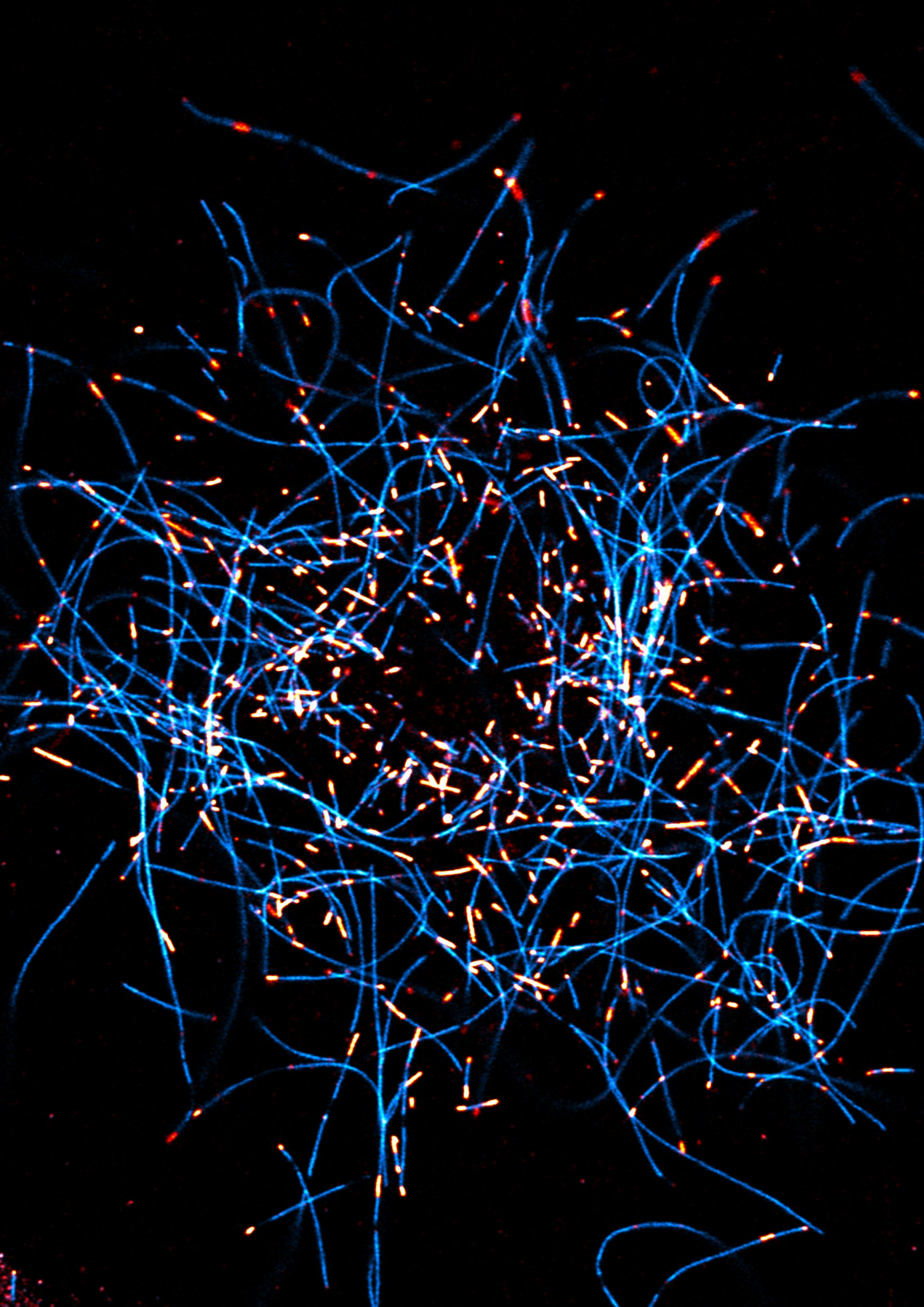

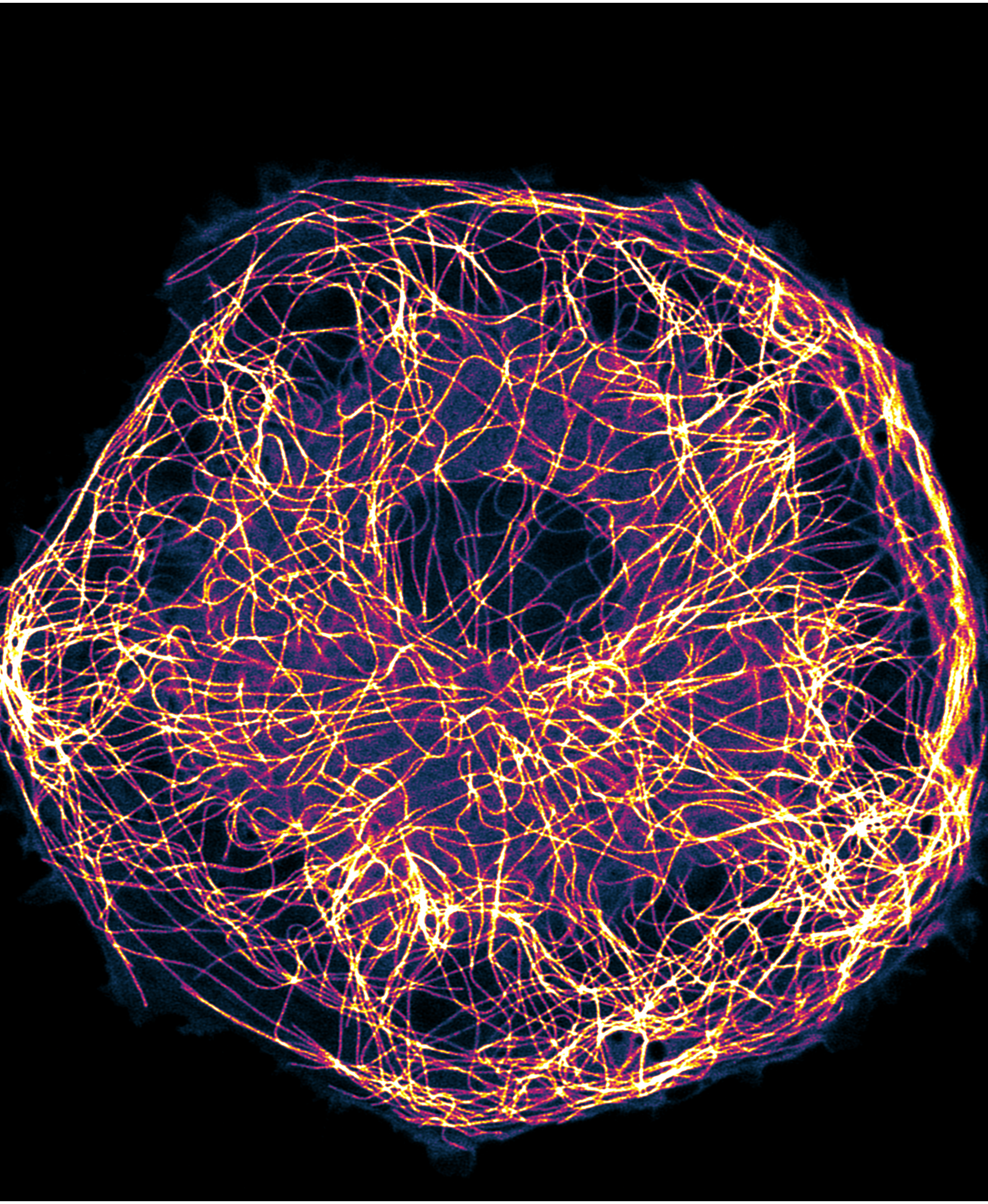

Chapter 2

Exploring microtubule self-repair under mechanical stress

In this chapter, I detail the core findings of my dissertation-wherein I explore the limits of microtubule self-repair by subjecting microtubules to bending and buckling forces. By developing an *in vitro* assay closely mimicking microtubule bending and buckling as seen in the intracellular environment, the study shows that inherent microtubule self-repair mechanisms can be overwhelmed when subjected to buckling forces and that additional intracellular factors help protect microtubule integrity under mechanical stimuli.

2.1 Study 1:

Exploring self-repair in microtubules subjected to bending and buckling forces (Nandakumar *et al.*)

As highlighted in Chapter 1, microtubules are continuously subjected to significant mechanical forces in the intracellular environment. Understanding how microtubule integrity is preserved under such conditions is pivotal to elucidating mechanisms that sustain cytoskeletal stability and response. Previous studies have reported that microtubules are predominantly exposed to mechanical stress arising from bending and motor-induced buckling forces in cells (Blob *et al.*, 2025; Bicek *et al.*, 2009; Brangwynne *et al.*, 2008). Notably, Schaedel *et al.*, 2015 showed that microtubules can self-repair when exposed to bending by orthogonal fluid flow, while Gazzola *et al.*, 2022, reported that microtubule self-repair spots were predominantly localized to curved regions and areas of lateral fluctuations. These findings suggest that mechanical deformation, particularly bending and buckling, can induce microtubule damage and trigger self-repair.

Building upon this, the study aimed to investigate microtubule self-repair in statically bent microtubules and in those subjected to kinesin-1-induced buckling (the latter being highly relevant as kinesin-1 is the most ubiquitous microtubule-based motor protein). Closer to physiological conditions, we used microtubules whose lattice was composed of GDP-tubulin, free of stabilizing agents. As intracellular force patterns are complex and challenging to quantify directly, we reconstituted microtubule bending and buckling *in vitro* to mimic mechanical deformations observed in cells. Using this *in vitro* setup that recapitulates dynamic microtubule shape fluctuations as seen in cells, the work explored microtubule damage and self-repair when exposed to bending and buckling stress. Ultimately, this study addresses the key question- “Are inherent self-repair mechanisms sufficient to preserve microtubule integrity under mechanical stimuli or is this response dependent on additional cellular factors?”. The results of the study are presented in the manuscript below:

Faculty NT
Cumulative form of the dissertation
Confirmation of the contribution of co-authors

Title of the dissertation:

Metastable Microtubules: dynamic instability, lattice plasticity and mechanosensing

Title of the publication with all necessary bibliographic information:

Kinesin-induced buckling reveals the limits of microtubule self-repair

Quality of the publication, e.g. review article, conference contribution, research article, etc.:

Research article

Review process or publication status (in preparation, submitted, accepted):

Accepted for publication in Advanced Science- https://doi.org/10.1002/advs.202521721

Explanation of the contributions of the co-authors:

Laura Aradilla Zapata (née Schaedel): conceptualized the study, designed experiments and wrote the manuscript. Secured funding and supervised the study.

Reza Shaebani: designed and performed theoretical simulations and wrote the Simulation methods. Secured funding and supervised the study.

Stefan Diez: conceptualized the study and provided critical feedback.

Ludger Santen: conceptualized the study, designed simulations and provided critical feedback.

Shweta Nandakumar: designed and performed all the experiments. Performed data and image analysis corresponding to Figures 1, 2, 3, 4, 6, 7 and Suppl. figures 1-5 and Suppl Fig 7 a,d,e, Suppl. Fig 8-10. Wrote the manuscript.

Jonas Bosche: designed and performed the simulations and analysis for Figure 5 and Suppl. figure 6, Suppl. Figure 7 b,c.

Mirko Wieczorek: wrote the python code for curvature anaylsis (Suppl Fig 2) and estimation of microtubule persistence length from thermal fluctuation analysis.

Constantin Matteo Albrecht : assisted with preparation of the HEK293 cell lysates used for experiments in figure 7c.

Mona Grünewald: Purified tubulin.

Belinda König: Purified tubulin.
Signature of the doctoral candidate:

Shweta N

Shweta Nandakumar

Signature of the **co-authors:**
(or, if applicable, the supervisor for **individual** co-authors – only in the event that these co-authors cannot be reached or do not have up-to-date contact details)

Name	Signature
Laura Aradilla Zapata (née Schaedel)	L. Aradilla
Reza Shaebani	03.10.25 Saarbrücken
Ludger Santen	Ludger S
Jonas Bosche	J. Bosche
Mona Grünewald	06.10.25
Belinda König	06.10.25
Mirko Wieczorek	09/10/25
Constantin Matteo Albrecht	06/10/2025

Kinesin-induced buckling reveals the limits of microtubule self-repair

Shweta Nandakumar [1], Jonas Bosche [2], Mirko Wieczorek [1], Constantin Matteo Albrecht [1], Belinda König[1], Mona Grünewald [1], Ludger Santen [2], Stefan Diez [3,4,5], Reza Shaebani [2*], Laura Schaedel [1,6*]

Affiliations:

[1] *Experimental Physics and Center for Biophysics, Saarland University, 66123 Saarbrücken, Germany*

[2] *Theoretical Physics and Center for Biophysics, Saarland University, 66123 Saarbrücken, Germany*

[3] *B CUBE - Center for Molecular Bioengineering, TUD Dresden University of Technology, 01307 Dresden, Germany*

[4] *Max Planck Institute of Molecular Cell Biology and Genetics, 01307 Dresden, Germany*

[5] *Cluster of Excellence Physics of Life, TUD Dresden University of Technology, 01062 Dresden, Germany*

[6] *PharmaScienceHub (PSH), 66123 Saarbrücken, Germany*

Abstract

Microtubules are stiff cytoskeletal polymers whose ability to rapidly switch between growth and disassembly relies on a metastable lattice. This metastability is also reflected in their sensitivity to environmental conditions and in intrinsic lattice dynamics, where spontaneous tubulin loss is balanced by tubulin incorporation from solution – a process that also enables microtubules to self-repair when damaged. Whether such intrinsic self-repair is sufficient to preserve microtubule integrity during dynamic molecular motor-induced buckling, which frequently occurs in cells, remains unclear. Here, we show that kinesin-driven microtubule buckling *in vitro* induces severe lattice damage, leading to extensive tubulin incorporation. In many cases, however, the damage exceeds the microtubules' capacity for self-repair, resulting in breakage. In contrast, microtubules survive continuous buckling substantially longer in the presence of intracellular factors. Our results identify the limits of intrinsic microtubule self-repair and demonstrate that additional cellular mechanisms are essential to maintain microtubule integrity under sustained mechanical load.

Introduction

Microtubules are highly dynamic cytoskeletal filaments that support intracellular organization and adapt rapidly to physiological cues [1]. Microtubule tip dynamics – alternating between growth and disassembly – is driven by GTP hydrolysis [1,2], which renders the microtubule lattice inherently metastable and particularly sensitive to environmental conditions such as temperature [3,4]. This inherent fragility not only enables microtubules to remain responsive to signals, but also makes them vulnerable to destabilization.

A manifestation of this metastability is intrinsic lattice dynamics, wherein tubulin subunits dissociate from the lattice, particularly at structural defects, and are replaced by free tubulin from solution [5]. This process occurs slowly but can be accelerated by repeated bending via orthogonal fluid flow [6] , the activity of severing enzymes and the non-enzymatic microtubule-associated protein (MAP) tau [7,8], and even the translocation of unloaded motor proteins [9,10,11]. Although other MAPs such as CLASP[12] and CLIP-170 [13] may support repair or stabilization, it is generally assumed that microtubules have sufficient intrinsic self-repair capacity to withstand damage[6,14,15]. However, in cells, microtubules are frequently exposed to strong and dynamic deformations [16,17] , including pronounced buckling caused by opposing motor forces and anchorage points within the cytoplasm [18,19,20,21,22,23,24]. Whether intrinsic self-repair is sufficient to maintain microtubule integrity under such sustained mechanical stress is unclear.

Here, we use a combination of *in vitro* reconstitution, a stochastic computational model, and supporting cellular data to investigate microtubule behavior under motor-induced buckling. We find that buckling leads to accelerated lattice damage and extensive tubulin incorporation, and that damage frequently exceeds the capacity of self-repair, resulting in microtubule breakage. However, in the presence of intracellular factors, microtubules are significantly more resilient. These findings reveal the limits of intrinsic microtubule self-repair and highlight the essential contribution of cellular mechanisms in preserving microtubule integrity under persistent mechanical load.

Results

1) Static curvature induces microtubule self-repair

Despite their high flexural rigidity [25], microtubules frequently adopt curved conformations in cells [26,27,28], suggesting that they are exposed to considerable intracellular forces. For example, in fixed PtK2 cells with endogenously labeled tubulin, we observed that many microtubules display locally highly curved regions (**Fig. 1a**). This raises the question whether static bending promotes lattice damage and repair. To test this, we reconstituted statically curved microtubules *in vitro* (**Fig. 1b**, see **Methods**): First, we polymerized dynamic microtubules from stabilized biotinylated seeds (step I) and stabilized their ends with biotin-tubulin caps (step II). Importantly, the GDP microtubule lattice between seed and cap was not stabilized. These microtubules were then introduced into streptavidin-coated flow chambers assembled from passivated cover glasses (step III), where the biotinylated ends attached to the substrate. We alternated the flow direction during chamber loading, frequently resulting in microtubules adopting bent conformations upon immobilization at both ends (step IV). The resulting microtubule curvatures are comparable to those of intracellular microtubules (**Suppl. Fig. 1d**). Next, we exposed these microtubules to soluble fluorescently labeled tubulin for 15 min to allow for incorporation (step V), followed by washout and imaging (step VI). We observed tubulin incorporation both in straight and bent microtubules, where incorporation events appear as localized stretches along the microtubule lattice (**Fig. 1c, Suppl. Fig. 1a**). While the length of individual incorporation stretches does not differ between bent and straight microtubules when analyzed along the entire microtubule (**Suppl. Fig. 1b**), focusing specifically on bent zones (see curvature analysis section in the **Methods**) reveals a modest increase in incorporation length compared to straight microtubules (**Fig. 1d(i)**). In contrast, the spatial frequency of incorporation events is substantially higher in bent microtubules (**Fig. 1d(ii)**), resulting in 28% of lattice lengths showing tubulin incorporation, compared to only 4% in straight microtubules (**Fig. 1d(iii)**). When grouping microtubules by curvature, we found a progressive increase in tubulin incorporation with increasing curvature (**Fig. 1e**). These observations suggest that static bending promotes lattice damage and subsequent self-repair *in vitro*.

We then proceeded to assess the relationship between curvature and tubulin incorporation in cells by reanalyzing a previously published dataset [29] of self-repair in PtK2 cells expressing endogenously GFP-tagged tubulin (represented here in magenta). These cells were micro-injected with 30 µM purified, Atto-565 labeled tubulin (represented here in green), followed by fixation after 4 min of incubation (**Fig. 1f,g**). Since we rarely observed globally straight microtubules in PtK2 cells, we decided to analyze microtubules section-wise (see **Methods**). Similar to our observations *in vitro*, we detected incorporation events along both straight and bent microtubule sections (**Fig. 1h, Suppl. Fig. 1c**). Tubulin incorporation stretches are longer (**Fig. 1i, left**) and more frequent (**Fig. 1i, center**) in bent microtubule sections compared to straight microtubule sections, overall leading to a larger proportion of lattice lengths with incorporations (**Fig. 1i, right**), reminiscent of our *in vitro* results.

Since the fluorescence signal of incorporation stretches in intracellular microtubules appears more intense compared to *in vitro* microtubules (suggesting a higher fraction of the lattice has been replaced at these sites), we then estimated the local amount of incorporated tubulin across protofilaments *in vitro* and in cells (see **Methods**). For this, we normalized the intensities of the incorporation stretches to the intensities of microtubule tips grown with tubulin of the same color, which we presume to consist of 13 protofilaments (**Fig. 1j, top**). This quantification serves as a direct readout of the lateral extent of tubulin incorporation, revealing that incorporation typically occurs over 1-3 protofilaments, occasionally reaching up to 9 protofilaments in cells (See

Methods, Suppl. Fig. 1e,f). Thus, in most cases, only a small portion of the lattice is exchanged. Together with the mean length of lattice showing incorporation (**Fig. 1d(iii) and Fig. 1i, right**), this analysis allowed us to estimate the total amount of tubulin turnover in each condition by accounting for both the longitudinal extent of incorporation along the microtubule and its lateral spread across protofilaments. **Fig. 1j (bottom)** shows that tubulin turnover is more pronounced in bent as opposed to straight microtubules, both *in vitro* and in cells, yet remains below 5%. Together, these data show that microtubule curvature leads to increased tubulin incorporation both *in vitro* and in cells. While previous work has shown that repeated bending cycles by orthogonal fluid flow can induce microtubule damage [6], our findings demonstrate that sustained static curvature is sufficient to enhance tubulin incorporation, indicating a direct mechanical contribution to lattice damage and repair.

Figure 1

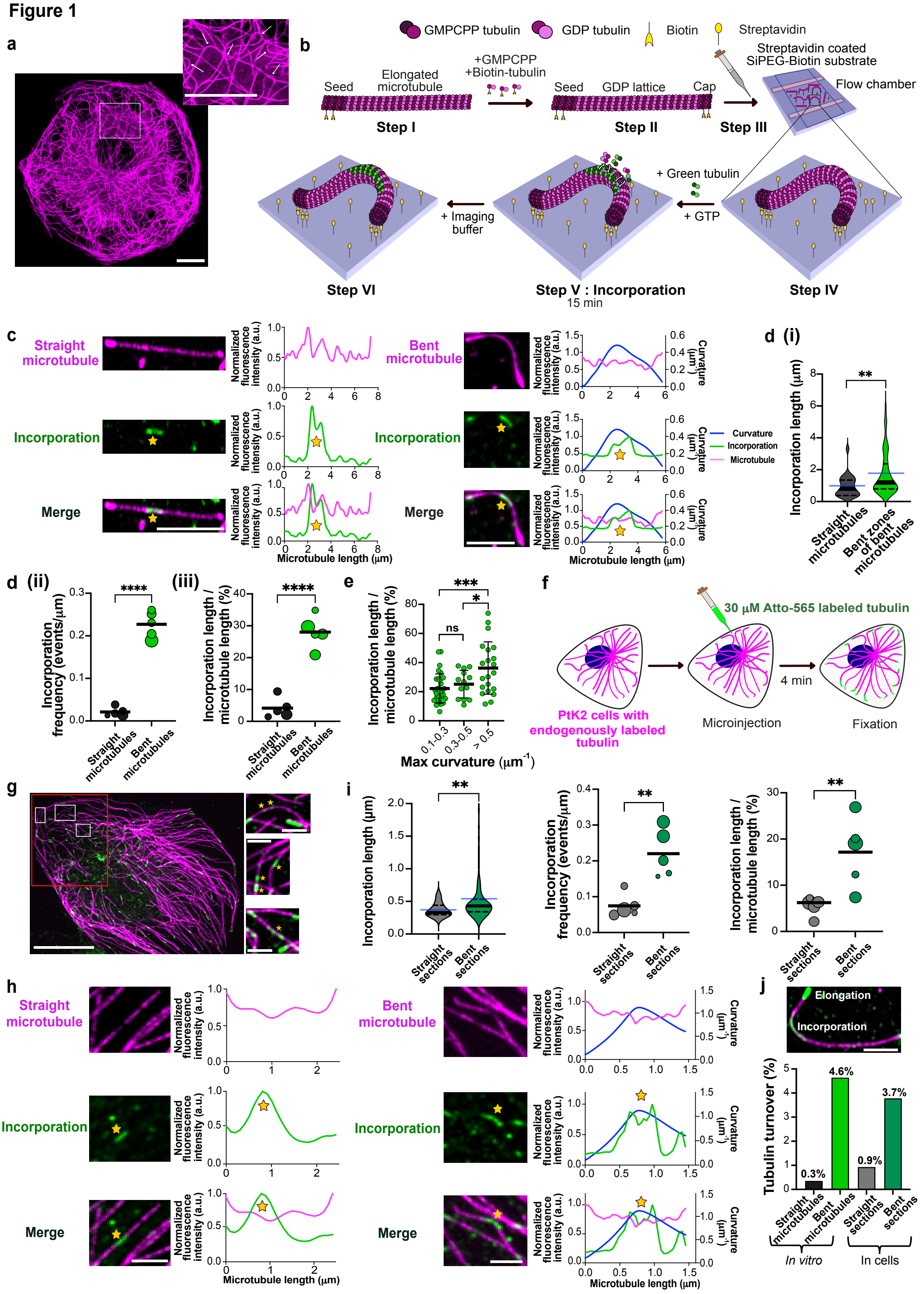

Figure 1: Static curvature triggers microtubule damage and consequent self-repair.
a, Microtubules adopt bent and buckled conformations in cells: Image of bent microtubules in a PtK2 cell (tubulin-eGFP, represented in magenta). Inset shows a zoomed-in image with white arrows

indicating bent microtubules. Scale bars: 10 µm. **b**, Schematic of the *in vitro* experimental setup used to assess self-repair in static bent microtubules. Capped GDP microtubules (shown in magenta) with biotinylated GMPCPP seeds and caps (Step I and II) were flushed onto a streptavidin coated flow chamber made from SiPEG-biotin passivated cover-glasses (Step III). Microtubules of various curvatures were obtained by alternating the flow direction (Step IV). Microtubules were then incubated with 5 µM green labeled tubulin for 15 min (Step V) followed by washing with imaging buffer (Step VI). **c**, Example images showing incorporation of green labeled tubulin (marked with a yellow star) in a straight and in a bent microtubule *in vitro*. Scale bar: 5 µm. Graphs represent line scans of the microtubule (magenta), the incorporation channel (green) and curvature (blue). Profiles have been normalized to 1 for the maximum value of the intensity (a.u.) for the microtubule and incorporation channel, respectively **d**, **(i):** Violin plot showing longer incorporation stretches in zones of high local curvature in bent microtubules *in vitro*. Total length of microtubules analyzed: 1,104 µm from three independent experiments (p= 0.0069 using Mann-Whitney test) (n= 23 incorporations for straight microtubules, n= 83 incorporations for bent microtubules). Black solid line represents the median and dotted lines represent the interquartile range. Blue line represents the mean. **(ii):** Bubble plot showing higher frequency of incorporations in bent microtubules when compared to straight microtubules *in vitro*. Bubble sizes scale with the total microtubule length analyzed. Each circle represents an independent dataset (comprising of 291, 295, 350, 165 and 65 µm of total microtubule length analyzed for bent microtubules and 311, 347, 340, 230 and 366 µm of total microtubule length analyzed for straight microtubules). The black line represents the mean. p<0.0001 using unpaired t-test. **(iii):** Bubble plot showing higher amount of lattice turnover, estimated as incorporation length/ microtubule length, in bent microtubules when compared to straight microtubules *in vitro*. Bubble sizes scale with the total microtubule length analyzed. Each circle represents an independent dataset (comprising 291, 295, 350, 165 and 65 µm of the total microtubule length analyzed for bent microtubules and 311, 347, 340, 230 and 366 µm of the total microtubule length analyzed for straight microtubules). The black line represents the mean. p<0.0001 using unpaired t-test. **e**, Scatter dot plot comparing the lattice length with incorporation in bent microtubules across different curvature ranges *in vitro*. Total length of microtubules analyzed: 1,104 µm from three independent experiments. Black lines represent the mean and S.D. p= 0.3597 (not significant; for curvatures 0.1-0.3 μm^{-1} and 0.3-0.5 μm^{-1}), p= 0.0006 (for curvatures > 0.5 μm^{-1} and 0.1-0.3 μm^{-1}) and p= 0.0493 (for curvatures > 0.5 μm^{-1} and 0.3-0.5 μm^{-1}) using unpaired t-test. **f,** Schematic of experimental setup used by Gazzola et al., 2023 to assess microtubule self-repair in PtK2 cells. 30 µM of ATTO-565 labeled tubulin (represented here in green) was microinjected into PtK2 cells expressing endogenous tubulin-eGFP (represented here in magenta) and the cells were fixed after 4 min and imaged. **g,** Example images showing microtubule self-repair in a PtK2 cell, scale bar: 20 µm. Box with red outline indicates a selected region of interest. Insets show zoomed-in images of microtubule sections with incorporations marked with a yellow star. Scale bars of inset images: 2 µm. **h**, Self-repair (marked with a yellow star) in both straight and bent microtubule sections in cells. Scale bar: 2 µm. Graphs represent line scans of the microtubule (magenta), curvature (blue) and the incorporation channel (green). Profiles have been normalized to 1 for the maximum value of the intensity (a.u.) for the microtubule and incorporation channel. **i**, **Left:** Violin plot showing longer incorporation stretches in bent microtubule sections in cells. Total length of microtubules analyzed: 401.96 µm from five cells (p= 0.0025 using Mann-Whitney test.) (n= 37 incorporations for straight sections and n= 84 incorporations for bent sections). Black line represents the median and dotted lines represent the interquartile range. Blue line represents the mean. **Center:** Bubble plot showing higher frequency of incorporations in bent microtubule sections when compared to straight microtubule sections in cells. Bubble sizes scale with the total microtubule length analyzed. Each circle represents an independent dataset from one cell (comprising of 130, 98, 57, 44 and 72 µm of total length analyzed for bent sections and 22, 56, 74, 36 and 153 µm of total microtubule length analyzed for straight sections. Black line represents the mean. p= 0.0022 using unpaired t-test. **Right:** Bubble plot showing higher amount of lattice length with incorporation estimated as incorporation length/microtubule length, in bent microtubule sections when compared to straight microtubule sections in cells. Bubble sizes scale with the total microtubule length analyzed. Each circle represents an independent dataset from one cell (comprising of 130, 98, 57, 44 and 72 µm of total length analyzed for bent sections and 22, 56, 74, 36 and 153 µm of total microtubule length analyzed for straight sections). Black lines represent the mean. p= 0.0099 using unpaired t-test. **j**, **Top:** Example image showing an incorporation stretch and the elongated tip that was used as a reference to estimate the amount of lateral tubulin incorporation (see Methods). Scale bar: 2 µm. **Bottom**: Higher % of tubulin turnover in bent microtubules, both in cells and *in vitro*. Three independent experiments were analyzed for each condition. n= 21 incorporations for straight microtubules (*in vitro)*, n= 51 incorporations for bent microtubules (*in vitro)*, n= 16 incorporations for straight sections (cells) and n= 32 incorporations for bent sections (cells). Refer methods for estimation of % tubulin turnover and **Suppl. Fig. 1e,f** for estimation of amount of lateral tubulin incorporation.

2) *In vitro* reconstitution of cell-like microtubule buckling

While the striking similarity between tubulin incorporation *in vitro* and in PtK2 cells highlights the role of microtubule curvature, our *in vitro* observations were made after an incubation time three times longer than that used in PtK2 cells (15 min vs. 4 min). This discrepancy suggests that additional factors contribute to microtubule damage and repair in PtK2 cells. When examining dynamic microtubules in live cells, it becomes apparent that local microtubule curvature often changes over time (**Fig. 2a; Suppl. Movie 1**), as has been described earlier [18]. While some microtubules maintain a curved conformation with little change over extended periods (**Fig. 2b (i)**), many exhibit dynamic buckling on short timescales (**Fig. 2b (ii)**). In rare instances, we observed microtubule breakage, typically occurring in regions of high curvature (**Fig. 2b (iii), Suppl. Fig. 3b**; see **Suppl. Fig. 3a** for quantification of different microtubule bending events in cells). While microtubule phenotype and the proportion of bending and buckling events may differ across cell types and stages of the cell cycle, existing literature suggests that this is a common feature among cell types. Our observations (**Fig. 2b**) and quantifications of microtubule deformation events (**Suppl. Fig. 3a**) and microtubule curvature in PtK2 cells (**Fig. 2g**) are consistent with observations reported in fibroblasts [27], LLC-PK1 epithelial cells [17], contracting cardiomyocytes [30], neuronal NG105-18 cells [31] and *Xenopus* melanophores [19]. These cell-based observations prompted us to investigate how dynamic microtubule buckling affects microtubule integrity.

Since the origin and magnitude of intracellular forces are difficult to determine, we sought to reconstitute microtubule buckling *in vitro*. Given that the dynamic, short-wavelength microtubule buckling in cells has been mainly attributed to molecular motor activity [17,23,26], we adapted a motor-based microtubule gliding assay setup to mimic this behavior (**Fig. 2c**) [32,33,34]. We first grew dynamic microtubules from biotinylated seeds and stabilized their ends with biotin-free GMPCPP-tubulin (see **Methods**). We then introduced these microtubules into flow chambers coated with streptavidin and GFP-labeled kinesin-1 immobilized via anti-GFP antibodies. All assays used purified kinesin-1 (heavy chain truncated to 560 aa, see **Methods**). Since the biotinylated seeds typically elongate at their plus ends, microtubules are effectively anchored at their minus ends to the streptavidin coated surface. When ATP is added, motor-driven translocation of the microtubule shaft leads to a build-up of axial compressive forces, thereby inducing microtubule buckling.

In our *in vitro* buckling assay, microtubules exhibit a range of dynamic deformation modes (**Fig. 2d-f; Suppl. Movie 2**). To describe this diversity more systematically, we distinguish three recurring deformation patterns: some microtubules show regular, flagella-like oscillations (**Fig. 2d**), characterized by a repeating motion pattern with regions of high curvature that originate near the anchor point and travel towards the free end (see **Suppl. Movie 3**). Others form chaotic loops without any apparent repeating pattern (**Fig. 2e**). Some also display a beating-like motion (**Fig. 2f**), which also repeats at regular intervals but lacks traveling regions of high curvature, and intermittently returns to relatively straight conformations.

To compare these deformation dynamics to those observed in PtK2 cells, we measured microtubule curvatures and rates of curvature change in both systems. The distributions are similar, with slightly higher curvatures in cells, indicating that our assay reproduces the dynamic shape fluctuations of buckling microtubules seen in cells (**Fig. 2g,h**), and reaches curvatures comparable to those of the bent zones in static bent microtubules (**Suppl. Fig. 3c**). While the precise intracellular force patterns remain elusive, these observations suggest that key aspects of motor-induced buckling can be reconstituted using a simplified *in vitro* system.

Figure 2

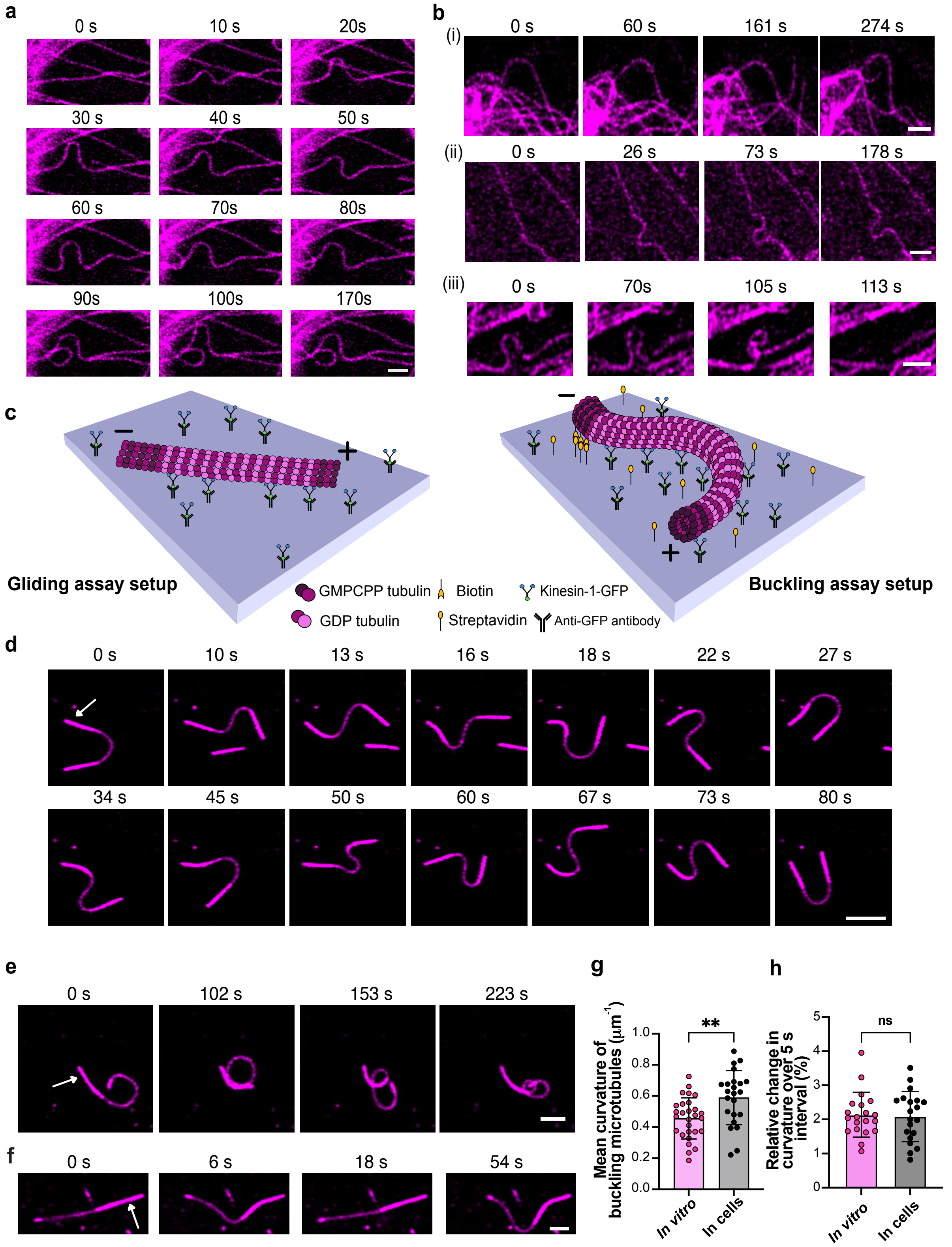

Figure 2: *In vitro* reconstitution of cell-like microtubule buckling.

a, Time-lapse sequence showing change in local microtubule curvature over time in endogenously labeled PtK2 cells (tubulin-eGFP, represented in magenta). Scale bar: 2 µm. **b**, Time-lapse sequence of microtubule bending and buckling events in PtK2 cells: **(i)** curved microtubule persisting in a bent form; **(ii)** dynamically buckling microtubule; **(iii)** breakage of a looping microtubule. Scale bars: 2 µm.

c, Schematic of the experimental setup used to reconstitute buckling *in vitro*. In typical gliding assays (left), kinesin-1-GFP motor proteins are immobilized onto an anti-GFP antibody coated glass surface and GDP microtubules glide over the layer of motors in the presence of ATP. In the buckling assay setup (right), the surface is coated with equal amounts of streptavidin and anti-GFP antibody. Using capped microtubules with seeds containing biotin, we immobilized one end (minus end) to the surface. When the mix with ATP is added, microtubules buckle dynamically. **d**, Time-lapse sequence of a microtubule displaying regular flagella-like oscillations. White arrow in the first frame indicates the position of the microtubule seed (minus end). Scale bar: 5 µm. **e**, Time-lapse sequence of a looping microtubule. White arrow in the first frame indicates the position of the microtubule seed (minus end). Scale bar: 2 µm. **f**, Microtubule showing a regular beating pattern. White arrow in the first frame indicates the position of the microtubule seed (minus end). Scale bar: 2 µm. **g**, Comparison of mean curvature of buckling microtubules in cells and *in vitro* (n= 28 timepoints, *in vitro* from 4 buckling microtubules from three independent experiments and n= 23 timepoints from 4 cells analyzed from 2 independent experiments). p= 0.0032 using unpaired t-test. Error bars represent the S.D. **h**, Comparison of rate of change in curvature in buckling microtubules in 5 s in cells and *in vitro* (n= 20 from three independent experiments for *in vitro* and from 5 cells analyzed from 2 independent experiments). p= 0.8125 (not significant; ns), using unpaired t-test. Error bars represent the S.D.

3) Kinesin-driven buckling causes extensive damage and self-repair

We then used our *in vitro* assay to study microtubule damage and self-repair in buckling microtubules (**Fig. 3a**). For this, we let capped GDP microtubules (magenta) buckle dynamically in the presence of free tubulin (green) for 15 min before washing out the labeled free tubulin and imaging. **Fig. 3b** shows an example image sequence of a buckling microtubule after washout. Buckling microtubules exhibit up to 12 µm long tubulin incorporation stretches that frequently extend along a large part of the microtubule lattice (**Fig. 3c,f; Suppl. Movie 5, 6**). In contrast, when keeping microtubules statically attached to motors using the non-hydrolysable ATP-analogue AMPPNP, we only observed tubulin incorporation stretches of less than 2 µm length (**Fig. 3d,f**). In gliding microtubules grown from biotin-free seeds (see **Methods**), incorporation stretches also appear much shorter than in buckling microtubules (**Suppl. Movie 4**), although they are longer than in static microtubules (**Fig. 3e,f**), consistent with previous reports [9,10,11]. The spatial incorporation frequency also increases from AMPPNP to gliding and buckling microtubules, though the difference in incorporation frequency between buckling microtubules and the other two cases is less pronounced (**Fig. 3g**). This may be due to overlapping incorporations that cannot be distinguished in our analysis, since buckling microtubules exhibit very long incorporation stretches. Overall, we observed tubulin incorporation along 60% of the microtubule lattice length in buckling microtubules (**Fig. 3h**), five times as much as in gliding microtubules and 50 times as much as in static microtubules. Quantification of the total amount of tubulin turnover by accounting for both the longitudinal extent and the lateral spread of incorporation (**Suppl. Fig. 7e**) reveals that buckling microtubules show, by far, the highest turnover (**Fig. 3i**). While even unloaded motors were previously shown to induce microtubule damage and subsequent self-repair [9,11,35,36], our observations reveal that kinesin-mediated buckling massively increases this effect.

Figure 3

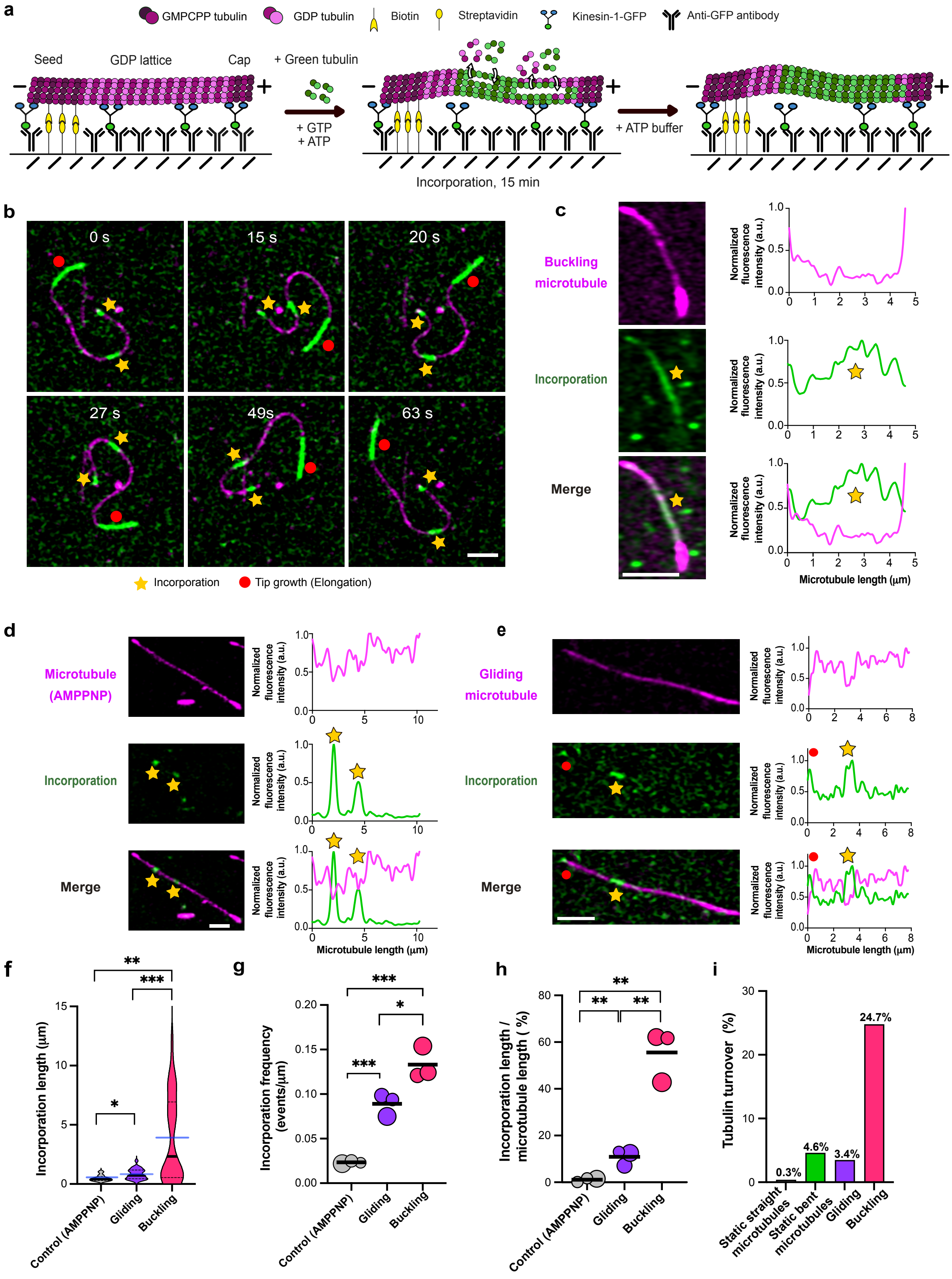

Figure 3: Extensive damage and consequent self-repair in buckling microtubules.
a, Schematic of the experimental setup used to assess self-repair in buckling microtubules *in vitro*. **b**, Time-lapse sequence of a buckling microtubule showing incorporations of green labeled tubulin (marked with a yellow star) and the elongated tip (highlighted with a red circle). Scale bar: 2 µm. **c**,

Example image showing incorporation of green labeled tubulin (marked with a yellow star) in a buckling microtubule. Scale bar: 2 µm. Graphs represent line scans of the microtubule (magenta) and the incorporation channel (green). Profiles have been normalized to 1 with the maximum value of the intensity (a.u.) of the microtubule and incorporation channel, respectively. Scale bar: 2 µm. **d**, Example image showing incorporation of green labeled tubulin (marked with a yellow star) in the buckling setup with static motors using AMPPNP. Graphs represent line scans of the microtubule (magenta) as well as the incorporation channel (green). Profiles have been normalized to 1 with the maximum value of the intensity (a.u.) of the microtubule and incorporation channel, respectively. Scale bar: 2 µm. **e**, Example image showing incorporation of green labeled tubulin (marked with a yellow star) in a gliding microtubule. Elongation of the microtubule tip is highlighted with a red circle. Graphs represent line scans of the microtubule (magenta) as well as the incorporation channel (green). Profiles have been normalized to 1 with the maximum value of the intensity (a.u.) of the microtubule and incorporation channel, respectively. Scale bar: 2 µm. **f**, Violin plots showing extensive incorporations in buckling microtubules. Total length of microtubules analyzed: 567 µm for gliding, 474 µm for buckling and 586 µm for control-AMPPNP from three independent experiments per condition. Black line represents the median and dotted lines represent the interquartile range. Blue lines represent the mean for each condition. p= 0.0018 (buckling-control), p= 0.0172 (gliding-control), and p= 0.0005 (gliding-buckling) using Mann-Whitney test (n= 9 incorporations for control-AMPPNP, n= 52 incorporations for gliding and n= 36 incorporations for buckling). **g**, Bubble plot showing a higher frequency of incorporations in buckling microtubules. Bubble sizes scale with the total microtubule length analyzed. Each circle represents an independent experiment (comprising of 226, 158 and 183 µm of total microtubule length analyzed for gliding; 142, 171 and 161 µm of total microtubule length analyzed for buckling and 218, 173 and 195 µm of total microtubule length analyzed for control-AMPPNP). Black line represents the mean. p= 0.0261 (for gliding-buckling); p= 0.0008 (gliding-control); p= 0.0005 (buckling-control) using unpaired-t-test. **h**, Bubble plot showing a higher amount of lattice length with incorporation, estimated as incorporation length/ microtubule length, in buckling microtubules *in vitro*. Bubble sizes scale with the total microtubule length analyzed. Each circle represents an independent experiment (comprising of 226, 158 and 183 µm of total microtubule length analyzed for gliding; 142, 171 and 161 µm of total microtubule length analyzed for buckling and 218, 173 and 195 µm of total microtubule length analyzed for control-AMPPNP). Black lines represent the mean. p= 0.0076 (gliding-control); p= 0.0010 (buckling-control) and p= 0.0026 (gliding-buckling) using unpaired t-test. **i,** Higher % of tubulin turnover in buckling microtubules. Total length of microtubules analyzed: 567 µm for gliding, 474 µm for buckling and 586 µm for control-AMPPNP from three independent experiments per condition. Refer methods for estimation of % tubulin turnover and **Suppl. Fig. 7e** for estimation of amount of lateral tubulin incorporation.

4) Limits of microtubule self-repair under kinesin-induced buckling

The pronounced tubulin incorporation observed in buckling microtubules suggests that these microtubules experience substantial lattice damage. This leads to the question whether microtubule self-repair is sufficient to counteract the damage sustained under such dynamic buckling. Since tubulin incorporation is the net outcome of damage and repair, we first assessed microtubule stability in the absence of free tubulin, where microtubules are known to spontaneously disassemble due to gradual tubulin loss even in the absence of external forces [8,37] . This condition serves as a reference point, removing the possibility of self-repair and allowing us to directly assess how strongly mechanical stress accelerates microtubule disassembly. We found that buckling microtubules frequently break and disassemble (**Fig. 4a**). Notably, we observed that breakage sites typically coincide with regions of high local curvature (**Fig. 4b; Suppl.**

Movie 7), similar to what is seen in cells (**Suppl. Fig. 3b** and in Odde et al., 1999 [27]). After just 4 min, 50% of the buckling microtubules disassemble, and after 10 min, all buckling microtubules disappear (**Fig. 4c**). By contrast, gliding microtubules persist longer, as reported in Triclin et al., 2021 [9]: 50% remain intact after around 14 min, and within 30 min, all gliding microtubules had disassembled. When kinesin motors are rendered static using AMPPNP, microtubule survival is markedly enhanced, with 85 % of microtubules remaining intact even after 30 min.

We next asked whether self-repair via tubulin incorporation could compensate for the damage observed under dynamic buckling (**Fig. 4d-f**). In the presence of free tubulin, gliding microtubules show markedly improved survival compared to the no-tubulin condition and statically-bound microtubules experience close to no loss (**Fig. 4f**), consistent with previous reports [9,11]. In contrast, buckling microtubules still disassemble rapidly, despite the availability of free tubulin (**Suppl. Movie 8**), typically after breakage in highly curved regions (**Fig. 4d,e,h; Suppl. Movie 7**). After just over 20 min, all buckling microtubules break and disassemble (**Fig. 4f**). Our observations suggest that breakage is more frequent and occurs on shorter timescales than in studies with taxol-stabilized microtubules [38,39,40], which, by design, were performed in the absence of free tubulin and did not account for self-repair.

To better understand the balance between damage and self-repair, we compared tubulin incorporation and microtubule survival after 15 min, in the presence of free tubulin across conditions (**Fig. 4g**). Microtubules with static motors (AMPPNP condition) show almost no detectable tubulin incorporation and remain nearly fully intact, indicating minimal lattice damage. In gliding microtubules, 30 % of the total initial microtubule length is lost due to breakage, and incorporation stretches appear along 8 % of the initial lattice length. Buckling microtubules, driven by the same motor density used for gliding (416 nM), show a greater loss of lattice length (49 %) and a much higher fraction of lattice length with incorporations (29 %). Strikingly, upon further increasing motor density (650 nM), microtubule lattice damage becomes catastrophic: 95 % of the initial length is lost, and no visible tubulin incorporation remains. This indicates that the rate of damage has surpassed the capacity for self-repair. Interestingly, the median value of curvature at the point of breakage in buckling microtubules is 1.7 μm^{-1} (**Fig. 4h**), closely matching the value of 1.5 μm^{-1} reported by Odde et al., 1999 for occasional microtubule breakage in fibroblasts [27].

Although buckling-induced microtubule breakage occurs predominantly at regions of high microtubule curvature, we did not observe intermediate conformations (i.e., locally strongly bent or kinked regions) consistent with gradual, localized softening prior to breakage. Instead, continual deformation during buckling is associated with sudden microtubule failure (**Fig. 4a,b**; **Suppl. Movies 7** and **8**), indicating a rapid transition from deformation to breakage. Consistently, quantification of microtubule curvature over time (**Suppl. Movie 3**) does not reveal a progressive increase in mean curvature, suggesting that any potential softened states, if present, are too short-lived to be experimentally resolved under our conditions.

Together, these results highlight the limits of microtubule self-repair: Statically anchored microtubules remain stable, and gliding microtubules sustain moderate damage that is efficiently repaired, in line with previous reports that self-repair protects microtubules against breakage from motor motility [9]. In contrast, buckling – especially at high motor density – induces severe lattice disruption that exceeds self-repair capacity. Thus, dynamic buckling represents a mechanical challenge to microtubule integrity that cannot be balanced by intrinsic self-repair alone. Based on our experiments, breakage typically occurs in regions of high curvature, suggesting curvature as a determinant of lattice disruption. However, it remains unclear whether these curved regions are also subjected to elevated motor forces, since in our assays we cannot resolve local force patterns along the microtubule.

Figure 4

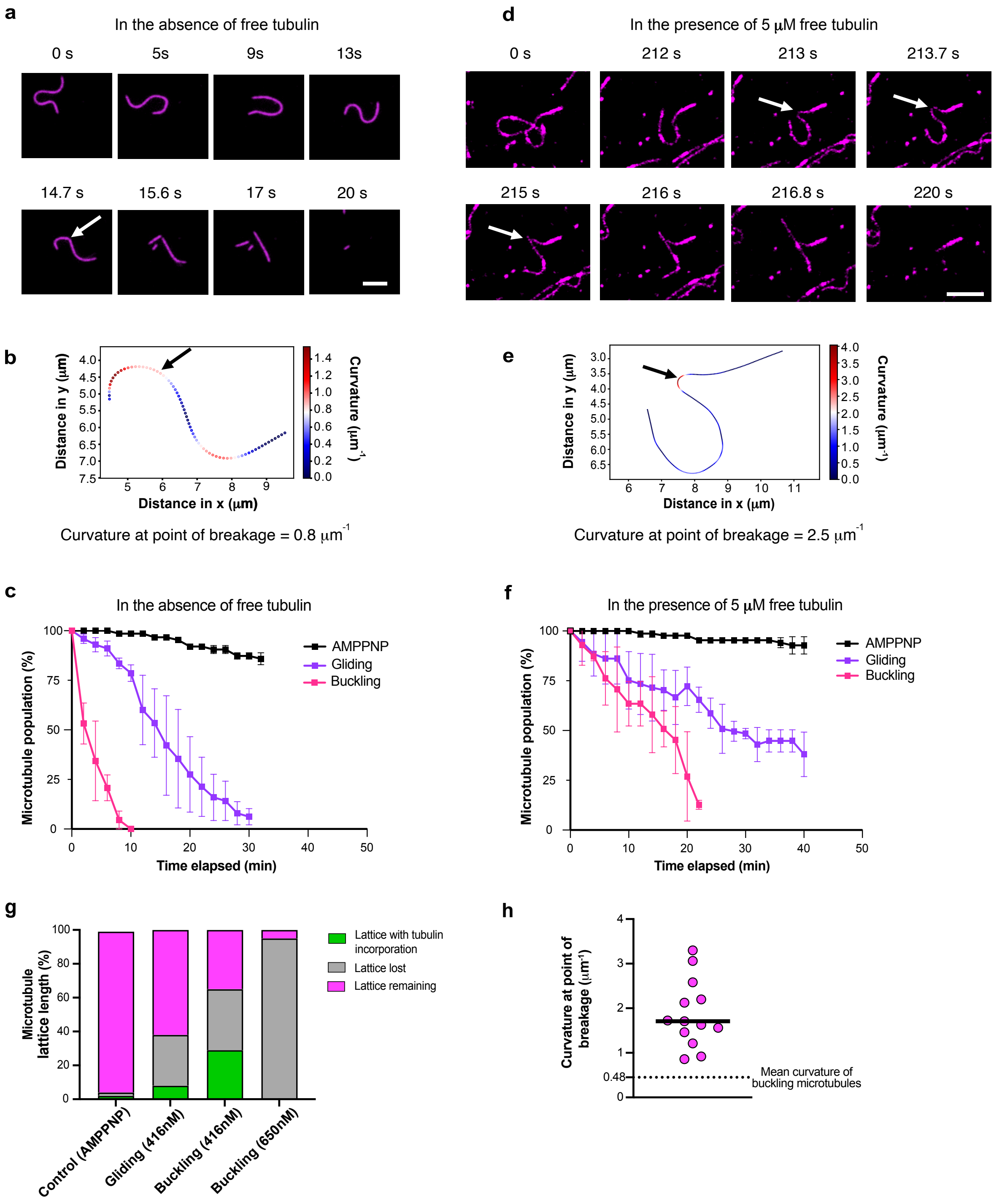

Figure 4: Motor-induced buckling damages microtubules beyond the limit of self-repair. **a**, Time-lapse sequence of a buckling microtubule breaking in the absence of free tubulin. White arrow in the frame at 14.7s indicate the point of breakage. Scale bar: 5 μm. **b**, Plot showing distribution of local curvature along the microtubule in **Fig. 4a** in the frame (at 14.7s) prior to microtubule breakage. Black arrow indicates point of breakage. **c**, Comparison of % microtubule population remaining in control (AMPPNP), gliding and buckling microtubules over time, in the absence of free tubulin. The symbols indicate mean ± S.D. Total length of microtubules analyzed: 567 μm for gliding, 474 μm for buckling and 586 μm for control-AMPPNP (no: of microtubules analyzed > 100) from two independent experiments per condition. **d**, Time-lapse sequence of a buckling microtubule breaking in the presence

of 5 µM free tubulin. Point of breakage indicated by a white arrow. Scale bar: 5 µm. **e**, Plot showing distribution of local curvature along the trace of the microtubule in **Fig. 4d** in the frame (at 213.7s) prior to microtubule breakage. Black arrow indicates the point of breakage. **f**, Comparison of % microtubule population remaining in control (AMPPNP), gliding and buckling assays over time in the presence of 5 µM free tubulin. The symbols indicate mean ± S.D. Total length of microtubules analyzed: 567 µm for gliding, 474 µm for buckling and 586 µm for control-AMPPNP (no: of microtubules analyzed >100) from two independent experiments per condition. **g**, Bar graph showing the relative proportion of microtubule lattice length lost, repaired (refer to **Fig. 3 g,h**) and remaining (refer **Fig. 4f**) at the end of 15 min, in the case of assays with AMPPNP, gliding microtubules (416 nM kinesin), buckling microtubules (416 nM kinesin), and buckling microtubules (650 nM kinesin). No: of microtubules analyzed > 100 from three independent experiments per condition. **h**, Curvature of buckling microtubules at point of breakage (n= 13 microtubules from eight independent experiments). Black line represents the median (1.71 µm^{-1}). Black dotted line represents the average curvature of buckling microtubules (0.48 µm^{-1}; Refer to **Fig. 2g**).

5) Worm-like chain model recapitulates microtubule buckling

To better understand the mechanical loads experienced by microtubules in our *in vitro* buckling assay, we developed a stochastic two-dimensional computational model that captures the key mechanical and dynamic features of our experimental system (**Fig. 5a**; see **Suppl. Simulation Methods** for a detailed description). We modeled microtubules as worm-like chains composed of 8-nm segments – equivalent to the length of a tubulin dimer – the typical step-size of kinesin [41,42]. Microtubules are fixed at their minus ends, mimicking the anchored seeds in our experiments. Motors are distributed on a grid at variable densities and modeled as point-like entities that can bind to the nodes between microtubule segments and step along the microtubule (**Fig. 5a**). Since the motors remain attached to the substrate, their stepping leads to microtubule buckling. The motor parameters - including attachment and detachment rates and force-dependent stepping kinetics - are based on literature values and our own measurements (see **Suppl. Table 1**; **Suppl. Fig. 5a-i**; **SI Simulation Methods**). Unless otherwise indicated, we performed simulations using 10 µm-long microtubules with 5 mm persistence length (L_p) and a motor density (ρ) of 400 µm^{-2}. Note that the model does not rely on any fit parameters tuned to our experimental system. Rather than aiming for a precise quantitative match, we chose a coarse-grained model designed to semi-quantitatively capture essential trends. To verify that the model reproduces our experimental observations both *in vitro* and in cells, we compared the mean microtubule curvature between simulations, experiments and buckling microtubules in PtK2 cells (**Suppl. Fig. 6a**).

By varying the motor density, we were able to reproduce the distinct dynamic behaviors observed in our experiments: flagella-like oscillations (**Fig. 5b**, compare to **Fig. 2d**; **Suppl. Movie 9**), looping (**Fig. 5c**, compare to **Fig. 2e**, **Suppl. Movie 10**), and beating motions (**Fig. 5d**, compare to **Fig. 2f**; **Suppl. Movie 11**). We then systematically explored the dependence of microtubule curvature on key parameters by constructing phase diagrams showing the mean microtubule curvature as a function of motor density, microtubule length, and microtubule persistence length (**Fig. 5e**).

This reveals intuitive trends: curvature increases with higher motor density and microtubule length and decreases with increasing microtubule stiffness.

To assess how motor-generated forces influence microtubule shape, we then examined how mean curvature depends on the mean force along the microtubule. **Fig. 5f** shows the mean microtubule curvature as a function of the mean force per microtubule segment at varying motor densities, which effectively increases the number of active motors on the microtubules (**Suppl. Fig. 6b**). Mean curvature scales predictably with the overall applied force.

Next, we aimed to determine which local motor force patterns are responsible for inducing buckling. **Fig. 5g** shows color-coded force profiles for twelve representative microtubules with different persistence lengths: soft (L_p = 1 mm), intermediate (L_p = 5 mm) and stiff (L_p = 10 mm). Notably, the force distribution is highly heterogeneous and does not consistently coincide with regions of high curvature. When correlating local curvature with the local force per segment, we found only a modest correlation ($r \approx 0.2$). This likely reflects the inherent complexity of the system, in which distributed and competing active forces act over and are transmitted along a filament with internal degrees of freedom.

To further investigate the relationship between force application and resulting curvature, we calculated the correlation between local force and curvature as a function of the spatial offset Δx between the force application point and the measured curvature. The correlation between local force and curvature is generally weak, with a peak at $\Delta x \approx 0.2$ µm (**Fig. 5h**), suggesting that curvature tends to arise slightly displaced with respect to the site of force application. This behavior can be intuitively understood with an analogy to a flexible rod that is exposed to compression: the resulting bend is not maximal at the point of force application but depends on how the rod distributes stress along its length. Soft microtubules show weaker correlations that decay more strongly with distance Δx compared to stiff microtubules (**Fig. 5h**). This is consistent with their higher susceptibility to noise, which makes their mechanical response less deterministic – also evident in their chaotic looping behavior (**Fig. 5e, bottom**).

Finally, we examined how local motor forces relate to microtubule breakage. In our experiments, microtubules consistently break at regions of high curvature (**Fig. 4h**), similar to what is seen in cells (**Fig. 2b, bottom**; [27]). Our measurements show that the curvature at sites of breakage is three times as high as the mean curvature of buckling microtubules (1.7 µm^{-1} compared to 0.48 µm^{-1}, see **Fig. 4h**). Consistent with the low correlation between force and curvature, our simulations reveal that for a given curvature, the force per microtubule segment varies substantially (see **Suppl. Fig. 6c** for a soft microtubule and **Suppl. Fig. 6d** for a stiff microtubule). Nevertheless, a clear trend emerges: higher local curvatures tend to be related to a slightly higher mean force per motor, both in soft and stiff microtubules (**Fig. 5i**). Notably, the model predicts the largest forces to be associated with curvatures in the range of 1 µm^{-1} (for stiff microtubules) to 2 μm^{-1} (for soft microtubules), which coincides with the curvature range where microtubule breakage is observed experimentally (median curvature at breakage is indicated by the dashed line in **Fig. 5i**, also refer **Fig. 4h**).

Interestingly, the force exerted on each segment of the filament displays a nonmonotonic relationship with the local curvature (**Fig. 5i**). At low curvatures, the curvature increases gradually with force. As deformation progresses, the system enters a nonlinear force-curvature regime characterized by an accelerated increase in curvature [43]. At very high curvatures, however, the force begins to decline, coinciding with topological transitions in the filament, such as the formation of loops. In this regime, the force required for further deformation may decrease, driven by abrupt, large-scale conformational changes of the filament. Overall, the model reveals that local curvature and local motor-generated forces only weakly correlate and are not linked in a simple manner.

Figure 5

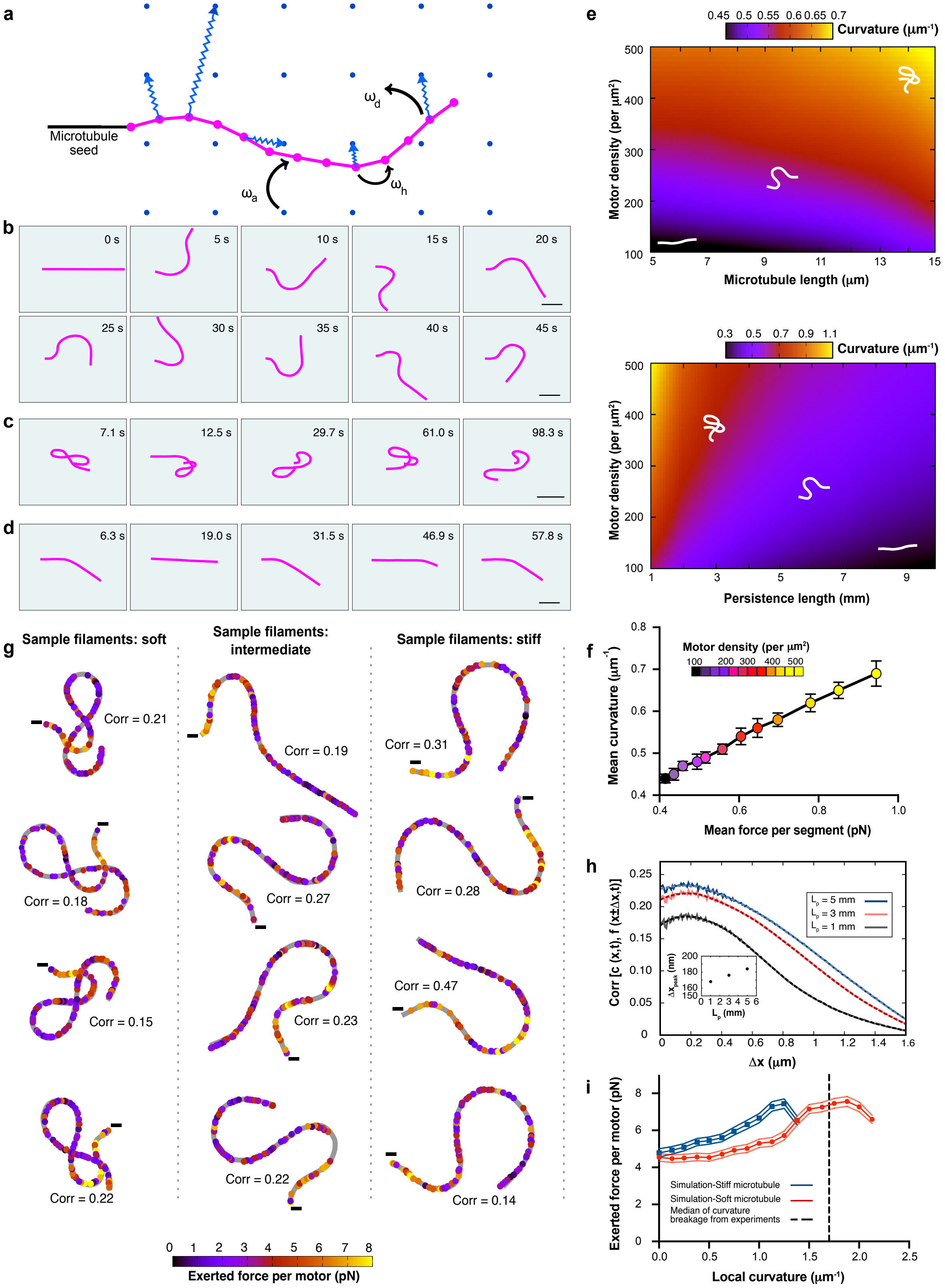

Figure 5: Worm-like chain model-based simulations capture microtubule deformation under active forces. a, Schematic of the simulation setup: motor proteins (represented as blue dots) are uniformly distributed on the substrate and interact with the microtubule by attaching, hopping along it, or detaching with rates ωa, ωh and ωd respectively. The minus end of the microtubule (seed, represented

in black) is kept fixed. Springs represent pulling forces exerted by attached motors. **b-d**, Representative microtubule conformations in different deformation regimes: **b**, regular flagella-like oscillations; **c**, loop formation; and **d**, regular beating. The motor density is ρ= 248, 494 and 123 μm^{-2}, respectively. Scale bars: 2 µm. Other parameters are set to default values mentioned in **Suppl. Table 1**. **e**, Numerical phase diagrams of microtubule deformation under active motor forces. Mean curvature of microtubules as a function of (top) microtubule length and motor density at a fixed persistence length L_p= 5 mm and (bottom) persistence length and motor density at a fixed microtubule length L= 10 µm. The heat maps display ensemble-averaged data over 10^5 filaments per parameter set. The underlying data are discretized into 20 bins along each axis, and a Gaussian smoothing filter was applied to generate the final color map. Schematic white filaments show representative microtubule configurations for corresponding mean curvature values. **f**, Mean curvature of the filament versus the mean force exerted on the filament per segment for L = 10 µm, L_p = 5 mm, and increasing motor density. The data is ensemble averaged over 10^3 filaments. **g**, Representative microtubule configurations from simulations, color-coded by the local active force exerted by molecular motors. Each dot represents an attached motor. Shown are examples for three levels of bending rigidity: soft filaments with L_p =1 mm (left), intermediate stiffness with L_p = 5 mm (middle), and stiff filaments with L_p = 10 mm (right). Other parameters: L = 10 µm, ρ = 494 μm^{-2}. In each panel, the gray line traces the filament backbone. Colored circles mark the positions of the active motors along the microtubule, with the color indicating the magnitude of the exerted force by each motor. Minus signs denote the fixed ends of the microtubules. 10−15% of the modeled microtubules segments are occupied by motors (refer to **Suppl Fig. 6b**). Configurations highlight differences in deformation patterns and force localization depending on filament stiffness. For each case, the corresponding curvature-force correlation is also shown, which is computed at the optimal spatial offset (within the narrow range [0.17, 0.20] µm) and averaged along the filament. **h**, Cross-correlation between the local curvature c(x,t) of a modeled buckling microtubule at position x and time t, and the local force f(x±Δx,t) exerted at spatially offset positions at the same time, plotted as a function of spatial offset Δx (See SI simulation methods for details of Pearson correlation calculation). Results are shown for varying persistence lengths from an ensemble of 10^5 microtubules. Solid lines represent raw simulation data, while dashed lines indicate smoothed curves obtained using a Savitzky-Golay filter. Default values for all other parameters are listed in **Suppl. Table 1**. Cross-correlation values are averaged over time and along the length of the filament. Inset shows the dependence of the correlation peak position on persistence length (L_p). **i,** Force exerted by each motor versus local curvature, shown for simulated stiff microtubule with L_p = 10 mm (dark blue) and soft microtubule with L_p = 1 mm (red). Other parameters: L = 5 µm, ρ = 400 μm^{-2}. Solid lines represent the mean, and shaded regions indicate standard deviations across the ensemble of 10^5 microtubules. Vertical dotted line (in black) represents the median curvature of breaking buckling microtubules (1.7 μm^{-1}) from **Fig. 4h**.

6) Microtubule damage arises from a combination of curvature and motor action

To summarize our findings so far, we have established that: (i) Static curvature is sufficient to induce microtubule damage and self-repair, but it neither leads to microtubule breakage nor reaches the levels of tubulin turnover observed in cells. (ii) Dynamic buckling, in contrast, causes extensive lattice disruption and frequent breakage, which typically occurs in regions of high curvature. (iii) Modeling reveals that local curvature and local motor-induced force patterns correlate only moderately, yet overall higher forces give rise to higher mean curvatures. Together, these observations indicate that curvature alone cannot account for the severe disruption seen during buckling, and suggest that curvature acts in concert with motor motility [9] and motor-induced forces to damage microtubules. To experimentally disentangle the contribution of force from curvature, we modified our buckling assay to isolate the effects of force. Specifically, we included biotinylated tubulin in both microtubule ends (seed and cap), allowing microtubules to be anchored at both ends (see **Methods, Fig. 6a**). This prevents buckling and keeps microtubules straight but still allows surface-attached motors to exert pulling forces on the microtubule lattice. We will refer to these microtubules as “double-anchored microtubules” hereafter.

Fig. 6b shows an example of such a double-anchored microtubule in the absence of free tubulin. Despite remaining straight, the microtubule eventually breaks and disassembles after approx. 16 min (**Suppl. Movie 12**). A survival analysis (**Fig. 6c**) confirms that double-anchored microtubules are significantly more stable than buckling ones, though much less so than static controls without active motors.

We reasoned that the reduced damage observed in the absence of free tubulin should result in less tubulin incorporation in the presence of free tubulin. To test this, we added free, green-labeled tubulin to the assay for 15 min (**Fig. 6d**). Double-anchored microtubules show occasional incorporation of free tubulin, as seen in the example in **Fig. 6e**. Quantification (**Fig. 6f-h; Suppl. Fig. 7a,e**) reveals that incorporation levels are slightly elevated compared to static microtubules, but remain significantly lower than those observed in buckling microtubules. This indicates that double-anchored microtubules undergo limited damage and self-repair, consistent with their increased stability in the absence of free tubulin, when compared to buckling microtubules. We did not observe a preferred location of breakage in double-anchored microtubules (**Suppl. Fig. 8**).

To determine whether these differences could be explained by differing motor forces, we compared the mean motor-generated force per microtubule segment between double-anchored and buckling microtubules in simulations across a range of motor densities (**Fig. 6i; Suppl. Fig. 7b,c**). The results show that double-anchored microtubules experience forces of comparable magnitude to buckling microtubules – particularly at intermediate and high motor densities, as used in our experiments – and far greater than in static bent (**Suppl. Fig. 7d**) as well as AMPPNP conditions.

In conclusion, despite being subjected to similar levels of motor-generated forces, only buckling microtubules exhibit extensive damage and self-repair. The comparable levels of tubulin loss and incorporation in gliding and double-anchored microtubules further suggest that motor motility, in addition to motor-generated forces, contributes to lattice disruption. Thus, lattice damage likely arises from motor movement (and the forces associated with it) and is markedly amplified in zones of high curvature. In summary, our observations support the view that damage in buckling microtubules stems from a combination of curvature and motor action, with force playing a surprisingly minor role and curvature acting as the key amplifier of motor-induced damage.

Figure 6

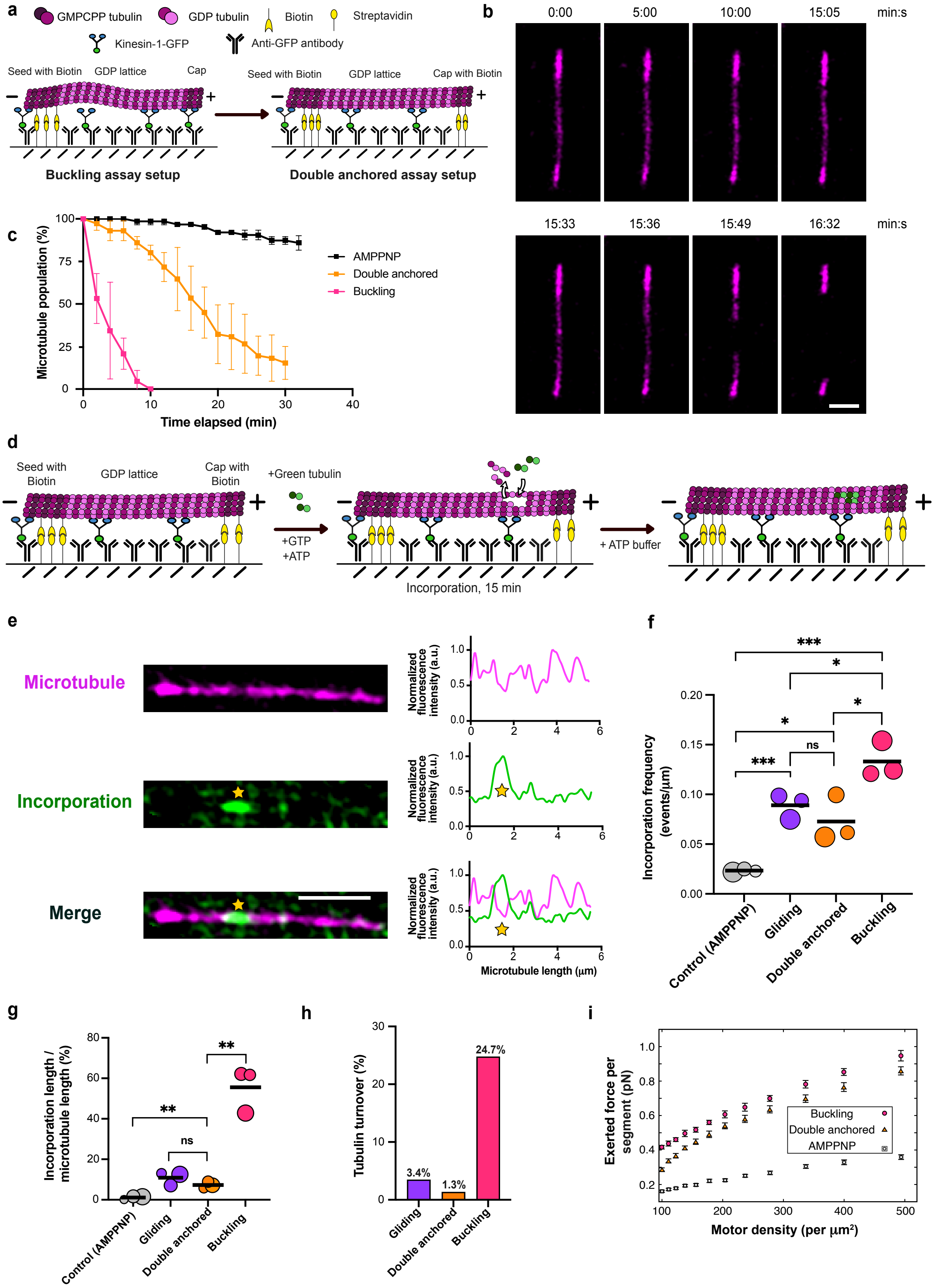

Figure 6: Combination of curvature and motor action contribute to extensive damage in buckling microtubules. a, Schematic of the experimental setup used to subject microtubules to pulling forces of kinesin (double-anchored assay). In this assay, both ends of the capped microtubule are anchored to the surface via biotin/streptavidin. **b**, Time-lapse sequence of a double-anchored microtubule subjected

to motor-induced pulling forces in the absence of free tubulin. Scale bar: 2 µm. **c**, Comparison of % microtubule population remaining in control (AMPPNP), double anchored and buckling assays over time in the absence of free tubulin. The symbols indicate mean ± S.D. (n> 100 microtubules analyzed in each condition from two independent experiments) **d**, Schematic of the experimental setup used to assess self-repair in double-anchored microtubules. **e,** Example image showing incorporation of green labeled tubulin (marked with a yellow star) in a microtubule (magenta) in the double-anchored assay. Scale bar: 2 µm. Graphs represent line scans of the microtubule (magenta) as well as the incorporation channel (green). Profiles have been normalized to 1 for the maximum value of the microtubule and incorporation channel, respectively. **f**, Bubble plot showing lower frequency of incorporations in double-anchored microtubules compared to buckling microtubules. Bubble sizes scale with the total microtubule length analyzed. Each circle represents an independent experiment. Data from three independent experiments comprising 98, 139 and 110 µm of the total microtubule length analyzed for double anchored microtubules. Refer **Fig. 3g** for details on total microtubule length analyzed for gliding and buckling microtubules. Black lines represent the mean. p= 0.0242 (for double-anchored-buckling); p= 0.0212 (double-anchored -control); p= 0.3432; not significant (double-anchored-gliding) using unpaired t-test. **g**, Bubble plot showing a lower percentage of lattice length with incorporation, estimated as incorporation length/ microtubule length, in the double-anchored assay when compared to buckling as well as control (AMPPNP). Bubble sizes scale with the total microtubule length analyzed. Each circle represents an independent experiment (comprising 98, 139 and 110 µm of total microtubule length analyzed for double anchored microtubules; Refer **Fig. 3h** for details on total microtubule length analyzed for gliding and buckling microtubules). Black lines represent the mean. p= 0.0017 (double anchored -buckling) and p= 0.1415, not significant (double anchored -gliding); p= 0.0077 (double anchored -control-AMPPNP) using unpaired t-test. Refer **Fig. 3h** for the p-values comparing control (AMPPNP), gliding and buckling. **h**, Lesser % of tubulin turnover in double anchored microtubules when compared to buckling microtubules. Total length of microtubules analyzed: 567 µm for gliding, 347 µm for double anchored and 474 µm for buckling microtubules from three independent experiments per condition. Refer to the methods for estimation of % tubulin turnover and **Suppl Fig. 7e** for estimation of amount of lateral tubulin incorporation. **i**, Effect of motor protein arrangement and mobility for three configurations: (1) motors distributed across the surface (leading to buckling), (2) motors arranged linearly beneath a straight microtubule (mimicking double-anchored microtubules), and (3) in presence of AMPPNP. Total forces exerted on each discretized node of the microtubule are plotted as functions of motor density. Parameters: L = 10 µm and L_p = 5 mm. Data are averaged over time and across five microtubules.

7) Intracellular factors enhance microtubule resilience to buckling-induced damage

The extensive damage observed in buckling microtubules, which often surpasses their intrinsic self-repair capacity, prompted us to explore how microtubules withstand mechanical stress in the intracellular environment – where bending and buckling are common, as in our *in vitro* system. Several microtubule-associated proteins (MAPs) have been implicated in promoting microtubule resilience to mechanical stress[13,44,45,46]. We therefore hypothesized that intracellular factors may protect microtubules from damage and help maintain their structural integrity.

To test this idea, we examined the survival of buckling microtubules in the presence of cell lysate from HEK293 cells, but in the absence of free tubulin (**Fig. 7a**). While the exact composition of the lysate is unknown, it contains soluble cytoplasmic components and could thus influence microtubule stability. Because cell lysate has previously been shown to modulate motor activity [47], we used a low concentration of 60 µg ml^{-1} or below to minimize such effects, as shown in Korten et al., 2013 [48]. Using low concentrations of cell lysate also ensures that any residual tubulin present is negligible. Tubulin constitutes 2-3.5 % of the total cellular protein content [49,50], and in our assay conditions the corresponding tubulin concentration falls within the picomolar range (**Suppl. Fig 9a-c**), rendering it unlikely to contribute measurably to microtubule repair. We tested the activity of kinesin motors both in the absence and in the presence of lysate and found the microtubule gliding velocity to be similar **Suppl. Fig. 9d**). Examples of buckling microtubules in the presence of 20 µg ml^{-1} HEK293 cell lysate and 60 µg ml^{-1} PtK2 cell lysate are shown in **Fig. 7b** and **Suppl. Fig. 9e**, respectively.

We observed that the addition of lysate during buckling increases microtubule survival: buckling microtubules remain intact for up to ~40 min, significantly longer than without lysate (**Fig. 7c, Suppl. Fig. 9f**). Since only negligible amounts of free tubulin are present in cell lysates, this enhanced survival suggests that factors present in the lysate reduce tubulin loss and stabilize the microtubule lattice. Interestingly, when comparing buckling microtubules in the absence and presence of lysate (**Fig. 2d vs. 7b**; **Suppl. Movie 13**), we noticed that microtubules visually appear softer in the lysate condition, since they buckle faster and with more pronounced curvature. This qualitative impression is supported by curvature quantification, which shows higher mean curvatures in the presence of lysate (**Fig. 7d, Suppl. Fig. 9e**). To better understand these observations, we used our computational model to compare the buckling behavior of soft (L_p = 1 mm) and stiff (L_p = 10 mm) microtubules. Soft microtubules show both a higher buckling frequency and greater mean curvature (**Suppl. Fig. 10a**), resembling the experimental data in the presence of lysate. In simulations, this experimental difference can be recapitulated by an approximate two-fold reduction in the persistence length (**Fig. 7e(i)(ii)**). Consistent with these predictions, estimates of microtubule persistence length derived from thermal fluctuation analysis (see **Methods**) reveals a 1.35-fold decrease in persistence length in the presence of 20 µg ml^{-1} HEK293 cell lysate (**Fig 7f).**

Alternatively, intracellular factors could modulate motor motility parameters. Model predictions indicate that reproducing the lysate data would require either a 2-7-fold increase in the attachment rate ω_a (**Suppl. Fig. 10b**) or a roughly two-fold decrease in the detachment rate ω_d (**Suppl. Fig. 10c**). Importantly, both scenarios increase the effective number of motors attached and thus cannot explain the higher survival in lysate, which would require the opposite effect (fewer attached motors). We therefore consider changes in motor parameters alone unlikely to account for the experimental data, unless additional protective factors overcompensate the increased damage.

Although we cannot currently identify the molecular players responsible for this effect, our findings are consistent with the possibility that intracellular factors contribute to microtubule survival under mechanical stress by enhancing microtubule flexibility.

Increased flexibility may allow microtubules to adopt strongly bent conformations without breaking, thus preserving lattice integrity under sustained deformation.

Figure 7

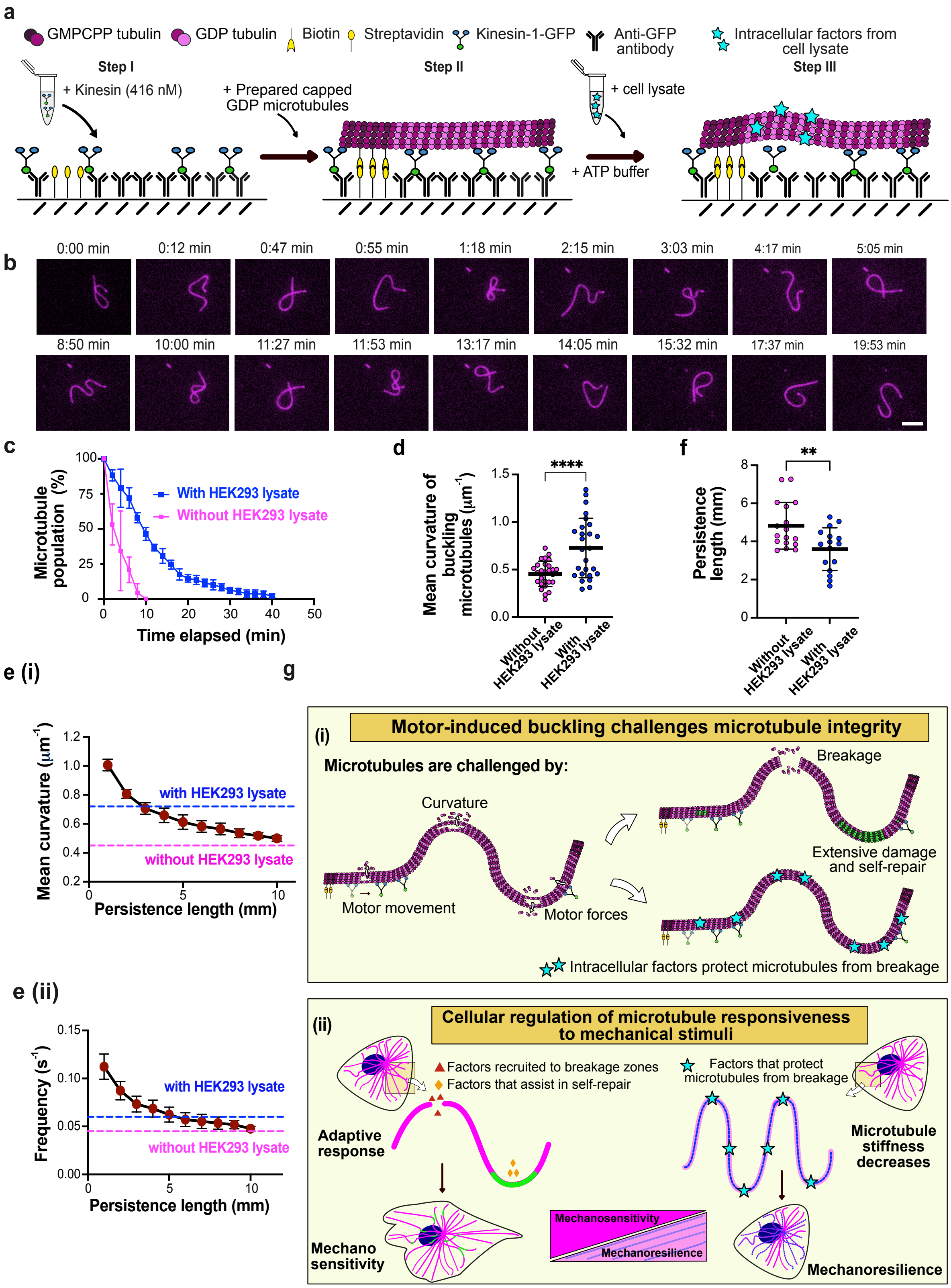

Figure 7: Intracellular factors protect buckling microtubules from breakage. a, Schematic of the experimental setup used to assess the influence of intracellular factors on microtubule survival in buckling assays: In step **I**, similar to the gliding and buckling assay setups, purified kinesin-1-GFP (416 nM) is immobilized on to an anti-GFP antibody coated surface. Then, prepared capped microtubules (step **II**) are added. Microtubule buckling (step **III**) is achieved by flushing in a mix containing ATP buffer (GTP, ATP) with 20 µg ml^{-1} HEK293 cell lysate. **b**, Time-lapse sequence showing survival of a buckling microtubule in presence of 20 µg ml^{-1} HEK293 cell lysate. Scale bar: 5 µm. **c**, Buckling microtubules survive longer in presence of cell lysate. Comparison of the percentage of the microtubule population remaining (in the absence of free tubulin) over time in the case of buckling microtubules both with and without 20 µg ml^{-1} HEK293 lysate (n> 100 microtubules analyzed in each condition from two independent experiments). The symbols and error bars indicate mean ± S.D respectively. **d**, Comparison of mean curvature in buckling microtubules in the presence and absence of HEK293 cell lysate. Black line represents the mean and error bars represent the S.D. $p<0.0001$ using an unpaired t-test. (Mean obtained from analyzing microtubule mean curvature at different timepoints from 4 microtubules in each case: n= 28 for without HEK293 lysate condition and n= 26 for with HEK293 lysate condition. Refer **Suppl. Fig. 9g** for comparison of lengths of microtubules analyzed). **e (i)** Mean curvature and **(ii)** oscillation frequency (bottom) as functions of microtubule persistence length at $L = 10$ µm and $\rho = 400$ µm^{-2}. The symbols and error bars indicate mean ± S.D respectively. Blue and pink dotted lines represent experimentally determined values with and without HEK293 lysate respectively. **f,** Microtubules are 1.35-fold softer in the presence of cell lysate. Plot showing comparison of persistence length (in mm) of microtubules with and without 20 µg ml^{-1} HEK293 cell lysate estimated by thermal fluctuation experiments (refer **Methods**). Black line represents the mean and error bars represent the S.D. $p= 0.0054$ using an unpaired t-test. Persistence length was estimated from analyzing atleast 60 frames for each microtubule over 20 mins for both conditions. n= 17 microtubules for without HEK293 lysate condition and n= 16 for with HEK293 lysate condition from three independent experiments each. **g (i)** Buckling microtubules are challenged by the combination of motor motility, forces and curvature resulting in extensive damage and self-repair or breakage. Intracellular factors protect microtubules and help enhance their survival under sustained deformation. **g(ii)** Our findings suggest that cells may use intracellular factors to regulate microtubule response to mechanical stimuli by factors specifically recruited to microtubule breakage zones and repair sites (mechanosensitivity) and by factors that decrease microtubule stiffness (mechanoresilience).

Discussion

In this study, we highlight the limits of intrinsic microtubule self-repair under mechanical stress induced by molecular motors and show that additional intracellular factors are required to maintain microtubule integrity during sustained dynamic buckling. Using an *in vitro* assay that mimics kinesin-driven buckling as observed in cells, we find that the combination of motor motility, motor-induced forces and high curvature inflicts substantial lattice damage that often exceeds microtubule self-repair capacity.

Previous work has established that kinesin motility itself can induce lattice damage and trigger tubulin incorporation along the lattice, even when the motors are not under load [9,10,11]. In these contexts, however, lattice damage is typically limited and largely counteracted by intrinsic self-repair, allowing microtubules to maintain structural integrity. Our experiments extend these findings by demonstrating that when kinesin activity is coupled to dynamic buckling, microtubule damage is induced by the combined effects of motor motility, active forces, and microtubule curvature. While forces of ~ 30 pN applied in motor-independent assays have been shown to extract tubulin dimers from the lattice, and coupled kinesin motors can likewise disrupt the lattice [51], our double-anchored assays display levels of microtubule damage and self-repair comparable to gliding microtubules and markedly lower than those observed under buckling conditions. This suggests that motor generated forces contribute to a similar extent as motor motility. By disentangling curvature, motor-driven gliding, and motor generated force using static bending, gliding, and double anchored configurations, respectively, we show that each factor alone produces comparatively modest lattice damage. In contrast, their simultaneous action during buckling causes extensive damage that often exceeds intrinsic self-repair capacity, leading to localized breakage at regions of high curvature. These observations suggest that curvature acts as a critical amplifier of motor-induced lattice damage, thereby defining a mechanical regime in which previously described self-repair mechanisms become insufficient. Consistently, a recent study reported enhanced bending, buckling, and microtubule fragmentation in cells containing kinesin condensates formed upon overexpression of kinesin-3 [52], in line with our observation of catastrophic filament failure at high motor densities.

Among the cytoskeletal filament types, microtubules stand out due to their unusual combination of properties: they are relatively stiff polymers, yet remarkably responsive to biochemical and mechanical stimuli [3,14,18]. Since the discovery of microtubule self-repair, it has been widely assumed that this mechanism alone is sufficient to counteract the mechanical forces and damage they sustain in cells [6,9,14,15]. However, our results challenge this notion. They reveal that in situations where microtubules are subjected to dynamic buckling by continuous motor activity, leading to high curvatures, as seen in cells, intrinsic self-repair mechanisms can be overwhelmed. In contrast, the presence of intracellular components markedly enhances microtubule resilience, enabling microtubules to survive under mechanically demanding conditions (**Fig. 7g(i)**).

Interestingly, microtubules show higher curvatures and are 1.35-fold times softer in the presence of cell lysate than in buffer alone, suggesting that intracellular factors may potentially contribute to microtubule resilience by modulating their mechanical properties. While changes in motor parameters such as altered attachment or detachment rates could also contribute to the observed buckling behavior, such changes alone would not readily account for the increased survival of microtubules in the presence of cell lysate. This observation therefore raises the possibility that microtubule stiffness in cells may be lower than previously estimated from *in vitro* measurements [18,53,54]. Reduced stiffness could serve as a protective function by allowing microtubules to adjust their shape under load – a form of mechanical compliance that may potentially be actively regulated in cells. For example, cells may selectively increase microtubule flexibility through recruitment of MAPs that reduce microtubule rigidity [55,56]. Tubulin post-translational modifications, particularly acetylation, have been proposed to enhance microtubule flexibility by weakening the lateral interactions between tubulin dimers [57]. However, in our experiments, it is unlikely that acetylating enzymes (if any) from the cell lysate contribute significantly to the observed microtubule resilience, as microtubules are subjected to mechanical stress from the onset of the experiment, whereas tubulin acetylation is characterized by comparatively slow enzymatic kinetics (catalytic rate of the acetylating enzyme αTAT1 is 0.4 hr $^{-1}$) that are unlikely to counteract early damage events [58].

More broadly, our findings suggest the intriguing possibility that cells may fine-tune microtubule rigidity and responsiveness to mechanical signals depending on functional needs (**Fig. 7g(ii)**). For example, primary cilia, which serve as sensory organelles, may benefit from the ability of microtubules to respond to subtle mechanical stimuli (mechanosensitivity), whereas motile cilia may require less sensitive microtubules to withstand repetitive mechanical stress (mechanoresilience). In plant cells, highly organized microtubule arrays guide morphogenesis by aligning with tensile stress patterns, often forcing them into strongly curved conformations [59]. By differentially regulating stiffness and stress responsiveness, cells may thus navigate the conflict between cell geometry and tension patterns. A better understanding of how microtubule properties are regulated in different contexts could reveal cell-type specific adaptations and vulnerabilities.

Note: Supplementary videos for this research article can be found at:
https://doi.org/10.1002/advs.202521721

(A video does indeed speak beyond a thousand words…)

Materials and Methods:

Cell culture and live cell imaging:

Male potoroo kidney epithelial cells (PtK2), stably expressing GFP-Tubulin (displayed in figure 2 in Magenta) were cultured at 37°C and 5% CO_2 in DMEM/F12 media (31331028, Gibco), supplemented with 10% Fetal Bovine Serum (FBS, Gibco A5670701) and 1% Penicillin-Streptomycin solution (15070063, Gibco). Human Embryonic Kidney cells (HEK293, DMSZ, ACC305) were cultured in Complete DMEM (high glucose with HEPES) media (Fisher Scientific, 42430025) with 10% Fetal Bovine Serum (heat inactivated at 56°C) and 1% Penicillin-Streptomycin solution at 37°C and 5% CO_2. For live cell imaging, PtK2 cells were seeded in confocal glass-bottom dishes (734-2904, VWR Avantor) coated with 0.01 mg ml^{-1} fibronectin, a day prior to imaging. Live cell imaging for observing dynamic microtubules was carried out using a 63x immersion oil objective (Zeiss) maintained at 37°C and 5% CO_2. Time-lapses of bending and buckling events in PtK2 cells were captured for a period of 5 min.

Purification and labelling of tubulin:

Tubulin free of Microtubule Associated Proteins (MAPs) was purified from fresh calf brains by three cycles of polymerization-depolymerization, using a combination of low and high salt buffers, followed by cation exchange chromatography, as previously described in [60]. Briefly, the first polymerization-depolymerization cycle was performed in low salt conditions (0.1 M PIPES, 0.5 mM $MgCl_2$, 2 mM EGTA and 0.1 mM EDTA). This was followed by the second cycle in high salt buffer [High Molarity PIPES Buffer: 1 M PIPES, pH 6.9, supplemented with KOH, 10 mM $MgCl_2$, 20 mM EGTA]. Subsequently MAP free tubulin was obtained after cation-exchange chromatography (Fractogel EMD SO3, Merck) in 50 mM PIPES, pH 6.8, supplemented with 1 mM $MgCl_2$ and 1 mM EGTA.

Fluorescently labeled tubulin (ATTO-488 and ATTO-565-labeled tubulin) and biotinylated tubulin were prepared according to the protocol described in Hyman et al.,1991 [60]. MAP-free tubulin obtained after cation exchange chromatography was polymerized at 37°C for 1 hour in BRB80 [Brinkley Buffer 80: 80 mM PIPES, pH 6.8, 1 mM EGTA and 1 mM $MgCl_2$] supplemented with 33% glycerol, 4 mM $MgCl_2$ and 1 mM GTP. The polymerized microtubules were layered onto prewarmed cushions of 0.1 M Na-HEPES, pH 6.8, 1 mM $MgCl_2$, 1 mM EGTA, 60% v/v glycerol. This was followed by high-speed centrifugation at 37°C for 1 hour. Then the pellet was resuspended in 0.1 M Na-HEPES, pH 8.6, 1 mM $MgCl_2$, 1 mM EGTA, 40% v/v glycerol. To this, 1/10th volume of 100 mM NHS-ATTO-565/488 (ATTO-Tec), or NHS-LC-LC-biotin (EZ-link, ThermoFisher) was added, and the mix was allowed to incubate for 10 min at 37°C. Subsequently, the labeling reaction was stopped using two volumes of BRB80, with 100 mM potassium glutamate and 40% v/v glycerol. The labeled microtubules were sedimented onto BRB cushions with 60% glycerol. Following this, an additional cycle of polymerization and depolymerization was performed before the labeled tubulin was aliquoted, snap-frozen and stored in liquid nitrogen till use.

Purification of Kinesin-1-GFP motor proteins:

Recombinant, truncated kinesin-1 motor protein was purified as previously described in [61]. The plasmid encoding for the kinesin-1 protein (human KIF5B heavy chain truncated to 560 aa; GFP and His tag at the C-terminus of the insert and backbone respectively), pET17_K560_GFP_His, was purchased from Addgene (15219, Cambridge, MA).The plasmid was transfected into Rosetta2 (DE3)-pLysS *E. coli* (VWR) and incubated with 0.2 mM IPTG at 16°C for 16 h. Following this, the cells were resuspended in cation-exchange buffer (6.67 mM Na-Acetate, 6.67 mM MES, 6.67 mM HEPES, 20 mM β-mercaptoethanol (BME), 0.2 mM ATP, and 0.2% Tween-20, pH 7.0 supplemented with a protease inhibitor cocktail) and lysed by sonication. The lysates were centrifuged at 38,000xg for 30 min at 4°C and loaded into a HiTrap SP Cation exchange column (HiTrap SP HP™, 17-1151-01, Cytiva). The column was then washed with cation exchange buffer supplemented with 50 mM KCl, followed by elution with cation exchange buffer supplemented with 300 mM KCl. The eluted fraction was then loaded on to a Ni-NTA column (HisTrap HPTM, 17-5247-01, Cytiva) after dilution with nickel loading buffer (Nickel buffer: 50 mM sodium phosphate buffer, pH 7.5, 5% w/v glycerol, 300 mM KCl, 1 mM $MgCl_2$, 0.2% w/v Tween-20, 10 mM BME, 0.1 mM ATP, supplemented with imidazole to a final concentration of 36 mM). This was followed by washing with nickel washing buffer (nickel buffer supplemented with KCl to a final concentration of 1000 mM and imidazole to a final concentration of 30 mM) and elution with nickel elution buffer (nickel buffer supplemented with imidazole to a final concentration of 300 mM). The collected fractions were centrifuged at 4,000 g for 30 minutes at 4 °C. To remove imidazole, the sample was dialyzed overnight against K560 buffer (50 mM Na-phosphate pH 7.5, 300 mM KCl, 5% glycerol, 1 mM $MgCl_2$, 1 mM DTT, 0.1 mM ATP). The sample was then loaded onto a gel filtration Superdex column (Superdex 200 Increase 10/300 GL, 28-9909-44, Cytiva) and eluted with K560 buffer. The eluted fractions were concentrated using a 30 kDa membrane filter by centrifugation at 4,000xg for 30 minutes at 4°C. Finally, the protein was snap-frozen in 5 µl aliquots and stored in liquid nitrogen till use. In the text and in figures, Kinesin-1-GFP is represented in cerulean blue (False color LUT).

Preparation of HEK293 cell lysates:

0.6 million HEK293 cells or PtK2 cells/well were seeded into two 6-well plates. After 48 h, cell lysates were prepared according to the protocol mentioned in [62]. Briefly, transfected cells were treated with trypsin and centrifuged at 450xg for 10 min at 4 °C. All steps after centrifugation were carried out on ice or at 4°C. The cell pellet (from two 6 well plates) was resuspended in 130 µl ice-cold lysis buffer ((BRB80 containing 0.05% Triton X-100 and protease inhibitors (10 µg ml^{-1} leupeptin, aprotinin and 4-(2-aminoethyl)-benzenesulfonyl fluoride; Sigma-Aldrich)). The resuspended mixture was transferred to an ice-cold 1.5 ml Beckman ultracentrifuge tube, and the cells were further lysed by pipetting. This was followed by sonication (4 short pulses at 12% Amplitude, MS-72 probe, Bandelin Sonoplus). The lysed mixture was further mixed by pipetting and then centrifuged at 33,800xg for 30 min at 4°C. The supernatant was aliquoted, snap-frozen in liquid nitrogen and stored at −80 °C. The total protein concentration was estimated using the Bichinchoninic acid protein assay (Pierce™ BCA protein assay kit, 23200, ThermoScientific). For buckling assays, 20 µg ml^{-1} of HEK293 and 60 µg ml^{-1} PtK2 cell lysate (final total protein concentration) was added along with ATP buffer.

Western blot for estimation of tubulin concentration in cell lysates:

The concentration of tubulin present in cell lysates (both HEK293 and) was quantified using western blot analysis. A western blot of dilution series of purified tubulin of known concentration as standard and dilution of cell lysates was performed (Refer **Suppl. Fig 9a**). The samples were boiled for 5 mins at 95°C in 1x Lamelli buffer (Bio-Rad), run on a 10% SDS-PAGE gel and transferred to a nitrocellulose membrane. The transfer was performed in 1x Blotting buffer (14.4 g Glycine, 3 g Tris-base, 10% Ethanol) for 1.5 hr. The immunoblots were subsequently blocked using 5% non-fat milk (68514-61-4, Roth) in 1x TBS (Tris-Buffered Saline). The blots were then incubated overnight in a 1:1000 dilution of alpha tubulin mouse monoclonal antibody (DM1A, 62204, ThermoFisher) in 5% non-fat milk in 1xTBS. The immunoblots were then washed thrice with 1xTBS-T and incubated in a 1:15000 dilution of secondary antibody (IRDye680RD goat anti-mouse antibody, LICORbio, 926-68070, in 5% non-fat milk in 1xTBS) for 1 hr. Following this, the blots were washed thrice in 1x TBS-T (Tris-Buffered Saline with 0.1 % Tween-20) before imaging using ChemiDoc gel imager (12009077, Bio-Rad).

Preparation of GMPCPP stabilized microtubule seeds:

Microtubule seeds were prepared by polymerizing 10 µM of tubulin (40% red fluorescent tubulin and 60% unlabeled or biotinylated tubulin) in BRB80 buffer supplemented with 0.5 mM GMPCPP (Guanosine-5'-[(α,β)-methyleno] triphosphate: slowly hydrolysable GTP analogue) (NU-405, Jena Bioscience) for 1 hour at 37°C. Following this, the above mixture was incubated with 1 µM Paclitaxel (Sigma) for 30 min at room temperature, centrifuged (21,300xg at 25°C for 15 min) and the pellet was resuspended in warm BRB80 supplemented with 0.5 mM GMPCPP. The prepared microtubule seeds were stored in liquid nitrogen until use.

Preparation of Capped GDP microtubules for *in vitro* assays:

Capped GDP microtubules in a single color (displayed in figures in magenta) were prepared with a lower proportion of fluorescent tubulin (12%) in the GDP lattice in contrast to the stabilized ends (40% labeled seeds and caps). Capped GDP microtubules were prepared by elongating prepared microtubules seeds with 10 µM of tubulin (12% labeled) in Elongation buffer (56 mM PIPES, 0.7 mM EGTA, 0.7 mM $Mgcl_2$, 38 mM KCl, 19 mM Phosphate buffer, pH 6.8), supplemented with 1 mM GTP for 40 min at 37°C. The sample with the polymerized microtubules was then immediately centrifuged (21,300x g for 15 min). The resulting pellet was resuspended in a resuspending mix containing Elongation Buffer supplemented with 0.5 mM GMPCPP and further incubated at 37°C to cap the ends of the microtubule. Capping helps prolong the lifetime of the microtubule and additionally allows for better visualization of lattice self-repair. The resuspended mix is then successively capped by adding 0.5 µM of tubulin (60% biotin, 40% fluorescent tubulin) in a stepwise manner (for a total of 10 times) every 15 min.

For microtubule static curvature and double anchored motor assays, GDP microtubules with seeds and caps containing biotin were prepared. For microtubules buckling assays, GDP microtubules were prepared using biotin-containing seeds and the caps were grown using 0.5 µM (60% unlabeled and 40% fluorescent) tubulin. For microtubules gliding assays, GDP microtubules were prepared using seeds (60% unlabeled and 40% fluorescent, without biotin) and the caps were grown using 0.5 µM tubulin (60% unlabeled and 40% fluorescent).

Cover-glass passivation:

For experiments analyzing static curvature of microtubules, cover-glasses were passivated with Silane-PEG-Biotin as follows: Cover-glasses were first wiped with lint-free KimWipe™ (Kimberly-Clark Professional™ 33670-04) tissues and 70% ethanol, incubated in Acetone for 30 min, followed by 96% ethanol for 15 min (gentle agitation at room temperature). The cover-glasses were subsequently rinsed in ultrapure water, incubated in Hellmanex III solution (2% in water, Hellmanex) for 2 h (gentle agitation at room temperature), washed in ultrapure water and dried. This was followed by treatment using an Deep-UVO cleaner (30 mW/cm² at 254 nm, 144AX-220 Jelight) for 30 min before incubation in 7:3 mix of tri-ethoxy-silane-PEG and tri-ethoxy-silane-PEG-biotin (30kDa, Creative PEG works)(final concentration of 1 mg ml^{-1} in 96% ethanol and 0.1% HCl), for 3 days with gentle agitation at room temperature. After 3 days, the PEGylated cover-glasses were extensively rinsed in 96% ethanol and ultrapure water, air-dried and stored at 4°C till use.

For gliding and buckling assays with kinesin-1 motor proteins, cover-glasses were wiped with lint-free KimWipe^{TM} tissues and 96% ethanol, rinsed in ultrapure water and sonicated in 2% Hellmanex-III solution at 60°C for 30 min. Following sonication, the cover-glasses were rinsed in ultrapure water, stored in ultrapure water at room temperature and air-dried just before use.

Assay to assess self-repair in static bent microtubules:

A flow chamber of an approximate volume of 60 µl was built by sandwiching two pieces of SiPEG-Biotin passivated cover-glasses using two strips of double-sided adhesive tape (70 µm height, 0000P70PC3003, LiMA, Couzeix, France). The flow chamber was first perfused with streptavidin (100 µg ml^{-1} in 1xBRB80; Fisher Scientific) for 1 minute. This was followed by a solution of 0.1 µg ml^{-1} PLL-g-PEG (Pll 20 K-G35-PEG2K, Jenkam Technology, in 10 mM Na-HEPES, pH 7.4) for 1 minute. Following a wash step with 1xBRB80, prepared capped GDP microtubules (diluted in 1xBRB80) were flushed in an alternative manner (to achieve bending) and incubated for 5 min before extensive washing with BRB80 supplemented with 1 mg ml^{-1} BSA (Bovine Serum Albumin, Sigma). Subsequently, an incorporation mix containing 5 µM Tubulin (100% ATTO-488, green labeled) in Elongation buffer supplemented with 1 mM GTP, an oxygen scavenger cocktail (22 mM DTT, 1.2 mg ml^{-1} glucose, 8 µg ml^{-1} catalase and 40 µg ml^{-1} glucose oxidase), 1 mg ml^{-1} BSA and 0.033% (w/v) methyl cellulose (1,500 cP, Sigma) was added and allowed to incubate at 37°C for 15 min. Owing to the high background resulting from usage of 100% labeled tubulin, incorporation events can only be detected after washout of free tubulin, prior to imaging. Therefore, following incubation, the chamber was perfused with 200 µl of imaging buffer (composition same as that of the incorporation buffer with an addition of 2 µM unlabeled tubulin-to keep microtubules stable for imaging). The chamber was then sealed with Valap before imaging.

Microtubule gliding assay:

In vitro gliding assays were performed in 20 µl flow chambers constructed from Hellmanex-sonicated cover-glasses and using double-sided tape. The chamber was first perfused with a 20 µl solution of 0.2 mg ml^{-1} Anti-Green-Fluorescent-Protein (GFP) Antibody (Invitrogen, A-11122) for 3 min. This was followed by further passivation using 1% w/v BSA solution in 1xHKEM buffer (10 mM HEPES buffer (pH 7.2), 50 mM KCl, 1 mM EGTA and 5 mM $MgCl_2$). Kinesin-1-GFP diluted in TicTac buffer (10 mM HEPES buffer (pH 7.2), 16 mM PIPES buffer (pH 6.8), 50 mM KCl, 5 mM $MgCl_2$, 1 mM EGTA, 20 mM dithiothreitol (DTT), 3 mg ml^{-1} glucose, 20 µg ml^{-1} catalase, 100 µg ml^{-1} glucose oxidase and 0.3% BSA) was added and allowed to incubate for 5 min. Subsequently the chamber was washed with TicTac buffer and prepared capped GDP microtubules (diluted in 1xBRB80) was added and allowed to incubate for 2 min, followed by extensive washing with TicTac buffer. ATP Buffer (10 mM HEPES buffer (pH 7.2), 56 mM PIPES buffer (pH 6.8), 50 mM KCl, 5 mM $MgCl_2$, 1 mM EGTA, 20 mM dithiothreitol (DTT), 3 mg ml^{-1} glucose, 20 µg ml^{-1} catalase, 100 µg ml^{-1} glucose oxidase, 0.3% BSA supplemented with 2.7 mM of ATP and 0.2% methyl cellulose) was then added to initiate motor activity. The chamber was sealed with Valap and immediately imaged. For control experiments, ATP was replaced with 2.7 mM of AMPPNP (Adenosine-5′-(β,γ-imido) triphosphate; A2647, Sigma-Aldrich) in the final buffer mix. For experiments with survival in the presence of free tubulin, 5 µM tubulin (100% unlabeled) was added to the ATP buffer. For gliding assays in the presence of HEK293 cell lysate, 20 µg ml^{-1} of cell lysate was added in the ATP buffer (all other steps were kept the same).

Microtubule buckling assay:

To achieve microtubule buckling, the flow chamber was first perfused with 100 µg ml^{-1} of streptavidin (diluted in 1x HKEM, Invitrogen, 434301) prior to the anti-GFP-antibody step. Capped GDP microtubules made from biotinylated seeds were used (all other steps were kept the same). All other steps were the same as the microtubule gliding assay described above. For buckling assays in the presence of HEK293 cell lysate, 20 µg ml^{-1} of cell lysate was added in the ATP buffer.

Incorporation in microtubule gliding and buckling assays:

To visualize self-repair (incorporation of free tubulin dimers) in buckling and gliding microtubules, an additional coating step (TicTac buffer supplemented with 2 µM unlabeled tubulin) was performed prior to addition of prepared GDP microtubules as free green tubulin dimers tend to attach to the layer of motors during the assay, effectively hindering the detection of the incorporated dimers [9]. To visualize self-repair, gliding and buckling microtubules were exposed to ATP buffer supplemented with 5 µM tubulin (100% labeled) and allowed to glide/buckle at 37°C for 15 min. Following incubation, the chamber was perfused with ATP buffer containing 2 µM unlabeled tubulin (to stabilize microtubules for imaging), sealed with Valap before imaging.

Single molecule photobleaching experiments to determine kinesin surface density:

Single molecule photobleaching (SMPB) was performed according to the protocol described previously in [63]. Briefly, a 1µM dilution of Kinesin-1- GFP in cold 1xHKEM was centrifuged to remove aggregates (15 min, 4°C, 215,000x g in a Type 70 Ti rotor [Beckman Optima XPN80]) prior to the assay. In a 20µl flow chamber made from Hellmanex sonicated cover-glasses, 20 µl of 0.2 mg ml^{-1} solution of Anti-GFP antibody was flushed in and incubated for 3 min. This was followed by a 1xHKEM wash step and then a 350 pM solution of Kinesin-1-GFP (further diluted in 1xHKEM) was added and incubated for 5 min. The chamber was then washed with 300 µl of 1xHKEM to remove unbound Kinesin-1 molecules and sealed using Valap. Photobleaching was achieved at 130 mW laser power with 500 ms exposure time (for 5 min) in continuous streaming mode using a 100x Olympus objective on an orbital TIRF Nikon Ti2e microscope. Recorded time-lapses were cropped and regions of interest (ROIs) with uniform illumination were chosen for analysis. Using Stowers Institute Fiji plugin, the fluorescent intensity traces of individual Kinesin-1-GFP molecules (represented in cerulean blue in **Suppl Fig. 5a(i)**) were obtained. From the step-like traces (refer **Suppl Fig. 5a(ii)**), we quantified the average fluorescent intensity of one Kinesin-1 molecule. To quantify the surface density of Kinesin-1 (refer **Suppl Fig. 5b**) at our working concentration of 416 nM, we repeated the above assay with 416 nM of kinesin-1-GFP and captured images using the same imaging conditions (65% Laser power with 500 ms exposure time, same camera gain and binning settings as above). ROIs with uniform illumination were chosen for analysis and average intensity of fluorescent Kinesin-1 at 416 nM was estimated. The experiment was performed on the same day and using the same imaging settings as the SMPB assay. The surface density (No: of Kinesins/μm^2) was estimated by dividing the average intensity of 416 nM Kinesin/ [(Average intensity of one Kinesin-1 molecule) * $(\text{Pixel size})^2$].

Single-Molecule motility experiments to estimate kinesin motility parameters:

For single molecule experiments to estimate motility parameters of Kinesin-1-GFP molecules (represented in cerulean blue in **Suppl Fig. 5**), an orbital TIRF microscope was used. Prior to the assay, a 1 µM dilution of Kinesin-1-GFP in cold 1xHKEM was centrifuged to remove aggregates (15 min, 4°C, 215,000x g). In a 20 µl flow chamber made from PEGylated cover-glasses, 20 µl of streptavidin (50 µg ml^{-1} in 1xHKEM; Fisher Scientific) was flushed in and allowed to incubate for 1 min. Following a wash step with 1xHKEM, prepared capped GDP microtubules with biotinylated seeds and caps (diluted in 1xBRB80) were flushed in and incubated for 5 min before extensive washing with 1xHKEM. Subsequently, motility buffer containing 500 pM Kinesin-1-GFP in TicTac buffer (containing the oxygen scavenger solutions to minimize bleaching of fluorophores) was flushed in. One still image of the microtubule was acquired. Motile kinesin-1 single molecules were captured in continuous streaming mode in the GFP channel (using the same image conditions as in the SMPB assay). The time-lapses were processed in Fiji and kymographs (Refer **Suppl Fig. 5c**) were generated using the KymoResliceWide plugin. Tracking the traces of kinesin-1-GFP molecules from kymographs from 50 frames with a temporal cutoff of 500 ms, distributions of the run length (distance traveled by an individual kinesin-1 molecule on a microtubule), dwell time (total residence time of individual kinesin-1 molecule on a microtubule), mean velocity and detachment rate of kinesin-1 molecules were estimated (**Suppl Fig. 5d-g)**.

Imaging:

63x oil immersion objective (Zeiss, Plan-Apochromat 63x/ NA= 1.40 oil DIC M27) of a Zeiss LSM 900 confocal microscope with an Axiocam 705 Mono camera (Zeiss) and Laser module 5 URGB (with laser lines 405, 488, 561 and 640 nm) was used for imaging. The microscope stage was kept at 37°C by means of a warm stage controller (Insert-P, PeCon). The temperature on the microscope stage was controlled with the incubator (PeCon) kept at 37°C. Time-lapses were recorded using ZenBlue software (version 3.2, Zeiss). Images were acquired of simultaneously of both 488 (using 0.08 mW laser power) and 565 (using 0.12 mW laser power) channels with a frame interval of 600 ms. Single-molecule experiments were performed on an objective-based orbital TIRF microscope (Nikon Ti2 Eclipse, modified by ViSitron Systems) equipped with an EMCCD Camera (Andor iXon Life) and Visitron Orbital 600 module with VS Laser Merge system with 4 laser lines (405, 488, 561 and 640). A 100x Olympus UPlanApo TIRF objective (100x/1.5 oil, correction collar set to 0.17 mm to match cover-glass thickness) was used for single-molecule experiments. Images were acquired of the 488-channel using 130 mW laser power and 500 ms exposure in continuous streaming mode for both photobleaching and single molecule motility experiments. The microscope stage was maintained at 37°C using a warm stage controller (OkoLabs). Time-lapses were recorded using VisiView software (version 6.0). Microtubule thermal fluctuations time-lapses were imaged using the 60x Oil immersion objective (NA = 1.42; correction collar set to 0.17 mm to match cover-glass thickness) of a Nikon Ti2E Epifluorescence microscope equipped with Lumencor Spectra III light engine, with solid -state illumination (380-750 nm). Images were acquired of the 565-LED using 10 mW laser power, 300 ms exposure with a frame interval of 10 s. Time lapses were recorded using NIS elements AR software (Nikon).

Image processing and quantification of incorporation stretches:

Videos were processed to improve the signal/noise ratio (subtract background and smooth functions of Fiji, version 1.53t) [64]. Self-repair events or incorporations were estimated from overlaid images (average of 3 frames) from time-lapses taken every 2 s. Incorporation stretches were identified from line scans (green fluorescence) along the magenta GDP microtubule lattice. A stretch of green fluorescence along the microtubule (in magenta as indicated in **Fig. 1c**) was regarded as an incorporation if it displayed a fluorescence intensity higher than 1.5 times that of the background as well as followed the lateral fluctuations of the microtubule. A decrease in the normalized intensity of the microtubule lattice is often observed at incorporation sites indicating self-repair (See **Suppl. Fig. 4).** The full-width-half-maximum (FWHM) distance from the intensity profile of the incorporation stretch was taken as the incorporation length. Accounting for the resolution limit of the microscope, incorporation stretches spanning less than 250 nm were disregarded from analysis.

For data on microtubule self-repair in cells, images of a microinjected cell were first divided into 4-5 ROIs (regions of interest, as indicated in **Fig. 1g** with a box with a red outline) and sections of microtubules (indicated with boxes with white outline in **Fig. 1g**) were analyzed. Incorporations found on bundled microtubules and at microtubule crossover sites (and up to 0.8 µm away from crossover sites) were disregarded from analysis. As mentioned in [29], longer incorporation stretches were found in microtubules located close to the microinjection sites owing to possible damage from microinjection. Hence, only microtubule sections found 10 µm or more from the microinjection site were considered for analysis.

Curvature analysis:

Images of both straight and bent microtubules were tracked using the Fiji plugin Jfilament2D [65] and the curvature of microtubules were estimated using a custom-made python script (see **Suppl Fig. 2** for analysis workflow). The obtained curve from JFilament2D was first smoothed by a parametric spline interpolation to remove noise. Then, the Menger curvature was calculated using three points spaced 120 nm apart. Curved microtubules displaying a maximum local curvature of 0.15 μm^{-1} or above were considered as bent. Bent zones of bent microtubules refer to sections of the bent microtubule with a mean local curvature above 0.2 μm^{-1}. Mean curvature over the entire microtubule was estimated by averaging the local curvature of all segments of the traced microtubule. Curvature at point of breakage of breaking buckling microtubules was estimated by taking an average of the local curvature of all segments in the region spanning 500 nm around the point of breakage.

Estimation of the microtubule persistence length:

Microtubule persistence length was estimated by analyzing thermal fluctuation of microtubules. For this, microtubules were elongated from biotin-containing microtubule seeds (attached to a streptavidin coated SiPEG-biotin cover-glass) using elongation buffer supplemented with 1 mM GTP and 11 µM tubulin for 15 min at 37°C. Following this the elongated microtubules were capped by flushing in a solution of elongation buffer supplemented with 0.5 mM GMPCPP and 2.5 µM tubulin and allowed to incubate at 37°C for 5 min. After washing with imaging buffer, the chamber was sealed, and microtubules were imaged every 10 s for 40 min. Persistence length was estimated by following the method reported in [25]. The filament coordinates were obtained by automatized tracing using T-SOAX software [66]. Analysis of these coordinates (calculation of tangent angles, cosine modes and fitting) was carried out via a custom-written python code (Refer **Rig. 7f** and **Suppl Fig. 5i**). For experiments with HEK293 lysate, 20 µgml^{-1} of cell lysate was flushed in with the imaging buffer prior to sealing of chamber and imaging.

Quantification of lateral tubulin incorporation and % of tubulin turnover:

The % tubulin turnover) across all conditions was estimated from quantifications of the lateral spread (across protofilaments) as well as longitudinal spread (along the microtubule lattice length, defined as incorporation length/microtubule length) of each incorporation event. The no: of protofilaments replaced was estimated from quantifications of the amount of lateral tubulin incorporation. The amount of lateral tubulin incorporation in incorporated stretches in all datasets was estimated by using stretches of microtubule elongation (stretches of 100% green-labeled tubulin that we occasionally observed beyond the cap- Refer **Fig. 1j, top, Suppl. Fig.1e**) as a reference stretch that we assumed to possess a 13-protofilament structure. The integrated fluorescence intensity of the incorporation, elongation stretch as well as the background was estimated using Fiji. The integrated elongation intensity ($I_{elongation}$) and incorporation intensity (I_{inc}) was obtained after subtracting the background intensity. As described in [5] [8], using the estimates of the incorporation length (FWHM), the integrated (I_{total}) fluorescence intensity of the elongation stretch, length of the tubulin dimer (L= 8 nm), we estimated the fluorescence intensity of a single tubulin dimer as (I_{dimer}) as $I_{dimer}=I_{elongation}*L/(FWHM*13)$. From the integral fluorescence intensity (I_{inc}) of the incorporation, we estimated the number of incorporated dimers as $N_{inc}=I_{inc}/I_{dimer}$. The values of N_{inc} from five frames per incorporation stretch were averaged to obtain the amount of lateral tubulin incorporation per incorporation in each condition. The no: of protofilaments replaced was calculated as N_{PF}= (% of lateral tubulin incorporation) *13. (Finally, tubulin turnover % was computed by multiplying the mean value of the incorporation length/microtubule length (estimate of the lattice length replaced) with the average amount of lateral incorporation for each condition.

Categorization of different microtubule bending events in cells:

Time-lapses of dynamic microtubules in live PtK2 cells were analyzed for quantification of microtubule bending events in cells. The bending events in cells were classified in to 'Bent persisting', 'Buckling', 'Looping' and 'Breakage' events (See **Suppl Fig. 3a**). A microtubule was considered to persist in the bent form without relative change in its curvature (less than 0.1-0.15 µm^{-1}) (like in **Fig 2b(i)**) for the period of observation (5 min). Microtubules showing dynamic change in curvature (See **Fig. 2a, 2b(ii)**) were classified as buckling. Buckling microtubules that were seen to adopt a loop-like conformation were categorized as looping microtubules. We also observed relatively rare instances of microtubule breakage following bending/buckling (like in **Fig. 2b (iii)** and **Suppl Fig. 3b**). A total of 4 cells from two independent experiments were analyzed.

Microtubule survival:

For microtubule survival experiments, time-lapses were recorded for 40 min with a frame interval of 10 seconds. The % microtubule population remaining was estimated by manually counting the no: of microtubules in each frame within the same field-of-view every 2 min.

Estimation of kinesin motility parameters:

Gliding velocity of microtubules both in the presence and absence of HEK293 cell lysate was estimated by tracking the movement of a gliding microtubule in 10 consecutive frames using MTrackJ Fiji plugin.

Kinesin motility parameters were estimated from kymographs generated from traces using the KymoResliceWide plugin.

Statistical analysis:

Statistical analysis was performed using GraphPad Prism software (version 9.5). To test the significance in the case of incorporation lengths and amount of lateral tubulin incorporation, Mann-Whitney test (two-tailed) was used as a non-parametric alternative to a t-test, as the distributions are non-Gaussian in nature. For comparisons of incorporation frequency, incorporation length/microtubule length, unpaired-t-test was used as the distributions have similar variances and are Gaussian in nature.

References:

[1] M. F. Carlier , "Guanosine-5'-triphosphate hydrolysis and tubulin polymerization. Review article.," *Molecular and cellular biochemistry,* vol. 47, no. 2, pp. 97-113, 1982.

[2] T. Mitchison and M. Kirschner, "Dynamic instability of microtubule growth.," *Nature,* vol. 312 (5991), pp. 237-242, 1984.

[3] D. K. Fygenson, E. Braun and A. Libchaber, "Phase diagram of microtubules. Physical review.," *E, Statistical physics, plasmas, fluids, and related interdisciplinary topics,* vol. 50, no. 2, p. 1579–1588, 1994.

[4] A. T. Molines, C. H. Edrington, S. C. Tetlalmatzi, F. Chang and G. J. Brouhard, "Microtubule dynamic instability is sensitive to specific biological viscogens in vitro," *bioRxiv,* vol. https://doi.org/10.1101/2024.05.27.596091, 2024.

[5] L. Schaedel, S. Triclin, D. Chrétien, A. Abrieu, C. Aumeier, J. Gaillard, L. Blanchoin, M. Théry and K. John, "Lattice defects induce microtubule self-renewal," *Nature Physics,* vol. 15, pp. 830-838, 2019.

[6] L. Schaedel, K. John, J. Gaillard, M. V. Nachury, L. Blanchoin and M. Théry, "Microtubules self-repair in response to mechanical stress," *Nature Materials,* vol. 14, pp. 1156-1163, 2015.

[7] A. Vemu, E. Szczesna, E. A. Zehr, J. O. Spector, N. Grigorieff, A. M. Deaconescu and A. Roll-Mecak, "Severing enzymes amplify microtubule arrays through lattice GTP-tubulin incorporation," *Science,* vol. 361, p. eaau1504, 2018.

[8] S. Biswas, R. Grover, C. Reuther, C. S. Poojari, R. Shaebani, S. Nandakumar, M. Grünewald, A. Zablotsky, J. S. Hub, S. Diez, K. John and L. Schaedel, "Tau accelerates tubulin exchange in the microtubule lattice," *Nature Physics,* pp. https://doi.org/10.1038/s41567-025-03003-7, 2025.

[9] S. Triclin, D. Inoue, J. Gaillard, Z. M. Htet, M. E. DeSantis, D. Portran, E. Derivery, C. Aumeier, L. Schaedel, K. John, C. Leterrier, S. L. Reck-Peterson, L. Blanchoin and M. Théry, "Self-repair protects microtubules from destruction by molecular motors," *Nature Materials,* vol. 20, pp. 883-891, 2021.

[10] B. G. Budaitis, S. Badieyan, Y. Yue, T. L. Blasius, D. N. Reinemann, M. J. Lang, M. A. Cianfrocco and K. J. Verhey, "A kinesin-1 variant reveals motor-induced microtubule damage in cells," *Current Biology,* vol. 32, pp. 2416-2429, 2022.

[11] M. Andreu-Carbó, S. Fernandes, M.-C. Velluz, K. Kruse and C. Aumeier, "Motor usage imprints microtubule stability along the shaft," *Developmental Cell,* vol. 57, pp. 5-18, 2022.

[12] A. Aher, D. Rai, L. Schaedel, J. Gaillard, K. John, Q. Liu, M. Altelaar, L. Blanchoin, M. Théry and A. Akhmanova, "CLASP mediates microtubule repair by restricting lattice damage and regulating tubulin incorporation," *Current Biology,* vol. 30, pp. 2175-2183, 2020.

[13] H. de Forges, A. Pilon, I. Cantaloube, A. Pallandre, A.-M. Haghiri-Gosnet, F. Perez and C. Poüs, "Localized mechanical stress promotes microtubule rescue," *Current Biology,* vol. 26, pp. 3399-3406, 2016.

[14] M. Théry and L. Blanchoin, "Microtubule self-repair," *Current Opinion in Cell Biology,* vol. 68, pp. 144-154, 2021.

[15] M. Romeiro Motta, S. Biswas and L. Schaedel, "Beyond uniformity: exploring the heterogeneous and dynamic nature of the microtubule lattice," *European Journal of Cell Biology,* vol. 102, p. 151370, 2023.

[16] C. M. Waterman-Storer and E. D. Salmon, "Actomyosin-based Retrograde Flow of Microtubules in the Lamella of Migrating Epithelial Cells Influences Microtubule Dynamic Instability and Turnover and Is Associated with Microtubule Breakage and Treadmilling," *J Cell Bio,* vol. 139, no. 2, pp. 417-434, 1997.

[17] A. D. Bicek , E. Tüzel, A. Demtchouk , M. Uppalapati, W. O. Hancock, D. M. Kroll and D. J. Odde, "Anterograde Microtubule Transport Drives Microtubule Bending in LLC-PK1 Epithelial Cells," *Molecular biology of the cell,* vol. 20, no. 12, p. 2943–2953, 2009.

[18] C. Brangwynne, F. MacKintosh and D. Weitz, "Force fluctuations and polymerization dynamics of intracellular microtubules," *Proc. Natl. Acad. Sci. U.S.A.,* vol. 104, no. 41, pp. 16128-16133, 2007.

[19] C. Pallavicini, A. Monastra, . N. G. Bardeci , D. Wetzler, V. Levi and L. Bruno, "Characterization of microtubule buckling in living cells," *European biophysics journal ,* vol. 46, no. 6, p. 581–594, 2017.

[20] I. A. Kent, P. S. Rane, . R. B. Dickinson, A. J. C. Ladd and T. P. Lele , "Transient Pinning and Pulling: A Mechanism for Bending Microtubules," *PloS one,* vol. 11, no. 3, p. e0151322, 2016.

[21] N. Shekhar, S. Neelam, J. Wu, A. J. Ladd, R. B. Dickinson and T. P. Lele, "Fluctuating Motor Forces Bend Growing Microtubules," *Cellular and molecular bioengineering,* vol. 6, no. 2, pp. 120-129, 2013.

[22] J. Wu, G. Misra, R. J. Russell, A. J. C. Ladd, T. P. Lele and R. B. Dickinson, "Effects of dynein on microtubule mechanics and centrosome positioning," *Molecular biology of the cell,* vol. 22, no. 24, p. 4834–4841, 2011.

[23] A. Blob , . D. Ventzke, U. Rölleke, . G. Nies, A. Munk, L. Schaedel and S. Köster, "Global alignment and local curvature of microtubules in mouse fibroblasts are robust against perturbations of vimentin and actin," *Soft Matter,* vol. 21, no. 4, pp. 641-651, 2025.

[24] A. Straube, . G. Hause, . G. Fink and G. Steinberg, "Conventional Kinesin Mediates Microtubule-Microtubule Interactions In Vivo," *Mol Biol Cell,* vol. 17, no. 2, pp. 907-916, 2006.

[25] F. Gittes, B. Mickey, J. Nettleton and J. Howard, "Flexural rigidity of microtubules and actin filaments measured from thermal fluctuations in shape," *Journal of Cell Biology,* pp. 923-934, 1993.

[26] C. P. Brangwynne, G. H. Koenderink, F. C. MacKintosh and D. A. Weitz, "Nonequilibrium microtubule fluctuations in a model cytoskeleton," *Physical Review Letters,* p. 118104, 2008.

[27] D. J. Odde, L. Ma, A. H. Briggs, A. DeMarco and M. W. Kirschner, "Microtubule bending and breaking in living fibroblast cells," *Journal of Cell Science,* pp. 3283-3288, 1999.

[28] J. Wu, R. B. Dickinson and T. P. Lele, "Investigation of in vivo microtubule and stress fiber mechanics with laser ablation," *Integrative Biology,* pp. 471-479, 2012.

[29] M. Gazzola, A. Schaeffer, C. Butler-Hallissey, K. Friedl, B. Vianay, J. Gaillard, C. Leterrier, L. Blanchoin and M. Théry, "Microtubules self-repair in living cells," *Current Biology,* pp. 122-133, 2023.

[30] P. Robison, M. A. Caporizzo, H. Ahmadzadeh, A. I. Bogush, C. Y. Chen, K. B. Margulies, V. B. Shenoy and B. L. Prosser, "Detyrosinated microtubules buckle and bear load in contracting cardiomyocytes," *Science,* vol. 352, no. 6284, p. aaf0659 , 2017.

[31] P. Rauch, P. Heine, B. Goettgens and J. Käs, "Forces from the rear: deformed microtubules in neuronal growth cones influence retrograde flow and advancement," *New J Phys ,* vol. 15, no. 015007 , 2013.

[32] S. A. Yadav, D. Khatri, A. Soni, N. Khetan and C. A. Athale, "Wave-like oscillations of clamped microtubules driven by collective dynein transport," *Biophysical Journal,* vol. 123, pp. 509-524, 2024.

[33] F. Gittes, E. Meyhöfer, S. Baek and J. Howard, "Directional loading of the kinesin motor molecule as it buckles a microtubule.," *Biophysical journal,* vol. 70, no. 1, pp. 418-429, 1996.

[34] A. Vilfan , S. Subramani, . E. Bodenschatz, . R. Golestanian and I. Guido , "Flagella-like Beating of a Single Microtubule," *Nano Lett,* vol. 19, no. 5, pp. 3359-3363, 2019.

[35] E. L. Dumont , C. Do and H. Hess, "Molecular wear of microtubules propelled by surface-adhered kinesins," *Nature nanotechnology,* vol. 10, no. 2, p. 166–169. doi:10.1038/nnano.2014.334, 2015.

[36] V. VanDelinder, P. G. Adams and G. D. Bachand , "Mechanical splitting of microtubules into protofilament bundles by surface-bound kinesin-1," *Scientific reports,* vol. 6, p. 39408. doi: 10.1038/srep39408, 2016.

[37] R. B. Dye, P. F. Flicker, D. Y. Lien and R. C. Williams Jr, "End-stabilized microtubules observed in vitro: Stability, subunit interchange, and breakage," *Cell motility and the cytoskeleton,* vol. 21, no. 3, p. 171–186, 1992.

[38] S. Tsitkov, J. Rodriguez, N. M. Bassir Kazeruni, M. Sweet, T. Nitta and H. Hess, "The rate of microtubule breaking increases exponentially with curvature," *Scientific Reports,* vol. 12, pp. https://doi.org/10.1038/s41598-022-24912-0, 2022.

[39] S. R. Nasrin, N. M. Bassir Kazeruni, J. B. Rodriguez 3rd, S. Tsitkov, A. Kakugo and H. Hess, "Mechanical fatigue in microtubules," *Sci Rep,* vol. 14, no. 1, 2024.

[40] A. M. R. Kabir, D. Inoue, T. Afrin, H. Mayama, K. Sada and A. Kakugo , "Buckling of Microtubules on a 2D Elastic Medium," *Scientific Reports,* vol. 5, no. 17222, 2015.

[41] A. G. Hendricks, E. L. F. Holzbaur and Y. E. Goldman, "Force measurements on cargoes in living cells reveal collective dynamics of microtubule motors," *Proceedings of the National Academy of Sciences of the United States of America,* vol. 109, no. 45, p. 18447–18452, 2012.

[42] C. Leduc, O. Campàs, K. B. Zeldovich, A. Roux, P. Jolimaitre, L. Bourel-Bonnet, B. Goud, J.-F. Joanny, P. Bassereau and J. Prost, "Cooperative extraction of membrane nanotubes by molecular motors," *PNAS,* vol. 101, no. 49, pp. 17096-17101, 2004.

[43] L. D. Landau and E. M. Lifshitz, Theory of Elasticity. Course of Theoretical Physics, New York: Pergamon Press, 1986.

[44] R. J. Ju, A. D. Falconer, C. J. Schmidt, M. A. E. Martinez, K. M. Dean, R. P. Fiolka, D. P. Sester, M. Nobis, P. Timpson, A. J. Lomakin, G. Danuser, M. D. White and N. K. Haass, "Compression-dependent microtubule reinforcement enables cells to navigate confined environments," *Nature Cell Biology,* vol. 26, no. 9, pp. 1520-1534, 2024.

[45] R. C. Eng, . R. Schneider, T. W. Matz, R. Carter, D. W. Ehrhardt, H. Jönsson, Z. Nikoloski and A. Sampathkumar, "KATANIN and CLASP function at different spatial scales to mediate microtubule response to mechanical stress in Arabidopsis cotyledons," *Current Biology,* vol. 31, no. 15, pp. 3262-3274, 2021.

[46] Y. Li, O. Kučera, D. Cuvelier, D. m. Rutkowski, M. Deygas, D. Rai, T. Pavlovič, F. N. Vicente, M. Piel, G. Giannone, D. Vavylonis, A. Akhmanova, L. Blanchoin and M. Théry, "Compressive forces stabilize microtubules in living cells.," *Nature materials,* vol. 22, no. 7, pp. 913-924, 2023.

[47] I. A. Telley, P. Bieling and T. Surrey, "Obstacles on the microtubule reduce the processivity of Kinesin-1 in a minimal in vitro system and in cell extract," *Biophysical journal,* vol. 96, no. 8, p. 3341–3353, 2009.

[48] S. Korten, . N. Albet-Torres, . F. Paderi, L. t. Siethoff, S. Diez, T. Korten, . G. t. Kronnie and A. Månsson, "Sample solution constraints on motor-driven diagnostic nanodevices," *Lab Chip ,* vol. 13, no. 5, pp. 866-876, 2013.

[49] G. Hiller and K. Weber, "Radioimmunoassay for tubulin: a quantitative comparison of the tubulin content of different established tissue culture cells and tissues," *Cell,* vol. 14, no. 4, pp. 795-804 , 1978.

[50] P. J. Anderson, "The structure and amount of tubulin in cells and tissues," *The Journal of biological chemistry ,* vol. 254, no. 7, pp. 2168-2171 , 1979 .

[51] Y.-W. Kuo, M. Mahamdeh, Y. Tuna and J. Howard, "The force required to remove tubulin from the microtubule lattice by pulling on its α-tubulin C-terminal tail," *Nat Commun,* vol. 13, no. 3651, pp. https://doi.org/10.1038/s41467-022-31069-x, 2022.

[52] Q. Geng, A. Bonilla, S. N. Sandwith and K. J. Verhey, "Multi-kinesin clusters impart mechanical stress that reveals mechanisms of microtubule breakage in cells," *J Cell Biol.,* vol. 224, no. 10, p. e202501070. doi: 10.1083/jcb.202501070, 2025.

[53] S. Chakraborty, J. Mahamid and W. Baumeister, "Cryoelectron Tomography Reveals Nanoscale Organization of the Cytoskeleton and Its Relation to Microtubule Curvature Inside Cells," *Structure,* vol. 28, no. 9, pp. 991-1003, 2020.

[54] C. Pallavicini , . V. Levi , . D. E. Wetzler , . J. F. Angiolini , . L. Benseñor, M. A. Despósito and . L. Bruno, "Lateral motion and bending of microtubules studied," *Biophysical journal,* vol. 106, no. 12, p. 2625–2635, 2014.

[55] D. Portran, M. Zoccoler, J. Gaillard, V. Stoppin-Mellet, . E. Neumann, I. Arnal, J. L. Martiel and M. Vantard, "MAP65/Ase1 promote microtubule flexibility," *Mol Biol Cell,* vol. 24, no. 12, pp. 1964-73, 2013.

[56] T. Sasaki , . K. Saito, D. Inoue, . H. Serk, . Y. Sugiyama, E. Pesquet, Y. Shimamoto and Y. Oda, "Confined-microtubule assembly shapes three-dimensional cell wall structures in xylem vessels," *Nature Communications,* vol. 14, no. 1, p. 6987, 2023.

[57] D. Portran, L. Schaedel, Z. Xu, M. Théry and M. V. Nachury, "Tubulin acetylation protects long-lived microtubules against mechanical aging," *Nature Cell Biology,* vol. 19, no. 4, pp. 391-398, 2017.

[58] A. Szyk , A. M. Deaconescu, J. Spector, B. Goodman, M. L. Valenstein , N. E. Ziolkowska, V. Kormendi, N. Grigorieff and A. Roll-Mecak, "Molecular basis for age-dependent microtubule acetylation by tubulin acetyltransferase," *Cell,* vol. 157, no. 6, p. 1405–1415, 2014.

[59] O. Hamant, D. Inoue, D. Bouchez, J. Dumais and E. Mjolsness, "Are microtubules tension sensors?," *Nature communications,* vol. 10, no. 1, p. 2360, 2019.

[60] A. Hyman, D. Drechsel, D. Kellogg, S. Salser , K. Sawin , P. Steffen, L. Wordeman and T. Mitchison, "Preparation of modified tubulins," *Methods in enzymology,* vol. 196, pp. 478-485, 1991.

[61] C. Utzschneider, B. Suresh, A. Sciortino, J. Gaillard , A. Schaeffer, S. Pattanayak, J.-F. Joanny, L. Blanchoin and M. Théry, "Force balance of opposing diffusive motors generates polarity-sorted microtubule patterns," *Proceedings of the National Academy of Sciences of the United States of America,* vol. 121, no. 49, p. e2406985121. doi: 10.1073/pnas.2406985121, 2024.

[62] A. Jijumon, S. Bodakuntla , M. Genova, M. Bangera, V. Sackett, L. Besse, . F. Maksut, V. Henriot, M. M. Magiera, M. Sirajuddin and C. Janke, "Lysate-based pipeline to characterize microtubule-associated proteins uncovers unique microtubule behaviours," *Nature cell biology,* vol. 24, no. 2, pp. 253-267, 2022.

[63] V. Stoppin-Mellet, . N. Bagdadi, Y. Saoudi and . I. Arnal, "Studying Tau-Microtubule Interaction Using Single-Molecule TIRF Microscopy," in *Cytoskeleton Dynamics, Methods in Molecular Biology,*, New York, Humana, 2020.

[64] J. Schindelin, I. Arganda-Carreras, E. Frise, V. Kaynig, M. Longair, T. Pietzsch, S. Preibisch, C. Rueden, S. Saalfeld, B. Schmid, J.-Y. Tinevez, D. J. White, V. Hartenstein and Eliceiri, "Fiji: an open-source platform for biological-image analysis," *Nature methods,* no. 9, pp. 676-682, 2012.

[65] M. B. Smith, H. Li, T. Shen, X. Huang, E. Yusuf and D. Vavylonis, "Segmentation and tracking of cytoskeletal filaments using open active contours," *Cytoskeleton,* vol. 67, no. 11, pp. 693-705, 2010.

[66] T. Xu, C. Langouras, M. A. Koudehi, B. E. Vos, N. Wang, G. H. Koenderink, X. Huang and D. Vavylonis, "Automated Tracking of Biopolymer Growth and Network Deformation with TSOAX," *Scientific Reports,* vol. 9, no. 1, p. 1717, 2019.

Contributing authors (alphabetical order):

Albrecht, Constantin Matteo
Bosche, Jonas
Diez, Stefan
Grünewald, Mona
König, Belinda
Nandakumar, Shweta
Santen, Ludger
Schaedel, Laura
Shaebani, Reza
Wieczorek, Mirko

LaS, RS, SD, LuS conceptualized and guided the project. LaS, SN, SD and MW designed the experiments. SN carried out the experiments and analysis. MG and BK purified the tubulin. MW assisted with image and curvature analysis. CMA assisted with cell lysate experiments and design of figure schematics. RS, LuS and JB designed, performed and analysed the simulations. LaS, SN and RS wrote the manuscript. All authors provided critical feedback.

Funding sources:

LuS, LaS, SD and RS were supported by the DFG grant SFB 1027. The work was financially supported by the European Research Council (ERC; grant no. StG 101115795 to LaS).

Acknowledgements:

The authors are thankful to Jérémie Gaillard and Laurent Blanchoin (Cytomorpho Lab, Grenoble) for sharing reagents and technical expertise. We are grateful to Morgan Gazzola and Manuel Théry (Cytomorpho Lab, IPGG, Paris) for sharing their previously published dataset on microtubule self-repair in cells. We thank Cordula Reuther and Rahul Grover (B-CUBE, TU Dresden) for sharing kinesin related expertise, Subham Biswas (Experimental Physics and Center for Biophysics, University of Saarland) for assistance with single molecule imaging and Karin John (LIPhy, Université Grenoble Alpes) for fruitful discussions.

Ethics declaration:

The authors declare no competing interests.

Data availability:

Curvature analysis code and source data underlying the main and supplementary figure plots will be made available in the Zenodo repository link: 10.5281/zenodo.16935847 upon publication. The custom simulation code is available upon reasonable request by contacting the corresponding authors.

Supplementary data table 1:

Parameter	Symbol	Value	Unit	Reference
Thermal persistence length	L_p	[1,10]	mm	This study (Suppl. Fig. 5i)
Default thermal persistence length	$L_{p,0}$	5	mm	This study (Suppl. Fig. 5i)
Microtubule length	L	[5,15]	μm	This study
Default microtubule length	L_0	10	μm	This study (Suppl. Fig. 5h)
Microtubule discrete units	ΔL	8	nm	[41],[42]
Hopping step size	d_h	8	nm	[41],[42]
Attachment rate	ω_a	[1,10]	s^{-1}	[42],[67],[68]
Default attachment rate	$\omega_{a,0}$	5	s^{-1}	[42],[67],[68]
Detachment rate	$\omega_{d,0}$	0.5	s^{-1}	This study (Suppl. Fig. 5g), [67], [68]
Hopping rate	$\omega_{h,0}$	81	s^{-1}	[67]
Motor density	ρ	[100,500]	μm^{-2}	This study
Default motor density	ρ_0	400	μm^{-2}	This study (Suppl. Fig. 5b)
Spring constant	k	0.0003	N/m	[69]
Detachment force	f_d	3	pN	[70],[71]
Attachment force	f_a	3	pN	[72],[73]
Motor stall force	f_s	6	pN	[74],[75]

Supplementary table 1: Parameters used in numerical simulations of microtubule deformation under active forces. For experimental data values obtained from experiments, please refer **Suppl. Fig. 5.**

Supplementary figure 1

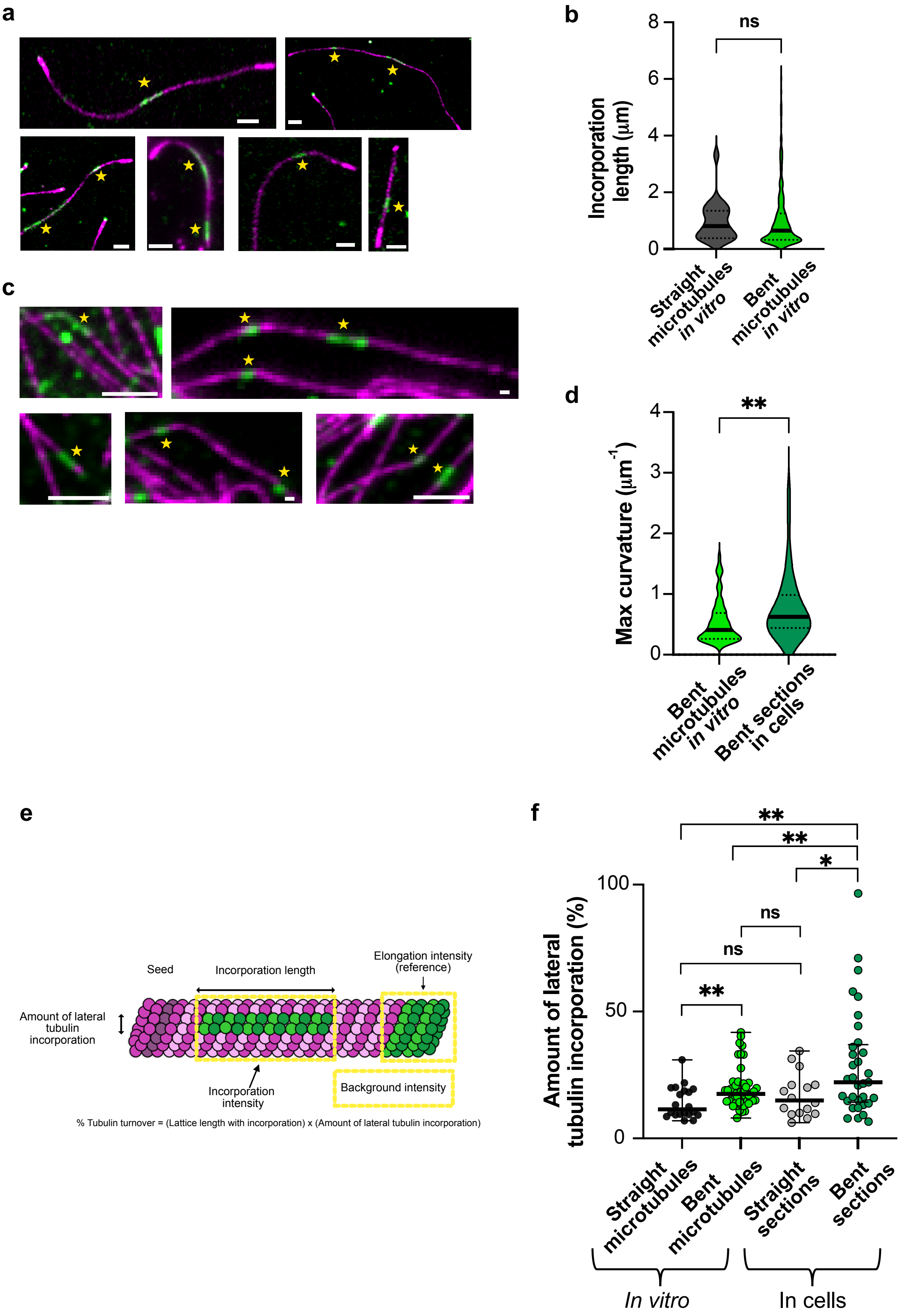

Supplementary Figure 1: a, Additional examples of incorporations (marked with a yellow star) in static straight and bent microtubules *in vitro* (scale bar: 2 μm) **b**, Comparison of incorporation length in static straight vs static bent microtubules *in vitro* (global). Black line represents the median and dotted lines, the interquartile range. p= 0.2905 (ns, not significant) using Mann-Whitney test. Total length of microtubule analyzed in both cases: 1,104 µm (n= 23 incorporations for straight microtubules and n= 263 incorporations for bent microtubules) **c**, Additional examples of incorporations (marked with a yellow star) in straight and bent sections in cells (scale bar: 2 µm) **d**, Comparison of curvature of static bent microtubules *in vitro* vs bent sections in cells. Black line represents the median and dotted lines, the interquartile range. p= 0.027 using an unpaired t-test (n= 127 *in vitro*; n= 36 in cells). **e,** Schematic showing the different parameters estimated to quantify the number of protofilaments and % tubulin turnover in a microtubule with incorporation (See **Methods). f,** Higher amount of lateral tubulin incorporation in bent microtubules, both in cells and *in vitro*. Three independent experiments were analyzed for each condition. n= 21 incorporations for straight microtubules (*in vitro)*, n= 51 incorporations for bent microtubules (*in vitro)*, n= 16 incorporations for straight sections (cells) and n= 32 incorporations for bent sections (cells). Black lines represent the median and error bars represent the interquartile range. Statistical test used: Mann-Whitney test. p= 0.0391 (straight sections, cells -bent sections, cells); p= 0.0024 (straight microtubules, *in vitro*-bent microtubules, *in vitro*); p= 0.0095 (bent sections, cells-bent microtubules, *in vitro*); p= 0.2411 (not significant; straight sections, cells-straight microtubules*, in vitro*); p= 0.2163 (not significant; straight sections, cells-bent microtubules, *in vitro*) and p= 0.2411 (not significant; straight sections, cells-straight microtubules, *in vitro*).

Supplementary figure 2

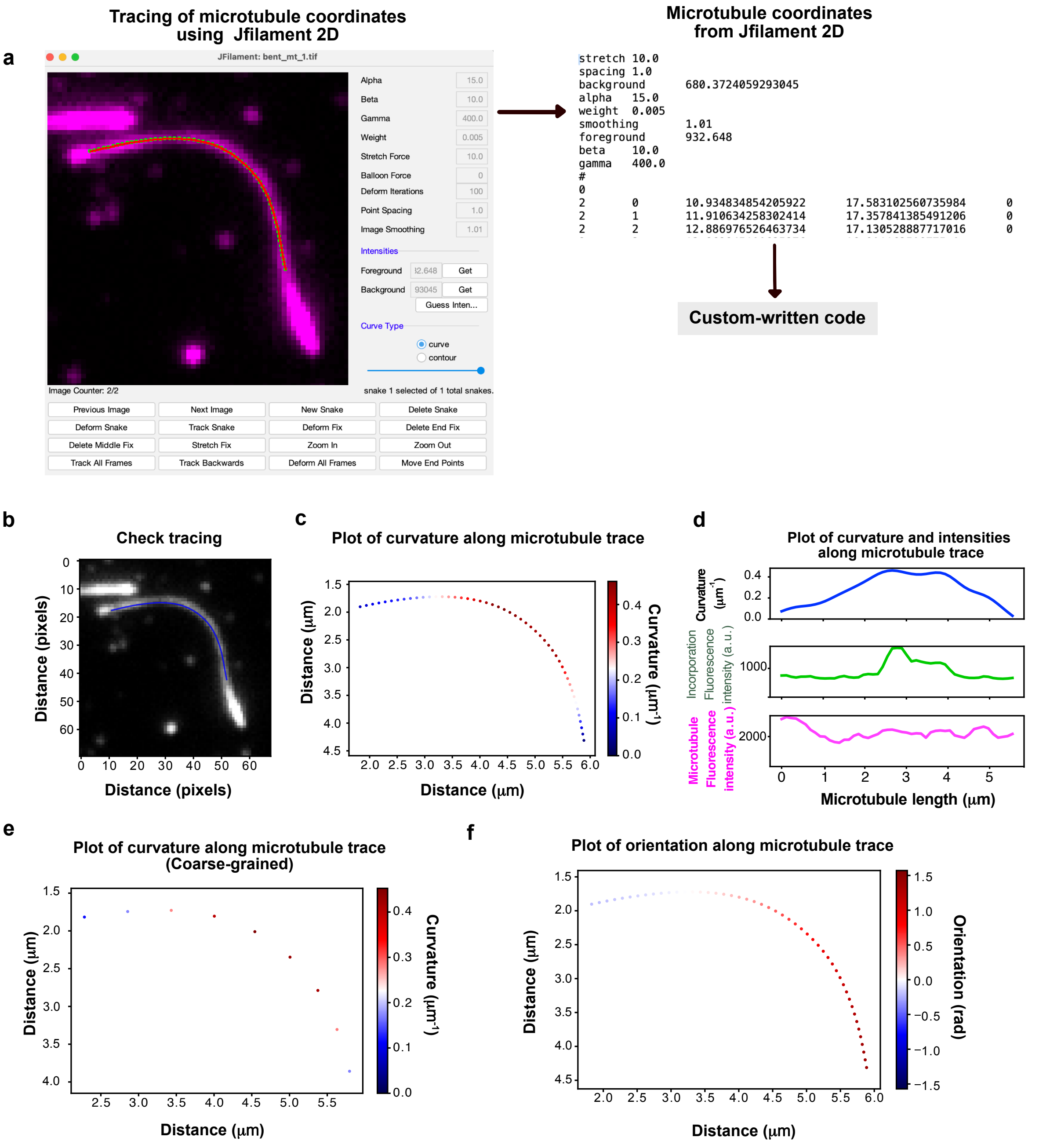

Tracing of microtubule coordinates using Jfilament 2D

JFilament: bent_mt_1.tif

Alpha 15.0
Beta 10.0
Gamma 400.0
Weight 0.005
Stretch Force 10.0
Balloon Force 0
Deform Iterations 100
Point Spacing 1.0
Image Smoothing 1.01

Intensities
Foreground 32.648
Background 93045

Curve Type
● curve
○ contour

Image Counter: 2/2

snake 1 selected of 1 total snakes.

Microtubule coordinates from Jfilament 2D

```
stretch 10.0
spacing 1.0
background      680.3724059293045
alpha   15.0
weight  0.005
smoothing       1.01
foreground      932.648
beta    10.0
gamma   400.0
#
0
2       0       10.934834854205922      17.583102560735984      0
2       1       11.910634258302414      17.357841385491206      0
2       2       12.886976526463734      17.130528887717016      0
```

Custom-written code

Supplementary Figure 2: Curvature analysis workflow. a, Microtubules were traced using the Fiji plugin JFilament 2D. The obtained coordinates were used to calculate the curvature and to plot the fluorescence intensities along the microtubule arclength using a custom-written code. **b,** *Output 1 from code:* Image of traced microtubule superimposed on the original microtubule image to check for accuracy of tracing. Checking the accuracy of tracing might be necessary if the obtained curve from JFilament 2D was additionally smoothed in the code. **c,** *Output 2 from code:* Plot of curvature (color-coded) along the traced microtubule **d,** *Output 3 from code:* Plot of curvature (μm^{-1}) and fluorescence intensities (a.u.) of both microtubule and incorporation channel along the microtubule length (μm). **e,** *Optional output 4 from code:* Plot of coarse-grained curvature (color-coded) along the microtubule segments. **f,** *Optional output 5 from code:* Plot of orientation (color-coded) along the traced microtubule. Microtubules showing a local curvature higher than 0.15 μm^{-1} were considered as bent.

Supplementary figure 3

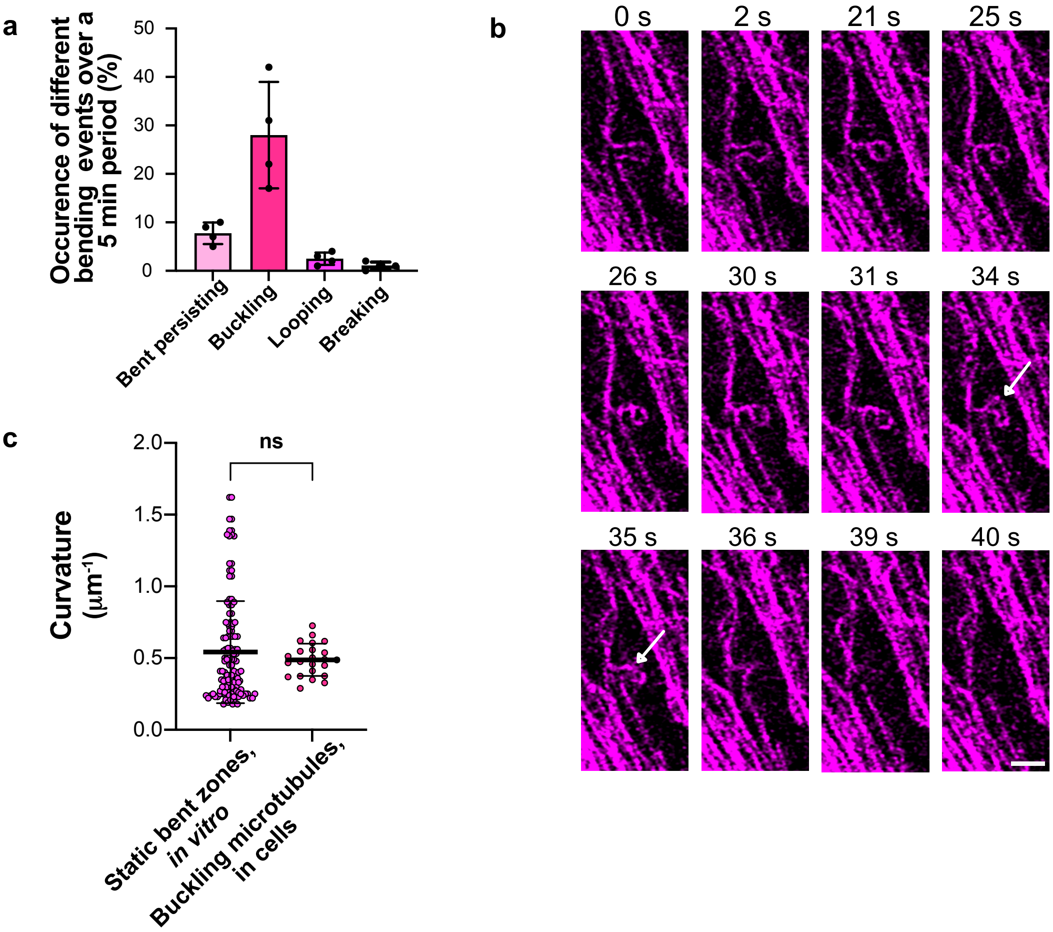

Supplementary Figure 3: a, *Quantification of different microtubule bending events* over a 5 min period in live PtK2 cells (with an endogenous tubulin-eGFP tag; represented in magenta). Error bars represent the S.D. Black dots represent individual cells. n= 4 cells analyzed from two independent experiments. **b,** Time-lapse sequence showing breakage at high curvatures (marked by white arrow) in a looping microtubule in a live PtK2 cell. Scale bar: 2 µm. **c,** Comparison of curvature between the bent zones of static bent microtubules (*in vitro* analyzed in **Fig 1d**) and buckling microtubules (in cells, analyzed in **Fig 2g**). Black line represents the mean and error bars represent the S.D. (n= 127 microtubules from static bent zones *in vitro* and n= 23 buckling microtubules, *in vitro* from three independent experiments). p= 0.4721 (not-significant; ns) using unpaired-t-test.

Supplementary figure 4

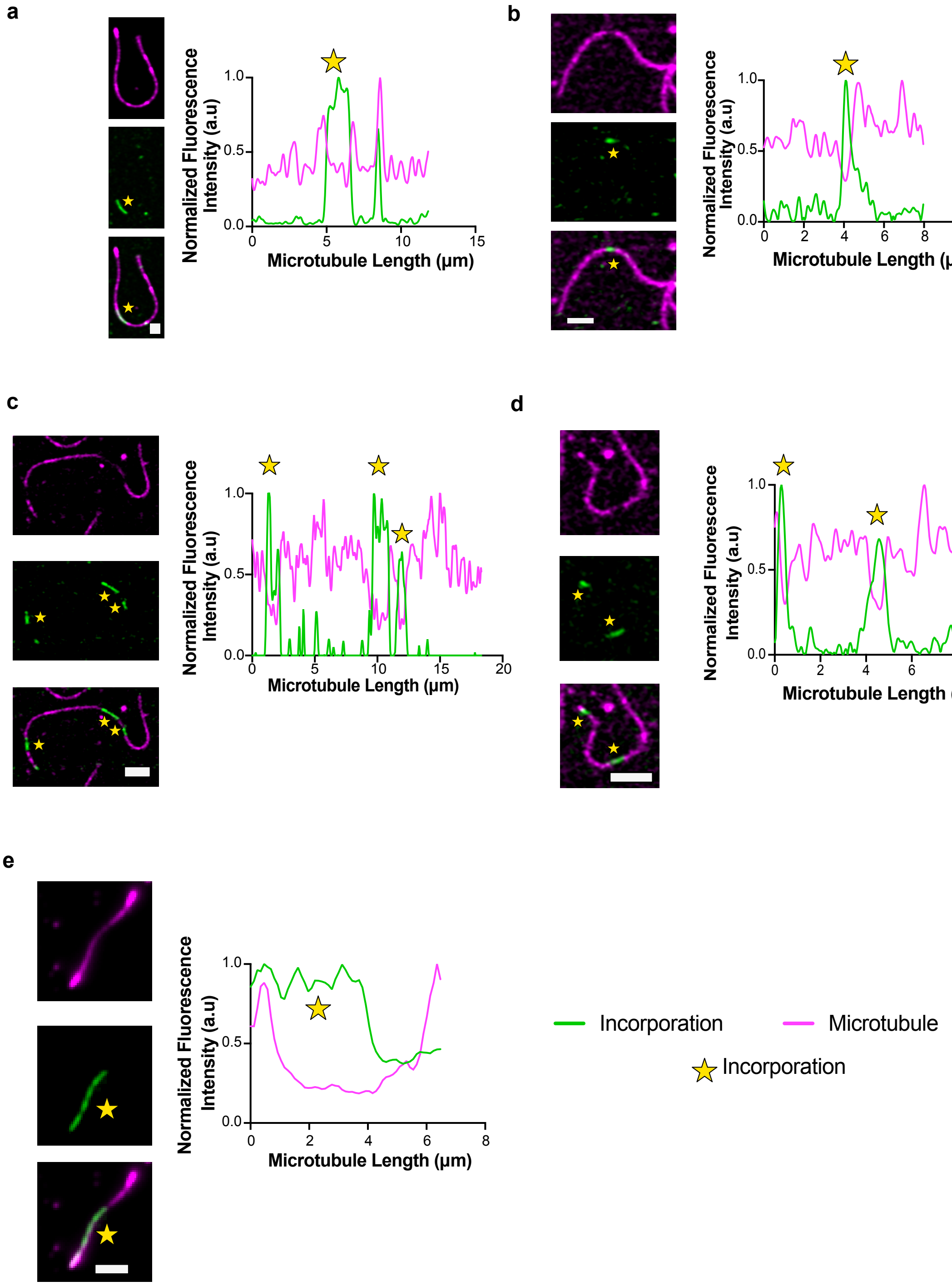

Supplementary Figure 4: a-e, Exemplary images with fluorescence intensity line scans of incorporations in buckling microtubules. We frequently observe a dip in the fluorescence intensity of the microtubule lattice (in magenta) at incorporation sites, indicating that a significant proportion of the lattice has been replaced. Scale bars: 2 µm.

Supplementary figure 5

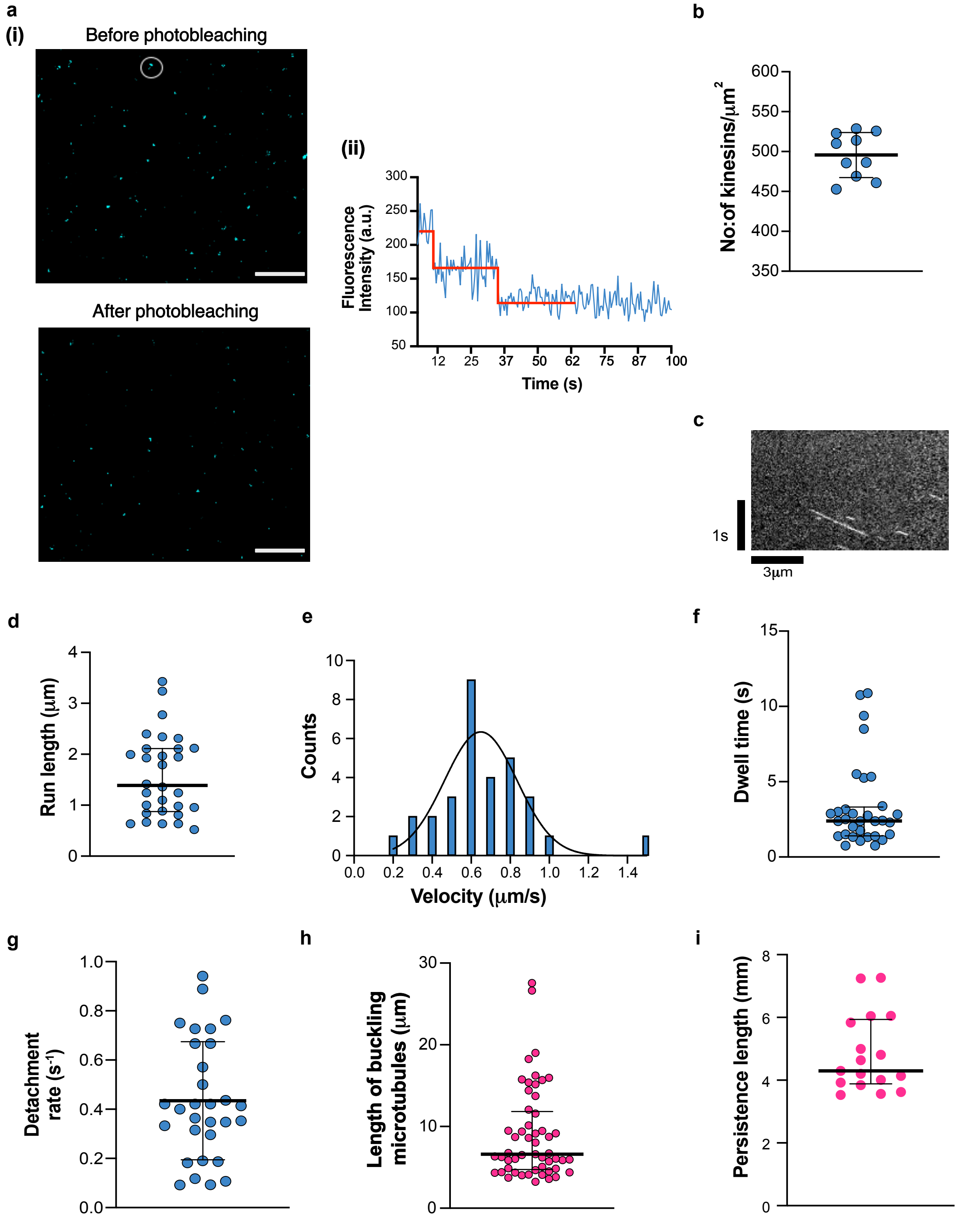

Supplementary Figure 5: *Data underlying experimental parameters for simulations: Single molecule photo-bleaching to estimate kinesin surface density:* **a,(i)** Example image of kinesin-1-GFP (represented in cerulean blue) molecules at 350 pM before and after photobleaching using a laser power of 130 mW in streaming mode, with 500 ms exposure time. White circle indicates a kinesin-1-GFP molecule that disappears over time due to photobleaching. Scale bar: 5 μm. **a,(ii)** Trace showing two-step photobleaching of the molecule circled in a(i). Red line is overlaid for better visualization of the two-step drop in fluorescence intensity **b,** Plot showing distribution of the surface density of kinesin-1 estimated from photobleaching experiments. Black line represents the mean and bars represent the S.D (n= 10 traces from 10 spots were analyzed from two independent experiments). *Single molecule motility studies to determine kinesin motility parameters:* **c,** Exemplary kymograph showing motile kinesin-1 molecules. **d,** Distribution of run length of kinesin-1 molecules. Black lines represent the median and the bars represent the interquartile range. **e**, Distribution of the velocities of kinesin-1 molecules. **f**, Distribution of dwell time of kinesin-1 molecules on microtubules. Black line represents the median and bars represent the interquartile range. **g**, Distribution of detachment rate of kinesin-1 molecules. Black lines represent the mean and bars represent the S.D. For the data underlying **Suppl. Fig. 5d-g**, n= 32 kymographs from 13 microtubules from two independent experiments were analyzed. **h,** Distribution showing length of buckling microtubules. Black lines represent the median and bars represent the interquartile range. (n= 53 microtubules from six independent experiments). **i,** Persistence length of microtubules from thermal fluctuation experiments (see **Methods**). Black lines represent the median and bars represent the interquartile range (n= 17 microtubules from three independent experiments).

Supplementary figure 6

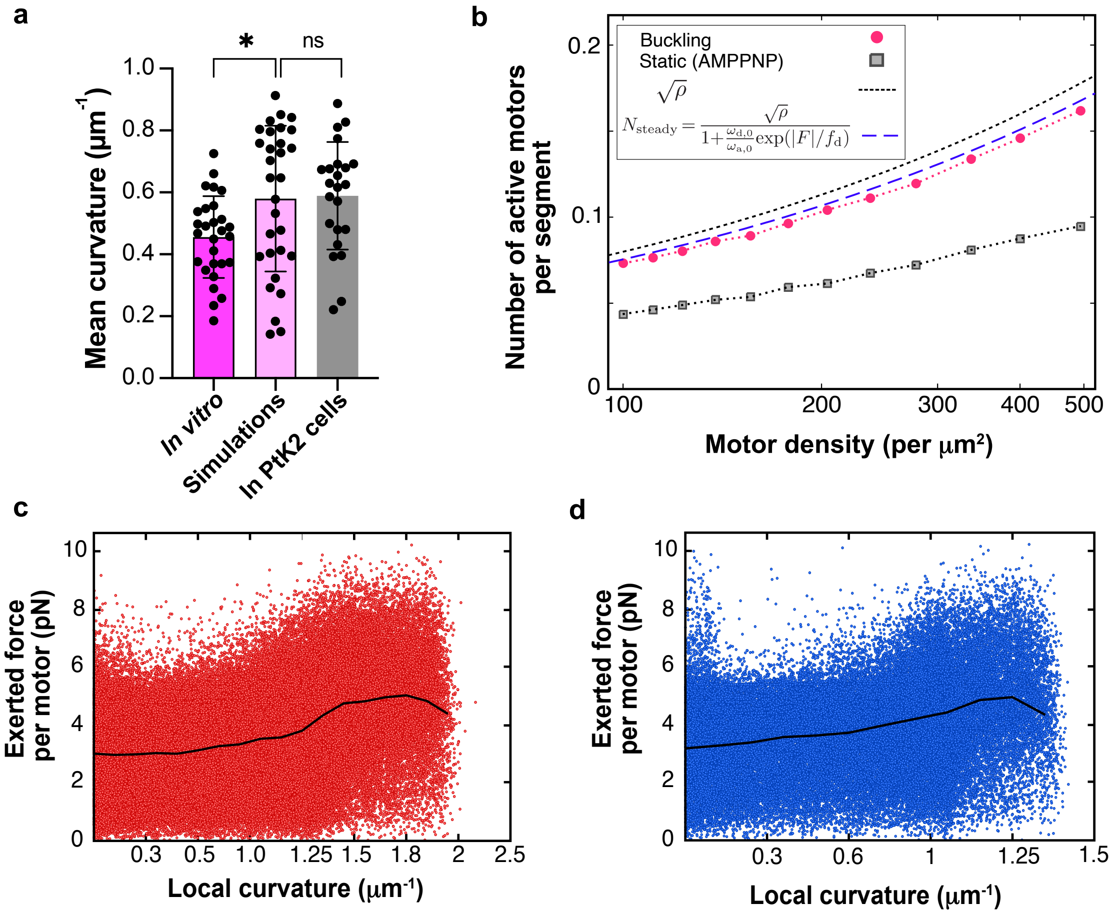

Supplementary Figure 6: a, *Comparison of mean curvature of buckling microtubules in experiments vs simulations vs in PtK2 cells. In vitro* (n= 28 timepoints, *in vitro* from 4 buckling microtubules from three independent experiments) and n= 23 timepoints from 4 PtK2 cells (analyzed from 2 independent experiments). Simulation results using a motor density of $\rho = 494\ \mu m^{-2}$, microtubule persistence length, L_p= 6 mm, and microtubule length, L= 10 µm. Error bars represent the S.D. p= 0.0174 (*in vitro*-simulations) and p= 0.8786 (simulations- in PtK2 cells) using unpaired t-test. **b**, *Lin-log plot of number of active motors per segment in a simulated buckling microtubule as a function of motor density.* The steady-state number of motors bound per microtubule segment can be estimated by analyzing the Markov chain balance of stochastic binding and unbinding events, yielding a value for N_{steady} (see SI simulation methods for details). In this equation, |F| is the absolute value of the average force exerted on the filament by the motors (for both buckling and AMPPNP conditions) at different motor densities (See **Fig 6i** and **Suppl. Fig. 7c**). In practice, the actual number of motors on the filament is slightly lower than this theoretical estimate, as the system remains in a transient dynamical regime and motor traffic along the filament has not yet reached equilibrium. *Scatter plots of the force exerted by each motor vs local curvature*, shown for a: **c**, soft microtubule with L_p= 1 mm (red dots) and **d**, stiff microtubule with L_p = 10 mm (blue dots). Other parameters include: L= 5 µm, $\rho = 400\ \mu m^{-2}$. Black line represents average values computed by binning the local curvature. Each plot includes data from 10^5 microtubule samples.

Note: Although the motor force values in the above scatter plots (**Suppl. Fig. 6c and 6d**) span a broad range (even beyond 10 pN), most data points cluster at lower forces. The observed high forces occur due to the large ensemble size in simulations (10^5 microtubule samples with $\sim 10^2$ motors along each). This enables us to observe statistically rare outcomes that would be difficult to capture in typical experimental datasets.

Supplementary figure 7

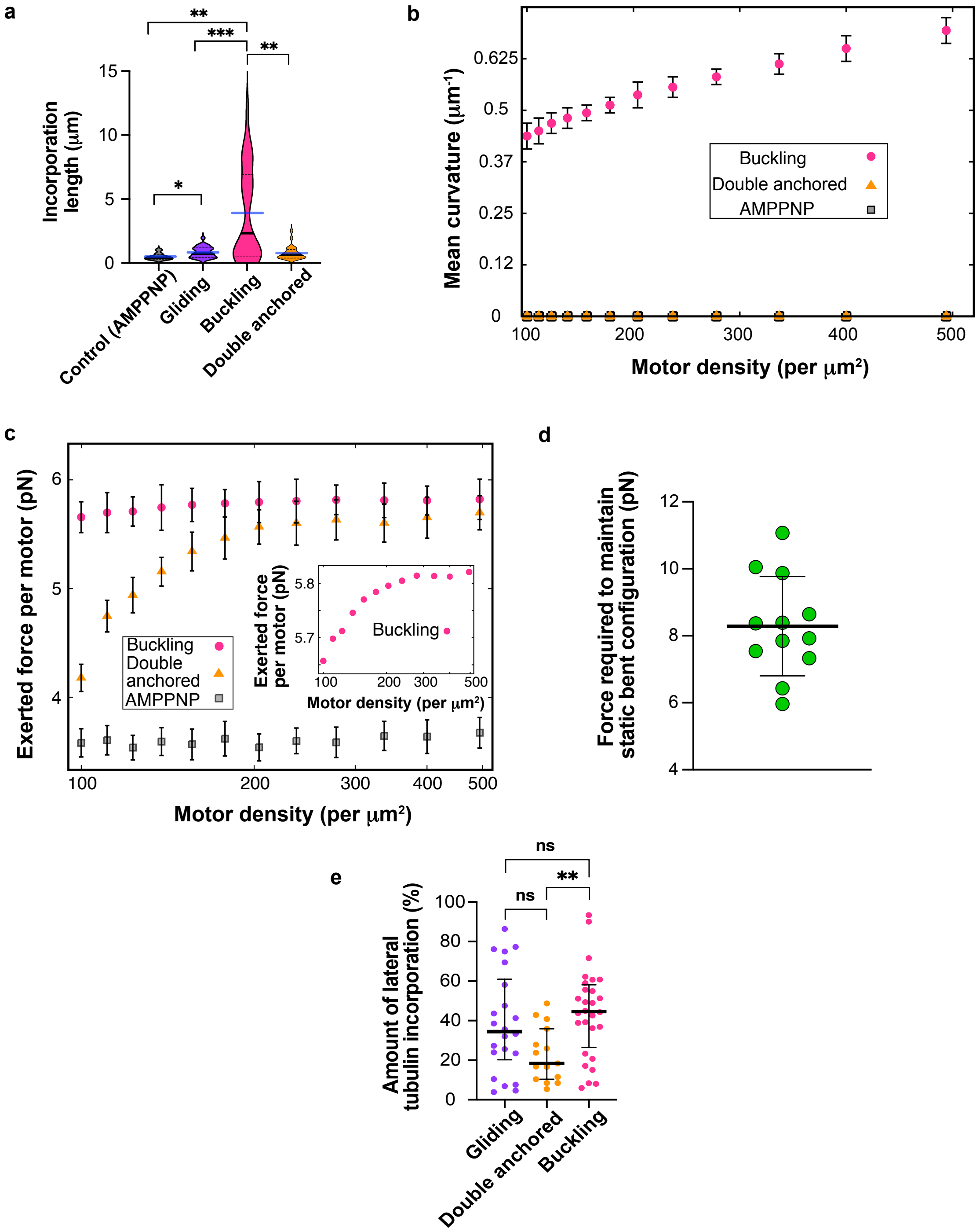

Supplementary Figure 7: a, *Incorporation length across different conditions*- control (AMPPNP), gliding, buckling and double-anchored microtubules. Black lines represent median, dotted lines represent the interquartile range and blue line represents the mean from three independent experiments in each case, comprising 98, 139 and 110 µm of the total microtubule length analyzed for double-anchored microtubules. For microtubule lengths analyzed in all other conditions, refer **Fig 3g** captions. p= 0.3442 (double anchored-gliding); p= 0.0012 (double-anchored -buckling); p = 0.0018 (buckling-control), p= 0.0172 (gliding-control), and p= 0.0005 (gliding-buckling) using Mann-Whitney test. Comparison between all other conditions are non-significant. **b,** *Effect of motor arrangement and* *mobility on microtubule dynamics*. Simulations compare three configurations: (pink circles) motors distributed across the surface leading to buckling, (orange triangles) motors arranged linearly beneath a straight microtubule (double-anchored), and (gray squares) in the presence of AMPPNP. Mean curvature of each discretized node of the microtubule is plotted as a function of motor density for all three cases. Microtubule parameters: L= 10 µm and L_p = 5 mm. Data are averaged over time and across five microtubules. **c,** *Mean force exerted per motor on a microtubule as a function of motor density in simulations* for buckling, double anchored and AMPPNP conditions. Microtubule parameters: L= 10 µm and L_p= 5 mm. The inset shows the same data as the buckling case in the main figure panel in the same figure, but over a narrower force range to better highlight the increasing trend. **d,** *Force (along the entire microtubule) required to maintain static bent microtubules in the bent configuration*. Refer to SI simulation methods for details. Black lines represent mean and S.D. (n= 12 static bent microtubules were analyzed from experimental data from three independent experiments). **e,** Higher amount of lateral tubulin incorporation in buckling microtubules. Black lines represent the median and bars represent the interquartile range. Statistical test used: Mann-Whitney test. p= 0.42, not significant (gliding-buckling); p= 0.1049, not significant (gliding- double-anchored); p= 0.0019 (double-anchored -buckling). 98, 139 and 110 µm of the total microtubule length analyzed for double- anchored microtubules. For microtubule lengths analyzed in all other conditions, refer **Fig 3g** captions. Data cumulative for three independent experiments in each condition.

Supplementary figure 8

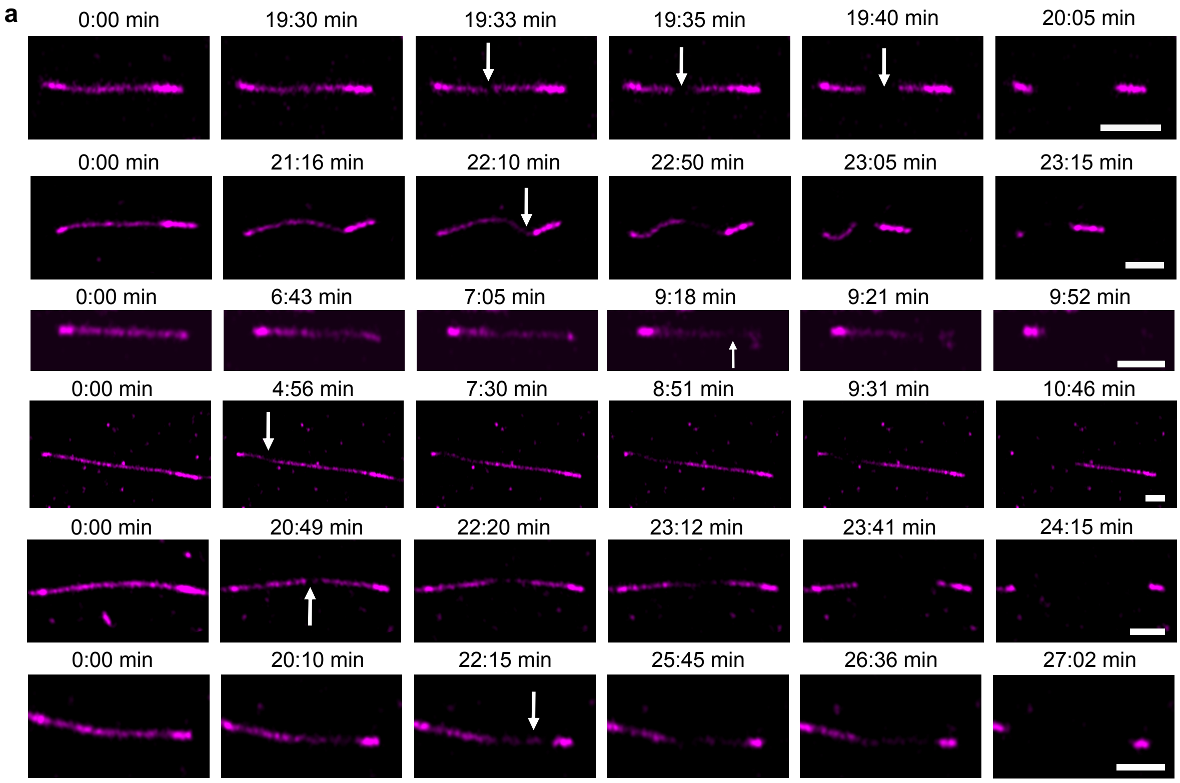

Supplementary Figure 8: a, Example images showing location and time of breakage in double-anchored microtubules. Scale bar: 2 µm.

Supplementary figure 9

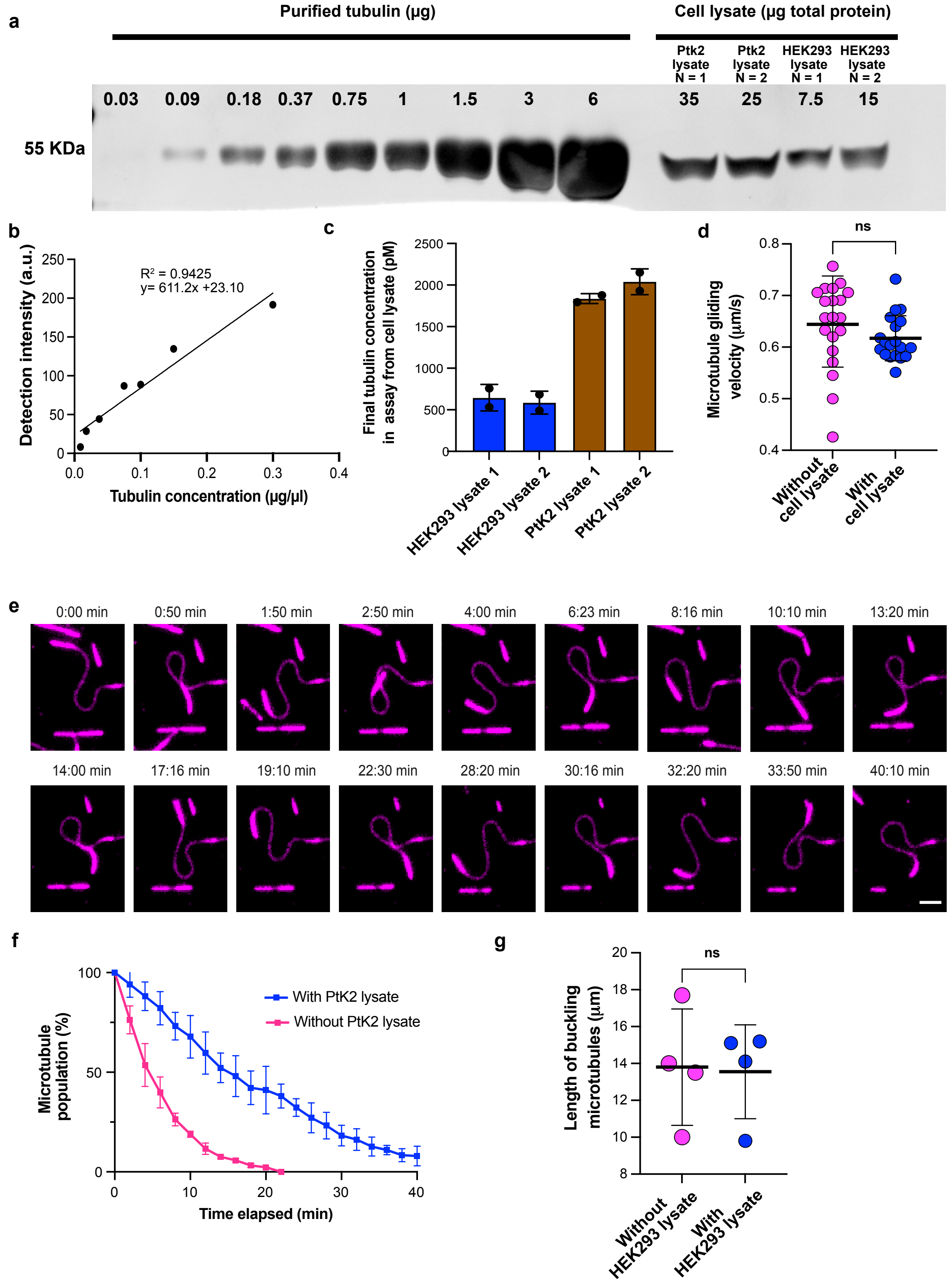

Supplementary Figure 9: a, Concentration of tubulin in cell lysates was estimated using quantitative western-blot analysis. Known concentrations of purified tubulin (0.03-6 µg) were loaded as standards with different dilutions of 2 independent lysates of HEK293 and PtK2 cells. **b**, Standard curve: Plot of intensities of purified tubulin bands in the immunoblot in **9a** vs the corresponding tubulin concentration in µg/µl. **c,** The standard curve in **b** was used to determine the tubulin content in the buckling assays shown in **Fig 7a-c** (HEK293 cells) and **9e,f** (PtK2 cells). Concentration values were obtained from 2 immunoblots from 2 lysates of HEK293 and PtK2 cell lysates. **d,** *Comparison of microtubule gliding velocity* with and without the addition of 20 µg ml^{-1} HEK293 cell lysate. Black lines represent mean and error bars represent the S.D. p= 0.2146 (not significant; ns) using unpaired t-test (n= 19 microtubules analyzed in each condition, from two independent experiments). **e,** Timelapse sequence showing buckling microtubule in the presence of 60 µg ml^{-1} PtK2 cell lysate. Scale bar: 2 µm. **f,** Buckling microtubules survive longer in presence of PtK2 cell lysate. Comparison of the percentage of the microtubule population remaining (in the absence of free tubulin) over time in the case of buckling microtubules both with and without 60 µg ml^{-1} PtK2 cell lysate (n> 100 microtubules analyzed in each condition from two independent experiments from 2 independent lysates). The symbols and error bars indicate mean ± S.D respectively. **g,** *Length of buckling microtubules* compared for estimating mean curvatures of buckling microtubules with and without the addition of 20 µg ml^{-1} HEK293 cell lysate (Refer **Fig 7d**). p= 0.9054 (not significant; ns) using unpaired t-test (n= 26 frames analyzed from 4 microtubules in each condition from three independent experiments).

Supplementary figure 10

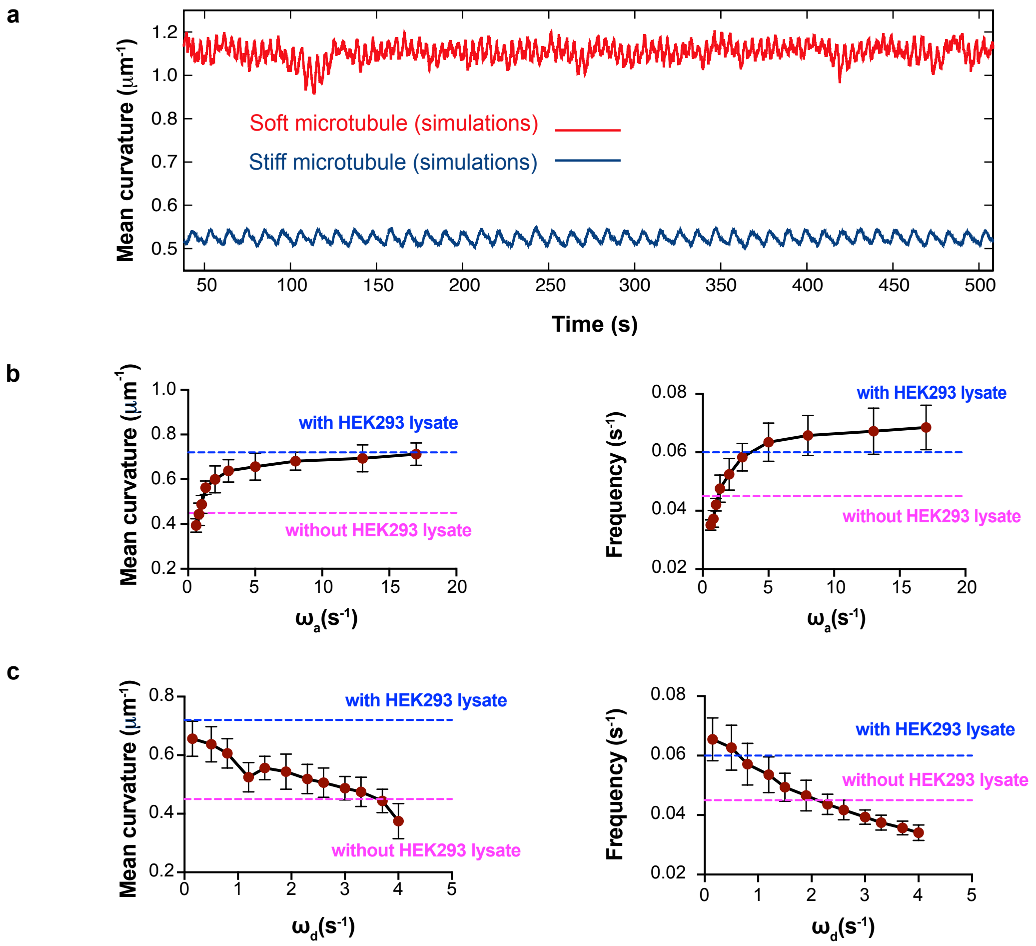

Supplementary Figure 10: a, Effect of microtubule stiffness on mean curvature. Examples of mean curvature evolution over time in simulations. The behavior of a soft microtubule (in red) with L_p = 1 mm is compared to a stiff microtubule (in dark blue) with L_p = 10 mm (slight bending phase). Other parameter values are L = 10 μm and ρ = 400 μm^{-2}. Mean curvature (left) and oscillation frequency (right) as a function of the motor attachment rate (ω_a), in **10b** and motor detachment rate (ω_d), in **10c** for a microtubule of L = 10 μm and L_p = 5 mm. The symbols and error bars indicate mean ± S.D respectively. Blue and pink dotted lines represent experimentally determined values with and without HEK293 lysate respectively.

Simulation Methods

Description of the microtubule:
Our numerical model describes the active bending of microtubules (MTs), which are represented as semi-flexible filaments subject to deformations from active forces generated by molecular motors. The energy of a given filament of length L and bending rigidity $k_{\text{bend}} = L_p k_B T$ (L_p being the persistence length of the filament) is calculated using the worm-like chain model [70, 71]:

$$E_{\text{filament}} = \frac{k_{\text{bend}}}{2} \int_0^L \left(\frac{\partial \theta(s)}{\partial s} \right)^2 ds, \tag{1}$$

where s is the contour length along the filament, $\theta(s)$ is the local tangent angle, and $\partial\theta(s)/\partial s$ is the local curvature. To simulate filament dynamics numerically, the filament is discretized into N segments of equal length ($\Delta L = \frac{L}{N} = 8\,\text{nm}$). The segments are assumed to be inextensible. The configuration of the filament is then parametrized by a set of angular coordinates θ_i corresponding to the orientation of each segment with respect to the x-axis. The discretized version of the Hamiltonian becomes:

$$E_{\text{filament}} = \frac{k_{\text{bend}}}{\Delta L} \sum_{i=1}^{N} \Big(1 - \cos\left(\theta_i - \theta_{i-1}\right) \Big). \tag{2}$$

The angle of the first segment is fixed at $\theta_0 = 0$. For a straight filament aligned with the x-axis, $E_{\text{filament}} = 0$. The position of each node $\mathbf{x}_i$ is given by:

$$\mathbf{x}_i = \sum_{j=0}^{i} \Delta L \begin{pmatrix} \cos(\theta_j) \\ \sin(\theta_j) \end{pmatrix}. \tag{3}$$

Active cross-linkers:

We model the action of active molecular motors stochastically. Motors (modeled as cross-linkers) attach from a 2D grid underlying the filament. Each cross-linker on this grid can stochastically attach to a node on the filament. Once attached, the cross-linker applies a force like a linear spring:

$$E_{\text{crosslink}} = \frac{k_{\text{spring}}}{2} \sum_{i=1}^{n} ||\mathbf{x}_{\text{link},i} - \mathbf{x}_{\text{grid},i}||^2, \tag{4}$$

where k_{spring} is the spring constant, $\mathbf{x}_{\text{link},i}$ is the node between adjacent segments of the filament, and $\mathbf{x}_{\text{grid},i}$ is the fixed point of the cross-linker on the grid. If the node is within a attachment radius d_{attach}, unbound motors can attach to the filament with rate ω_{a}. While the attachment rate can be force-dependent in general (i.e. $\omega_{\text{a}}(F) = \omega_{\text{a,0}} \exp\left(-\frac{|F|}{f_{\text{a}}}\right)$ with f_{a} being the characteristic attachment force), here we report the results for a constant ω_{a}.

In contrast, the detachment rate depends on the force:

$$\omega_{\text{d}}(F) = \omega_{\text{d,0}} \exp\left(\frac{|F|}{f_{\text{d}}}\right), \tag{5}$$

where f_d is the characteristic detachment force and $|F|$ is the absolute value of the force exerted on the filament by the motor. To avoid unrealistically large forces and numerical instabilities, a maximum motor extension length of $40\,$nm was imposed. Once attached, motors can walk along the filament from the fixed end toward the free end. The step size d_h is constant ($d_\mathsf{h} = \Delta L = 8\,$nm). Similar to the detachment rate, the hopping rate is also force-dependent. If the force and motion direction are aligned the hopping rate is given by

$$\omega_\mathsf{h}(F) = \min\left[2\,\omega_{\mathsf{h},0}, \omega_{\mathsf{h},0}\left(1 + \frac{|F|}{f_\mathsf{s}}\right)\right], \tag{6}$$

otherwise

$$\omega_\mathsf{h}(F) = \max\left[0, \omega_{\mathsf{h},0}\left(1 - \frac{|F|}{f_\mathsf{s}}\right)\right], \tag{7}$$

where f_s is the stall force and $\omega_{h,0}$ is the load-free hopping rate. In the simulation, we assume a separation of timescales: the relaxation of the filament is much faster than the timescale of motor dynamics. Therefore, after each motor update (attachment, detachment, or stepping), the shape of the filament is re-equilibrated. Nevertheless, this equilibrated configuration will change in the next time step since the status of motors evolves with time (including new attachments, new detachments, and motor position updates). The choice of the initial nodes to attach motors to the filament and their updates because of motor dynamics are carried out using the Gillespie algorithm. After each step, the energy of the system is minimized using a gradient descent method.

The mean force per motor is computed by evaluating the elastic stretching force of each motor, modeled as a linear spring. Specifically, for each active motor, we calculate the product of the spring constant and the displacement vector between the position of the motor on the filament and its fixed attachment point on the grid. The mean force per motor is then obtained by averaging these forces over all active motors bound to the filament. To determine the mean force per discrete filament segment, we first sum the force vectors from all motors that are attached to the same node of the filament. This vector sum represents the total force exerted on that segment. Finally, we compute the average over all such segments along the filament to obtain the mean force per discrete segment. To quantify the local curvature of the filament, we assign a curvature value to each internal node based on the positions of three successive nodes along the discretized filament. For each triplet of adjacent nodes, we compute the radius of the circle that passes through all three points. The local curvature at the central node is then defined as the inverse of this radius.

To investigate the spatial relationship between local curvature and force along the filament, we computed the cross-correlation function Corr(Δx) between the local curvature $c(x,t)$ and the local force $f(x{\pm}\Delta x, t)$, evaluated at spatially offset positions along the filament. This function quantifies the correlation between curvature at position x and force at a neighboring position $x{\pm}\Delta x$, yielding a value between 1 and -1, indicating positive and negative correlation, respectively.
The cross-correlation was calculated using the standard Pearson correlation coefficient formula: Corr$(\Delta x) = \frac{\langle (c(x,t)-\langle c\rangle)(f(x\pm\Delta x,t)-\langle f\rangle)\rangle}{\sigma_c\sigma_f}$. Here, the parameters enclosed within $\langle\rangle$ are obtained by averaging over filament segments at a given time t, and σ_c and σ_f are the standard deviations of the curvature and force, respectively.

Estimation of the steady-state number of bound motors:

To compute the steady-state number of motor proteins attached to a microtubule filament, we model motor binding and unbinding as a stochastic two-state Markov process influenced by an external force. Motors bind with a force-dependent attachment rate $\omega_{\text{a}}(f) = \omega_{\text{a,0}} \exp\left(-\frac{|F|}{f_{\text{a}}}\right)$ and detach with a rate $\omega_{\text{d}}(f) = \omega_{\text{d,0}} \exp\left(\frac{|F|}{f_{\text{d}}}\right)$ (see Eq. 5). $|F|$ is the absolute value of the average force exerted on the filament by the motors at different motor densities (refer Fig 6i). By analyzing the Markov chain balance of stochastic binding and unbinding events, the steady-state fraction of available motors which remain bound can be obtained as $\frac{1}{1+\frac{w_{d,0}}{w_{a,0}} \exp(|F|(1/f_d+1/f_a))}$. Given a surface motor density ρ, the number of motors geometrically available to interact with the filament is approximately $\sqrt{\rho}$, per micrometer.
Therefore, the steady-state number of motors that remain bound yields

$$N_{\text{steady}} = \frac{\sqrt{\rho}}{1 + \frac{w_{d,0}}{w_{a,0}} \exp(|F|(1/f_d + 1/f_a))}$$

In case of a constant (force-independent) ω_{a}, as in our simulations, the relation for the steady-state number of bound motors reduces to

$$N_{\text{steady}} = \frac{\sqrt{\rho}}{1 + \frac{w_{d,0}}{w_{a,0}} \exp(|F|/f_d)}$$

Estimation of forces acting on statically bent microtubules in experiments:

To estimate the force exerted on statically bent microtubules observed in experiments (Refer Fig 1c, right), we model the microtubule as a semiflexible filament confined to two dimensions and clamped at one end [41]. The full shape of the microtubule is extracted from microscopy images. An external force with unknown x- and y-components is assumed to act at the free end. Our goal is to determine the force that best reproduces the observed static configuration under these boundary conditions. For the numerical simulations, the filament is assumed to have a given bending rigidity and is discretized into segments, as described above. To estimate the applied force, we fix the position and orientation (tangent angle) at the fixed end, the components of a trial force at the free end and obtain the equilibrium configuration of the filament. If the applied trial force differs from the true value, the resulting shape evolves away from the experimentally observed configuration and the position of the free end changes. Thus, for each trial force we compute the Euclidean distance between the simulated and observed position of the free end. By scanning across a range of trial force values, we identify the one that minimizes this distance as the optimal force reproducing the observed filament shape under the given constraints.

Supplementary references:

[67] M. Rank and E. Frey, “Crowding and Pausing Strongly Affect Dynamics of Kinesin-1 Motors along Microtubules,” Biophysical journal, vol. 115, no. 6, pp. 1068-1081, 2018.

[68] M. J. I. Müller, S. Klumpp and R. Lipowsky, “Tug-of-war as a cooperative mechanism for bidirectional cargo transport by molecular motors,” Proceedings of the National Academy of Sciences of the United States of America, vol. 105, no. 12, pp. 4609-4614, 2008.

[69] C. M. Coppin , D. W. Pierce, L. Hsu and R. D. Vale, “The load dependence of kinesin’s mechanical cycle,” Proceedings of the National Academy of Sciences of the United States of America, vol. 94, no. 16, p. 8539–8544, 1997.

[70] A. Kunwar, S. K. Tripathy, J. Xu, M. K. Mattson, P. Anand, R. Sigua, M. Vershinin, R.J. McKenney, C. C. Yu , A. Mogilner and S. P. Gross , “Mechanical stochastic tug-of-war models cannot explain bidirectional lipid-droplet transport,” Proceedings of the National Academy of Sciences of the United States of America, vol. 108, no. 47, p. 18960–18965, 2011.

[71] M. C. Uçar and R. Lipowsky, “Collective Force Generation by Molecular Motors Is Determined by Strain-Induced Unbinding,” ACS Nano Lett, vol. 20, no. 1, pp. 669-676, 2020.

[72] M. J. Schnitzer, K. Visscher and S. M. Block , “Force production by single kinesin motors,” Nat Cell Biol, no. 2, pp. 718-723, 2000.

[73] K. Svoboda and S. M. Block, “Force and velocity measured for single kinesin molecules,” Cell, vol. 77, no. 5, p. 773–784, 1994.

[74] K. Visscher, M. J. Schnitzer and S. M. Block , “Single kinesin molecules studied with a molecular force clamp,” Nature, vol. 400, pp. 184-189, 1999.

[75] B. H. Blehm, T. A. Schroer, K. M. Trybus, Y. R. Chemla and P. R. Selvin, “In vivo optical trapping indicates kinesin’s stall force is reduced by dynein during intracellular transport,” PNAS, vol. 110, no. 9, pp. 3381-3386, 2013.

[76] A. Marantan, L. Mahadevan, “Mechanics and statistics of the worm-like chain”, Am.J. Phys. 86, 2018.

[77] I. Weber, C. Appert-Rolland, G. Schehr and L. Santen, “Non-equilibrium fluctuations of a semi-flexible filament driven by active cross-linkers”, EPL 120, 38006, 2017.

2.2 Limitations of the study and potential areas for future optimization

Similar to previous studies on microtubule self-repair (Schaedel *et al.*, 2015; 2019), observing incorporation of free tubulin into the existing microtubule lattice is only possible after a period of 10-15 min, following washout of free tubulin in solution. This technical constraint arises from the high background fluorescence from use of 100% labelled free tubulin in solution. As a result, self-repair sites can only be visualized after washout of free tubulin following an incubation period of 15 min. In all assays, the time of incubation during incorporation (15 min) was thus kept consistent across all conditions. During analysis, only incorporations above the set thresholds defined based on the resolution limit and background noise were taken into consideration. In this way, the quantifications of the study may underestimate the incorporation frequencies observed. Future studies employing super-resolution microscopy may allow for more sensitive detection of smaller incorporation sites, thereby improving accuracy. Emerging techniques like 2-color spectral STORM (may be a good choice for detecting incorporations in fixed cells or samples as shown in Gazzola *et al.*, 2023) or lattice light-sheet microscopy (fast imaging with low phototoxicity with a resolution of 100 nm) are potential alternatives. However, care must be taken to ensure that these methods are not detrimental to sample integrity (particularly in terms of photobleaching) and can also provide sufficient temporal resolution that is required to capture microtubule dynamics in real time.

Kinesin-based assay systems are limited by inherent heterogeneity in terms of kinesin surface density and the active fraction of motors (influenced by the type of kinesin construct used and quality of purification) [Grover *et al.*, 2016; Dumont *et al.*, 2012]. All the experimental results reported in this dissertation were performed using the same batch and concentration of purified kinesin (416nM of rkin560-GFP: Kinesin-1 heavy chain, truncated to 560aa; Addgene pET17_K560_GFP_His). By immobilizing kinesin motors to the surface via anti-GFP antibodies, we ensured that the surface density of kinesin was maintained in the same range (300-500 kinesins/μm^2 as estimated using single-molecule photo-bleaching experiments) across all assays. Nevertheless, minor heterogeneity cannot be entirely ruled out. In the future, use of FLIC (Fluorescence Interference Contrast) microscopy can reveal kinesin binding events and kinetics (as demonstrated in VanDelinder *et al.*, 2019). This may be particularly useful for investigating how MAPs or intracellular factors influence motor dynamics, as well as aid in fine-tuning the simulation parameters for more physiologically accurate models.

The major limitation of the buckling assay setup stems from the stochastic and relatively weak attachment of streptavidin and, in consequence, microtubules (with biotin labelled minus ends) to the surface. Though surfaces treated and coated with the same concentration of streptavidin were used across all assays, only 30-50 % of microtubules in one field-of-view buckle for the complete duration of the experiment. As the objectives of the present study focused on observing the damage and self-repair in buckling microtubules, the analysis was restricted to this fraction of buckling microtubules. Improved passivation techniques—such as the use of anti-biotin antibodies or SiPEG-Biotin-based surface coatings—may provide more specific attachment and increase the proportion of buckling filaments.

Similarly, use of SiPEG-based surface passivation in combination with non-ionic surfactants like Pluronic F-127 may also offer better passivation by preventing non-specific absorption, in assays with free tubulin, labelled MAPs in solution, or cell lysates. This, in turn would help enhance the signal/background ratio in self-repair assays and facilitate the detection of smaller tubulin incorporation spots that were disregarded from our analysis due to the thresholds we set to distinguish incorporations from background. (Note: Although PLL-PEG coatings offer superior passivation, particularly against labelled MAPs, my trials (as well as insights from personal Communication with Thomas Surrey, CRG Barcelona) suggest that its use inhibits kinesin processivity.).

The above study is also limited by the lack of direct force measurements. As the central aim of this work was to investigate curvature-induced effects on microtubule damage and repair, forces were inferred indirectly from filament shapes and through simulations that reproduced experimentally observed dynamic fluctuations. The semi-quantitative model used incorporated experimentally derived parameters such as surface motor density, dwell time, and motor dissociation rates; however, it did not account for the full vectorial nature of the forces exerted by motors on the buckling filament. Future studies employing Atomic Force Microscopy (AFM) or optical tweezers could provide more precise, direct quantification of the forces that induce lattice breakage, although these approaches may prove challenging given the fragility of GDP-lattices devoid of stabilizing agents. Additionally, combining custom cell-stretching devices with live-cell imaging could allow controlled application of compressive forces to cells, enabling measurement of critical loads that trigger microtubule buckling and breakage *in vivo*.

A major finding of this work is that the presence of intracellular factors helps boost microtubule survival; however, at this stage, the specific factor(s) that might be responsible for this effect remain unidentified. Estimates from experiments and simulations indicate that these factors might carry out this effect by reducing microtubule persistence length, making microtubules more flexible and thus more resilient to mechanical stress. Kinesin processivity (estimated as microtubule gliding velocity-refer extended data Fig 7a in the manuscript above) remained unaffected in the presence of 20 μg/ml HEK293 cell lysates. Nevertheless, these factors might affect motor dynamics in a subtle manner that is not reflected in motor processivity parameters. Preliminary attempts were made in this direction; however, achieving reliable imaging at single-molecule concentrations with adequate spatial and temporal resolution proved technically challenging with the current imaging setup. Future implementation of Fluorescence Interference Contrast (FLIC) microscopy or other surface-sensitive imaging approaches could help overcome these limitations by enabling high-contrast visualization of individual motor–microtubule interactions in complex biochemical environments.

As with most *in vitro* systems involving reconstitution from purified components, the results were determined using system-specific buffer conditions, tubulin concentration, and tubulin source. MAP-free tubulin purified from bovine calf brains that is naturally rich in post-translational modifications (PTMs) was used in all experiments. Microtubule response to mechanical stress may vary with use of tubulin derived from different source tissue or with distinct PTM composition (refer Chapter 4 for results using HeLa tubulin). Care was taken to ensure that all batches of purified tubulin were MAP-free, and identical buffer compositions, temperature (37ºC) and tubulin concentrations were used for all assays and across all conditions.

2.3 Future directions and outlook

The *in vitro* assay developed serves as a critical framework for exploring microtubule response to mechanical stress. Building upon the findings and limitations discussed above, several promising research avenues emerge that can further deepen our understanding of microtubule mechanics, self-repair, and mechanosensing.

Identifying the intracellular component(s) that help confer mechanical resilience to microtubules is an important next step in extending the findings of this study, as well as towards exploring how microtubule response is regulated in cells. Such factors may include specific microtubule-associated proteins, cytolinkers, or small regulatory molecules present in the cytosolic milieu that tune filament flexibility or repair capacity. MAPs are the most compelling of candidates to investigate. Recent studies report the recruitment of plus-end binding MAPs -EB1 and CLASP (CLIP Associated Protein) away from the tip and to the lattice when cells are mechanically challenged (Ju *et al.*, 2024; Li *et al.*, 2023, Aher *et al.*, 2022). MAPs that bind to the growing microtubule ends (collectively called +TIPs) are predominantly known to stabilize microtubules. The EB (end-binding) family of proteins are known to recognize the GTP-like structural state of the microtubule lattice at the growing tip (Guesdon *et al.*, 2016; Maurer *et al.*, 2011). Therefore, it would be interesting to explore if EB recruitment to the lattice under stress occurs as a result of EB recognizing zones of strain or zones of self-repair.

As an initial screening approach, experiments using lysates from cells overexpressing different MAPs could help identify potential candidates that enhance microtubule resilience. Once potential candidates are identified, further characterization of their interaction with microtubules under stress may help offer additional insights: Do these factor(s) act directly on the microtubule lattice to increase flexibility? Do they modulate tubulin mechanics to alter lattice conformation- thus making microtubules more flexible? Or do they influence motor motility either directly by interacting with motors or indirectly through microtubule lattice-mediated effects? Answering these questions will help elucidate the molecular mechanisms that enable microtubules to sustain and recover from mechanical stress.

As described in the section above, combining custom cell-stretching devices with advanced imaging modalities could facilitate direct measurement of critical loads that induce microtubule buckling, fracture, or depolymerization in real time. The same experiments could be performed on cells that have been knockdown/knockout of potential MAPs to validate the role of these MAPs in conferring microtubule stability under mechanical stress.

A natural progression of this work also involves the integration of cellular and molecular complexity into reconstituted systems. *In vivo*, microtubules exist in the presence of MAPs, cytolinkers and consist of different subsets composed of tubulin of different isoforms and with a diverse range of post-translational modifications. In cells, microtubules exhibit faster tip dynamics and tubulin turnover on the timescale of a few minutes (Gazzola *et al.*, 2023), and microtubule breakage is relatively rare. Experiments using tubulin purified from distinct cell types or using PTM-modified tubulin could help identify how biochemical diversity influences lattice repair and damage tolerance. This would be particularly useful for gaining insight into microtubule mechanics in sensory microtubule-based organelles like cilia that is known to be rich in PTMs and experience continual mechanical loading.

Another compelling direction would be to determine the contribution of molecular motors to self-repair in cells. Microinjection experiments to assess self-repair in kinesin/dynein knockdown cells could provide direct evidence for the contribution of motor activity to microtubule damage and integrity.

In conclusion, the present study establishes a conceptual and experimental framework for understanding how mechanical stress modulates microtubule integrity. By delineating the boundary between repair and failure under kinesin-induced buckling, it advances our perception of the microtubule lattice as a dynamic, self-maintaining structure rather than a static, passive filament.

2.4 References (for limitations and outlook sections)

Dumont, E.L., Ghazi, A. & Hess, H. (2022). The Relationship of Motor Attachment Geometry and Velocity Fluctuations in Kinesin-Microtubule Gliding Motility Assays, Biophysical Journal, 102(3), 368-369.

Geng, Q, Bonilla, A, Sandwith, S.N., Verhey, K.J. (2025). Multi-kinesin clusters impart mechanical stress that reveals mechanisms of microtubule breakage in cells. J Cell Biol, 224(10):e202501070.

Grover, R., Fischer, J., Schwarz, F.W., Walter, W.J., Schwille, P., & Diez, S. (2016). Transport efficiency of membrane-anchored kinesin-1 motors depends on motor density and diffusivity, PNAS, 113(46), E7185-7193.

Guesdon, A., Bazile, F., Mohan, R.M., Monier, R., Garcia, S… Chrétien, D. (2016). EB1 interacts with outwardly curved and straight regions of the microtubule lattice. Nature cell biology, 18(10), 1102-1108.

Li, Y., Kučera, O., Cuvelier, D., Rutkowski, D.M., Deygas, M., Rai, D., Pavlovič, T., Vicente, F.N., Piel, M., Giannone, G., Vavylonis, D., Akhmanova, A., Blanchoin, L., Théry, M. (2023). Compressive forces stabilize microtubules in living cells, Nature materials, vol. 22, no. 7, pp. 913-924.

Maurer, S. P., Fourniol, F. J., Bohner, G., Moores, C. A., & Surrey, T. (2012). EBs recognize a nucleotide-dependent structural cap at growing microtubule ends. Cell, 149(2), 371-382.

Personal Communication, Thomas Surrey, CRG Barcelona.

VanDelinder, V., Imam, Z.I. & G. Bachand. (2019). Kinesin motor density and dynamics in gliding microtubule motility. Sci Rep 9, 7206.

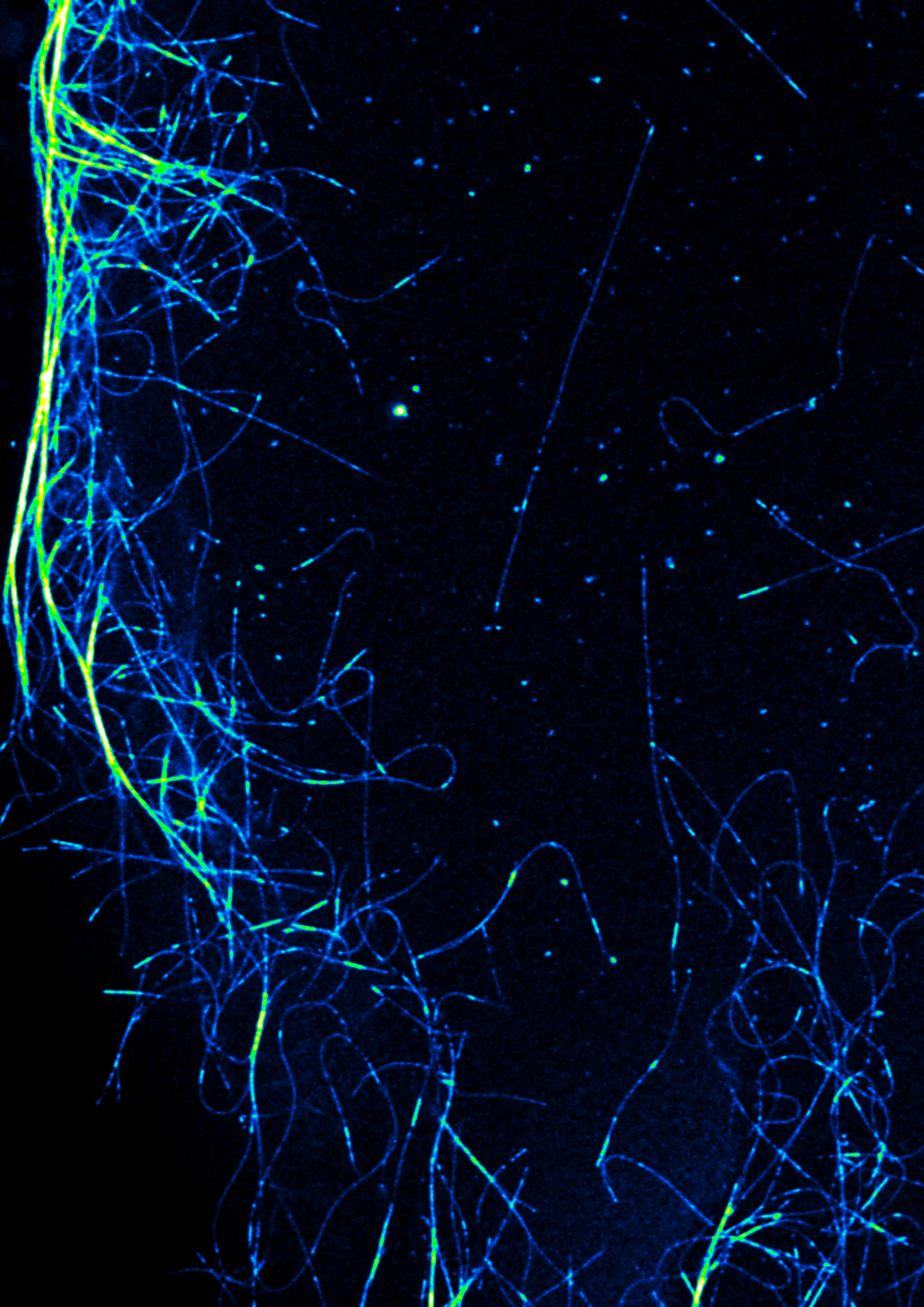

Title of the dissertation:

Metastable Microtubules: Dynamic Instability, Lattice Plasticity and Mechanosensing

Chapter 3: Microtubule lattice dynamics is mediated by defect propagation

Explanation of the contributions of the co-authors in the following chapter 3:

Laura Aradilla Zapata (née Schaedel): conceptualized the study, designed experiments. Supervised the study.

Karin John: conceptualized the study, designed simulations. Supervised the study.

Shweta Nandakumar: Designed the experiments. Writing: sections 3.1, 3.2, 3.3.1, 3.3.2, 3.4, 3.5 and 3.6. Performed the experiments and data analysis corresponding to Figure 3.2, 3.4, 3.5. Provided experimental expertise for data shown in Figure 3.8.

Amir Zablotsky : Performed the simulations and corresponding data analysis underlying Figures 3.3, 3.6 and 3.7. Designed the figure panels shown in figures 3.3, 3.6 and 3.7 and provided the initial written draft of interpretation of results and data analysis in Section 3.3.3 and the associated Annexure 1.

Subham Biswas : Performed the experiments and corresponding data analysis for results shown in Figure 3.8.

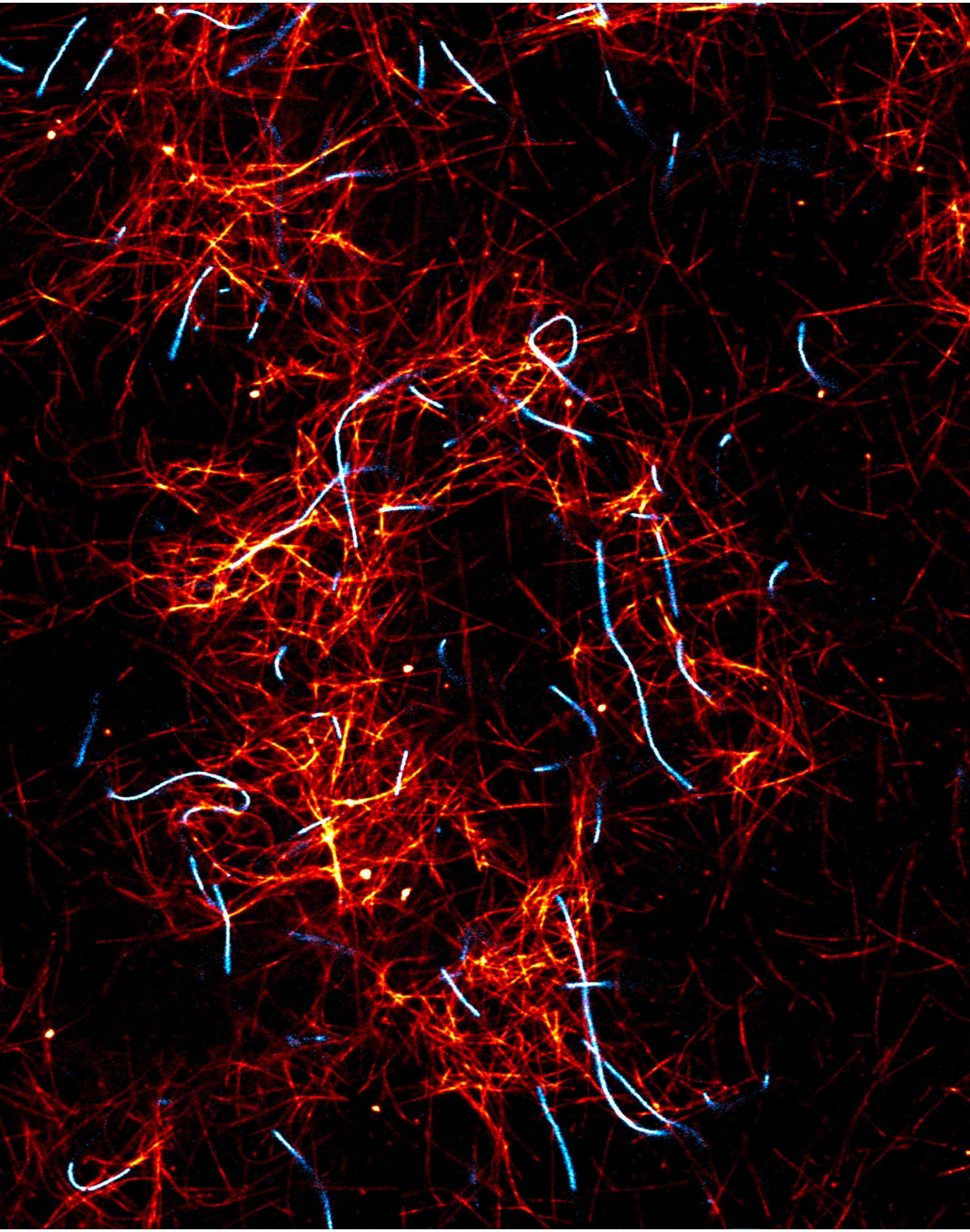

Chapter 3

Microtubule lattice dynamics is mediated by defect propagation

From self-repair to lattice dynamics: this chapter explores the role of defects (irregularities in the microtubule lattice structure) in modulating microtubule lattice plasticity. This chapter details preliminary findings on the propagation of defects using tubulin incorporation as a readout. Further, the findings highlighted show how microtubule lattice dynamics can be modulated by bending stress (curvature) as well as the presence of MAPs.

3.1 From self-repair to lattice dynamics

In the previous chapter, it was demonstrated how buckling and bending stress triggers microtubule self-repair by incorporation of free tubulin from solution into the microtubule lattice (Fig 1 in Nandakumar *et al.*). I also observed tubulin incorporation in straight microtubules (albeit at lower frequencies than in bent) across all my assays. This suggests that tubulin exchange in the lattice is an inherent, spontaneous process that occurs even in the absence of forces that cause damage.

Consistent with this view, Schaedel *et al.*, 2019, showed that tubulin turnover is an intrinsic property of microtubules, mediated by the presence of defects or lattice irregularities. This led to a conceptual shift from describing these tubulin turnover events as 'microtubule self-repair' to a broader definition as 'microtubule lattice dynamics' or 'lattice plasticity' (Motta, Biswas *et al.*, 2023).

As mentioned previously, the microtubule lattice is not completely homogenous and contains several defects like protofilament transitions (Chretién *et al.*, 1992) or monomer or dimer vacancies that lead to lattice-type transitions (**Fig 3.1a, b**). Such defects act as weak spots in the lattice that disrupt local tubulin-tubulin contacts, thereby facilitating tubulin incorporation. Using a simple, kinetic Monte Carlo model framework, Schaedel *et al.*, 2019 showed that localized tubulin turnover preferentially occurs in the vicinity of such dislocations. In this way, defects may provide a passive "breathing" mechanism for microtubules to spontaneously renew their lattice.

Recent cryo-EM studies further confirm that monomer vacancies that lead to lattice-type transitions (**Fig 3.1b**) are the most frequent of defects found in microtubules grown *in vitro* and occur in microtubules constituted from *Xenopus* extracts (Guyomar *et al.*, 2022). Defects may serve as local hotspots of tubulin turnover owing to their nature to propagate before elimination in what is termed the 'Lego-like mechanism' (Motta, Biswas *et al.*, 2023; Lecompte and John, 2022). Much like how in a Lego wall with one missing brick, it is sterically difficult to fill the hole without removing neighbouring bricks, it is sterically impossible to incorporate new GTP-tubulin dimers into a monomer-sized hole. Only when a neighbouring dimer leaves the lattice and the defect enlarges, can new GTP-tubulin dimers be incorporated into the lattice (See **Fig 3.1b**). Thus, the propagation and eventual elimination of a defect must involve loss of neighbouring dimers in the immediate vicinity of the defect. The microtubule lattice is anisotropic, with longitudinal bonds being stronger than lateral bonds. This anisotropy has significant implications for how defects propagate. In an isotropic lattice (A=1; **Fig 3.1c, right**), tubulin loss will propagate equally in both the lateral and longitudinal direction. Whereas, in the case of an anisotropic lattice (A>1; **Fig 3.1c, left**), where longitudinal bonds are stronger than the lateral bonds, the loss of a longitudinal neighbour (resulting in 2 weak and 1 strong bonds remaining) produces a greater local destabilization than the loss of a lateral one (resulting in 1 weak and 2 strong bonds remaining). As a result, defect propagation and, in consequence, tubulin turnover occurs preferentially along the protofilament in the longitudinal direction (**Fig 3.1c**).

According to this view, the defect does not simply remain static but instead propagates along the lattice till it reaches the end and is effectively eliminated or meets another defect to be effectively neutralized (annealing). In this way, the presence and movement of defects result in tubulin loss and consequent incorporation of new tubulin subunits into the lattice thus mediating inherent microtubule lattice dynamics. In this framework, microtubule self-repair may then be interpreted as a case of incorporation of new tubulin subunits to counteract accelerated local tubulin loss resulting from damage. Therefore to understand how microtubule respond to mechanical stress, it is first important to characterize the mechanisms governing inherent lattice dynamics. In particular, elucidating how defects propagate and how different external effectors (like force and MAPs) influence this process will provide critical insights into the adaptive properties of microtubules.

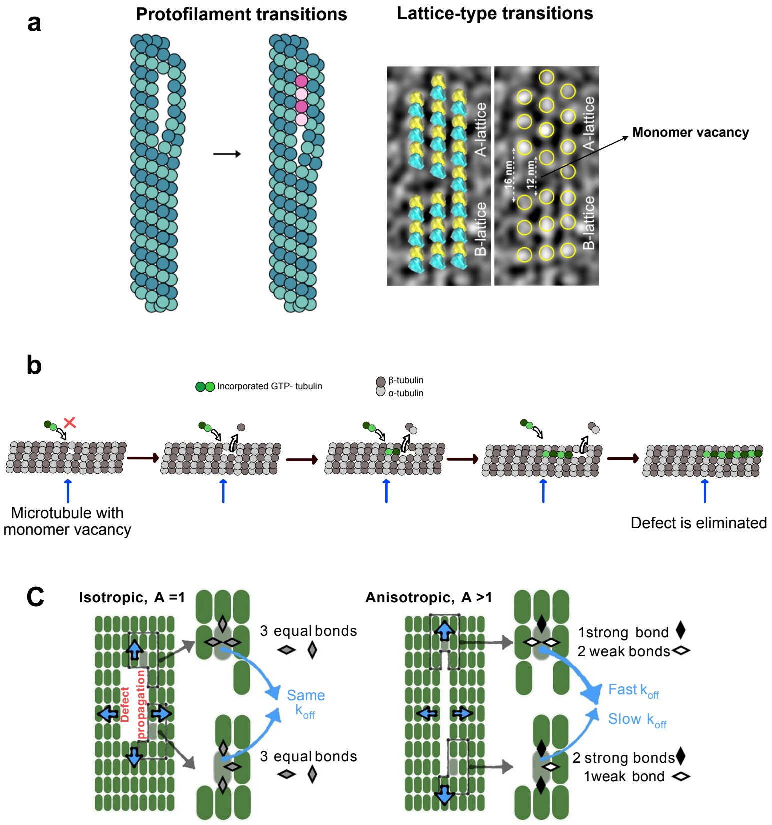

Fig 3.1: (a) Left: Schematic showing microtubule with protofilament transition that serves as a site for tubulin incorporation into the lattice (taken from Motta, Biswas *et al.*, 2023). **Right:** Cryo-ET image showing monomer vacancies at lattice-type transition defects (taken from Guyomar *et al.*, 2022). **(b)** Schematic of 'Lego-like mechanism'

showing defect mobility for a microtubule with a monomer vacancy. Blue arrow indicates the initial position of the defect. **(c) Left:** In an isotropic lattice, vacancies propagate longitudinally and laterally at the same rate. **Right:** in an anisotropic lattice with stronger longitudinal than lateral bonds, tubulin loss and defect mobility along the longitudinal direction is favored (taken from Biswas *et al.*, 2025).

3.2 Study 2: Tubulin turnover is mediated by defect mobility

Though previous studies have estabilished the defect dependent nature of microtubule lattice dynamics (Biswas *et* al., 2025; Schaedel *et al.*, 2019), little is known about how these defects propagate to effect tubulin loss and consequent tubulin incorporation into the lattice. I then set out to investigate how microtubule lattice defects propagate, specifically their pattern and dominant mode of movement. Direct observation of defect motion poses a significant experimental challenge as defects are nanoscale-sized and heterogeneous in terms of their type and frequency of occurrence. Detection and visualization of defects to identify their type and location in the microtubule lattice is currently only possible through advanced cryo-EM/ET techniques. These techniques only provide us with individual snapshots and do not track their location in real time. To bypass this limitation, I sought to infer defect movement indirectly using tubulin incorporations as a dynamic readout.

3.2.1 Multi-cycle tubulin incorporation experiments capture temporal evolution of lattice dynamics

To visualize how incorporation patterns evolve over time, sequential cycles of tubulin incorporation was performed, using fluorescent tubulin of a different colour for each cycle (**Fig 3.2a**). As shown in **Fig 3.2a,** prepared straight, capped GDP-microtubules (Atto-647 labelled, depicted in grey) were first incubated in a solution of green (Atto488)-labelled free tubulin (1st incorporation cycle) for 15 min (Step I) and then in a solution of red (Atto565)-labelled free tubulin (represented in magenta here, 2nd incorporation cycle) for the next 15 min (Step II). At the end of 30 min, the chamber was washed with imaging buffer and imaged (Step III). The pattern and length of 1st and 2nd cycle incorporations were estimated (**Fig 3.2b**). This experimental design enables the spatial and temporal tracing of defect-driven tubulin exchange, helping us to gain insight into the mode and persistence of defect propagation in the lattice.

According to the hypothesis-that tubulin incorporation results from defect propagation, the pattern of incorporations should predominantly show adjacent 1st (green) and 2nd (magenta) incorporations, indicating defect mobility along the lattice. Alternatively, some microtubules may show only primary (green) incorporations resulting from defects that were eliminated in the first incorporation cycle (either since it reached the end of the lattice or annealed with another defect). Upon classification of the 1st and 2nd cycle incorporations (**Fig 3.2d**), it was found that 48 % of the incorporations were next to each other (adjacent), consistent with continuous defect propagation along the lattice. 34 % showed only green stretches (1st incorporations, primary), indicating defects that were resolved after a single propagation cycle. 15 % showed overlaps of both green and magenta stretches, suggesting that there may be regions of coexistence of successive incorporations, possibly as a result of defects switching to neighbouring protofilaments or propagating in the lateral direction. A very small proportion (1.2 %) of the incorporations showed only magenta stretches (2nd incorporations, secondary), likely representing diffusively moving defects or defects incurred during the second cycle. The same trend was further validated with three-cycle tubulin incorporation experiments (**Fig 3.2c**). For this, capped GDP microtubules were prepared using only unlabelled tubulin and subjected them to three rounds of incorporation (each for 15 min) using green labelled, red labelled (shown in magenta) and far-red labelled (shown in cyan) free tubulin. Using a combination of Interference Reflection Microscopy (IRM) and fluorescence microscopy, microtubules were visualized, and the pattern of tubulin turnover over time was traced.

It was found that short microtubules (see first panel in Fig 3.2) showed sequential tubulin turnover along the entire lattice length, implying that over time, one might expect renewal of the complete microtubule, both in the longitudinal (along the length of the microtubule) as well lateral (across protofilaments) direction. These events are more easily detected in shorter microtubules owing to the shorter distance defects need to propagate in order to be eliminated. Together, these results demonstrate that tubulin turnover is governed by the movement and persistence of lattice defects, which propagate along the protofilament axis until they are either eliminated by reaching the microtubule end or anneal with another defect. This pattern of adjacent, continuous incorporations provides strong evidence that defect motion in the microtubule lattice underlies tubulin turnover.

Modes of defect propagation: diffusive and ballistic regimes

Understanding the pattern and mechanism underlying inherent defect propagation is important for gaining insight into the dynamically adaptable nature of microtubules. Analogous to crystalline solids and metals, defect propagation can occur in two distinct regimes: diffusive or ballistic. In the diffusive regime, defect motion is random, stochastic and driven primarily by local lattice rearrangements. This would imply that defects may show localized movement over a few neighboring dimers, occasionally resulting in partial loss of previously incorporated dimers, too and erasure of newly incorporated stretches. In contrast, the ballistic regime is characterized by persistent, directional, defect propagation wherein defects move along the more energetically favorable path (most likely along the longitudinal direction) owing to the lattice anisotropy (Biswas *et al.*, 2025; Lecompte & John, 2022; Pertsinidis and Ling, 2001). Such a motion would result in continuous incorporations of similar lengths as the defect travels along the lattice before being eliminated (See Fig 3.1b).

To determine whether microtubule lattice defects propagate predominantly via diffusive or ballistic motion, I traced the spatial pattern of 1st and 2nd-cycle tubulin incorporations. If propagation were ballistic, successive incorporation cycles would produce adjacent stretches of comparable lengths, reflecting a persistent trajectory of the moving defect. In contrast, a diffusive regime would yield variable incorporation lengths, as random defect movement would erase segments of the first incorporation during subsequent incorporation cycles.

Analysis showed no significant difference in the lengths of 1st incorporations between single-cycle and two-cycle experiments (**Fig. 3.2e**), suggesting that the first incorporation cycle is unaffected by the presence of second incorporations. Strikingly, I found no significant differences in 1st and 2nd incorporation lengths in two-cycle experiments (**Fig 3.2f**), indicating that tubulin loss predominantly occurs in a directional and persistent manner. Together, these findings strongly support a model in which microtubule lattice dynamics are dominated by ballistic defect motion.

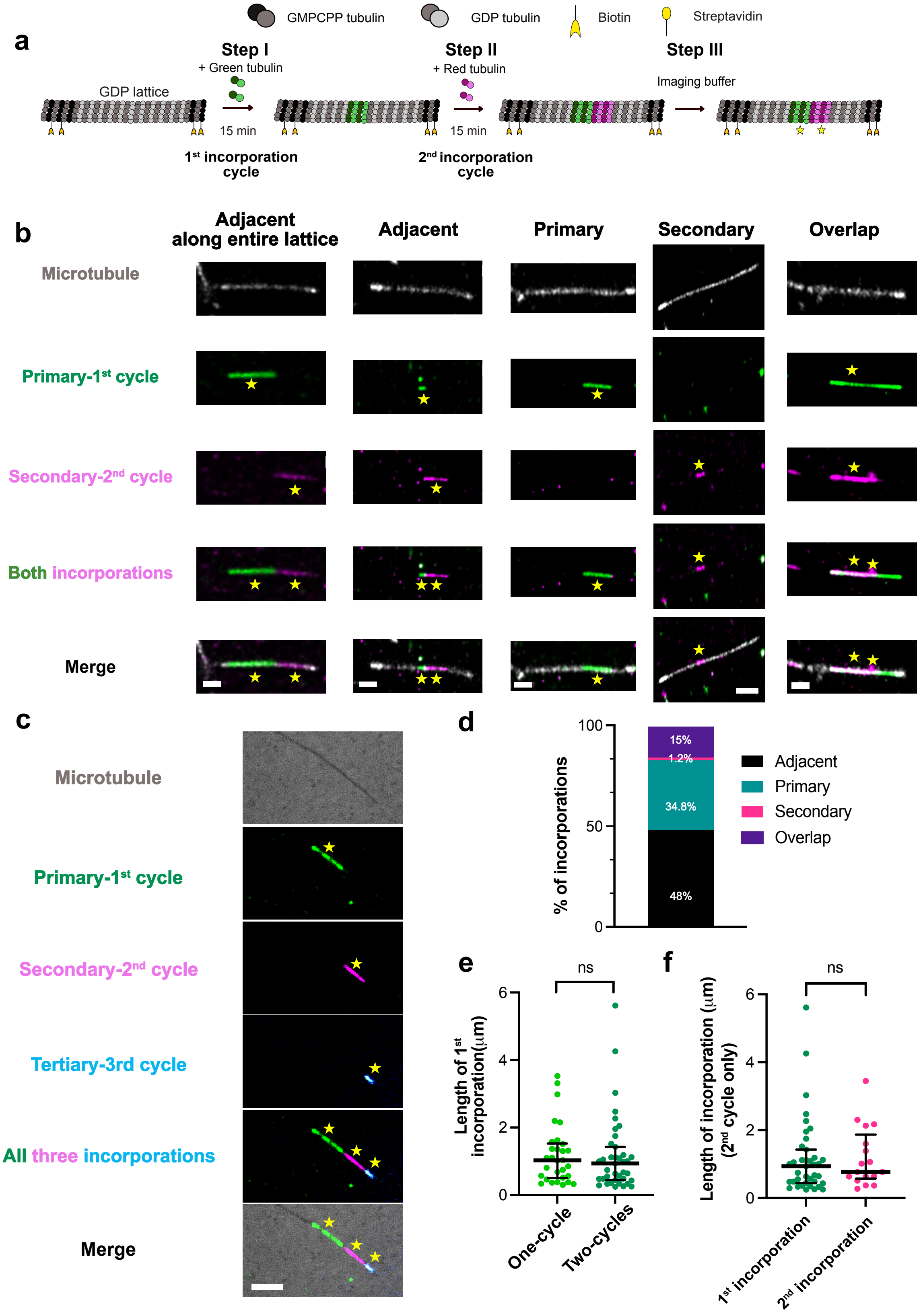

Fig 3.2: **(a)** Schematic of experimental setup for two cycle tubulin incorporation experiments. Prepared capped GDP-microtubules are flushed into streptavidin coated SiPEG-Bt passivated surfaces. The microtubules were first incubated in a solution of free, green-labelled tubulin for 15 min (Step I), followed by a second incorporation step with red-labelled tubulin (shown in magenta here) (Step II) followed by washout and imaging (Step III). **(b)** Exemplary images showing the pattern of incorporations from two-cycle incorporation experiments. Scale bars: 2 μm. **(c)** Exemplary images showing the pattern of incorporations from three-cycle incorporation experiments. Scale bar: 5 μm. **(d)** Classification of incorporations into adjacent, primary, secondary, and overlap (n= 39 incorporations from three independent experiments). **(e)** Comparison of the length of primary-1st incorporations between one and two cycle tubulin incorporation experiments. Black line represents the median and bars represent the inter-quartile range. p= 0.4609 (ns; not significant) using Mann-Whitney test (n= 30 incorporations for one cycle and n= 39 incorporations for two cycles from three independent experiments). **(f)** Comparison of the length of primary-1st incorporations and secondary-2nd incorporations in two-cycle tubulin incorporation experiments. Black line represents the median and bars represent the inter-quartile range. p= 0.5626 (ns; not significant) using Mann-Whitney test (n= 39 incorporations for 1st incorporations and n= 17 for 2nd incorporations from three independent experiments).

3.2.2 Kinetic Monte Carlo (KMC) model recaptures experimental trends

(The simulation results presented in this section were performed and analyzed by Amir Zablotsky under the supervision of Dr Karin John, LIPhy, Université Grenoble Alpes.)

To further explore how lattice defects influence tubulin turnover, along with collaborators we used a simple, robust Monte Carlo model (previously described in Biswas *et al.*, 2025; Schaedel *et al.*, 2019) to model defect mobility and tubulin turnover. We modeled the defect movement for monomer vacancies that are known to be most frequent *in vitro* and lead to multi-seam structures. The schematic of a microtubule cross-section with a monomer vacancy is shown in **Fig 3.3 ai**.

Such vacancies lead to lattice-transitions with heterotypic contacts amidst homotypic contacts at the seam (**Fig 3.3 aii**). In the model, we assumed that homotypic contacts are stronger and more stable. As shown in **Fig 3.3aii**, the dimer below the vacancy has stable lateral homotypic contacts, whereas the dimer above has weaker lateral heterotypic contacts, thus rendering it more unstable. The detachment rate of the dimers above and below the defect was computed according to the bond energies of the respective lateral contacts, like mentioned previously (Biswas *et al.*, 2025). The difference in stability of the lateral bonds at homotypic -> heterotypic transitions found at the seam, is computed using the ratio $\frac{\Delta G(\text{lat,hetero})}{\Delta G(\text{lat,homo})}$.

$\frac{\Delta G(\text{lat,hetero})}{\Delta G(\text{lat,homo})} = \mathbf{1}$ would represent lattice symmetry and translate to both types of lateral bonds having the same bond energies. Whereas values less than 1 would correspond to weaker heterotypic contacts. Evidence from cryo-EM studies indicate that these transitions lead to increased lateral gaps between protofilaments (LaFrance *et al.*, 2022) and microtubules exhibiting ectopic A-lattice (heterotypic) seams were reported to depolymerize at an accelerated rate (Katsuki *et al.*, 2014). These findings indicate that homotypic to heterotypic transitions are inherently weak regions and suggest that lower values of $\frac{\Delta G(\text{lat,hetero})}{\Delta G(\text{lat,homo})}$ may be more physiologically relevant.

In our simulations, we modeled sequential cycles of tubulin detachment and incorporation to mimic experimental conditions. For simplicity, we model the propagation of defects along a single protofilament only. Each step constitutes one dimer detachment and a dimer being incorporated into the lattice.

We simulated dimer loss and incorporation over 2 subsequent iterations of equal steps. N_{step} is the total number of exchanged dimers at the end of both the 1st and 2nd incorporation cycles. We then plotted the ratio of 1st incorporation length (L_{1st}) to 2nd incorporation length (L_{2nd}) across varying values of $\frac{\Delta G(\text{lat,hetero})}{\Delta G(\text{lat,homo})}$. At $\frac{\Delta G(\text{lat,hetero})}{\Delta G(\text{lat,homo})}$ =1 (lattice symmetry), we see that the ratio is 0.5, indicative of diffusive motion, but at relevant values (<0.99) denoting weaker heterotypic bonds, the ratio of incorporation lengths remained equal to 1, indicating ballistic motion (**Fig 3.3b)**.

These results recapture experimentally observed trends seen in **Fig 3.2f.** We can thus conclude that lattice asymmetry or the presence of weaker lateral heterotypic bonds mediate ballistic defect propagation.

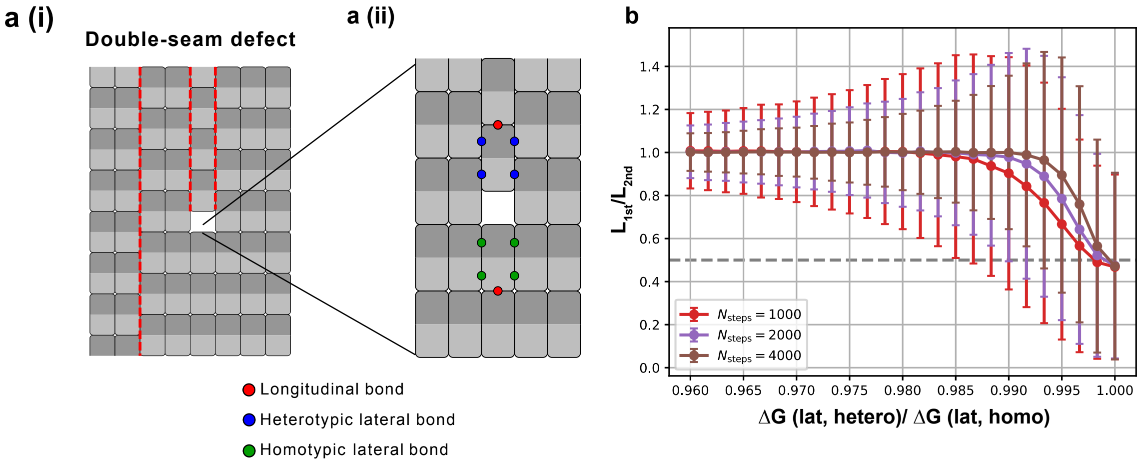

Fig 3.3: (a) (i) Schematic of a microtubule cross-section with double-seams that induce the creation of a monomer defect. **(a)(ii)** At the monomer vacancy, we observe lattice transitions from dimers having homotypic -> heterotypic contacts. Based on the difference in bond energies, a seam penalty (indicated as the ratio of bond energies of the heterotypic to the homotypic) can be quantified. **(b)** Plot of the ratio of 1st to 2nd incorporation lengths over a range of ratios denoting the difference between bond strengths.At physiologically relevant values, the ratio is one, indicating equivalent lengths and ballistic mode of propagation.

3.3 Study 3: Curvature accelerates tubulin turnover

3.3.1 Defect-dependent nature of tubulin turnover in response to bending stress

As tubulin exchange or turnover in the microtubule lattice is mediated by defects, I next asked whether the increased tubulin turnover observed in bent microtubules is also dependent on the presence of defects. I decided to test this simply by manipulating the frequency of defects by preparing capped-GDP-microtubules using slow-growth conditions. It was previously shown that microtubule growth rate and defect frequency are dependent on tubulin concentration used for growth (Schaedel *et al.*, 2019). Accordingly, I prepared 2 sets of capped GDP-microtubules- one grown under slow growth conditions (6 μM, **having fewer defects**) and one set under normal-growth conditions (10 μM, **relatively having more defects**) as shown in **Fig 3.4a**. Both sets of microtubules were then subjected to static curvature assays, and the pattern and frequency of tubulin incorporation spots were then analyzed as described in Nandakumar *et al.*, Chapter 2.

It was observed that even under slow-growth conditions, bent microtubules showed a higher frequency of tubulin incorporations than straight microtubules (**Fig 3.4b**), indicating that the effect of curvature still triggers enhanced local tubulin loss and consequent incorporation of new tubulin subunits (self-repair). However, I found that the difference in incorporation frequency between straight and bent microtubules (**Fig 3.4c**), decreased from 10-fold (under normal growth conditions) to 3-fold (under slow growth conditions), indicating that microtubule tubulin turnover in response to bending stress is also defect-dependent.

These observations suggest that the enhanced tubulin exchange observed in bent microtubules (Study 1-Nandakumar *et al.*) likely arises from tubulin loss due to defect mobility that is further accelerated when microtubules are subjected to bending stress.

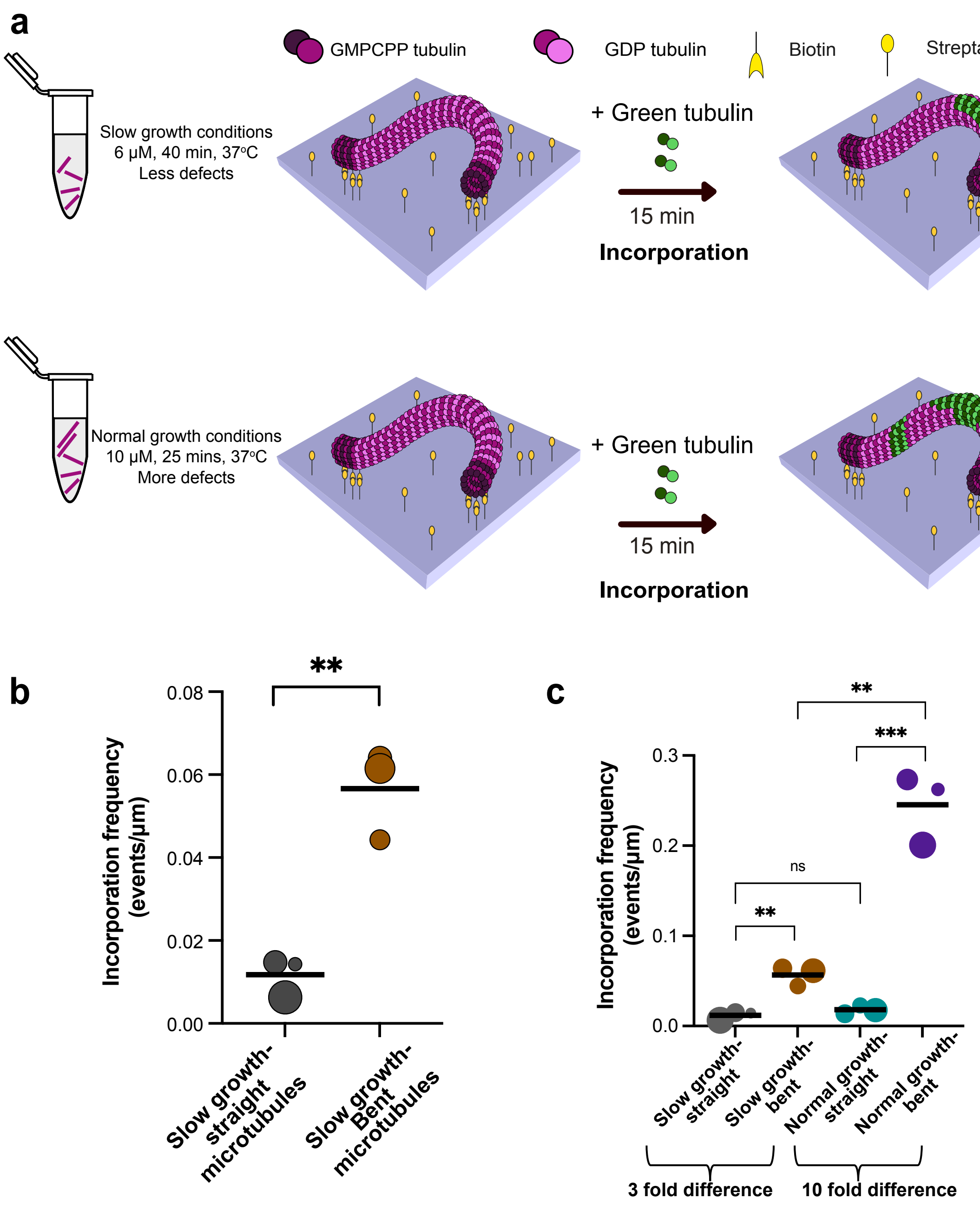

Fig 3.4: (a) Schematic of experimental setup: Capped GDP-microtubules were prepared under both slow (6 μM) and normal growth (10 μM) conditions to control the defect frequency. Both samples were subjected to static curvature incorporation assays. **(b)** Bubble plot showing a higher proportion of incorporations in bent relative to straight microtubules under slow growth conditions. Bubble size scales with the total microtubule length analyzed. Black line represents the mean. Data from 3 independent experiments. p= 0.0027 using unpaired t-test. Total microtubule lengths analyzed: 140, 195, 248 μm for bent-slow growth and 135, 317 and 139 μm for straight-slow growth. **(c)** Bubble plot comparing incorporation frequencies in straight and bent microtubules under both slow and normal growth conditions. Bubble size scales with local microtubule length analyzed. Black line represents the mean. From 3 independent experiments. p= 0.0013 (Bent-slow growth vs bent-normal growth), p= 0.0006 (Bent-normal growth vs straight-normal growth), p= 0.1788 (not significant, ns; straight-normal growth vs straight-slow growth) using unpaired t-test. Total microtubule lengths analyzed: 140, 195, 248 μm for bent-slow growth; 135, 317 and 139 μm for straight-slow growth; 294, 350 and 103 μm for bent- Normal growth and 311, 366 and 248 μm for straight-normal growth.

3.3.2 Two-cycle tubulin incorporation in bent microtubules

The intriguing observations in the previous section imply that in bent microtubules, tubulin exchange might result from a combination of tubulin loss in response to curvature as well as from defect mobility. This prompts the question: "To what extent does each of these processes contribute to the overall tubulin turnover observed in bent microtubules?". To address this, I repeated two-cycle incorporations with bent microtubules. This will enable us to distinguish between tubulin loss arising from bending stress and that driven by defect mobility. If curvature-induced tubulin loss is the dominant process, we should observe only primary 1st cycle incorporations with minimal subsequent incorporations from the second cycle.

Accordingly, capped GDP-microtubules were prepared under normal-growth conditions (Atto-647 labelled, denoted in grey in **Fig 3.5a**) and subjected to bending stress using the static curvature assay mentioned in Nandakumar *et al.* (Step I). They were then incubated first in a solution of free green labelled tubulin (Step II) for 15 min, followed by a second incorporation step with red-labelled tubulin for 15 min (shown in magenta here) (Step II), followed by washout and imaging (Step III). The pattern of 1st and 2nd incorporations observed were estimated (**Fig 3.5b**).

Quantifications revealed that the major proportion of incorporations were primary (49%) in nature (**Fig 3.5d**). The increased % of primary (only 1st) incorporations in bent microtubules relative to straight microtubules suggests that self-repair (within 15 min) helps counteract tubulin loss caused by local curvature. This can also be seen in the reduced incorporation frequency of 2nd cycle incorporations when compared to the 1st cycle incorporations in bent microtubules (**Fig 3.5c**). Interestingly, I found about 37% of the incorporations to show a sequential (adjacent) pattern. This suggests that defect propagation persists even under bending stress. These findings imply that local curvature-induced tubulin loss might act in tandem with defect-driven lattice dynamics to accelerate tubulin exchange in bent microtubules.

It is thus essential to further investigate the interplay between local curvature and defect mobility in the microtubule lattice, particularly the effect of local curvature on the bonds between tubulin dimers, as previous modelling studies have implicated that microtubules undergo cross-sectional flattening when bent (Memet *et al.*, 2015). It would also be interesting to explore how the effect of bending stress due to local curvature propagates in a lattice free of defects.

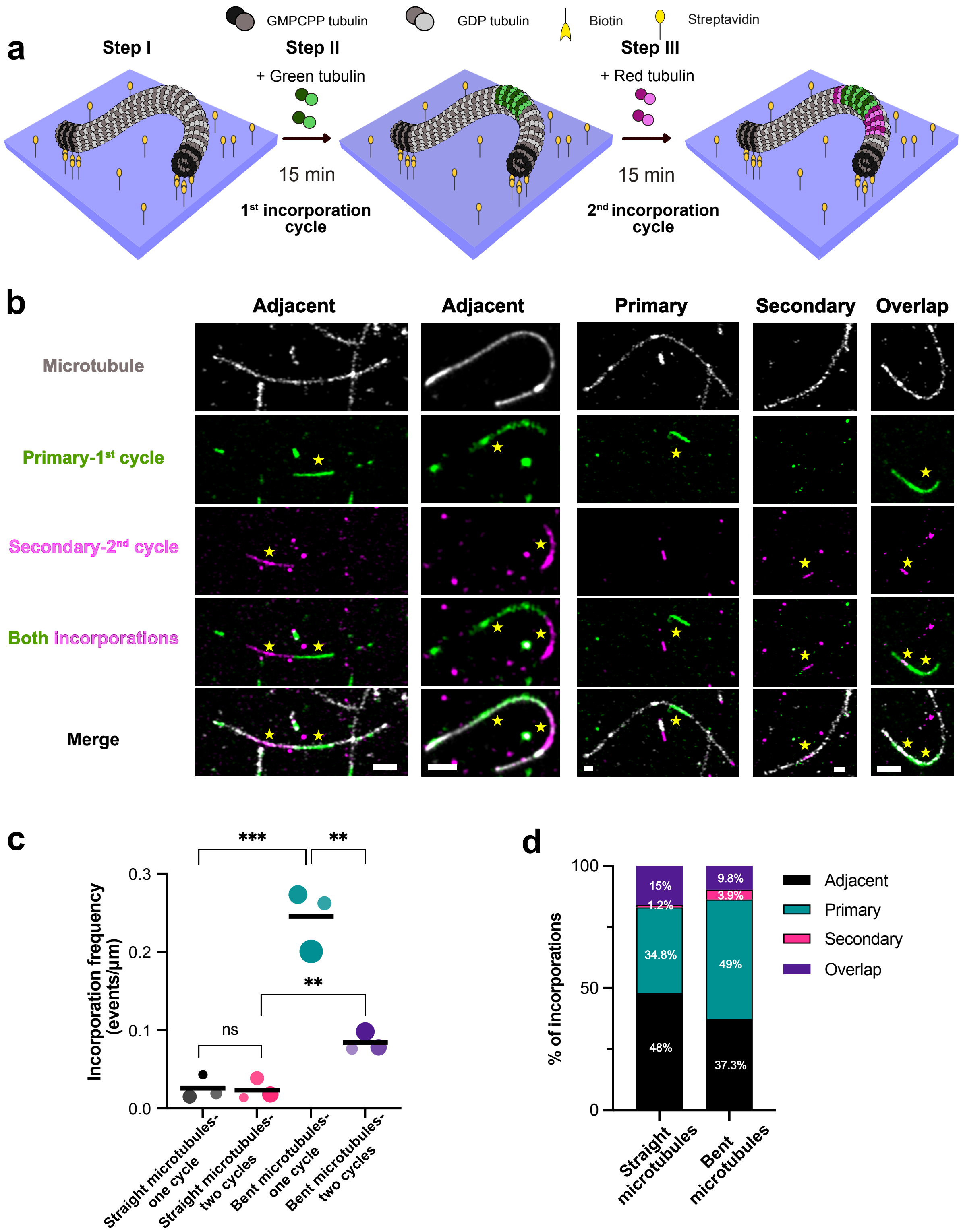

Fig 3.5: **(a)** Schematic of experimental setup for two-cycle tubulin incorporation experiments in bent microtubules. Prepared capped GDP-microtubules are flushed into streptavidin-coated SiPEG-Bt passivated surfaces. Alternating flow direction during chamber loading results in microtubules adopting bent shapes (Step I). The microtubules were first incubated in a solution of free green-labelled tubulin for 15 min (Step II) followed by a second incorporation step with red-labelled tubulin (shown in magenta here) (Step III) followed by washout and imaging. **(b)** Exemplary images showing the pattern of incorporations. Scale bar: 2 µm **(c)** Bubble plot showing decrease in frequency of 2nd cycle incorporations relative to 1st cycle incorporations in bent microtubules, indicating effective defect elimination. Bubble sizes scale with the total microtubule length analyzed. Each circle represents an independent dataset from three

independent experiments. Black lines represent the mean. p= 0.84 (not significant, ns; straight one cycle- straight one cycle); p=0.0024 (bent-one cycle vs bent-two cycle); p=0.0044 (straight-two cycles vs bent-two cycles); p=0.0008 (straight-one cycle vs bent-one cycle). Total microtubule lengths analyzed**:** 257, 140 and 92 μm for bent-two cycles; 117, 72, and 45 μm for straight-two cycles; 294, 350 and 103 μm for bent-one cycle and 311, 366 and 248 μm for straight-one cycle. **(d)** Comparison of the pattern of incorporations between straight and bent microtubules (n=35 incorporations for straight microtubules and n= 51 for bent microtubules from three independent experiments).

3.3.3 Coarse-grained dimer-scale mechanical model shows local curvature accelerates tubulin loss and microtubule breakage

To gain further insights into how curvature (bending stress) affects microtubule lattice dynamics, along with our collaborators, we developed a dimer-scale coarse-grained mechanical model of a microtubule based on our experimental results.
(The simulation results presented in this section were performed and analyzed by Amir Zablotsky under the supervision of Dr Karin John, LIPhy, Université Grenoble Alpes).

As shown in **Fig 3.6a,** the fundamental unit of the mechanical model is the tubulin dimer, modelled as a rigid molecule comprised of two spherical monomers of diameter σ, two lateral α−binding sites, two lateral β−binding sites, and two longitudinal binding sites (one for the α and the other for the β monomer). The two monomers are placed one on top of the other, so the separation between their centres is equal to σ. Then, the longitudinal and lateral binding sites are placed over the surface of the monomers so that the ground state of an ensemble of dimers is a straight microtubule with the canonical structure. To achieve this, lateral binding sites on both sides of the dimer have a slight offset in the dimer's longitudinal direction to reproduce the 3-start helix, and they are positioned forming a slight angle with the dimer centreline to reproduce the 13 protofilament (PF) lattice.

From the attractive potentials between the dimers (See Annex-1), we can identify the total lattice binding energy (Eq. 1) as the binding energy of a fully surrounded dimer at equilibrium, and the lattice anisotropy (Eq. 2) to quantify the relative strength between the interactions with the longitudinal and lateral dimer neighbours:

$$\Delta G_b = 2\Delta \mathrm{Glong} + 4\Delta \mathrm{Glat} \qquad - (1)$$

$$A = \frac{\Delta \mathrm{Glong}}{2\Delta \mathrm{Glat}} \qquad - (2)$$

To study the effects of curvature on the lattice, the microtubule was bent by applying opposing forces at both ends (in the longitudinal direction) of a straight microtubule (See **Fig 3.6b)**. This was achieved by applying a force of magnitude 'F' to a single dimer close to the extreme ends of the microtubule. The force was applied until both ends of the microtubule are at a desired distance 'd' (corresponding to a resulting curvature). Then both the forces and velocities of the dimers are

set to zero. Following a transient regime, all the dimers accommodate to the configuration with the minimum energy.
The resulting equilibrium configuration is the static microtubule with a macroscopic strain $\varepsilon = (d - L_{MT}) = L_{MT}$, where L_{MT} is the length of the microtubule (See **Fig 3.6b)**. We can then measure different quantities such as the dimers' position, stress, potential energy, etc. When analysing the stress along the lattice of a microtubule, we measure the stress tensor of each dimer and then use it to compute the signed Von Mises stress (refer to Annexure 1 for further details). Using this model, we then set out to investigate microtubule breakage, stress propagation, and defect-related lattice dynamics under bending stress. All simulations are performed using the LAMMPS molecular dynamics package (Thompson et al., 2022).

Curvature exponentially increases the rate of microtubule breakage

We first modelled the effect of curvature on a perfect lattice (free of defects). Once the microtubule starts to bend, we observe cross-sectional flattening (as reported in previous modelling studies- Memet *et al.*, 2015). This causes the dimers constituting the protofilaments on the inner side of the curved microtubule to be subjected to compressive stress that increases towards the innermost protofilament (PF No. 1), while the dimers on the outer side experience tensile stress that increases towards the outermost protofilament (PF No. 8) (**Fig 3.6c).**

As a critical curvature is reached, the lattice develops a kink. At a strain of 0.382, stress is localized at the sides of the developed kink (**Fig 3.6c)**. The stress then spreads in the lateral direction (**Fig 3.6c)**, resulting in the microtubule eventually undergoing breakage. Quantifying the maximum local curvature of buckling microtubules revealed an average maximum of 2.5 μm^{-1} (See Fig 4h of Nandakumar *et al.*, Chapter 2). **Fig 3.6d** captures the evolution of breakage of a bent microtubule having a maximum local curvature $c \simeq 2.5\ \mu m^{-1}$. The first dimer detaches from the inner side of the bent microtubule, and the hole left behind continues to grow in size via successive detachment of neighbouring dimers. Once the hole propagates across all 13 protofilaments, the microtubule breaks.

A plot of microtubule breakage rate as a function of local curvature reveals an exponential increase in breakage rate with increasing curvature (blue line in **Fig 3.6e).** These results recapture our observations of breakage of buckling microtubules at high curvatures (refer to Fig 4h of Nandakumar *et al.*, Chapter 2). We then repeated the simulations for microtubules with defects by introducing a dimer defect. We find that the microtubule breakage rate is higher in the case of microtubules with dimer-sized hole, as the first step of lattice disruption-dimer loss has already been fulfilled (**Fig 3.6e).**

We then estimated the off-rate of a dimer in a perfect lattice with increasing curvature (**Fig 3.6f)** by measuring the potential energy of each dimer and using the Arrhenius equation. The off rate increases with curvature, reaching values up to four times higher than what we see for a perfect lattice. Notably, dimers located at the innermost and outermost protofilaments of the bent microtubule have a higher detachment rate, related to the increased stress (shown below).

It is important to keep in mind that whilst curvature increases the detachment rate of a dimer by four-fold, the enhancement of detachment rates caused by the presence of a pre-existing defect can reach several orders of magnitude even at curvature = 0 μm^{-1} (Biswas *et al.*, 2025). That means as soon as the first dimer is removed, the resulting vacancy dramatically destabilizes the neighbours in its vicinity, accelerating tubulin loss. However, curvature also accelerates or changes the off rate around a defect. In this way, curvature and defects may act in tandem to accelerate tubulin loss and promote breakage.

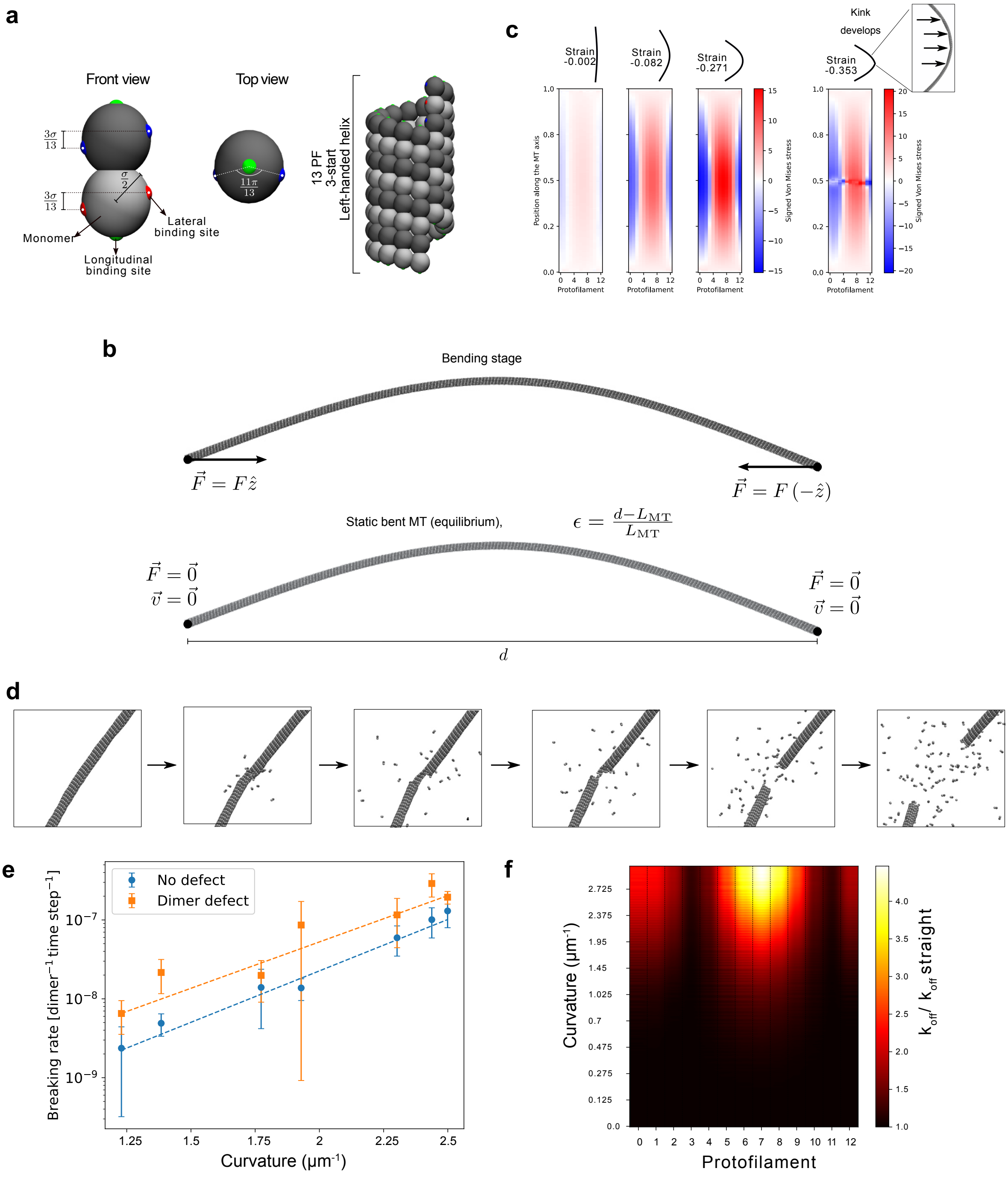

Fig 3.6: **(a)** Three-dimensional representation of the dimer model. Each dimer is treated as a rigid molecule, so the relative positions of the monomers and binding sites are fixed. Fifty-two dimers are arranged in the equilibrium configuration, resulting in a straight canonical structure microtubule. **(b)** Two forces equal in magnitude and opposite

in direction are applied to a dimer at each extreme of the MT in order to bend it. Once the tips are at the desired distance from each other, they are kept in place by setting the force and velocity to zero, and after a transient regime the MT reaches its equilibrium configuration. **(c)** Stress along the lattice in four bending stages: The first three correspond to low to high strain in the non-kink regime, and the fourth one corresponds to a microtubule that develops a kink in the lattice (indicated by black arrows in the zoomed-in microtubule inset). Kinks form at the lattice when a critical local curvature is surpassed. **(d)** Snapshots of a bent microtubule breaking in the high-strain regime. **(e)** Microtubule breakage rate increases exponentially with the local curvature (blue line). Breakage rate increases in the presence of dimer defects (Orange line). **(f)** Detachment rate of a fully surrounded dimer (perfect lattice) as a function of its protofilament number and local curvature, normalized by the detachment rate of the fully surrounded dimer in the straight configuration.

Presence of defects and curvature destabilizes lateral contacts

We then modelled how the presence of a dimer defect influences stress propagation in a bent microtubule. **Fig. 3.7a** shows a grid map depicting the difference in Von Mises stress of dimers that are in the vicinity of a dimer-sized hole in a bent microtubule. Across all protofilament positions, the stress difference was computed by comparing the stress value of each dimer in a bent, defect-containing lattice with that in a bent, perfect lattice.

Interestingly, the analysis revealed a distinct redistribution of local stress around the defect. While the stress on the lateral neighbours increases, the stress on the longitudinal neighbours is slightly reduced, suggesting that dimer vacancies modulate local stress distribution in a significant manner. Upon introduction of a dimer defect in the lattice of a bent microtubule (PF i, row n in **Fig. 3.7b** below), the remaining dimers on the lattice accommodate to minimize energy given this new condition. The dimers directly above and below the vacancy, (i ; n − 1) and (i ; n + 1), are now missing a longitudinal bond that was used to enforce curvature in the protofilament, thus allowing them to straighten by shortening the remaining longitudinal bond.
But due to the lateral bonds with their neighbours in protofilaments i − 1 and i + 1 (See **Fig. 3.7b)**, the straightening of dimers (i ; n − 1) and (i ; n + 1) produces a slight straightening in their lateral neighbours as well. However, these lateral neighbouring dimers still have the second longitudinal bond with dimers at the positions (i −1; n) and (i +1; n). Therefore, stress increases in the lateral neighbours of the hole due to the "pulling" action of their straightening longitudinal neighbours.

Thus, dimers positioned above and below the defect along the protofilament (in the longitudinal directions) are stabilized, and this is reflected in the decrease in their stress value. In contrast, the dimers at the sides of the hole in the lateral direction are destabilized as seen by the increase in their stress values (**Fig. 3.7a)**.

The absence of a dimer allows the longitudinal neighbours to release some of the pre-stress in the lattice caused by curvature. But at the same time, it further weakens/destabilizes the lateral neighbours surrounding the defect and promotes their detachment. In this way, the lattice anisotropy and detachment rate of neighbouring dimers are also affected.

We next quantified how lattice anisotropy varies with increasing curvature (**Fig. 3.7c**.) At curvature = 0 μm^{-1}, we see that the lattice anisotropy is A = 1.2, as we defined for a straight lattice, and as the curvature grows, this value decreases. The lattice anisotropy is a measure of how strong longitudinal bonds are when compared to the lateral bonds, so a higher anisotropy means that the breakage will tend to propagate in the longitudinal direction, while a smaller anisotropy speeds up the propagation around the cross-section in the lateral direction.

To further investigate how curvature affects dimer detachment rate in the vicinity of a defect, we calculated the detachment rate of the longitudinal, k_{14} (c), and lateral neighbours, k_{22} (c), in the vicinity of a defect. We then compared this to the corresponding rate in the same bent microtubule but without a defect (k_{24} (c)). **Fig 3.7d** shows these detachment rates of the dimers longitudinal and lateral to the defect, normalized by k_{24} (c), to specifically estimate the defect's contribution to the detachment rate. As curvature increases, the detachment rate for the longitudinal neighbours of the hole reduces, while the detachment rate for the lateral neighbours increases. This is consistent with our findings on stress distribution, wherein we observed that longitudinal neighbours get stabilized and the lateral ones are destabilized.

These results indicate that while vacancies in straight microtubules preferentially propagate along the longitudinal direction, increasing local curvature redirects and enhances defect propagation laterally, facilitating faster breakage.
Thus, local curvature has a two-fold effect:
(1) It exponentially increases the detachment rate of tubulin dimers,
(2) Promotes lateral propagation of tubulin loss by decreasing lattice anisotropy, leading to faster breakage.

However, it is important to note that the magnitude of curvature-induced enhancement in dimer-detachment rates is orders of magnitude smaller than that caused by a pre-existing defect. In other words, while bending destabilizes lateral contacts, its destabilizing effect is secondary to that produced by a defect. This implies that in bent microtubules, lattice dynamics is primarily mediated by the presence and mobility of defects, with curvature serving as an amplifying factor that further promotes tubulin loss and defect propagation.

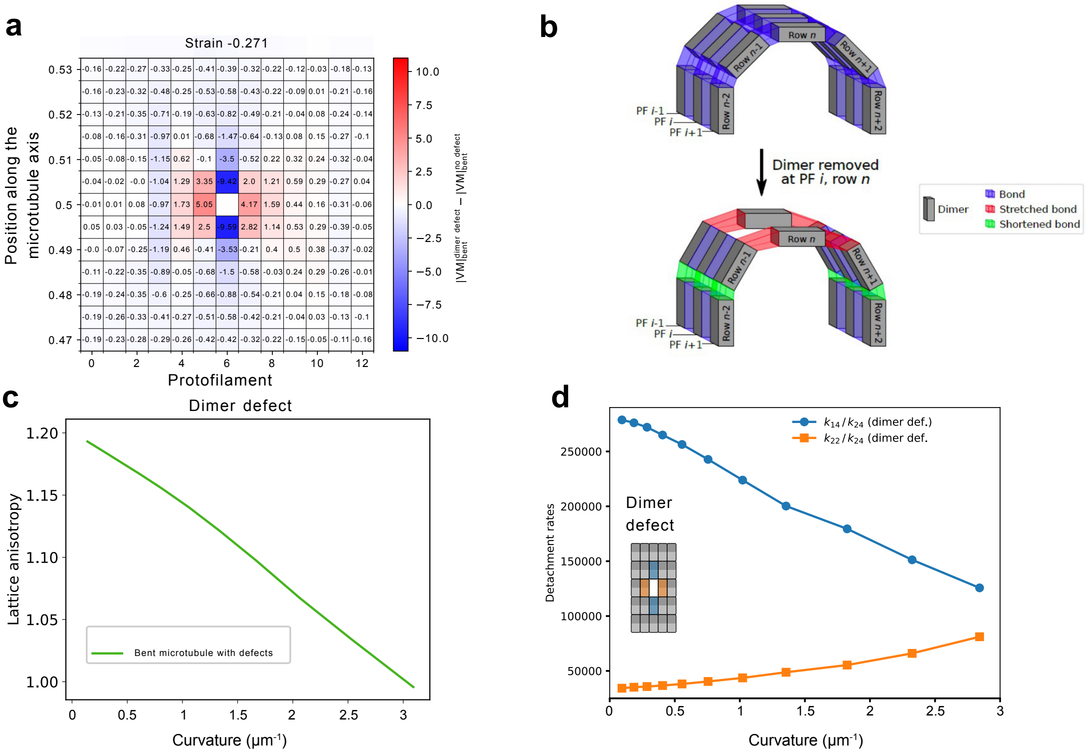

	0		2		4		6		8		10		12
0.53	-0.16	-0.22	-0.27	-0.33	-0.25	-0.41	-0.39	-0.32	-0.22	-0.12	-0.03	-0.18	-0.13
	-0.16	-0.23	-0.32	-0.48	-0.25	-0.53	-0.58	-0.43	-0.22	-0.09	0.01	-0.21	-0.16
0.52	-0.13	-0.21	-0.35	-0.71	-0.19	-0.63	-0.82	-0.49	-0.21	-0.04	0.08	-0.24	-0.14
	-0.08	-0.16	-0.31	-0.97	0.01	-0.68	-1.47	-0.64	-0.13	0.08	0.15	-0.27	-0.1
0.51	-0.05	-0.08	-0.15	-1.15	0.62	-0.1	-3.5	-0.52	0.22	0.32	0.24	-0.32	-0.04
	-0.04	-0.02	-0.0	-1.04	1.29	3.35	-9.42	2.0	1.21	0.59	0.29	-0.27	0.04
0.5	-0.01	0.01	0.08	-0.97	1.73	5.05		4.17	1.59	0.44	0.16	-0.31	-0.06
	0.05	0.03	-0.05	-1.24	1.49	2.5	-9.59	2.82	1.14	0.53	0.29	-0.39	-0.05
0.49	-0.0	-0.07	-0.25	-1.19	0.46	-0.41	-3.53	-0.21	0.4	0.5	0.38	-0.37	-0.02
	-0.11	-0.22	-0.35	-0.89	-0.05	-0.68	-1.5	-0.58	-0.03	0.24	0.29	-0.26	-0.01
0.48	-0.19	-0.24	-0.35	-0.6	-0.25	-0.66	-0.88	-0.54	-0.21	0.04	0.15	-0.18	-0.08
	-0.19	-0.26	-0.33	-0.41	-0.27	-0.51	-0.58	-0.42	-0.21	-0.04	0.03	-0.13	-0.1
0.47	-0.19	-0.23	-0.28	-0.29	-0.26	-0.42	-0.42	-0.32	-0.22	-0.15	-0.05	-0.11	-0.16

Fig 3.7: (a) Schematic representation of the bonds' changes in Von Mises stress when a dimer defect is introduced to the lattice of a curved microtubule. **(b)** Schematic representation showing how lateral bonds are destabilized in the vicinity of a dimer defect in a bent microtubule. **(c)** Effective lattice anisotropy in the surroundings of a dimer defect as a function of the local curvature. **(d)** Detachment rate of the longitudinal and lateral neighbours of a dimer defect, normalized by the detachment rate of a fully surrounded dimer, as a function of the local curvature.

3.4 MAPs modulate defect mobility-insights from Biswas *et al.*, 2025

In cells, microtubules exist in the presence of MAPs, and many MAPs have been implicated in modulating microtubule dynamics. CLASP 2α was shown to promote tubulin incorporation along the lattice (Aher *et al.*, 2020). Severing MAPs like Katanin are known to recognize defects and selectively sever microtubules with defects (Davis *et al.*, 2002). It is interesting to then ask if MAPs (particularly those that are known to confer stability) also modulate defect mobility and tubulin turnover? In this section, I highlight the results from a recent study from my lab that highlight how the neuronal MAP- Tau influences tubulin exchange along the microtubule lattice.

In neurons, microtubules exist in association with the neuronal MAP-Tau. In a recently published study from our lab, we showed that Tau can accelerate defect mobility and, consequently, tubulin exchange along the microtubule lattice (Biswas *et al.*, 2025).

(The two-cycle incorporation experiments presented in this section were performed and analyzed by Subham Biswas using the protocol I had established. I am a co-author of this publication.)

In this study, it was found that the presence of nanomolar amounts of Tau led to longer and more frequent incorporations (**Fig 3.8 a, b**). Performing 2-cycle tubulin incorporation experiments using the assay described in section 3.2 (**Fig 3.8c**), the study analysed the pattern of incorporations (**Fig 3.8d**) and found that a higher proportion (50%) were adjacent in nature and 25% comprised of just primary incorporations (**Fig 3.8e**), indicating that Tau mediates defect elimination from the lattice. Using a KMC model, similar to the one detailed in section 3.2.2, it was found that Tau mediates this effect by increasing lattice anisotropy to A= 2.1, thereby strengthening longitudinal bonds and weakening lateral bonds. In this manner, Tau promotes movement of defects and, in consequence, tubulin incorporation in the longitudinal direction.

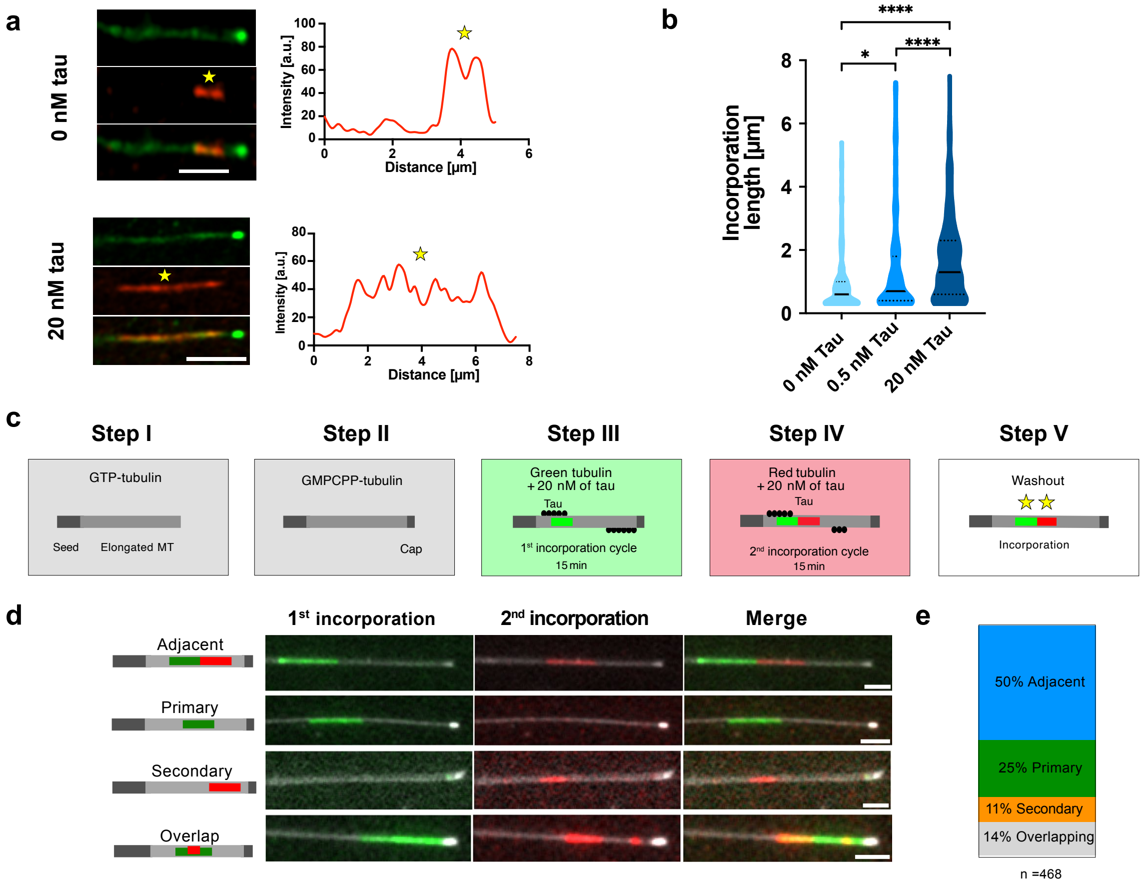

Fig 3.8 (taken from Biswas *et al.*, 2025): Tau accelerates defect mobility along the microtubule lattice: **(a)** Longer tubulin incorporations (in red) along the microtubule lattice (green) in the presence of 20 nM Tau. Scale bar: 5 µm. Yellow stars denote incorporations. **(b)** Length of tubulin incorporation stretches increase in the presence of tau. Thick black lines represent the median and inter-quartile range. P = 0.033, P < 0.0001 and P < 0.0001 for 0 nM versus 0.5 nM, 0.5 nM versus 20 nM and 0 nM versus 20 nM, respectively. (n= 126 incorporations analyzed for 0 nM, 187 incorporations for 0.5 nM and 249 incorporations for 20 nM Tau from 3 independent experiments. **(c)** Schematic of *in vitro* experimental setup used to assess defect mobility in presence of Tau. GDP-microtubules were elongated from seeds and capped using GMPCPP-tubulin (Step I and II). The capped-GDP microtubules (shown in grey) were first incubated in a solution of free, green-labelled tubulin & 20 nM Tau for 15 min (Step III) followed by a second incorporation step with red-labelled tubulin and 20 nM Tau (Step IV) followed by washout and imaging (Step V). **(d)**

Inset showing pattern of incorporations. Scale bar: 5 µm. **(e)** Classification of pattern of first and second incorporations in the presence of 20 nM Tau (n=468 incorporations from three independent experiments).

3.5 Preliminary conclusions and outlook

The presence of lattice defects and irregularities in the microtubule lattice thus serves as hotspots of structural plasticity that allow for localized lattice remodeling, tubulin turnover, and adaptation. Beyond being imperfections in the lattice, defects help tune microtubule dynamics in response to stress and the presence of MAPs.

The first study presented above extends the observations reported in Schaedel *et al.*, 2019. Using a combination of two-cycle tubulin incorporation experiments with a simple kinetic Monte-Carlo model, it is shown that the process of tubulin turnover is dependent on defect propagation along the lattice until it is eliminated or anneals with another defect. By correlating experimentally observed incorporation lengths with KMC model predictions from our collaborators, we show that for multi-seam defects, the nature of defect propagation is predominantly ballistic in nature. Further work is needed to establish if the direction of propagation is biased, based on microtubule polarity (Do defects and, in consequence, tubulin incorporation propagate mainly towards the growing plus end?). This can be explored by performing two-color tubulin incorporation using microtubule seeds that are polarity marked to identify plus-ends. Alternatively, picomolar amounts of kinesin-1-GFP motors (that walk towards the plus-end) can be flushed in after the experiment is completed, to identify plus-ends.

Whilst the present KMC model focuses on modelling multi-seam defects that seem to propagate predominantly ballistically in nature, diffusive defect motion can also occur. Modelling of monomer vacanices along an A-lattice seam is currently ongoing to gain more clarity in this direction. The stochastic and slow propagation of diffusive defects may result in incorporations of the size of a few nm that may fall below our detection limits. Thus, an important next step would be to get insights from modelling simulations on the average no: of dimers (incorporation length) that these diffusively moving defects travel across, and if this can be detected using current imaging setups.

Recent advances in cryo-ET techniques have helped identify the presence of lattice openings and discontinuities in cellular microtubules (Guyomar *et al.*, 2022; Chakraborty *et al.*, 2020; Atherton *et al.*, 2018). These findings suggest that though microtubule nucleation and protofilament numbers are regulated in cells, the microtubule lattice *in vivo* is far from being uniform. This emphasizes the physiological relevance of exploring the role of lattice defects in influencing lattice remodeling. Future studies combining high-throughput cryo-ET with *in vitro* reconstitution experiments under controlled growth conditions, particularly using cell-lysates, may help gain insights into the spatial distribution and nature of lattice defects. Cryo-EM studies on microtubules subjected to incorporation assays with free gold-labelled tubulin may help us visualize zones of tubulin turnover directly.

In the second half of this chapter, it is seen that effectors modulate lattice dynamics by modulating the inherent lattice anisotropy, influencing defect mobility, and, in consequence, tubulin turnover.

The neuronal MAP tau accelerates defect mobility in the longitudinal direction by increasing lattice anisotropy (by stabilization of longitudinal contacts and weakening of lateral contacts). In this way, longer tubulin incorporation stretches along the length of the microtubule were seen in the presence of 20 nM Tau (Biswas *et al.*, 2025).

In contrast, increasing local curvature destabilizes lateral contacts between tubulin dimers, decreasing the lattice anisotropy and promoting defect mobility in the lateral direction, thus leading to increased tubulin turnover across protofilaments. This matches our findings of higher % of lateral tubulin incorporation that was found in bent microtubules when compared to straight microtubules (**Supplementary Fig 1f** in manuscript Nandakumar *et al.*; Chapter 2). In this way, curvature acts as a key amplifier of microtubule turnover or breakage.

These findings can be extended to further comprehend our findings observed in buckling microtubules. Modelling studies found that the walk of motors alone can enhance lattice plasticity and accelerate tubulin loss and turnover (Lecompte and John., 2023). Combined with my findings in Study 1, we can conclude that the enhanced breakage observed in buckling microtubules (**Fig 4** in the manuscript Nandakumar *et al.*) results from tubulin loss induced by motor-motility that is further amplified by curvature. Buckling microtubules are subjected to continuous deformation, which may account for a tubulin loss rate that can no longer be balanced by incorporation of new tubulin subunits, thus resulting in buckling microtubules breaking even in the presence of free tubulin. In this way, curvature acts as a 'final nail in the coffin' in the case of buckling microtubules. Further experiments aimed at quantifying the survival of bent microtubules in the absence of free tubulin will provide insights into the timescale of propagation of stress due to local curvature and breakage in bent microtubules.

From these findings, we postulate that effectors (such as force, motors, or MAPs) may mediate lattice dynamics by influencing tubulin loss and consequent tubulin turnover by modulating lattice anisotropy (either by stabilization or destabilization of contacts between tubulin dimers). In the cellular context, these mechanisms may underlie how microtubules adapt to cues.

It is interesting to ponder on how lattice remodeling might be influenced when 2 or more of these effectors act in parallel- eg, when a microtubule coated with a particular MAP is subjected to bending or buckling forces. Given the tubulin diversity *in vivo*, exploring lattice dynamics in microtubules reconstituted from tubulin of different isoforms or PTMs (particularly acetylation, which is central to many cellular processes, is a marker for stable microtubules and postulated to weaken lateral contacts) might provide further insights into another layer of regulation of lattice dynamics in cells.

3.6 References

1. Aher A, Rai D, Schaedel L, Gaillard J, John K, Liu Q, Altelaar M, Blanchoin L, Thery M, Akhmanova A. (2020). CLASP Mediates Microtubule Repair by Restricting Lattice Damage and Regulating Tubulin Incorporation. Curr Biol. 30(11):2175-2183.e6.
2. Atherton, J., Stouffer, M., Francis, F., & Moores, C. A. (2018). Microtubule architecture in vitro and in cells revealed by cryo-electron tomography. Acta crystallographica. Section D, Structural biology, 74(Pt 6), 572–584.
3. Biswas, S., Grover, R., Reuther, C., Poojari, C.S., Shaebani, R., **Nandakumar, S.**, Grünewald, M., Zablotsky, A., Hub, J.S., Diez, S., John, K., Schaedel, L. (2025).Tau accelerates tubulin exchange in the microtubule lattice. Nat. Phys. 21, 1616–1628.
4. Chakraborty S, Mahamid J, Baumeister W. (2020) Cryoelectron Tomography Reveals Nanoscale Organization of the Cytoskeleton and Its Relation to Microtubule Curvature Inside Cells. Structure. Sep 1;28(9):991-1003.e4.
5. Chrétien, D. & Fuller, S. D. (2000). Microtubules switch occasionally into unfavourable configurations during elongation. J. Mol. Biol. 298, 663–676
6. Chrétien, D., Metoz, F., Verde, F., Karsenti, E. & Wade, R. (1992). Lattice defects in microtubules: protofilament numbers vary within individual microtubules. J. Cell Biol. 117, 1031–1040.
7. Davis, L. J., Odde, D. J., Block, S. M., & Gross, S. P. (2002). The importance of lattice defects in katanin-mediated microtubule severing in vitro. Biophysical journal, 82(6), 2916–2927.
8. Guyomar, C. *et al.* (2022).Changes in seam number and location induce holes within microtubules assembled from porcine brain tubulin and in Xenopus egg cytoplasmic extracts. eLife 11, e83021
9. Katsuki, M., Drummond, D. R. & Cross, R. A. (2014). Ectopic A-lattice seams destabilize microtubules. Nat. Commun. **5**, 3094.
10. LaFrance, B. J. *et al.* (2022).Structural transitions in the GTP cap visualized by cryo-electron microscopy of catalytically inactive microtubules. Proc. Natl Acad. Sci. USA 119, e2114994119
11. Lecompte, W. & John, K. Molecular motors enhance microtubule lattice plasticity. APS. 1, 013012 (2023).
12. Memet, E., Hilitski, F., Morris, M. A., Schwenger, W. J., Dogic, Z., & Mahadevan, L. (2018). Microtubules soften due to cross-sectional flattening. eLife, 7, e34695.
13. Motta, M.R., Biswas, S., Schaedel, L. (2023). Beyond uniformity: Exploring the heterogeneous and dynamic nature of the microtubule lattice. European journal of cell biology. 102(4), 151370.
14. Pertsinidis, A. & Ling, X. S. (2001). Diffusion of point defects in two-dimensional colloidal crystals. Nature 413, 147–150.
15. Schaedel, L., Triclin, S., Chrétien, D., Abrieu, A., Aumeier, C., Gaillard, J., Blanchoin, L., Théry, M., & John, K. (2019). Lattice defects induce microtubule self-renewal. Nature physics, 15(8), 830–838.
16. Thompson, A.P., Aktulga, H.M., Berger, R., Bolintineanu, D.S., Brown, W.M., Crozier, P.S., Veld, P.J., Kohlmeyer, A., Moore, S.G., Nguyen, T.D., Shan, R., Stevens, M.J., Tranchida, J., Trott, C., Plimpton, S.J. (2022). LAMPPS- a flexible simulation tool for particle-based materials modeling at the atomic, meso and continuum scales. Computer Physics Communications, 271, 108171.
17. Zablotsky, A. & John, K. The impact of lattice defects on the microtubule shaft and tip dynamics (in preparation).

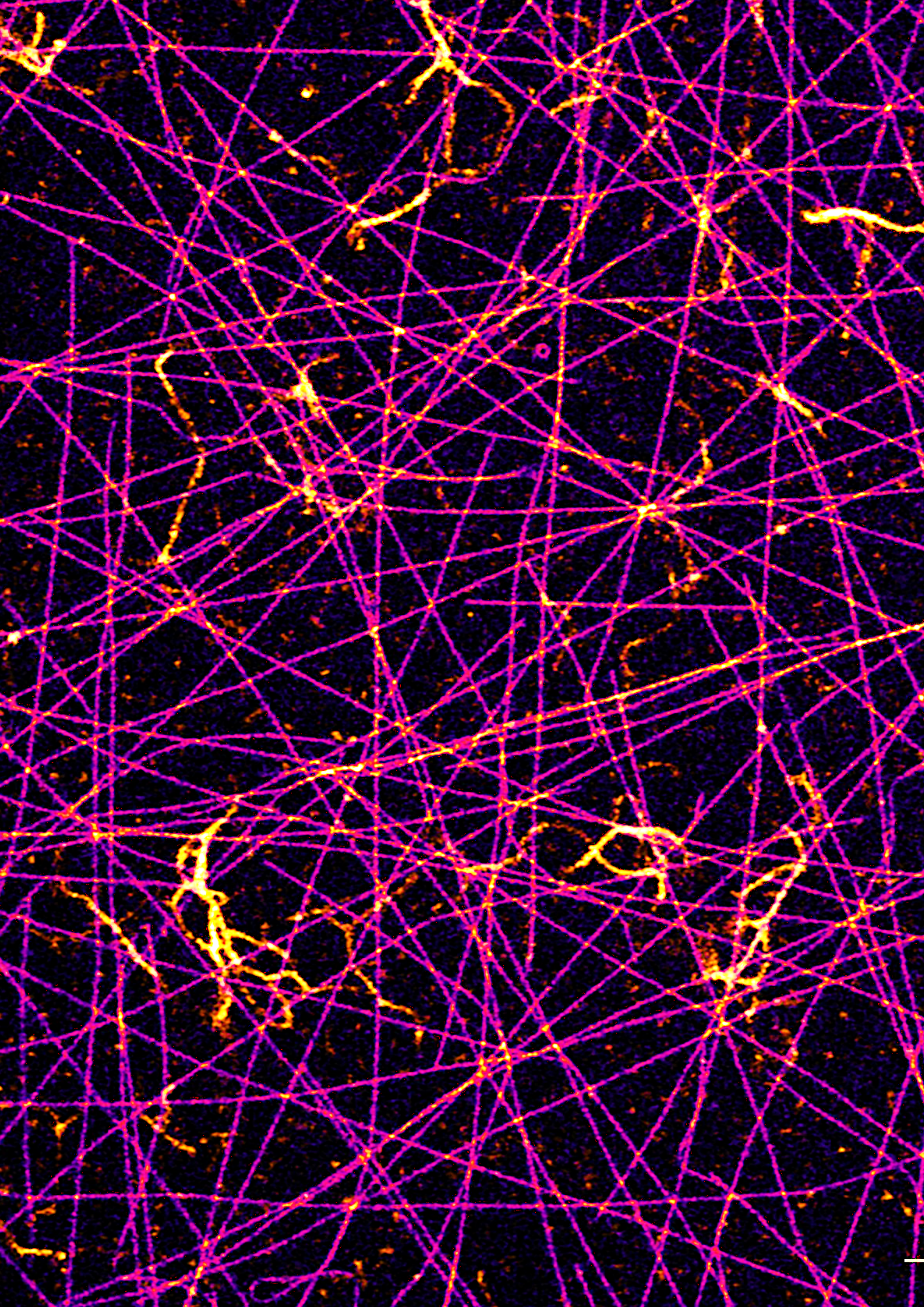

Title of the dissertation:

Metastable Microtubules: Dynamic Instability, Lattice Plasticity and Mechanosensing

Chapter 4: Role of the tubulin code in modulating microtubule response to mechanical stress

Explanation of the contributions of the co-authors in the following chapter 4:

Laura Aradilla Zapata (née Schaedel): conceptualized and supervised the study

Carsten Janke : conceptualized and supervised the study.

Shweta Nandakumar: Designed experiments. Writing: All sections of chapter 4 (sections 4.1-4.4). Performed the buckling experiments and data analysis corresponding to Figure 4.1. Interpretation of data and results underlying Figure 4.1.

Sinda Khanfir: Purified tubulin from HeLa S3 cells that was used in experiments depicted in Fig 4.1.

Chapter 4

Role of the tubulin code in modulating microtubule response to mechanical stress

This chapter showcases preliminary findings on how the tubulin code, comprising tubulin post-translational modifications and isotypes, regulates microtubule response to mechanical force. Using tubulin purified from HeLa cells, I show how the tubulin code may potentially serve as an additional facet of regulation of microtubule lattice plasticity and response.

4.1 Tubulin code and its implications on microtubules

The diverse repertoire of tubulin isotypes and PTMs serves as a great resource for the cell to regulate and (re)organize the intracellular microtubule network locally as an adaptive response to external mechanical stimuli. PTMs like acetylation have also been found to increase microtubule flexibility and enhance microtubule survival under fluid flow (Portran *et al.*, 2017; Xu *et al.*, 2017).

The term 'tubulin code' serves as a good umbrella term to encompass the combined influence of both tubulin isotypes and PTMs, reflecting their interplay that is difficult to disentangle experimentally. Nonetheless, it is important to keep in mind that how tubulin isotypes and PTMs may act and regulate microtubule behaviour are not the same. **Table 4.1** summarizes the important differences between tubulin isotypes and PTMs. It is important to note that whilst PTMs specifically modify the C-terminal tails (CTTs) of α & β tubulin, differences in sequence variations of tubulin isotypes translate into variations in CTTs as well as in the lateral and longitudinal dimer interface. A hotspot of sequence variations between tubulin isotypes may be the M-loop located in the β-tubulin subunit (Chew & Cross, 2025; Roll-Mecak, 2020).

Characteristic	Tubulin isotypes	PTMs
Difference in	Tubulin gene products (amino acid sequence)	Chemical modification- attachment of side groups on C-terminal tails (CTT) of α or β-tubulin.
Mediated by	Gene encoded (permanent)	Enzymes. Some modifications (acetylation, detyrosination and glutamylation) are reversible.
Influences	Tubulin fold, lattice geometry (alterations in lattice spacing) and CTT modifications	Surface charge, hydrophobicity and flexibility of CTTs.
Functional implications	Dynamics, drug tolerance, lattice properties and stability. May also influence binding and interactions with MAPs and motors due to altered lattice conformations.	Interaction of MAPs, motors and stability.

Table 4.1: Summary of key differences in the effects of tubulin isotypes and PTMs on microtubules (Janke & Magiera, 2020; Roll-Mecak *et al.*, 2020, Gadadhar *et al.*, 2017).

The expression pattern of both tubulin isotypes and PTMs is significantly different among different cell types and tissues, based on functional requirements. All the experiments detailed in the previous chapters were performed with purified bovine brain tubulin, which is known to be naturally enriched in PTMs like acetylation and polyglutamylation (Genova *et al.*, 2023; Wolff *et al.*, 1992) and several tubulin isotypes (Vemu *et al.*, 2017). We thus asked if the microtubule response to mechanical stress would differ if we used purified tubulin from cells, specifically HeLa S3 cells.

The profiles of tubulin isotypes and PTMs are significantly different in tubulin purified from HeLa cells. Tubulin from HeLa cells has markedly lower levels of polyglutamylation and polyglycylation when compared to brain tubulin. Tubulin from HeLa S3 cells was found to also express different levels of β-tubulin isotypes, notably β-1 and β-3 as highlighted in **Table 4.2**.

Tubulin from	**β1**	**β2**	**β3**	**β4**
Bovine brain	3%	58%	25%	14%
HeLa S3 cells suspension	80-90%	0%	0%	10-20%

Table 4.2: Difference in β-tubulin isotypes composition in brain vs HeLa tubulin (Davis *et al.*, 2009; Newton *et al.*, 2002; Banjeree & Ludunea, 1992).

4.2 Study 4: PTM and tubulin isotypes modulate microtubule response to mechanical stress

The differences in tubulin isotypes and PTMs expressed in HeLa cells could potentially influence microtubule behaviour under mechanical stress. I tested this by subjecting microtubules made from HeLa and bovine brain tubulin to kinesin-driven buckling assays, as mentioned in Nandakumar *et al.* Purification of HeLa tubulin was performed by Sinda Khanfir (under the supervision of Dr. Carsten Janke, Institute Curie, Paris) using a previously described protocol (Bodakuntla *et al.*, 2020). I present preliminary results in the section below.

Accordingly, I first prepared capped-GDP microtubules using bovine brain and HeLa tubulin, subjected them to kinesin-1-driven buckling in the absence of free tubulin (**Fig 4.1a**). Interestingly, comparing their respective survival times (**Fig 4.1b, c**), it was found that HeLa microtubules displayed enhanced survival under kinesin-induced buckling, surviving almost 3 times longer than microtubules made from brain tubulin. This indicates that HeLa microtubules are mechanically resilient and possess a higher resistance to mechanical stress-induced breakage.

As outlined in Nandakumar *et al.*, enhanced microtubule survival under kinesin-induced buckling can result from a reduction in microtubule rigidity or by alteration of motor motility parameters. Accordingly, the distinct tubulin isotypes and PTM patterns in HeLa microtubules may modulate lattice structure/spacing, making microtubules less stiff and more resilient against buckling stress. Alternatively, motor motility parameters may be altered due to altered lattice conformation or due to presence of modifications (PTMs) along the surface. Although the results are still preliminary, I did not observe any drastic changes in microtubule buckling proportion, abnormal buckling patterns, or microtubule gliding speeds, so it is unlikely that motor landing rates or dwell times were affected. Future single-molecule TIRF motility assays will help clarify whether altered kinesin motility parameters contribute to these observations.

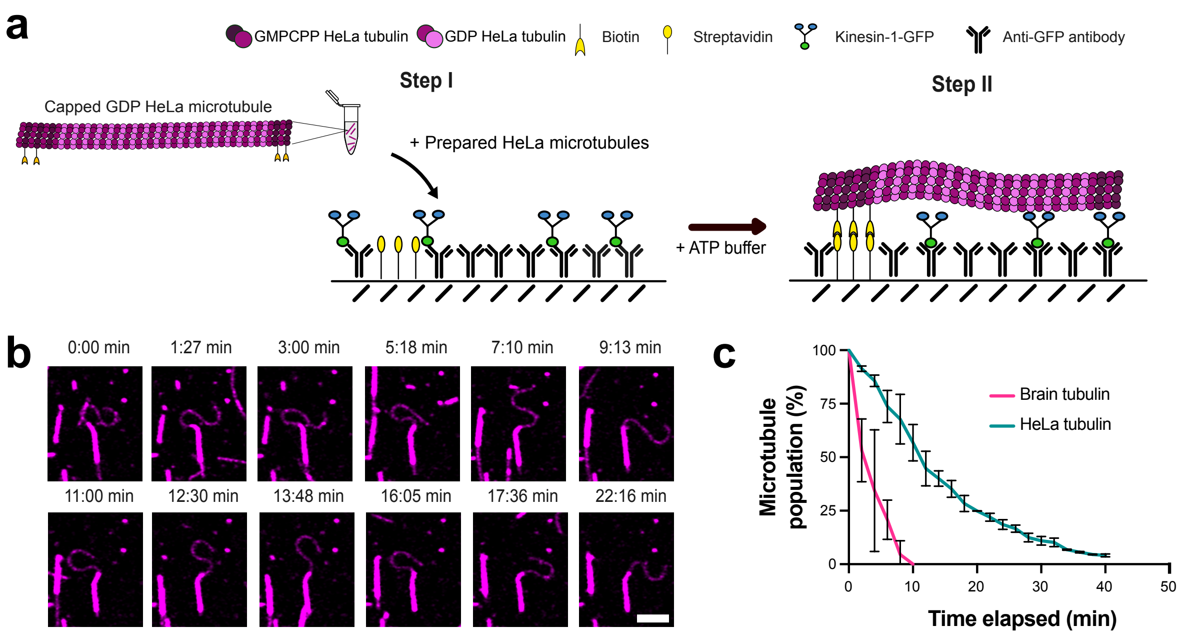

Fig 4.1: (a) Schematic of experimental setup used to assess survival of HeLa microtubules to kinesin-induced buckling. Capped GDP microtubules were prepared using tubulin purified from HeLa cells and added to kinesin immobilized surfaces (Step I). Buckling was induced by the addition of ATP buffer (Step II). **(b)** Time-lapse sequence showing HeLa microtubules survive longer. Scale bar: 5 µm. **(c)** Survival plot showing enhanced survival of HeLa microtubules when compared to microtubules made from bovine brain tubulin. Error bars represent mean and S.D., n> 80 microtubules in both cases from two independent experiments.

Another intriguing question is which aspect of the tubulin code underlies enhanced survival in HeLa microtubules - is it due to differences in PTM patterns or isotype composition?

The major difference in PTM expression levels in HeLa when compared to brain tubulin is the lower levels of polyglutamylation. Kinesin-1 motility was found to be sensitive to levels of polyglutamylation (Sirajuddin *et al.*, 2014). A recent study investigated kinesin-1 motility on microtubules constituted from mouse brain tubulin lacking polyglutamylation (by knockout of TTL1 and TTL7 polyglutamylases). The study reported increased run length and interaction time of kinesin-1 motors on microtubules lacking polyglutamylation (Genova *et al.*, 2023). This would mean that if a lack of polyglutamylation was a contributing factor for the difference observed between brain and HeLa microtubules, one should observe decreased microtubule survival. But instead, the opposite effect is seen, suggesting that lower levels of polyglutamylation cannot alone account for the increased survival.

Differences in tubulin isotypes may be a key contributing factor. Tubulin isotypes are known to influence the mechanical properties of microtubules by modifying lattice structure and dynamics (Janke & Magiera, 2020). The biggest difference in tubulin isotypes is the high level of β1 isotype and the lack of β2 and β3 isotypes. The extreme bending of microtubules in the marginal band (a ring-like structure constituted by microtubules) in blood platelets has been attributed to a higher occurrence of β1-isotype in platelet microtubules (Wang *et al.*, 1986). Knockout of tubulin β1 was shown to incur severe abnormalities in the microtubule organization in platelets (Kunishima *et al.*, 2009). Though there is no direct evidence linking β1-isotype enrichment to microtubule flexibility, these studies suggest that β1-tubulin may confer greater microtubule flexibility and enhance survival under mechanical stress.

4.3 Future directions and outlook

These preliminary findings suggest a potential role of the tubulin code in influencing microtubule response and stability under mechanical stress. These results emphasize the importance of considering the rich, biochemical diversity of tubulin in the cellular environment whilst interpreting microtubule-based functional studies.

Future experiments planned aim at detangling the relative contributions of PTMs and isotypes. In this direction, in addition to single-molecule kinesin motility assays, we will estimate the persistence length of HeLa microtubules by performing thermal fluctuation experiments. Additionally, along with our collaborators at Institute Curie, I will perform comparative studies using:

(i) Polyglutamylation-deficient mouse brain tubulin from TTL1 and TTL7 (major polyglutamylases in the brain) knockout mice, to test whether reduced polyglutamylation enhances survival under buckling stress.
(ii) β3 tubulin-deficient mouse brain tubulin (from TUBB3 knockout mice) to assess the effect of the lack of β3 isotype.
(iii) Platelet-derived tubulin (enriched in β1 isotype) to directly assess if this isotype confers increased flexibility and mechanoresilience. Estimating the persistence length of platelet tubulin microtubules will also help us obtain direct evidence on the influence of β1 isotype on microtubule flexibility.

Further, experiments assessing the role of different PTMs, particularly acetylation (enriched in neurons and cilia) and detyrosination (enriched in cardiomyocytes), on microtubule response under mechanical stress may help us gain further insights into how the tubulin code governs microtubule mechano-adaptation in specific cellular contexts.

In cells, microtubules exist as mosaics of different tubulin isotypes. The spatial organization of tubulin isotypes and PTMs in cells is yet unexplored. A recent *in vitro* study showed that copolymerizing a mixture of α1β3 and α1β4 tubulin resulted in sectioned microtubules with localized differences in lattice composition and protofilament numbers (Prakash *et al.*, 2025). The study also found that specific MAPs showed preferential binding to distinct sections on the lattice, suggesting an interplay of tubulin code and MAP code to locally modulate response. Whether this selective binding arises from recognition of modifications in the C-terminal tails or through recognition of specific lattice states remains an important open question. Taxol was also found to act differently on α1β3 when compared to α1β4 lattices (Chew & Cross, 2023). Thus, differences in tubulin isotype composition across different cell types might explain the variability observed in the action and tolerance of microtubule targeting agents (Roll-Mecak, 2020; Gan *et al.*, 2010).

Cells may use levels of tubulin isotypes and PTMs to adapt as a response to the binding of effectors (motors, MAPs, MTAs). This prompts the question: "What is the minimal section of the lattice enriched with a particular isotype/modification for an effector (MAP or motors) to induce an effect on microtubule behaviour?"

Also interesting to explore is the combinatorial effects of tubulin isotypes and PTM. Owing to the complex environment in cells as well as the existence of compensatory mechanisms, *in vitro* reconstitution experiments using purified PTM-modified tubulin offer the perfect framework for studying specific modifications in isolation and then in combination to understand specific contributions.

4.4 References:

1. Banerjee, A., and Luduena, R. F. (1992). Kinetics of colchicine binding to purified b-tubulin isotypes from bovine brain. J. Biol. Chem. 267, 1333.
2. Bodakuntla S, Jijumon AS, Janke C, Magiera MM. (2020) Purification of Tubulin with Controlled Posttranslational Modifications and Isotypes from Limited Sources by Polymerization-Depolymerization Cycles. J Vis Exp. (165).
3. Chew, Y. M., & Cross, R. A. (2025). Structural switching of tubulin in the microtubule lattice. Biochemical Society transactions, 53(1), BST20240360
4. Chew, Y.M. & Cross, R.A. Taxol acts differently on different tubulin isotypes. Commun. Biol 6, 946 (2023).
5. Davis A, Martinez S, Nelson D. and Middleton K. (2009). A Tubulin Polymerization Microassay Used to Compare Ligand Efficacy. Meth. Cell Biol. 95, Ch 18, p.327-347.
6. Gadadhar S, Bodakuntla S, Natarajan K, Janke C.(2017). The tubulin code at a glance. J Cell Sci. 130(8):1347-1353.
7. Gan PP, McCarroll JA, Po'uha ST, Kamath K, Jordan MA, and Kavallaris M. (2010). Microtubule dynamics, mitotic arrest, and apoptosis: drug-induced differential effects of betaIII-tubulin. Mol Cancer Ther 9, 1339–1348.
8. Genova, M., Grycova, L., Puttrich, V., Magiera, M. M., Lansky, Z., Janke, C., & Braun, M. (2023). Tubulin polyglutamylation differentially regulates microtubule-interacting proteins. The EMBO journal, 42(5), e112101.
9. Janke C, Magiera MM. (2020). The tubulin code and its role in controlling microtubule properties and functions. Nat Rev Mol Cell Biol. 21(6):307-326.
10. Kunishima, S., Kobayashi, R., Itoh, T. J., Hamaguchi, M. & Saito, H. (2009). Mutation of the beta1-tubulin gene associated with congenital macrothrombocytopenia affecting microtubule assembly.Blood 113, 458–461.
11. Newton, C. N., DeLuca, J. G., Himes, R. H., Miller, H. P., Jordan, M. A., and Wilson, L. (2002). Intrinsically slow dynamic instability of HeLa cell microtubules in vitro. J. Biol. Chem. 277, 42456–42462.
12. Portran D, Schaedel L, Xu Z, Théry M, Nachury MV. (2017). Tubulin acetylation protects long-lived microtubules against mechanical ageing. Nat Cell Biol. 19(4):391-398.
13. Prakash, M., Chew, Y.M., Ondruskova, D., Miksatko, J., Dodokova, A., Krishnan, A., Janke, C., Cross, R.A., Lansky, Z., Braun, M. (2025). Tubulin isotypes polymerise into sectioned microtubules that locally regulate protein binding. bioRxiv preprint. doi.org/10.1101/2025.03.12.642813.
14. Roll-Mecak A. (2020). The Tubulin Code in Microtubule Dynamics and Information Encoding. *Developmental cell*, *54*(1), 7–20.
15. Vemu, A., Atherton, J., Spector, J. O., Moores, C. A., & Roll-Mecak, A. (2017). Tubulin isoform composition tunes microtubule dynamics. Molecular biology of the cell, 28(25), 3564–3572.
16. Wang, D., Villasante, A., Lewis, S. A. & Cowan, N. J. (1986) The mammalian beta-tubulin repertoire: hematopoietic expression of a novel, heterologous beta-tubulin isotype. J. Cell Biol. 103, 1903–1910.
17. Wolff, A., De Nechaud, B., Chillet, D., Mazarguil, H., Desbruyères, E., Audebert, S., ... & Denoulet, P. (1992). Distribution of glutamylated alpha and beta-tubulin in mouse tissues using a specific monoclonal antibody, GT335. European journal of cell biology, 59, 425-425.

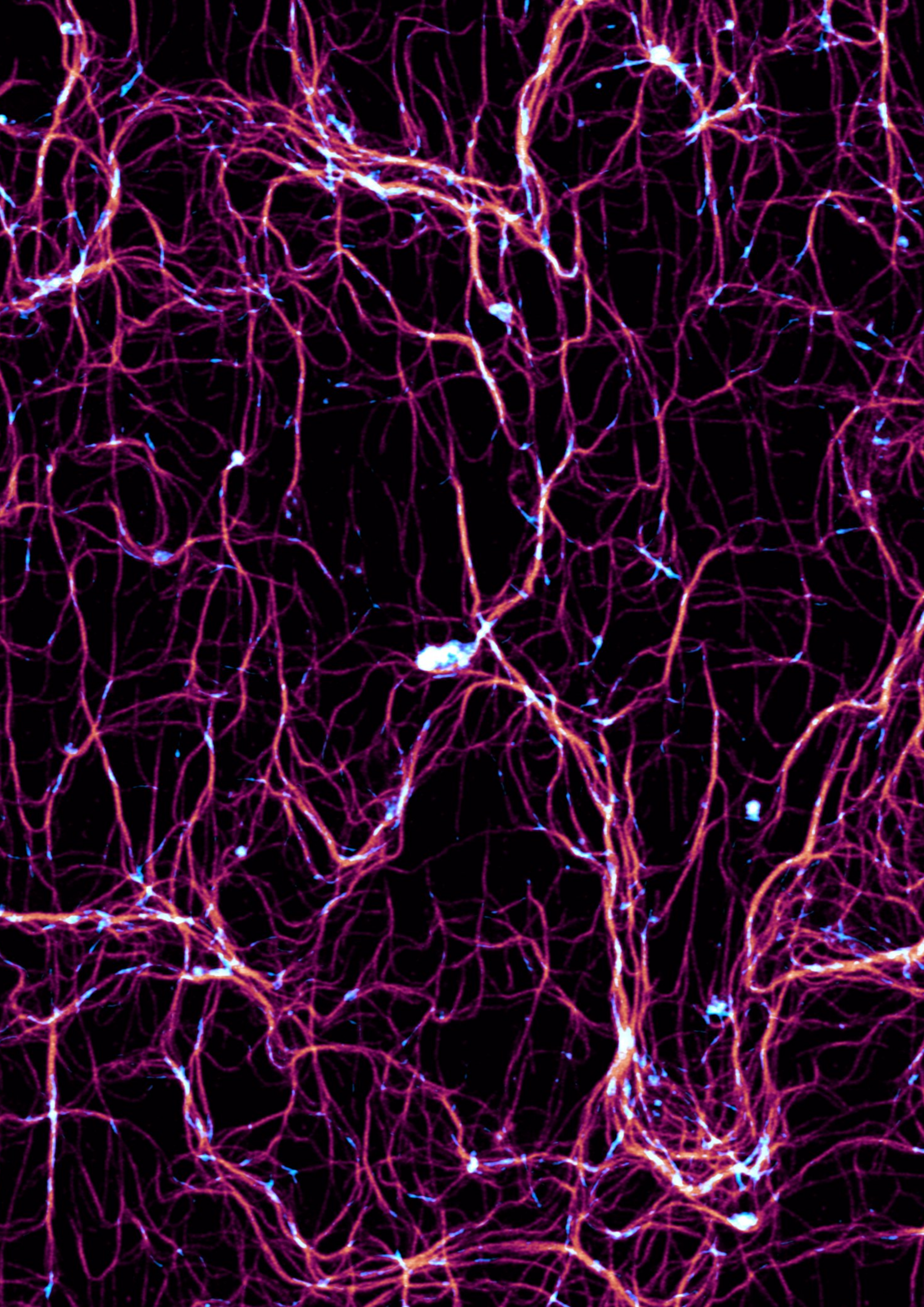

Chapter 5

Modulation of microtubule dynamics by microtubule destabilizing agents and its implications on cellular function

The cellular microtubule network is sensitive to both mechanical and biochemical cues. Modulation of microtubule dynamics has important downstream changes that effect cellular adaptive response, which is crucial to processes like symmetry-breaking, cell polarization and migration. Microtubule Targeting Agents (MTA) interfere with microtubule dynamics as well as mechanics and thus are widely used as chemotherapeutic agents. Here, along with collaborators, I characterise the depolymerizing potential of a promising new microtubule depolymerizing drug- Pretubulysin at the single, dynamic microtubule level. Together with immune cell-based studies from our collaborators, we report how microtubule destabilization by pretubulysin results in enhanced migration of T-cells.

5.1 Pretubulysin

Anti-mitotic drugs (or tubulin binding compounds) are used in many chemotherapeutic regimes with good success. Microtubule (MT) targeting agents bind to diverse sites on tubulin dimer and effect either a stabilizing or destabilizing effect, thus modulating microtubule dynamicity and mass. Large-scale synthesis of these drugs from their natural sources is difficult, expensive and their chemical synthesis is complex. It has also been observed that the action of these drugs is highly tissue/cell specific (eg: Taxol is more effective against ovarian, mammary and lung tumours but ineffective against most solid tumours). In some cases, resistance is conferred by overexpression of cellular membrane transporters. In cells, MTs usually exist in association with several regulatory proteins (MAPs and cytoskeletal crosslinkers) that may stabilize them against depolymerization (MT-based resistant mechanisms). It has also been reported that different tubulin isotypes found in specific cells may also influence MT stability.

Pretubulysin- A precursor of Tubulysin

Tubulysins are potent MT binding agents produced by myxobacteria sp. (*Angiococcus discoformis*) and Pretubulysins are a natural precursor of Tubulysin, which was successfully synthesized on the large scale (Ullrich *et al.*, 2009).

Isolation of Tubulysin from its natural source is expensive, as the yield from fermentation is low and its subsequent purification involves multiple chromatography steps. Alternatively, Pretubulysin can be chemically synthesized, is less complex and more stable. Chemically, Pretubulysin lacks the N,O-acetal and acetoxy moieties that are present in Tubulysin but it was shown that these groups aren't essential for its biological activity (Iqbal *et al.*, 2022; Ullrich *et al.*, 2009).

Current knowledge on Pretubulysin: Hermann *et al.*, 2012 showed that Pretubulysin is as potent as Tubulysin and reported an increase in cell apoptosis in treated cell populations and a reduction in cell migration (Rath *et al.*, 2012) Braig *et al.*, 2014 tested the efficacy of Pretubulysin in cancer cell lines and found that it induces cell apoptosis at nanomolar concentrations, augments degradation of anti-apoptotic Mcl-1 and affects TRAIL (TNF-related apoptosis inducing ligand), a common target for adjuvant therapies (Kubisch *et al.*, 2014). It has also been shown to possess anti-vascular properties (Kretzschmann *et al.*, 2014).

5.2 Study 5: Pretubulysin is a potent MT destabilizing agent and treatment of cytotoxic T lymphocytes with pretubulysin results in enhanced cell migration

In addition to their central role in mitosis, microtubule dynamics is also essential for cell polarization and migration.

In the study below (Montalvo *et al.*,), it is shown how targeting microtubule dynamics, particularly inducing microtubule depolymerization in cells using the MT depolymerizing drug-pretubulysin, has implications on cell migration.

In addition, the study characterizes the MT depolymerizing potential of Pretubulysin in comparison to most used MT destabilizing drug -Nocodazole.

Faculty NT
Cumulative form of the dissertation

Template for the confirmation of the share of co-authors

Title of dissertation:

Metastable Microtubules: Dynamic Instability, Lattice Plasticity and Mechanosensing

Title of article:

Pretubulysin-induced microtubule disassembly improves T cell search efficiency

Quality of the publication, e.g. review article, conference contribution, research article:

Research article

Review process or publication status

Preprint on bioRxiv

Contributions of the co-authors

Bin Qu: Conceptualization, designed experiments, interpreted data and wrote the manuscript. Secured funding and supervised the study.

Franziska Lautenschläger: Conceptualization, designed experiments, interpreted data and wrote the manuscript. Secured funding and supervised the study.

Galia Montalvo Bereau: Designed and performed experiments, prepared figures (Figure 1., Figure 3 D-F., Figure 4., Figure 5 A-C) and wrote the manuscript.

The experiments performed along with the corresponding analyses are as follows:

- *CTL preparation and cell culture*: 80 %
- *Microfabrication of 1D channels*: 100%
- *1D migration experiment*: 100%
- *Preparation of Collagen Matrix*: 100%
- *3D killing experiment and analysis*: 80 %
- *3D infiltration experiment and analysis*: 100%
- *Real-time deformability cytometry (RT-DC)*: 100%
- *Immunostaining*: 100%
- *Quantification of fluorescence intensity*: 100%

Laura Aradilla-Zapata (née Schaedel): Provided expertise and reviewed the results: *In vitro reconstitution assays.*

Marcel Lauterbach: Provided expertise and performed: *1D migration tracking and analysis.*
Natasha Cowley: Performed the experiment and corresponding analysis: *Active droplet simulations.* Prepared Figure 5 D-E.

Renping Zhao: Performed the following experiments and corresponding analyses:

- CTL preparation and cell culture: 20 %
- 3D killing experiment and analysis: 20 %

Reza Shaebani: Provided expertise, performed the experiments and corresponding analysis: *Persistent random search simulations*. Prepared Figure 2.

Rhoda Hawkins: Provided expertise and reviewed the results: *Active droplet simulations.*

Shweta Nandakumar: Performed the experiments and corresponding analysis: *In vitro reconstitution assays*. Prepared Figure 3 A-C.

Signature of the doctoral candidate:

Shweta.N

Shweta Nandakumar

Signatures of supervisors for individual co-authors and the first author were obtained.

Name	Signature
Franziska Lautenschläger	7/10/25
Laura Aradilla-Zapata (née Schaedel)	06.10.25 L. Aradilla
Reza Shaebani	08.10.25
Galia Magela Montalvo Bereau	

Pretubulysin-induced microtubule disassembly improves T-cell search efficiency

Galia Montalvo [1,2], Reza Shaebani[3,4] Shweta Nandakumar [4,] Natasha Cowley[5], Renping Zhao[2], Rhoda Hawkins[5,6], Markus Hoth[2], Marcel Lauterbach[7], Laura Schaedel [4], Bin Qu[2] * and Franziska Lautenschläger[1,4] *

1. Department of Experimental Physics, Saarland University, Saarbrücken, Germany
2. Biophysics, Center for Integrative Physiology and Molecular Medicine (CIPMM), School of Medicine, Saarland University, Homburg, Germany.
3. Department of Theoretical Physics, Saarland University, Saarbrücken, Germany.
4. Center for Biophysics, Saarland University, Saarbrücken, Germany.
5. Department of Physics and Astronomy, University of Sheffield, Sheffield, United Kingdom
6. African Institute for Mathematical Sciences, Ghana
7. Molecular Imaging, Center for Integrative Physiology and Molecular Medicine (CIPMM), School of Medicine, Saarland University, Homburg, Germany.

Email: bin.qu@uks.eu; f.lautenschlaeger@physik.uni-saarland.de

Keywords: T cells, CTLs, microtubules, Pretubulysin, cytoskeleton, 3D killing, searching

Abstract

Cell migration is a crucial process for cytotoxic T lymphocytes (CTLs) to navigate effectively through three-dimensional (3D) environments to locate their target cells and execute their cytotoxic function successfully. However, impaired CTLs infiltration into solid tumors remains a significant challenge, often limiting the efficacy of immunotherapies. To address this challenge, recent evidence suggests microtubules as a promising target, since perturbing microtubule (MT) stability improves T-cell migration and killing efficiency in dense matrices, but the underlying mechanisms remain poorly understood. Here, we make use of Pretubulysin, a known MT depolymerizer, to unmask mechanisms of how MT stability influences T-cell migration. We found that complete disassembly of the microtubule network by Pretubulysin increased CTLs infiltration and migration in a 3D environment. Using a persistent random walk model, we proved the ability of Pretubulysin to enhance T-cell search efficiency in a broad range of scenarios. Interestingly, we found that depolymerizing microtubules in activated T cells leads to localized actomyosin accumulation at the uropod, altering cell mechanics and favoring stronger contraction forces at the rear of the cell. This results in faster and more persistent migration. Using Pretubulysin as a specific tool, we propose a mechanism for how MT-disassembly enhances the search efficiency of T cells.

These insights may be very valuable to optimize immune therapies against solid tumors.

Significance Statement

The results of our study underscore the significance of microtubule disruption with Pretubulysin in enhancing the function of cytotoxic T lymphocytes (CTLs). By inducing rapid and potent depolymerization of microtubules, Pretubulysin treatment results in profound changes in CTLs behavior and mechanics. Notably, Pretubulysin-treated CTLs exhibit increased migration speed and persistence, leading to improved infiltration and killing efficiency in complex 3D environments. These enhancements are explained by alterations in cell stiffness, morphology, and the re-localization of cytoskeletal elements, particularly, enrichment of actomyosin activity at the uropod. By elucidating the molecular mechanisms underlying these effects, our findings provide valuable insights into the intricate interplay between cytoskeletal dynamics and CTLs function. Ultimately, this knowledge may pave the way for the development of novel immunotherapeutic strategies targeting the cytoskeleton to boost T cell-mediated cytotoxicity in the treatment of various diseases.

Main Text

Introduction

Cell migration is a key feature of immune function, and immune cells are particularly specialized to migrate in nearly all tissues within the human body (1). This motility and the capability to infiltrate into tissues is essential for cytotoxic CD8$^+$ T cells, also known as cytotoxic T lymphocytes (CTLs), to efficiently locate tumorigenic or pathogen-infected cells for efficient removal of these aberrant cells (2). This remarkable capacity is the result of migration patterns and related searching strategies, optimized to maximize their chance of finding cognate target cells. CTL search efficiency is correlated with migratory properties such as speed and persistence (3,4). We have described a universal coupling between speed and persistence in which faster cells move more persistently, which depends on both actin polymerization and cell polarization that inherently coexist in actomyosin-driven motion (5). T cells use amoeboid locomotion, in which cell shape changes dynamically and polarize with rapid generation of protrusions at the leading edge and a uropod at the posterior region. In this process, high actomyosin contractility serves as the major force-generating machinery (6).

Two major components of the cellular cytoskeleton, actin and microtubules (MT) are dynamically coupled and regulated to coordinate migration (7). During

T cell migration, the formation for protrusions at the leading edge is driven by polymerization of branched F-actin, which pushes the plasma membrane and provides the primary driving forces for the cell to move forward. Meanwhile, the microtubule-organizing center (MTOC) is located at the uropod, behind the nucleus (8), opposite to the case for mesenchymal motility, in which the MTOC is positioned between the nucleus and the leading edge (9). MTOC positioning plays a decisive role in defining T cell polarity to govern migration direction (8). For migrating T cells, actomyosin contractions at the uropod allow its detachment from the substrate for further migration and provide rear-ward squeezing forces to facilitate the nucleus to migrate through confined spaces (6). The seemingly distinct networks of actin and microtubules can interact and influence each other's dynamics (10). At the interface between T cells and the target cells, actomyosin dynamics influence microtubule disassembly (11).

In vivo, CTLs must navigate through complex 3D environments to locate their target cells. The extracellular matrix (ECM), composed of fibrous proteins (such as collagen), plays a crucial role in maintaining tissue architecture. However, in the context of solid tumors, the ECM often becomes condensed, creating a physical barrier that hinders CTLs infiltration and evades immune surveillance. This limitation contributes significantly to the low efficacy of adoptive immunotherapy against solid tumors. The confined spaces within the dense ECM impair CTLs migration and reduce killing efficiency (12). Recent research has highlighted the potential of targeting MTs to enhance CTLs function, particularly in condensed 3D matrices. Disrupting the MT network using agents like Nocodazole, or the chemotherapeutic drug Vinblastine significantly improves CTLs migration (increasing speed and persistence) and killing efficiency in 3D environments, especially within dense collagen matrices (12,13). In T cells, MT network disruption enhances surface tension (13) and activates Rho A (14), a key regulator for cell contractility. Additionally, at the interface between T cells and target cells, MT dynamics play an essential role in regulating cell contractility (15). Similarly, in migrating dendritic cells, MT dynamics influence protrusion retraction and overall migration, also involving Rho A (16). Despite these insights, the precise mechanisms by which MT disruption improves T cell motility in 3D environments is not yet fully understood.

In this work, we used Pretubulysin, a MT destabilizing drug, to inhibit MT polymerization, and found that the complete MT disassembly by Pretubulysin substantially boosted the infiltration of CTLs into 3D collagen and enabled CTLs to navigate through narrow channels more rapidly and persistently. Our simulations using persistent random search models suggest that CTLs, with disrupted MTs, can penetrate deeper into tissues and exhibit a higher killing efficiency—a feat unattainable by control CTLs, even in greater numbers. Furthermore, we observed that a repositioning of the actomyosin network towards the uropod contributed to enhanced migration speed as predicted by viscous droplet simulation. In conclusion, our findings demonstrate that MT disassembly induces a reorientation of the actomyosin network from the leading edge to the uropod. This reorientation is crucial for accelerating T cell movement and improving their killing efficiency in 3D environments. Furthermore, our work underscores the promising potential of MT targeting within CTLs as a strategy to enhance the effectiveness of adoptive immunotherapy for solid tumors.

Results

Pretubulysin is a potent tool to depolarize the MT network, thereby increasing search and cytotoxic efficiency in 3D environments

To investigate how the microtubule (MT) network governs CTLs function in 3D, we focused on infiltration and migration, as infiltration enables CTLs to enter tissues and proper motility allows CTLs to locate their cognate target cells. To manipulate the dynamics of MTs, we used Pretubulysin, an innovative drug with potent microtubule depolymerization capacity to treat cancer cells (17–20). To examine infiltration, CTLs were fluorescently labeled with CFSE and placed on top of a collagen matrix (Figure 1A). The focal plane was at the bottom of the matrix, allowing visualization of infiltrated cells. We observed that Pretubulysin-treated CTLs appeared at the focal plane at much earlier time points (Figure 1B) with greater numbers (Figure 1C). This result indicates that the MT network plays a pivotal role in governing CTLs infiltration into 3D matrices.

Regarding CTLs migration in a 3D context, we reported earlier that CTLs preferably enter pre-existing confined tunnels in collagen matrices (21). To gain further insights into this aspect with full control over parameters, we used microfabricated channels to mimic the tunnels found in collagen and tracked the Hoechst-labeled T cells (Figure 1D). We found that Pretubulysin-treated CTLs were substantially faster (Figure 1E) and more persistent (Figure 1F) compared to the DMSO-treated control groups, suggesting that microtubule disassembly promotes CTLs motility under confinement in a 3D environment. Notably, the effect of Pretubulysin in enhancing CTLs migration was more potent than Nocodazole at both the low (1 µM) and the high (10 µM) concentrations (Figure1E-F). Concerning the fraction of highly persistent CTLs (persistence > 0.8), at the low concentration, this fraction was doubled for the Pretubulysin-treated group (81%) relative to the Nocodazole-treated counterparts (39%); at the high concentration, the difference between

Pretubulysin- and Nocodazole-treated CTLs was reduced but still present (91% vs 73%).

To examine the impact of Pretubulysin on CTLs killing function, we applied a 3D killing assay, in which tumor cells stably expressing pCasper, an apoptosis reporter, were embedded in collagen matrices and following solidification, CTLs were added from above (22). We compared Pretubulysin with Nocodazole, a well-known and widely used microtubule-disrupting drug (12,13). Results of the 3D killing assay, both the time lapse (Figure 1H) and the quantification (Figure 1I), show that both Pretubulysin and Nocodazole enhanced CTLs killing efficiency in 3D matrices compared to DMSO. Remarkably, at the low concentration, Pretubulysin was much more potent in enhancing CTLs killing efficiency in 3D, relative to Nocodazole (Figure 1H, I). Importantly, the effect of Pretubulysin at 1 µM is comparable to that of Nocodazole at 10 µM (Figure 1H, I). Furthermore, lytic granule release was not affected by complete MT disassembly induced by Pretubulysin or Nocodazole (Supplementary Figure 1). These findings demonstrate that disruption of the MT network promotes CTLs motility and persistence, thus offering a reliable and powerful way to enhance CTLs killing efficiency in 3D. In this regard, Pretubulysin is about 10-fold more potent when compared to Nocodazole.

Increase in speed and persistence is responsible for enhanced migration and killing efficiency of CTLs in 3D

To obtain a detailed understanding of the influence of migration speed and persistence on the infiltration efficiency of CTLs, we performed persistent random search simulations in 3D, mimicking the experimental conditions (see Materials and methods). The CTLs were modeled as persistent random walkers which enter the 3D space from the top surface (Figure 2A, starting plane), migrate until they reach the target cells at the bottom plane (Figure 2A, Target area), and each CTL/target contact was assumed to result in target destruction. In our previous experiments of CTLs migration in 3D collagen matrices (21) we analyzed CTLs migration mean speed and persistence at different collagen densities. Those experimental data were used as input for our simulations as the control group. The speed and persistence of Pretubulysin-treated CTLs in 3D collagen matrices were estimated based on the quantifications obtained from our microfluidic channel experiments (presented in Figure 1). For our experiments, we assumed that the migration through narrow paths created by CTLs in 3D collagen matrices is similar to the motion in our 1D microfluidic channels. This assumption was validated by the satisfactory match between the killing kinetics obtained from simulations and experiments (Supplementary Figure 2).

CTLs are responsible for killing targets in various regions of the body, requiring them to patrol environments of different sizes. In our experiments, the thickness of the collagen matrix (i.e. the initial distance between the starting plane and target area) was approximately 1.5 mm. We then asked how the observed improvement of infiltration efficiency by Pretubulysin treatment depends on the choice of matrix thickness (height, h). To address this, we varied the thickness in the simulations and compared the migration efficiency of control and Pretubulysin-treated CTLs. The number of migrating cells that reached the target area at the bottom plate decreased with increasing layer thickness, but with different rates for control and Pretubulysin-treated CTLs (Figure 2B). As shown in the inset of Figure 2B, the difference between control and treated cells increases with height. Specifically, with a twofold increase in height from 1.5 to 3.0 mm, the ratio of infiltrated treated cells to control cells that reach the target area grows from approximately 6 to 108, indicating a nearly 17-fold increase.

We further analyzed the relationship between CTLs killing efficiency and the matrix thickness (h). We quantified the killing efficiency by the killing halftime (t_{50}), which is the time required to eliminate 50% of the targets. The difference in t_{50} between control and Pretubulysin-treated CTLs increases with height (Figure 2C). These results suggest that the advantage of Pretubulysin treatment becomes even more pronounced with increasing h, *i.e.* in larger environments. Another key factor that can considerably influence the killing efficiency of CTLs is the ratio of CTLs to target cells. In our experiments, the ratio ($N_{CTLs}/N_{targets}$) was 5. To understand the impact of this ratio on CTLs killing efficiency, we varied the initial number of CTLs over a wide range in the simulations. Figure 2D shows an example of the numerical results for both control and Pretubulysin-treated cells at collagen matrix density 2 mg/ml. We observed that for both the control and Pretubulysin-treated groups, increasing the relative number of CTLs decreased t_{50}, thereby enhancing the killing efficiency. This improvement continues until the ratio of $N_{CTLs}/N_{targets}$ reached between 10 and 20 (Figure 2D). Notably, with the same ratio of $N_{CTLs}/N_{targets}$, the killing efficiency of the Pretubulysin-treated group was higher compared to that of the control group (Figure 2D). These findings suggest that CTLs migration in 3D plays a critical role in regulating their killing efficiency. We note that the lower bound on t_{50} (*i.e.* the saturation value) is imposed by the minimum travel time of CTLs to cross the collagen layer and reach the target area with a given mean speed and persistence.

We also examined the integrative impact of speed and persistence on CTLs migration and killing efficiency using persistent random search simulations. By varying the migration speed and persistence of the searchers, we measured the number of CTLs which reached the target area and t_{50} with parameters used in experiments (h = 1.5 mm and $N_{CTLs}/N_{targets}$ = 5). The surface plots show that the number of cells which arrive at the target area drastically decreases (Figure

2E) while t_{50} increases (Figure 2F) with decreasing the migration speed and/or persistence.

Disassembly of MT network results in enrichment of F-actin and myosin at the uropod

To characterize the depolymerizing potential of Pretubulysin at the single, dynamic MT level in a controlled environment, we performed microfluidics based *in vitro* reconstitution assays using purified tubulin.

In these assays, short biotin-containing microtubule fragments (in red, Fig 3A) were attached using neutravidin onto a passivated coverslip and used as 'seeds' to induce microtubule growth. Microtubules (in green, Fig 3A) were elongated from these seeds using 10 µM Atto-488- labeled purified tubulin. Subsequently, the drug mix containing the drug (0.1, 1 and 10µM of Pretubulysin/Nocodazole), 1 mM GTP and 10 µM Atto-488 labeled tubulin (to prevent microtubule disassembly from dilution) was flushed in. The use of a microfluidic circuit helped to suitably control the addition of the drug mix without moving the microtubules in the field-of-view under observation.

We observed rapid depolymerization of microtubules as soon as we flushed in Pretubulysin (even at lower concentrations of 0.1µM), accompanied by a loss of 60-88% of microtubule mass (See Fig 3 B-D) when compared to the Control (DMSO).

In the case of treatment with 10 µM (and lower concentrations) of Nocodazole, we observed that most MTs entered a state of 'pause' immediately after flushing in of the drug mix (See Supp fig. 3) with no significant MT shrinkage. Our observations match those reported by Vasquez *et al*., 1997, wherein they report that MTs, both grown *in vitro* from purified tubulin as well as in Newt lung cells, seemed to enter a 'pause' state with loss of dynamicity, following treatment with nanomolar concentrations of Nocodazole. We observed this phenomenon up to a concentration of 50 µM Nocodazole, above which we observed a 10.2% loss of MT mass, wherein microtubules shrink until a certain length and then seemed to enter the pause state (See Supp fig. 3)

From our *in vitro* experiments at the single, dynamic microtubule level, we can conclude that Pretubulysin acts as a potent, microtubule depolymerizing agent that causes rapid depolymerization of microtubules when compared to Nocodazole which effects a loss in microtubule dynamicity with no significant loss in microtubule mass when compared to the Control (DMSO).

As MTs are the most rigid cytoskeletal filaments (23), we postulated that MT disassembly induced by Pretubulysin would soften CTLs, facilitating them to infiltrate and migrate more easily. To test this, we determined CTLs stiffness with the Real-Time Deformability-Cytometry (RT-DC, Figure 3E), in which the cells were flowed through a microfluidic channel (20 µm) and the shear stress-induced cell deformation was used to calculate the apparent Young´s modulus (24). Pretubulysin treatment induced reduced deformation without changing the cell sizes (Figure 3F, G). Concomitantly, the Young's moduli of CTLs were enhanced after Pretubulysin treatment compared to the DMSO-treated counterparts (Figure 3H). These results indicate that MT disassembly does not lead to softening but rather stiffening of CTLs. Based on emerging evidence of actin-microtubule crosstalk, we then investigated the influence of MT disassembly on actin and myosin activity.

The MT network and dynamics play a critical role in actin cytoskeleton dynamics as well as acto-myosin contractility, which are essential for cell motility (25). To further understand how MT disassembly enhances CTLs infiltration and migration in 3D, we examined the distribution of filamentous actin (F-actin) and phosphorylated myosin (pMyosin) using immunostaining. In the DMSO-treated control CTLs, F-actin was primarily located at the leading edge and around the nucleus, with pMyosin surrounding the nucleus and present in both the protrusions and the uropod (Figure 4A, DMSO). Colocalization of F-actin and pMyosin was observed mainly in the perinuclear region and along the contour of the leading edge and the uropod (Figure 4A, DMSO). In comparison, in Pretubulysin-treated CTLs, F-actin was primarily located in the uropod and around the nucleus, with pMyosin also enriched in the uropod (Figure 4A, Pretubulysin). Colocalization of F-actin and pMyosin was found predominantly in the uropod and the perinuclear region (Figure 4A, Pretubulysin). Quantification of our results shows that the levels of both F-actin and pMyosin were increased in Pretubulysin-treated CTLs relative to their counterparts (Figure 4B). Notably, colocalization between F-actin and pMyosin was also enhanced after Pretubulysin treatment (Figure 4C). These findings indicate that disassembly of the MT network repolarizes actin network and the associated acto-myosin contractility to the rear part of CTLs.

While analyzing the images, we noticed that the morphology of Pretubulysin-treated CTLs were also altered. To confirm this, we stained α-tubulin and nuclei in CTLs. In control cells, the MT network was clearly visible with a bright spot indicating the MTOC (Figure 4D, DMSO). In Pretubulysin-treated CTLs, α-tubulin did not form filaments, but was relatively evenly distributed in the cytosol, and a relatively bright spot, likely the MTOC, could still be identified (Figure 4D, Pretubulysin). The orientation of CTLs was determined by MTOC positioning, which is always located at the uropod during migration. Interestingly, in MT-disassembled CTLs, the nucleus appeared to be relocated from its usual position at the front side edge (Figure 4D, Pretubulysin). Quantification of these results shows that when the MT network was disassembled by Pretubulysin, the uropod grew (Figure 4E) and the leading edge shrank (Figure 4F). The enlarged uropod might be a result of enrichment of actin and pMyosin, leading to enhanced contractile forces in this region.

Actomyosin enrichment at the rear increases' migration speed

Since actomyosin contractility plays an indispensable role in cell migration, we investigated whether the relocation of actomyosin to the uropod has any functional impact on migration. To address this question, we first quantified the relative cellular distribution of F-actin and pMyosin. We evaluated the fluorescence intensity in two specific compartments: the back and the front of the cell (as explained in Materials and Methods). Three representative images are shown in Figure 5A, for each, DMSO- and Pretubulysin-treated CTLs. Quantification of the results again confirmed that F-actin and pMyosin are significantly accumulated at the back of Pretubulysin-treated CTLs compared to the DMSO control, with an enhancement of around 10-fold for F-actin, and around 100-fold for pMyosin (Figure 5B).

To gain further insights into the relationship between actomyosin distribution and cell migration behavior, we modeled amoeboid cell migration as a viscous droplet with an active boundary, which is analogous to the cell's cortex. The relative cellular distribution of F-actin and pMyosin (back/front) was referred to as the concentration ratio in this model. As shown in Figure 5D, actomyosin concentration was placed along the droplet boundary, considering two situations: Droplet 1 with a low concentration ratio, representing DMSO-treated cells; and Droplet 2 with a high concentration ratio, resembling Pretubulysin-treated CTLs. The concentration profile is shown by the color scale (Figure 5D), where c is normalized by c_0, the average droplet concentration. Both droplets have equal total and average concentration. The simulations show that for a motile active droplet, the translational velocity was dependent on the boundary concentration of actomyosin: higher droplet speeds were obtained for droplets with greater concentration at the back of the cell, relative to the front of the cell (Figure 5E). These results show that enrichment of actomyosin leads to enhanced migration speed.

Discussion

In summary, our work establishes Pretubulysin as a potent MT disrupting agent that induces complete MT disassembly. Compared to Nocodazole, Pretubulysin treatment can further enhance CTLs migration and killing efficiency in 3D collagen, particularly in dense collagen. Notably, MT-disassembled CTLs exhibit increased speed and persistence in microfabricated narrow channels, which mimic the confining tunnels in collagen matrices. This characteristic leads to overall enhanced motility and faster searching efficiency in 3D environments, as suggested by our random persistent searcher simulations. Furthermore, we observed that MT disassembly results in elongation of uropod and repolarization of F-actin and phosphorylated myosin from the protrusions at the leading edge towards the elongated uropod. This redistribution of the actomyosin network provides additional pushing forces for cell motility, favoring accelerated migration, as predicted by viscous droplet models. Our findings offer valuable insights into the intricate interplay between cytoskeletal dynamics and T cell function, offering potential avenues for enhancing immunotherapeutic strategies targeting T cell-mediated cytotoxicity. The MT network of T cells emerges as an attractive target that can be specifically disrupted to maximize the efficacy of immune cell-related therapies. While MT depolymerization agents have received considerable attention as cytotoxic drugs, there is a notable scarcity of studies examining their effects on T cells. The existing studies predominantly focus on cancer cells rather than immune cells (26–28). Also, despite promising success, the therapeutic utility of many MT depolymerization agents is impeded by issues such as toxicity and resistance, prompting active exploration of novel compounds. Pretubulysin serves as a good example, which is a synthetic precursor of Tubulysin with accessible chemical synthesis while maintaining a powerful antitumoral activity (19,20,29). CTLs can navigate through 3D tissues very fast (10–15 μm/min) and are confined by existing tunnels and cellular networks embedded in the extracellular matrix (30). In dendritic cells, MT dynamics is important for navigating the cells through pillar forests, by modulating retraction of protrusions via RhoA and its exchange factor Lfc (16). For adherent cells, disruption of MTs inhibits trail retraction and therefore impairs cell migration on 2D surfaces and transmigration through a membrane with pores (31). Interestingly, by perturbing the MT, the migratory parameters of the cell can be affected: impaired migration is observed with MT stabilization (13,32). Our results show that in T cells, at least in CTLs, migration persistence and speed are coordinated by the MT network. Our random persistence searcher simulations suggest that persistence and speed can collectively tailor the searching and killing efficiency of CTLs in 3D environments.

In addition to their mechanical properties, MTs are a repository of guanine nucleotide exchange factors that activate small GTPases regulating actin assembly and actomyosin contractility (28,33). Therefore, disruption of MTs can alter cell mechanics not only by changing the microtubule network mechanics, but also by inducing changes within the actin cytoskeleton (34). Previous studies have reported that pharmacological dissociation of microtubules leads to increased contractility (13,15,28). Also, the crosstalk between microtubules and cellular contractility has been shown to regulate cell shape and the mechanical properties of migrating cells. The enhanced cell stiffness in MT-disassembled CTLs could be attributed to enhanced actomyosin contractility. Although MTs do not directly contribute to the generation of forces that drive cell migration, they are involved in the regulation of actin-dependent motility via guanine nucleotide exchange factor GEF-H1, in what has been recently described as the microtubule-contractility axis (13). GEF-H1 is inactive when bound to MT and becomes activated when MT are depolymerized, either because of inherent dynamic instability or after treatment with microtubule-depolymerizing compounds. Activated GEF-H1 promotes the activation of Rho, which in turn induces the upregulation of myosin II contractility and actin polymerization (33–36). It is also reported that GEF-H1 plays an essential role in crosslinking the MT network and contractility in CTLs (13).

Actomyosin contractility provides the primary driving forces for cells, including T cells, to move. To facilitate crossing the endothelial barrier, T cells use myosin-driven contractility to squeeze the nucleus through the endothelial junctions. The efficiency of migration is tuned by the degree of force generated and the extent of traction provided (37). Actin polymerization is essential for force generation by T cells but dynamic MT at the interface also plays a fundamental role (15). Actomyosin contractility at the uropod has been described as fundamental in generating the forces that drive migration in amoeboid cells (6). In this work, we observed that in Pretubulysin-treated CTLs, F-actin and p-Myosin were redistributed from the protrusions to the uropod. The results from viscous droplet models suggest that enrichment of actomyosin at the uropod per se can increase migration speed compared to universal distribution. This symmetry-break in the distribution of the cytoskeletal elements results in morphology changes, mechanical perturbations, and migration enhancement of CTLs, which can then kill their targets more efficiently.

Materials and Methods

Antibodies and Reagents. The following antibodies were used: α-Tubulin, pMyosin, pGEFH1 mAb antibody (DM1A, Cell Signaling Technology), and Alexa Fluor 405 conjugated goat anti-mouse IgG (H+L) cross-absorbed secondary antibody (ThermoFisher Scientific). The following reagents were used: Hoechst 33342 (ThermoFisher Scientific), Alexa Fluor 488 or Alexa Fluor 594 phalloidin (ThermoFisher Scientific), CellMask™ Deep Red Actin Tracking Stain (Invitrogen) DAPI mounting medium (Invitrogen), Carboxyfluorescein succinimidyl ester (CFSE), FibriCol® type I collagen Solution (Bovine, Advanced Biomatrix), cell-Tak (Corning), poly-dimethylsiloxane (PDMS) (RTV-615; Momentive Performance Materials), poly(L-lysine)-graft-poly(ethylene glycol) (PEG-PLL) (Susos, Dübendorf, Switzerland). The following drugs were used: Pretubulysin (synthesized as described in (29)), Nocodazole (Sigma-Aldrich); The compounds were dissolved in DMSO to a concentration of 10 mM and stored at −20 °C. For experiments, the compounds were diluted in cell culture medium.

CTLs preparation and cell culture. Human peripheral blood mononuclear cells (PBMCs) of healthy donors were isolated from the Leukocyte Reduction System Chamber using a gradient centrifugation method (450 g, 30 min) with Lymphocyte Separation Medium 1077 (PromoCell). Remaining red blood cells were removed by the lysis buffer (155 mM NH4Cl, 10 mM KHCO3, 0.1 mM EDTA, pH=7.3). For migration and killing experiments, PBMCs were stimulated with Streptococcal Enterotoxin A (SEA) at 0.5 µg/ml for 30 minutes and then diluted 50X in AIMV medium (ThermoFisher Scientific) containing 10% FCS and Interleukin-2 (50 U/ml). After 5 days in culture, CTLs were isolated using Human CD8+ T Cell Isolation Kit (Miltenyi Biotec). All CD8+ T cells were cultured in AIM V medium (ThermoFisher Scientific) containing 10% fetal calf serum (FCS) and 1% Penicillin-Streptomycin. Alternatively, Human primary CD8+ T Cells were negatively isolated from PBMCs using Dynabeads™ Untouched™ Human CD8+ T Cells Kit (ThermoFisher Scientific) and stimulated with Dynabeads™ Human T-Activator CD3/CD28 (ThermoFisher Scientific) toghether with recombinant human IL-2 (ThermoFisher Scientific). NALM-6 pCasper cells were generated by Knörck *et al*. (32) and were cultured in RPMI-1640 (ThermoFisher Scientific) containing 10% FCS and 1% Penicillin-Streptomycin in the presence of puromycin (0.2 µg/ml).

CTLs treatment with drugs. Cells were treated with Pretubulysin at 10 µM and DMSO at 0.1 % for 30 minutes prior the experiments. For 1D migration experiments, cells were loaded in medium with the corresponding drug. For 3D migration, infiltration, and killing experiments, cells were washed after drug treatment, before being placed on top of collagen layer. For immunofluorescence microscopy, cells were fixed immediately after drug treatment (30 minutes). For RTDC experiment, treated cells were resuspended in cell carrier buffer with drugs at the corresponding concentration.

Microfabrication of 1D channels. Using nanoscribe-generated stamps, microchannels were fabricated by pouring polydimethylsiloxane (PDMS) precursor mixture (Sylgard 184, base : curing agent = 10 : 1) and curing at 70°C for 2 h. Then, circular-shaped reservoirs (2mm) were drilled, and shape was adjusted using a razor blade. Resized PDMS chip was cleaned, sonicated 30 sec in 70% ethanol, dried by blowing clean air, and activated together with the culture dishes by air (or oxygen) plasma () treatment during 30 sec at 300 mTorr. Chips were incubated in the oven at 65 °C for 1 hr to strengthen the binding. For coating the microchannels, the whole structure was activated by air plasma at 300 mTorr for 1 min to promote the entry of liquid into the channels, 0.5 mg/mL PLL-PEG was added and incubated for 30 min. Afterward, chambers were washed with PBS.

1D migration experiment. The chambers prepared with PLL-PEG-coated channels were equilibrated for 1 h at 37°C with cell culture medium with

Pretubulysin 10µM or DMSO 0.1%, before loading the cells. Cells were stained with Hoechst 33342 (200 ng/ml) for 30 minutes at 37°C and 5% CO2. Treated CTLs were loaded in the chambers in 10 µl at 20 Mio cells/ml and the chip was covered with medium. A Video Nikon epi-fluorescence microscope with a 10X objective lens (Plan-Neofluor, NA = 0.5) and Andor camera was used for imaging. The chamber was mounted on the microscope stage equipped with an incubator system (Live Cell Instrument, Korea) maintaining 37°C and 5% CO2 for live cell imaging. Cells migrated spontaneously for 15 hours and images were acquired every 3 minutes.

1D migration tracking and analysis. Custom-written routines in Matlab (Mathworks, Natick, USA) were used for tracking analysis. First, images were rotated (bilinear interpolation) so that the channels are perfectly horizontal in the movies. To obtain a flatfield for correction of inhomogeneous background over the field of view (FOV), a large (30x30 pixels) median filter was applied to each fluorescence image. This removes all cells, leaving a flatfield, which was subsequently subtracted from each frame.
Positions of microfluidic channels were automatically identified. [Extensive explanation: Positions of the microfluidic channels were identified as follows: First a maximum intensity projection over time was calculated, then all pixels were summed horizontally, leading to a peak for each channel that contained at least once a fluorescent cell. These peaks were detected with MATLAB's findpeaks command]. Non-channel regions were replaced by the average intensity of the image. The resulting images were smoothed with a Gaussian filter of 5 pixels full width at half maximum.

Cells were identified as local intensity maxima (Matlabs command imregionalmax) exceeding a threshold in the resulting images. Cells were subsequently tracked (i.e. re-identified in consecutive frames) by minimizing the squared distance between all particles in consecutive frames as described in (38). Each microfluidic channel was treated separately during tracking. Cell speeds were calculated as displacement between frames divided by the time interval between frames.

Preparation of Collagen Matrix. Briefly, bovine collagen type I stock solution (10 mg/ml) was neutralized with 0.1 N NaOH solution on ice to reach pH 7.0-7.4. 10×PBS was added into the neutralized collagen to a dilution factor of 1:10. The collagen solution was further diluted with PBS to the final concentrations used and incubated for 1 hour at 37°C with 5% CO2 for fibrillation.

3D killing experiment. For killing assays, NALM-6 cells stably expressing apoptosis reporter pCasper-pMax (referred to as NALM-6-pCasper) were used as target cells. NALM-6-pCasper were pulsed with staphylococcal enterotoxin A (SEA, 0.1 µg/ml) for 40 min at 37°C with 5% CO2, prior to killing assays.

Target cells were resuspended in chilled collagen solution, transferred in 96-well plates, and pelleted by centrifugation at 4°C (200 g, 7.5 min). Afterwards, the mix target cells-collagen (45 µL/well?) was solidified in the incubator for 1 hr. CTLs were added on top of solidified collagen in medium without drug or DMSO. Images were acquired by ImageXpress (Molecular Devices) with Spectra X LED illumination (Lumencor) at 37°C with 5% CO2 for 24 hours. As described previously (35), fluorescence of pCasper-pMax was acquired using LEDs 470/24 for excitation and the following filter sets (Semrock): Ex 472/30 nm, Em 520/35 nm for GFP and Em 641/75 nm for RFP/FRET. A 20× S Fluor 0.75 numerical aperture objective (Nikon) was used.

3D infiltration experiment. CTLs were stained with CFSE (5 µM in PBS/4.5% FCS) at room temperature for 15 min, washed once with PBS, then resuspended in AIMV/10% FCS, and kept at 37°C with 5% CO2 for recovery during 1 hr. Then, CTLs were treated with Pretubulysin 10 µM or DMSO and loaded on top of solidified collagen matrix. Images were acquired by ImageXpress (Molecular Devices) with Spectra X LED illumination (Lumencor) at 37°C with 5% CO2. Images were acquired from the bottom of the well every 20 minutes for 24 hours.

Immunostaining. CTLs were immobilized on coverslips using the Cell-Tak adhesive (Corning). Briefly, a master mix containing Cell-Tak adhesive was first prepared with a mixture of sodium bicarbonate (75 g/L), sodium hydroxide (40 g/L) and Cell-Tak (2.03 g/L) at a volume ratio of 291:5:4. For each coverslip, 187 µl of master mix was added, incubated at room temperature for 20 minutes, washed with PBS three times and completely dried. Next, cells were added to the cell-Tak treated coverslip immediately after Pretubulysin or DMSO treatment and incubated for 2 minutes. Unadhered cells were carefully washed off with medium. Right after, immobilized cells were fixed with pre-warmed paraformaldehyde (PFA, 4%) for 10 minutes at room temperature. Next, cells were washed twice with PBS, permeabilized with Triton -100 (0.05%) and blocked with 2% BSA in PBS for 1 hour. Staining with the indicated antibody or Phalloidin was performed in PBS/BSA 2% for time and dilution indicated in the antibodies and reagents section. DAPI was added to the slides for nuclei staining and coverslips were placed on mounting slides for imaging. Fixed/stained cells were imaged using the 63x immersion oil objective (Zeiss, Plan-Apochromat 63x/1.40 oil DIC M27) of a Zeiss LSM 900 confocal microscope with the Axiocam 705 Mono camera (Zeiss).

Real-time deformability cytometry (RT-DC). To assess the stiffness of CTLs RT-DC1 was used. CTLs were treated with Pretubulysin or DMSO after which they were resuspended in 100 µl of Cell Carrier B solution (phosphate-buffered saline with the addition of long-chain methylcellulose polymers of 0.6 w/v%) with drugs. A 20 µm microfluidic PDMS chip was assembled on the stage of an inverted microscope (Zeiss). The cell suspension was loaded on the chip using a syringe pump. The cells flowing through the microfluidic channel deform due to the shear stresses and pressure gradient caused by the flow profile. Each event is imaged live using a CMOS camera. At least 3000 events were acquired for each condition and experiment, flowrate used in the range from 0.04 to 0.12 µls-1, according to the range suggested by the manufacturer for used channel size and carrier buffer. The stiffness of the cells was analyzed using ShapeOut (Zell Mechanik, Dresden) and the statistical significance of the results was also calculated using linear mixed models in the software.

Quantification of fluorescence intensity. Microscope data was analyzed using ImageJ/Fiji. For protein intensity quantification, Sum Intensity projections were generated for each cell and background was subtracted. Based on actin staining, the cell border was established. Considering the nuclei, two compartments were analyzed (at the back and at the front of the nuclei). The mean intensity fluorescence in the region (for f-actin and for pMyosin) and the area were automatically obtained with the software, the total f-Actin and total pMyosin were calculated by multiplying MFI*Area.

***In vitro* reconstitution assays**:

Tubulin purification and labeling: Tubulin was purified from fresh bovine brains by three cycles of temperature dependent assembly and disassembly in Brinkley Buffer 80 (BRB80 buffer; 80mM PIPES, pH 6.8, 1mM EGTA, 1mM $MgCl_2$ and 1mM GTP) and consequently labeled with biotin and fluorescently labeled with ATTO488 (ATTO-TEC, AD488) and ATTO565 (ATTO-TEC, AD565) dyes as described in (39).

Preparation of Silane-PEG -Biotin passivated cover glasses: Cover glasses were cleaned in Acetone, 96% ethanol, Hellmanex III solution (2% in water, Hellmanex) followed by treatment using an UV cleaner before incubation in a 9:1 or 7:3 mix of tri-ethoxy-silane-PEG and tri-ethoxy-silane-PEG-biotin (30kDa, PSB-2014, Creative PEG works) as described in (39). Microfluidic Circuit Fabrication: The microfluidic device was fabricated with PDMS (Sylgard 184, Dow Corning) using standard soft lithography. TFE Teflon tubing (Supelco, inner diameter: 0.8mm, outer diameter: 1.58mm, Merck) was inserted into the port serving as an outlet. Tubing with 0.03 mm inner and 1.58 mm outer diameter was used to connect the inlet with sample reservoir, via a manual shut-off valve to a pressure controlled microfluidic pump (LineUP Flow EZ 345 mbar, Fluigent).

***In vitro* reconstitution experiments using microfluidics:** For the *in vitro* assays, 10mM stock solutions of Pretubulysin and Nocodazole (dissolved in DMSO) were further diluted in 1xBRB80 buffer. The PDMS chip was placed on a passivated cover glass and fixed on to the microscope stage. The chip was first perfused with a solution of 1xBRB80. The surface was then perfused with 300ml of Neutravidin (50 µg µl−1 in BRB80; Pierce), followed by 300 µl of PLL-g-PEG (PII 20K-G35-PEG2K, Jenkam Technology) at 0.1 mg/ml in 10 mM Na-HEPES buffer (pH =7.4) before another wash with 1xBRB80 to remove the excess, unbound neutravidin and PLL-g-PEG. ATTO-565 labeled Biotin microtubule seeds prepared according to (39) were flowed into the chamber and the unbound seeds were washed out immediately using BRB80 supplemented with 1% BSA. The seeds were then elongated by addition of the Elongation mix containing 10 µM of tubulin (20% ATTO-488 labeled) in BRB80 supplemented with 1 mM GTP, an oxygen scavenger cocktail (20 mM dithiothreitol, 1.2 mg ml−1 glucose, 8 µg ml−1 catalase and 40 µg ml−1 glucose oxidase), 0.1% BSA and 0.025% methyl cellulose (1500 cp, Sigma). After 10 min of elongation, the elongation mix containing 10 µM of tubulin (to prevent microtubule disassembly due to dilution) along with various concentrations of the drugs (Pretubulysin/Nocodazole) was perfused into the chamber. For control experiments, just the elongation mix containing 10µM of tubulin with equivalent concentrations of DMSO was flushed in. Microtubules were imaged before, during and after addition of each drug.

Time-lapse recording (with a frame interval of 0.99 s) was performed using line scan mode in the Zen blue software (version 3.2, Zeiss). Videos were processed to improve the signal/noise ratio (subtract background and smooth functions of ImageJ, version 1.53t). The kymographs corresponding to the time-lapse sequences were drawn using the inbuilt resliced function in ImageJ and the depolymerization velocity was estimated using a customized ImageJ macro. Microtubule mass before and after drug addition was calculated by measuring the total length of microtubules in a single field of view over a period of 8 min.

Persistent random search simulations. We performed Monte Carlo simulations of a discrete-time random walk process in a 3D box of lateral sizes L×L and height h. We used default values L = 5.6 mm and h = 1.5 mm, unless mentioned otherwise. The simulation box, shown in Figure 2A, was laterally confined with reflecting boundaries. In the vertical direction, the system was confined between an upper entry plate and an absorbing boundary at the bottom to mimic the experimental conditions. Starting from a random position on the top surface with a random incident angle towards the bulk, each random walker continued the motion until hitting and eliminating one of the targets located on the bottom plate. The area of each target was ~ 200 µm^2 and a total number of ~25000 targets were distributed randomly on the bottom plate. Each target was eliminated upon first contact with a searcher. The killing kinetics was monitored in a target zone of area 0.7 mm^2 at the center of the bottom plate; see Fig.2A. The time step of the simulations was chosen to be Δt = 30 s. The random walkers performed a persistent random walk with the given mean speed and persistence. At each step of the simulation, the directional change θ of the walker with respect to the previous direction of motion was obtained from θ = arccos(p) (40,41). An azimuthal angle perpendicular to the direction of motion was also chosen randomly from the range [0, 2π]. Next, the position was updated according to an instantaneous speed randomly extracted from an exponential distribution with the given mean value. The extension of this algorithm to multistate processes (42,43) was employed in (21) to distinguish between different categories of CTLs speeds in collagen matrices at relatively short time scales. However, the single-state persistent random walk mode has been employed for the present study since the time scales are beyond the transient dynamic's regime.

Active droplet simulations. The active droplet is modelled as a viscous fluid with an active boundary, implemented using the immersed boundary method. Full details of the numerical implementation of the hydrodynamics and immersed boundary can be found in (44). The active boundary of the droplet has an associated concentration representing active particles which spontaneously polarizes, leading to gradients in boundary tension driving droplet motion. To set the concentration profile to values similar to those seen in experiment we set a concentration maximum by introducing a tangential forcing term on the boundary above a threshold concentration. We set the concentration threshold to for the low and high case respectively, where c_0 is the average concentration, corresponding to the initial uniform concentration on the boundary.

Statistical Analysis. For RT-DC, linear mixed model included in the ShapeOut software. GraphPad Prism 9.5.1 Software (GraphPad) was used for statistical analysis of the rest of experiments. D'Agostino and Pearson tests were used to test normality. Between two paired groups, paired t-test was used for normal distribution, and a Wilcoxon matched-pairs signed rank test was used for non-normal distribution. Between two unpaired groups, unpaired t-test was used for normal distribution and Mann–Whitney–U-test was used for non-normal distribution. To compare three or more groups, a one-way ANOVA test was used, and multiple comparisons were done with Dunn's multiple comparisons test.

Ethical Considerations. Research carried out for this study with healthy donor material (leukocyte reduction system chambers from human blood donors) is authorized by the local ethic committee [declaration from 16.4.2015 (Ha 84/15; Prof. Dr. Rettig-Stürmer) and amendment from 23.03.2021 (Ha 84/15; Prof. Dr. Markus Hoth)].

References

1. Fowell DJ, Kim M. The spatio-temporal control of effector T cell migration. Vol. 21, Nature Reviews Immunology. Nature Research; 2021. p. 582–96.
2. Barry M, Bleackley RC. Cytotoxic T lymphocytes: All roads lead to death. Vol. 2, Nature Reviews Immunology. European Association for Cardio-Thoracic Surgery; 2002. p. 401–9.
3. Wortel IMN, Textor J. Interpreting T-cell search "strategies" in the light of evolution under constraints. PLoS Comput Biol. 2023 Feb 1;19(2).
4. Shaebani MR, Jose R, Santen L, Stankevicins L, Lautenschläger F. Persistence-Speed Coupling Enhances the Search Efficiency of Migrating Immune Cells. Phys Rev Lett. 2020 Dec 28;125(26).
5. Maiuri P, Rupprecht JF, Wieser S, Ruprecht V, Bénichou O, Carpi N, *et al*. Actin flows mediate a universal coupling between cell speed and cell persistence. Cell. 2015 Apr 9;161(2):374–86.
6. Dupré L, Houmadi R, Tang C, Rey-Barroso J. T lymphocyte migration: An action movie starring the actin and associated actors. Vol. 6, Frontiers in Immunology. Frontiers Research Foundation; 2015.
7. Moreau HD, Piel M, Voituriez R, Lennon-Duménil AM. Integrating Physical and Molecular Insights on Immune Cell Migration. Vol. 39, Trends in Immunology. Elsevier Ltd; 2018. p. 632–43.
8. Kopf A, Kiermaier E. Dynamic Microtubule Arrays in Leukocytes and Their Role in Cell Migration and Immune Synapse Formation. Vol. 9, Frontiers in Cell and Developmental Biology. Frontiers Media S.A.; 2021.
9. Thé M, Racine V, Piel M, Pé Pin § A, Dimitrov A, Chen Y, *et al*. Anisotropy of cell adhesive microenvironment governs cell internal organization and orientation of polarity. Vol. 103, CELL BIOLOGY. 2006.
10. Pimm ML, Henty-Ridilla JL. New twists in actin-microtubule interactions. Vol. 32, Molecular Biology of the Cell. American Society for Cell Biology; 2021. p. 211–7.
11. Rey-Suarez I, Rogers N, Kerr S, Shroff H, Upadhyaya A. Actomyosin dynamics modulate microtubule deformation and growth during T-cell activation. Mol Biol Cell. 2021 Aug 19;32(18):1641–53.
12. Zhao R, Zhou X, Khan E, Yang W, Schwarz EC, Del Campo Bécares A, *et al*. Disruption of microtubule network rescues impaired killing of CD8 + T cells in high density extracellular matrix.
13. Tabdanov ED, Rodríguez-Merced NJ, Cartagena-Rivera AX, Puram V V., Callaway MK, Ensminger EA, *et al*. Engineering T cells to enhance 3D migration through structurally and mechanically complex tumor microenvironments. Nat Commun. 2021 Dec 1;12(1).
14. Takesono A, Heasman SJ, Wojciak-Stothard B, Garg R, Ridley AJ. Microtubules regulate migratory polarity through Rho/ ROCK signaling in T cells. PLoS One. 2010 Jan 19;5(1).
15. Hui KL, Upadhyaya A. Dynamic microtubules regulate cellular contractility during T-cell activation. Proc Natl Acad Sci U S A. 2017 May 23;114(21):E4175–83.
16. Kopf A, Renkawitz J, Hauschild R, Girkontaite I, Tedford K, Merrin J, *et al*. Microtubules control cellular shape and coherence in amoeboid migrating cells. Journal of Cell Biology. 2020;219(6).

17. Braig S, Wiedmann RM, Liebl J, Singer M, Kubisch R, Schreiner L, *et al*. Pretubulysin: a new option for the treatment of metastatic cancer. Cell Death Dis. 2014;5.
18. Herrmann J, Elnakady YA, Wiedmann RM, Ullrich A, Rohde M, Kazmaier U, *et al*. Pretubulysin: From hypothetical biosynthetic intermediate to potential lead in tumor therapy. PLoS One. 2012 May 17;7(5).
19. Kubisch R, Von Gamm M, Braig S, Ullrich A, Burkhart JL, Colling L, *et al*. Simplified pretubulysin derivatives and their biological effects on cancer cells. J Nat Prod. 2014 Mar 28;77(3):536–42.
20. Kern S, Truebenbach I, Höhn M, Gorges J, Kazmaier U, Zahler S, *et al*. Combined antitumoral effects of pretubulysin and methotrexate. Pharmacol Res Perspect. 2019 Feb 1;7(1).
21. Sadjadi Z, Zhao R, Hoth M, Qu B, Rieger H. Migration of Cytotoxic T Lymphocytes in 3D Collagen Matrices. Biophys J [Internet]. 2020 Dec 1 [cited 2024 May 22];119(11):2141–52. Available from: http://www.cell.com/article/S0006349520308250/fulltext
22. Zhao R, Yanamandra AK, Qu B. A high-throughput 3D kinetic killing assay. Eur J Immunol. 2023 Nov 1;53(11).
23. Pegoraro AF, Janmey P, Weitz DA. Mechanical properties of the cytoskeleton and cells. Cold Spring Harb Perspect Biol. 2017 Nov 1;9(11).
24. Mietke A, Otto O, Girardo S, Rosendahl P, Taubenberger A, Golfier S, *et al*. Extracting Cell Stiffness from Real-Time Deformability Cytometry: Theory and Experiment. Biophys J. 2015 Nov 17;109(10):2023–36.
25. Schmidt CJ, Stehbens SJ. Microtubule control of migration: Coordination in confinement. Vol. 86, Current Opinion in Cell Biology. Elsevier Ltd; 2024.
26. Steinmetz MO, Prota AE. Microtubule-Targeting Agents: Strategies To Hijack the Cytoskeleton. Vol. 28, Trends in Cell Biology. Elsevier Ltd; 2018. p. 776–92.
27. Xiangrong X, Yao L, Yao A. The Recent Developments of ADCs with the Tubulysins as the Payloads. Mini-Reviews in Medicinal Chemistry [Internet]. 2023 Feb 21 [cited 2024 May 14];23(18):1797–805. Available from: https://www.eurekaselect.com/article/129615
28. Chang YC, Nalbant P, Birkenfeld J, Chang ZF, Bokoch GM. 3GEF-H1 couples nocodazole-induced microtubule disassembly to cell contractility via RhoA. Mol Biol Cell. 2008 May;19(5):2147–53.
29. Ullrich A, Chai Y, Pistorius D, Elnakady YA, Herrmann JE, Weissman KJ, *et al*. Pretubulysin, a potent and chemically accessible tubulysin precursor from Angiococcus disciformis. Angew Chem Int Ed Engl [Internet]. 2009 Jun 2 [cited 2024 May 24];48(24):4422–5. Available from: https://pubmed.ncbi.nlm.nih.gov/19431172/
30. Krummel MF, Bartumeus F, Gérard A. T cell migration, search strategies and mechanisms. Vol. 16, Nature Reviews Immunology. Nature Publishing Group; 2016. p. 193–201.
31. Ganguly A, Yang H, Zhang H, Cabral F, Patel KD. Microtubule dynamics control tail retraction in migrating vascular endothelial cells. Mol Cancer Ther. 2013 Dec;12(12):2837–46.

32. Lautenschlä Ger F, Paschke S, Schinkinger S, Bruel A, Beil M, Guck J. The regulatory role of cell mechanics for migration of differentiating myeloid cells [Internet]. Available from: www.pnas.org/cgi/content/full/
33. Krendel M, Zenke FT, Bokoch GM. Nucleotide exchange factor GEF-H1 mediates cross-talk between microtubules and the actin cytoskeleton. Nat Cell Biol. 2002;4(4):294–301.
34. Joo E, Olson MF. Regulation and functions of the RhoA regulatory guanine nucleotide exchange factor GEF-H1. Vol. 12, Small GTPases. Taylor and Francis Ltd.; 2021. p. 358–71.
35. Pineau J, Pinon L, Mesdjian O, Fattaccioli J, Duménil AML, Pierobon P. Microtubules restrict F-actin polymerization to the immune synapse via GEF-H1 to maintain polarity in lymphocytes. Elife. 2022 Sep 1;11.
36. Azoitei ML, Noh J, Marston DJ, Roudot P, Marshall CB, Daugird TA, *et al*. Spatiotemporal dynamics of GEF-H1 activation controlled by microtubule-And Src-mediated pathways. Journal of Cell Biology. 2019 Sep 2;218(9):3077–97.
37. Krummel MF, Friedman RS, Jacobelli J. Modes and mechanisms of T cell motility: Roles for confinement and Myosin-IIA. Vol. 30, Current Opinion in Cell Biology. Elsevier Ltd; 2014. p. 9–16.
38. Westphal V, Rizzoli SO, Lauterbach MA, Kamin D, Jahn R, Hell SW. Video-rate far-field optical nanoscopy dissects synaptic vesicle movement. Science (1979) [Internet]. 2008 Apr 11 [cited 2024 May 23];320(5873):246–9. Available from: https://www.science.org/doi/10.1126/science.1154228
39. Schaedel L, Triclin S, Chrétien D, Abrieu A, Aumeier C, Gaillard J, *et al*. Lattice defects induce microtubule self-renewal. Nat Phys. 2019 Aug 1;15(8):830–8.
40. Sadjadi Z, Shaebani MR. Orientational memory of active particles in multistate non-Markovian processes. Phys Rev E. 2021 Nov 1;104(5).
41. Tierno P, Shaebani MR. Enhanced diffusion and anomalous transport of magnetic colloids driven above a two-state flashing potential. Soft Matter [Internet]. 2016 Mar 30 [cited 2024 May 14];12(14):3398–405. Available from: https://pubs.rsc.org/en/content/articlehtml/2016/sm/c6sm00237d
42. Shaebani MR, Rieger H. Transient Anomalous Diffusion in Run-and-Tumble Dynamics. Front Phys. 2019 Sep 18;7.
43. Shaebani MR, Rieger H, Sadjadi Z. Kinematics of persistent random walkers with two distinct modes of motion. Phys Rev E. 2022 Sep 1;106(3).
44. Whitfield CA, Hawkins RJ. Immersed Boundary Simulations of Active Fluid Droplets. PLoS One [Internet]. 2016 Sep 1 [cited 2024 May 23];11(9):e0162474.

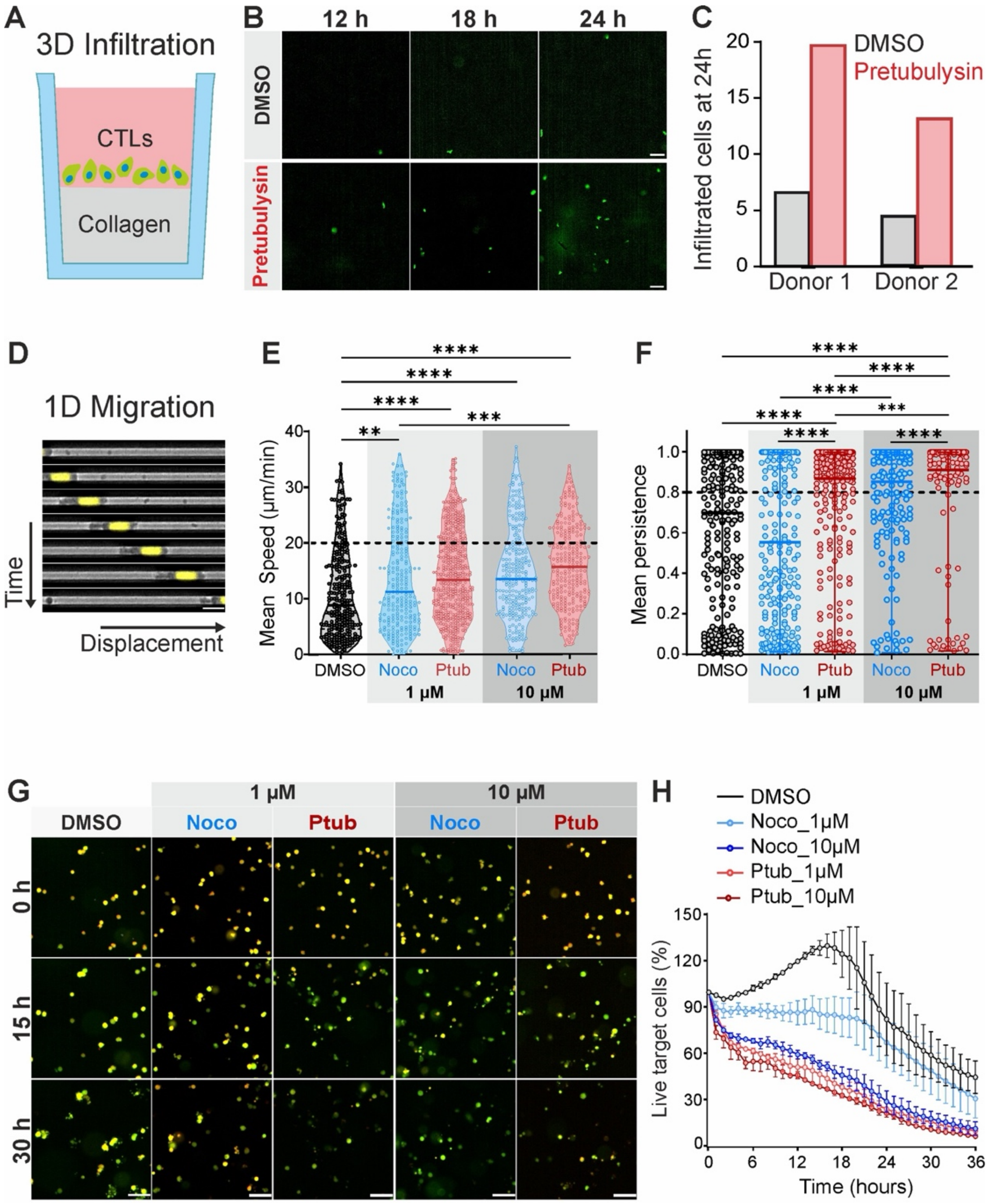

Figure 1. Pretubulysin enhances CTLs function in 3D by improving migration parameters.

Figure 1. Pretubulysin enhances CTL function in 3D by improving migration parameters. (A) Scheme of CTLs infiltration into 3D collagen matrix. CTLs were stained with carboxyfluorescein succinimidyl ester (CFSE), treated with DMSO or Pretubulysin (1µM and 10 µM) for 30 min and added on top of solidified collagen matrix (collagen represented in grey, CTLs culture medium without any drug is represented in pink). Cells were visualized as they reached the bottom of the well.

(B) Images taken at different timepoints during the 3D infiltration assay from one representative donor treated with DMSO or Pretubulysin (10 µM). CFSE-CTLs were visualized at the bottom of the plate (in green). Scale bar is 50 µm.

(C) Quantification of particles after 12 hours. Graph represents data from three individual donors (shown with a color code) in duplicate treated with DMSO or Pretubulysin (1μM and 10 μM).

(D) Images taken at different timepoints during the 1D migration assay from one representative donor. Hoechst-stained CTLs (yellow nuclei) were treated with DMSO or drugs and loaded on PEG-coated channels (length: 400 μm; width: 5 μm; height: 5 μm). Cells migrated spontaneously for 15 hours and images were acquired every 2 minutes. Scale bar is 10 μm.

(E-F) Time lapse videos were analyzed for automatic tracking of CTLs from four different donors treated with DMSO, Nocodazole at 1 μM or 10 μM, or Pretubulysin at 1 μM or 10 μM. In the graphs, each dot represents the mean speed (E) or mean persistence (F) of the track. For statistical analysis, one-way ANOVA and the Kruskal-Wallis test for multiple comparisons were used (in (E) **** p<0.0001, *** p=0.0009; in (F) **** p<0.0001, DMSO vs. 1 μM Noco *** p=0.0002, 0.1 μM Ptub vs. 10 μM Ptub *** p=0.0003).

(H) Images taken at different timepoints during the 3D killing assay of cells from one representative donor treated with DMSO, Nocodazole at 1 μM or 10 μM, or Pretubulysin at 1 μM or 10 μM. Live target cells are orange–yellow, apoptotic target cells are green, and dead cells lose fluorescence. Scale bar is 50 μm.

(I) Quantification of target cell death during the 3D killing assay. Dots represent the mean value of four donors, error bars represent the standard deviation (SD).

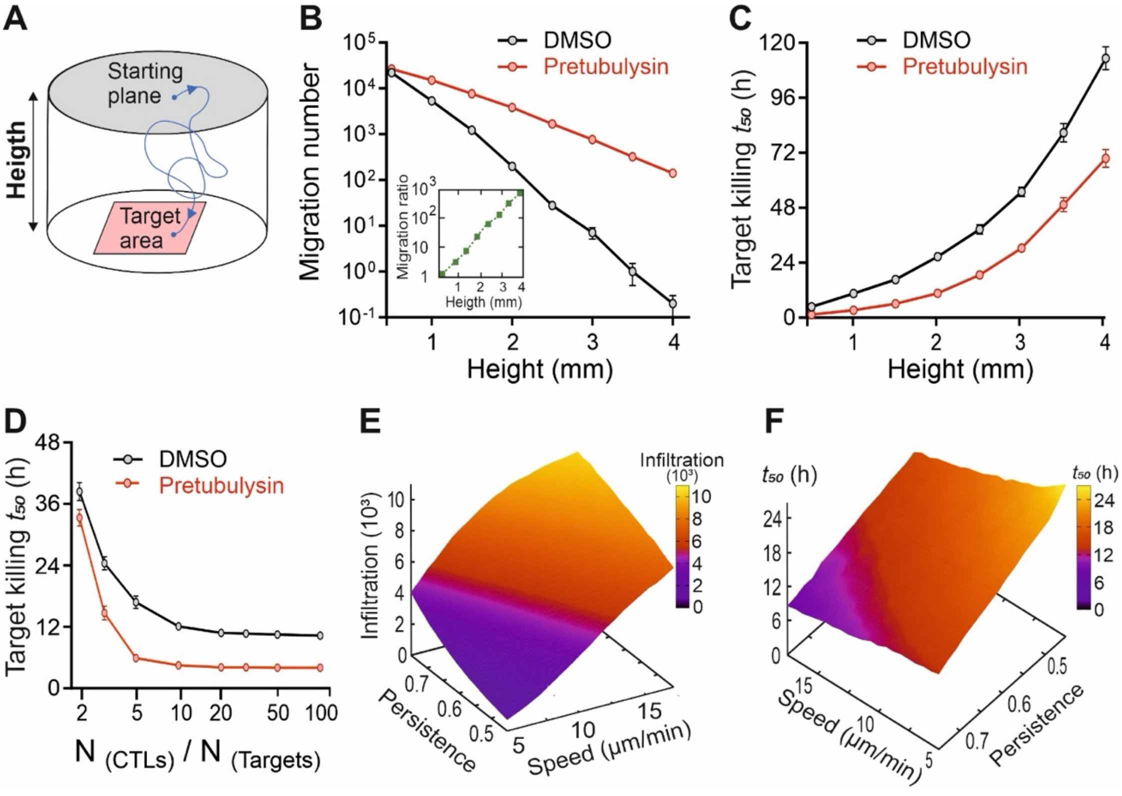

Figure 2. Quantification of migration and killing efficiency of control and Pretubulysin-treated CTLs in 3D obtained from persistent random search simulations.

A) Comparison of killing kinetics between simulations and experimental data. Time evolution of the covered area by target cells is shown for experiments and corresponding simulations using the experimental cell motility data. Inset: Schematic of the simulation setup. CTLs were modeled as persistent random walkers entering the medium from the top surface, indicated as “starting plane”, and migrating until they reach the target cells at the bottom plate, indicated as “target area”.

(B) Dependence of migration efficiency on the thickness of collagen matrix (height) for control and Pretubulysin-treated cells. The inset indicates that the ratio between the number of treated and control cells which reached the target area increases by several orders of magnitude upon a few-fold increase of the collagen matrix height.

(C) Killing capacity versus collagen matrix height for treated and control CTLs. The difference between the killing halftime t_{50} (i.e. the time spent to eliminate 50% of the targets) of control and treated cells grows with increasing collagen thickness.

(D) Killing capacity in terms of the ratio between the initial number of CTLs and target cells ($N_{CTLs}/N_{targets}$) for treated and control CTLs.

(E) Number of migrating cells reaching the target area in terms of mean speed and persistence.

(F) Killing halftime (t_{50}) versus mean speed and persistence.

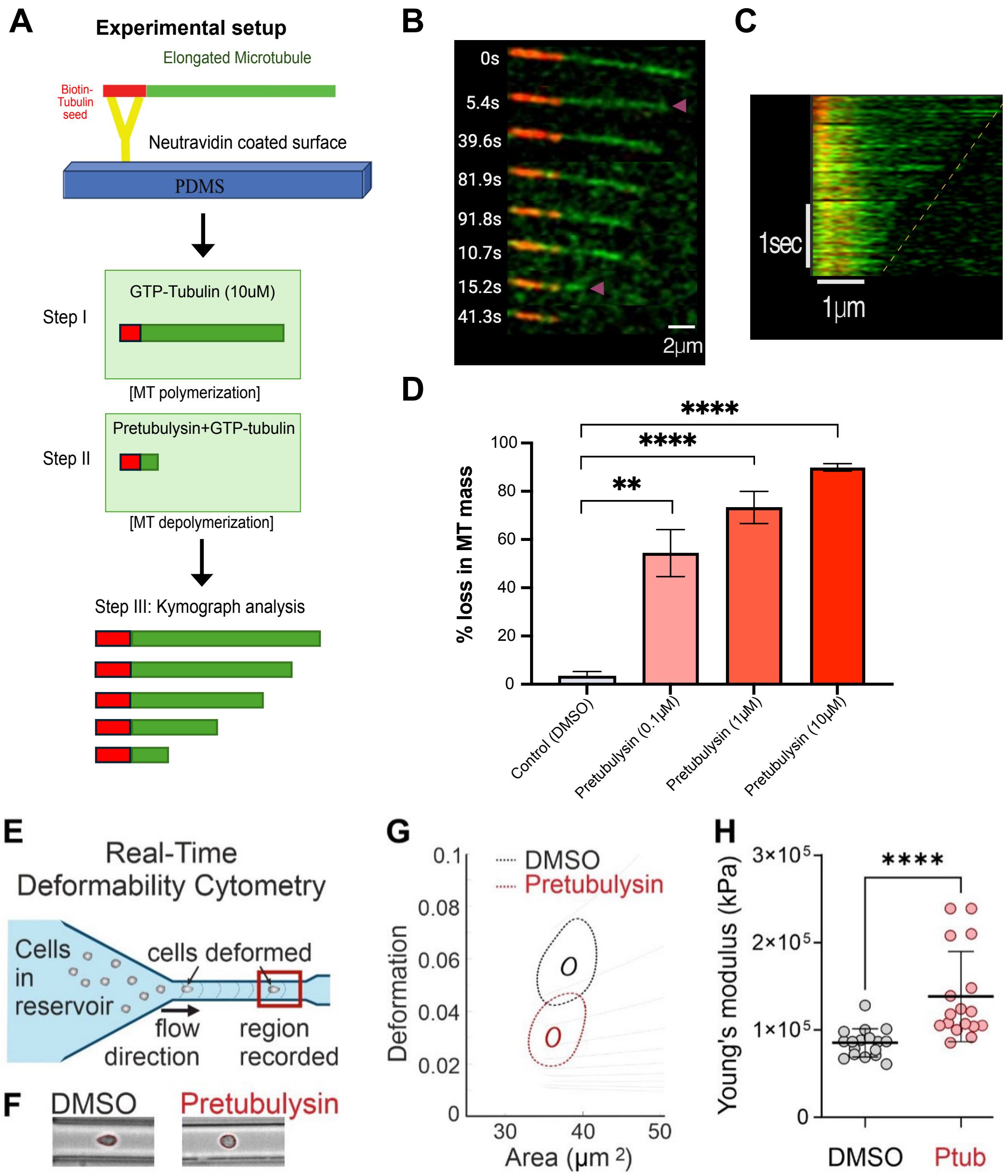

Figure 3. Pretubulysin is a potent microtubules depolymerization agent and stiffens CTLs.

(A) Scheme of the microfluidics based *in vitro* reconstitution assays using purified tubulin: short biotin-containing microtubule fragments (red) were attached using neutravidin (yellow) on to a passivated and used as 'seeds' to induce MT growth. Microtubules (green) were elongated from these seeds by continuous flushing of labeled tubulin. In a second step, drug and labeled tubulin is flushed in.
(B-C) Representative Kymographs depicting microtubule length distribution.
(D) Quantification of Pretubulysin disassemble capacity on Microtubules. Dots represent individual experiments; results are presented as Mean ± SD. The Mann-Whitney test was used for statistical significance (*** p<0,0001, **p<0,0017).

(E) Scheme of real-time deformability cytometer setup: a 20 µm microfluidic PDMS chip was assembled on the stage of an inverted microscope. The cell suspension was loaded on the reservoir and deformed by shear stresses and pressure gradient caused by the flow profile.
(F) Representative images of cells during real-time deformability cytometer showing the typical bullet shape for control cells (DMSO) versus round shape observed for Pretubulysin treated CTL.
(G) Kernel density estimate plot depicting cell area versus deformation obtained for one representative experiment. Pretubulysin treatment makes CTLs less deformable than DMSO-treated control cells.
(H) Apparent Young´s modulus was calculated and analyzed using linear mixed models available with the ShapeOut2.0 software. The results obtained from 3 different donors are represented on the graph, where one dot represents one experiment and error bars represent standard deviation of the mean. At least 3000 events were acquired for each condition in every experiment. For statistical analysis, one-way ANOVA and Kruskal-Walli test for multiple comparisons was used ($p<0.0001$).

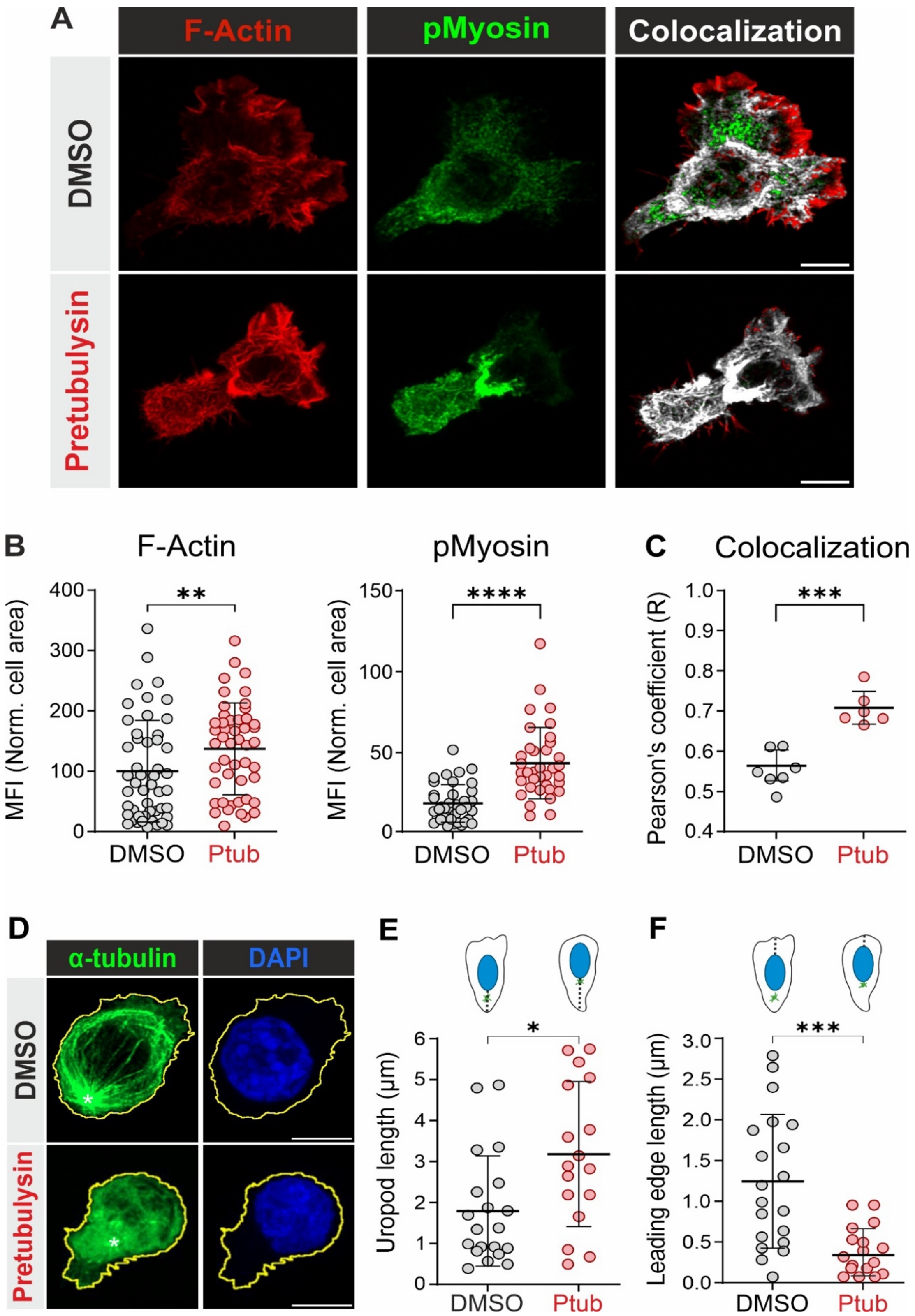

Figure 4. Pretubulysin alters cytoskeleton and morphology of CTLs.
(A) z-stack of representative CTLs treated with DMSO or Pretubulysin (10 µM), immobilized on cell-tack coated coverslips, fixed/permeabilized and immune-stained for F-actin (red), pMyosin (green) and the colocalized region of F-actin and pMyosin (grey). Colocalization analysis was carried out using ImageJ coloc2 plugin. Scale bar=10 µm.

(B) Quantification of F-Actin and pMyosin fluorescent signal on CTLs treated with DMSO or Pretubulysin (10 µM). Treated CTLs were immobilized on cell-tack coated coverslips and fixed/permeabilized for immune-staining. Cell border based on actin staining was defined as ROI, F-Actin and pMyosin in the region were quantified using Sum Intensity Projections with ImageJ and normalized with the cell area. Dots represent individual cells from at least 2 different donors, error bars represent the standard deviation of the mean (mean ± SD). The Mann-Whitney test was used fdor statistical significance (**p=0.0089). Scale bar=10um.

(C) Pearsons's correlation coefficient was calculated using ImageJ coloc2 plugin. Dots represent individual cells; error bars represent the standard deviation of the mean (mean ± SD). The Mann-Whitney test was used for statistical significance (*** p=0.0004). Scale bar=10um.

(D) Maximal Intensity projection of one representative cell for each condition (DMSO and Pretubulysin 10 µM), immobilized on cell-tack coated coverslips showing that Pretubulysin induced MT network disassembly on CTLs. Cell border based on actin staining is shown in yellow, α-tubulin in green and nucleus in blue. The arrows indicate the MTOC. Scale bar=10 µm.

(E-F) Length of the uropod and of the leading edge were calculated manually using ImageJ from fluorescent confocal images. Schematics on top of the graphs represent CTLs in the 2 conditions -DMSO or Pretubulysin (10 µM) treated-, the nucleus in blue, the MTOC in green and the dotted line represents the distance measured: uropod, from the cell edge to the nuclei; leading edge, from the nuclei to the cell edge. On the graphs, dots represent individual cells from 2 donors, error bars represent the standard deviation of the mean (mean ± SD). For statistical significance, the Mann-Whitney test was used for analyzing the back and front distance (p<0,0165 and p<0,0001 respectively).

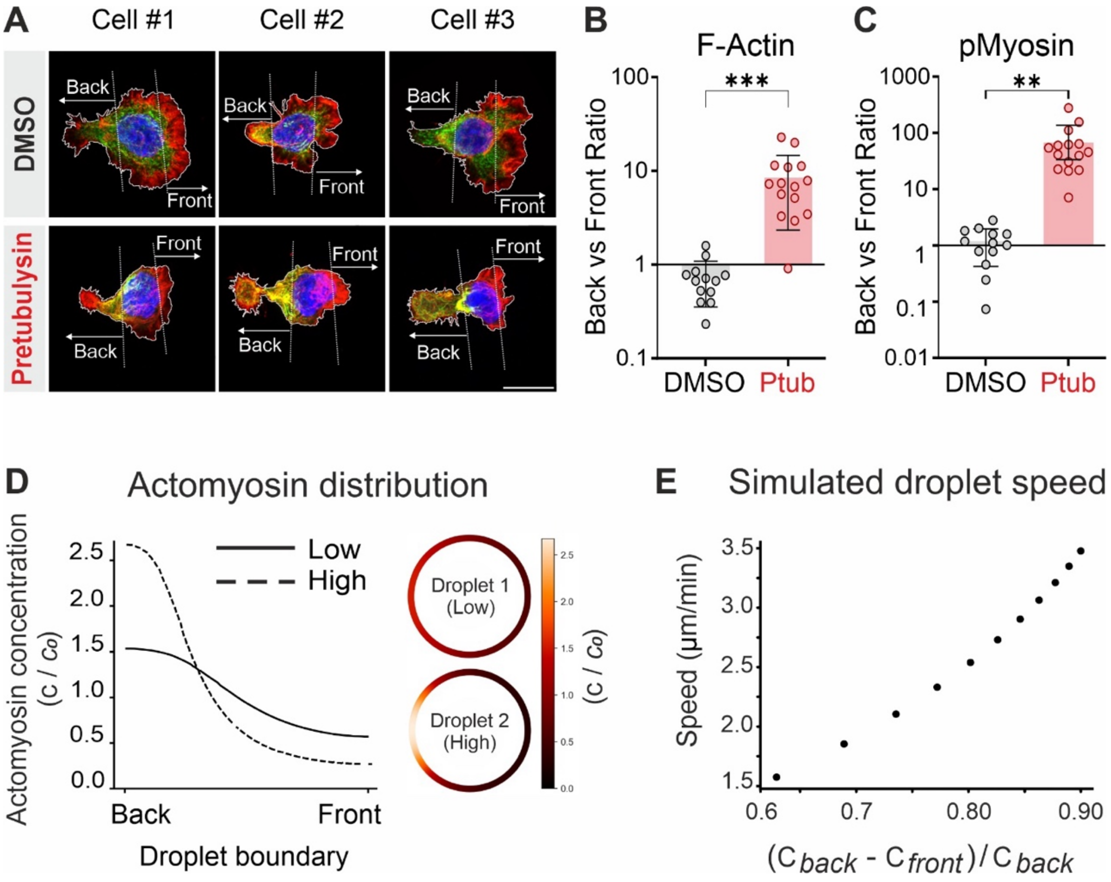

FIGURE 5. Microtubule disruption-induced actomyosin accumulation at the uropod favors migration.

(A) Maximal Intensity projection of 3 cells for each condition: DMSO and Pretubulysin (10 M), immobilized on cell-tack coated coverslips. F-actin is shown in red, pMyosin in green and the nucleus in blue. The cell border (white) was established based on actin staining. The regions "back" and "front" were defined by the positioning of the nuclei and are represented with dotted lines (white) defined by the position of the nuclei. Scale bar=10 µm.

(B-C) Sum Intensity Projections were generated using ImageJ. Total F-Actin (B) and pMyosin (C) were calculated on the regions "back" and "front" (MFI * region area). The graph represents the ratio between Front and Back. Dots represent individual cells and the mean ± SD is shown. The unpaired Student's t-test with Welch's correction was used for statistical significance (*** p=0.0002 for F-Actin and **p=0.0023).

(D-E) Using computational methods amoeboid cell migration was modeled as a viscous droplet with an active boundary analogous to the cell's cortex. (D) A concentration of actomyosin, *c*, was placed on the boundary considering the experimental values. Droplet 1 represents an example of low difference between back and front (low ratio), comparable with the experimental data obtained for control (DMSO) CTLs. Droplet 2 represents an extreme example of high difference between back and front (high ratio) comparable with the experimental data obtained for Pretubulysin (10 µM) treated CTLs. The concentration profile is shown by the color scale, where *c* is normalized by c_0, the average droplet concentration. Both droplets have equal total and average concentration. (E) Droplet speed against concentration -difference normalized by the concentration at the back of the droplet. The calculations indicate that greater difference in actomyosin from front to back leads to faster migration.

Figure Supplementary 1. CTLs degranulation capacity is not affected with Microtubule depolymerization with Pretubulysin or Nocodazole.

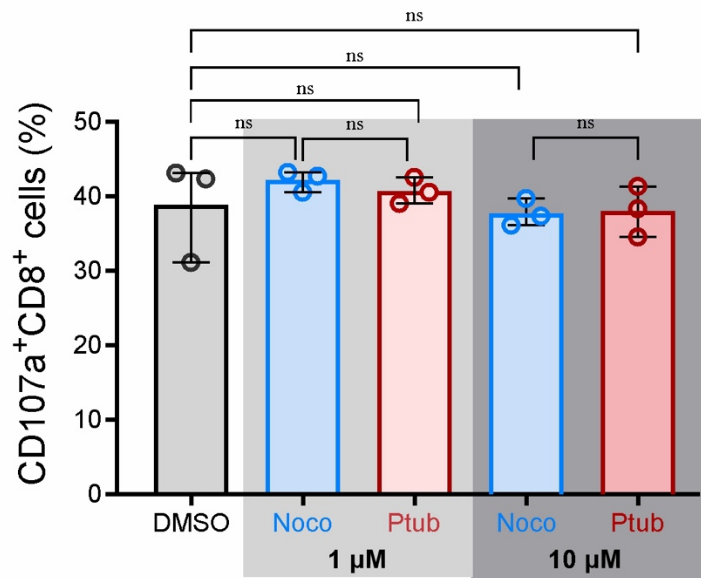

Figure Supplementary 2. Comparison of Killing Kinetics Between Simulations and Experimental Data

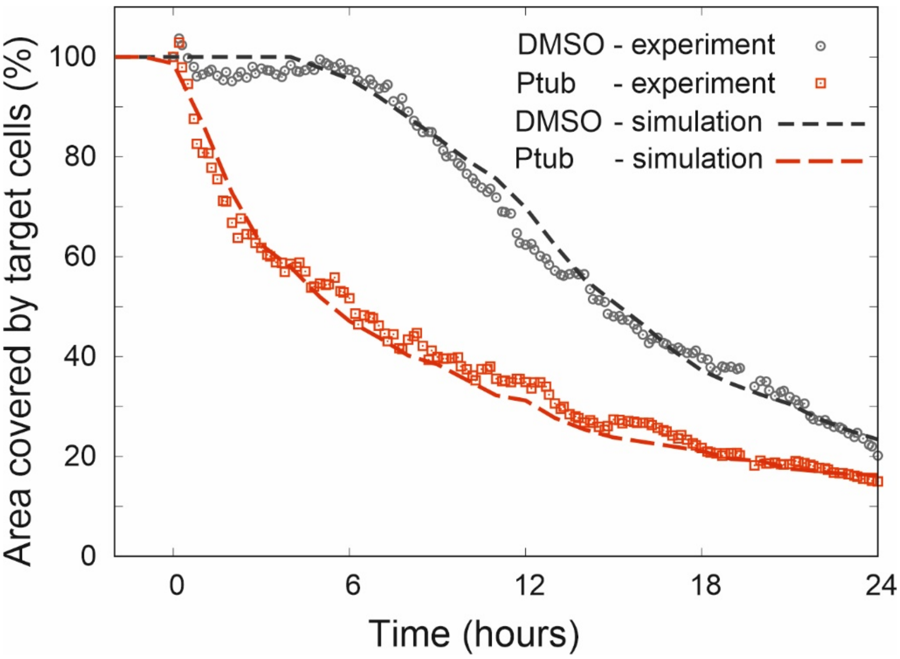

Figure Supplementary 3:

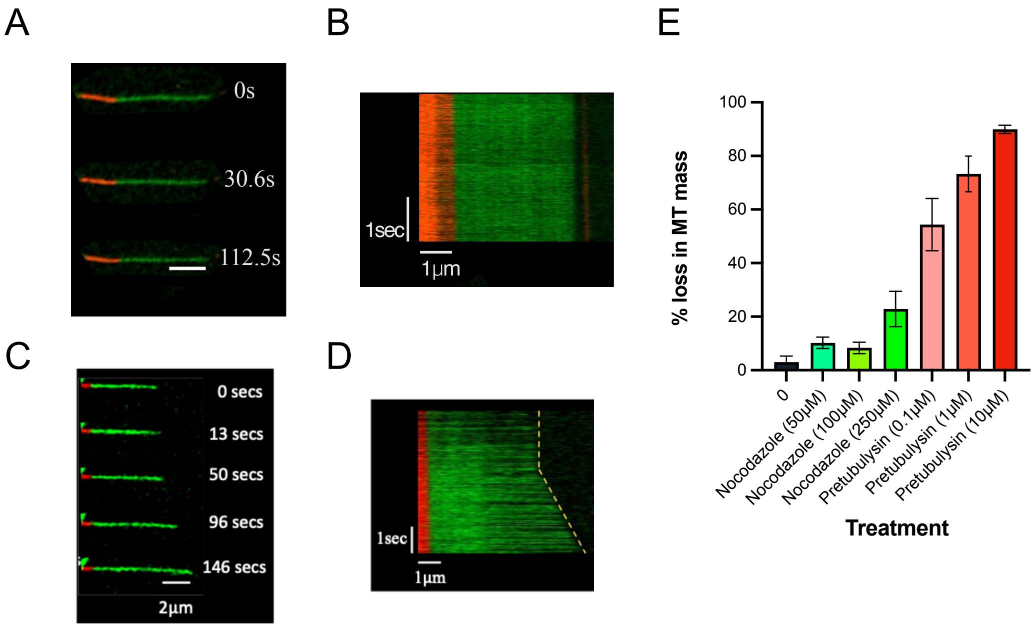

A. Timelapse sequence showing microtubule pause (with no subsequent change in microtubule length) following treatment with 10 µM Nocodazole (Scale bar-2 m). Images are representative of three independent experiments.

B. Kymograph from A, depicting no change in microtubule length vs time after treatment with 10 µM Nocodazole.

C. Timelapse sequence showing microtubule pause and then elongate following treatment with 10 µM Nocodazole (Scale bar- 2 m). Images are representative of three independent experiments.

D. Kymograph from C, depicting pause and increase in microtubule length vs time after treatment with 10 µM Nocodazole.

E. Comparison of % loss in microtubules mass following treatment with Nocodazole (50, 100 and 250 µM), Pretubulysin (0.1, 1 and 10 µM) with Control (DMSO). Data represent Mean ± SD from three independent experiments. Unpaired t- test was used for statistical significance.

Supplementary table 1:

P-values of comparison in % loss of MT mass between tested concentrations of Nocodazole and Pretubulysin with Control (DMSO) (Statistical analysis: Unpaired t-test).

	Control (DMSO)	Pretubulysin 0.1	Pretubulysin 1	Pretubulysin 10
Control (DMSO)	-	0.0025	<0.0001	<0.0001
Nocodazole (50)	0.0158	0.0038	<0.0001	<0.0001
Nocodazole (100)	0.0414	0.0034	<0.0001	<0.0001
Nocodazole (250)	0.0079	0.0211	0.0007	<0.0001

5.3 Further characterization of the microtubule depolymerizing action of pretubulysin:

The potent microtubule depolymerizing activity of Pretubulysin (PT) prompted us to further explore its effect on microtubule dynamics at low concentrations to gain insight into its mode of action.

(The results presented in the section are from the master thesis research work of Mirko Wieczorek, who performed the experiments and analyzed the data under my guidance).

5.3.2 At low concentrations, Pretubulysin interferes with microtubule growth and increases catastrophe frequency

As shown above in Montalvo *et al.*, Pretubulysin induced immediate microtubule depolymerization at high concentrations. We then asked if low concentrations of Pretubulysin would perturb microtubule dynamicity parameters. For this, we tested the effect of Pretubulysin at concentrations wherein we observed microtubule survival -40 and 80 nM. We found that at both these concentrations, microtubule dynamicity was affected by the presence of pretubulysin (**Fig 5.1a**). Particularly, we found a 3.4-fold increase in catastrophe frequency between control (0 nM PT) to 80 nM PT. This indicates that even at low concentrations, Pretubulysin interferes with microtubule dynamics.

5.3.3 Proposed mechanism of action of Pretubulysin

Based on our findings, we propose a possible mechanism of action for the effect of Pretubulysin in **Fig 5.1c.** Microtubule elongation occurs by longitudinal association of tubulin dimers, that is associated with a change in curved-to-straight conformation of the tubulin dimer (Refer introduction).

X-ray structure of Pretubulysin bound tubulin (from our collaborators: Andrea Prota, PSI, Switzerland) shows that Pretubulysin binds to the vinca site located at the intra-dimer interface (**Fig 5.1b)**. Preliminary MST (Microscale Thermophoresis) assay results reveal a binding constant K_d = 1.97 μM for pretubulysin. These match results from MD simulations (Credits: Enrique Araujo, Prof. Dr. Franziska Lautenschläger, and Alejandro Leon, Prof. Dr. Jochen Hub) predict a dissociation constant of 1.6 μM.

This is indicative of a strong binding that may potentially lock the tubulin dimer in its inherent curved conformation. Therefore, as shown for other vinca site binders, binding of Pretubulysin may prevent the straightening of dimers that is required for further protofilament elongation.

In this way, binding of Pretubulysin to a tubulin dimer at the growing interface would 'poison' the dimer and prevent further protofilament elongation, leading to perturbations in microtubule dynamics (at low concentrations) and complete catastrophe at high concentrations (**Fig 5.1c**). Alternatively, Pretubulysin (at high concentrations) may also sequester free tubulin in solution into assembly-incompetent structures, thus reducing the effective free tubulin concentration. Future studies using ultracentrifugation pelleting-down techniques and electron microscopy may help offer insights in this direction.

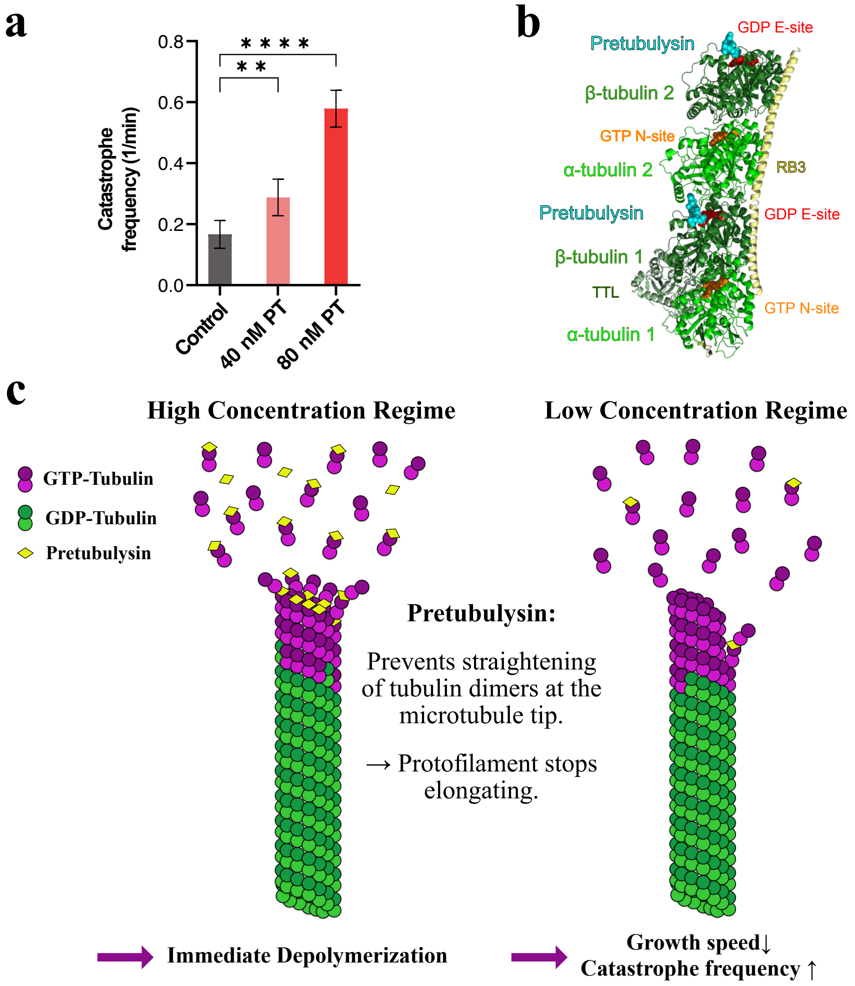

Fig 5.1: (a) Low concentrations of PT increased MT catastrophe frequency by 3.4-fold. Bar plot shows the mean catastrophe frequency and error bars represent the SEM. > 275 min of growth time from at least three independent experiments were analyzed for each condition. **(b)** Overview of the X-Ray structure of pretubulysin bound to the T2R-TTL Complex. The stathmin-like Protein RB3 (pale yellow), the Tubulin—Tyrosine Ligase (TTL) (pale green), and tubulin (grey) are shown in ribbon representation. GTP (orange), GDP (red) and PT (green) are displayed in spheres representation. Data was obtained from Andrea Prota (PSI, unpublished), and the image was created with Pymol. **(c)** Proposed mechanism of action of Pretubulysin: At high concentrations, PT is bound to multiple protofilaments of the microtubule. This stops their elongation and forces the complete MT into a catastrophe. At low concentrations, PT only occasionally stops the elongation of a single protofilament, which perturbs microtubule dynamics.

5.4 References

1. Braig, S., Wiedmann, R. M., Liebl, J., Singer, M., Kubisch, R., Schreiner, L., Abhari, B. A., Wagner, E., Kazmaier, U., Fulda, S., & Vollmar, A. M. (2014). Pretubulysin: a new option for the treatment of metastatic cancer. Cell death & disease, 5(1), e1001. https://doi.org/10.1038/cddis.2013.510
2. Herrmann, J., Elnakady, Y. A., Wiedmann, R. M., Ullrich, A., Rohde, M., Kazmaier, U., Vollmar, A. M., & Müller, R. (2012). Pretubulysin: from hypothetical biosynthetic intermediate to potential lead in tumor therapy. PloS one, 7(5), e37416.
3. Iqbal, N., Zahoor, A. F., Rasool, N., Khan, S. G., Akhtar, R., & Ahmad, R. (2022). Synthetic Approaches to the Total Synthesis of Tubulysin and its Fragments: A Review. Current organic synthesis, 19(4), 507–542.
4. Kretzschmann, V. K., Gellrich, D., Ullrich, A., Zahler, S., Vollmar, A. M., Kazmaier, U., & Fürst, R. (2014). Novel tubulin antagonist pretubulysin displays antivascular properties in vitro and in vivo. Arteriosclerosis, thrombosis, and vascular biology, 34(2), 294–303.
5. Kubisch, R., von Gamm, M., Braig, S., Ullrich, A., Burkhart, J. L., Colling, L., Hermann, J., Scherer, O., Müller, R., Werz, O., Kazmaier, U., & Vollmar, A. M. (2014). Simplified pretubulysin derivatives and their biological effects on cancer cells. Journal of natural products, 77(3), 536–542.
6. Rath, S., Liebl, J., Fürst, R., Ullrich, A., Burkhart, J.L., Kazmaier, U., Herrmann, J., Müller, R., Günther, M., Schereiner, L., Wagner, E., Vollmar, A.M., Zahler,S. (2012). Anti-angiogenic effects of the tubulysin precursor pretubulysin and of simplified pretubulysin derivatives. British Journal of Pharmacology, 167(5), 1048-1061.
7. Ullrich, A., Chai, Y., Pistorius, D., Elnakady, Y. A., Herrmann, J. E., Weissman, K. J., Kazmaier, U., & Müller, R. (2009). Pretubulysin, a potent and chemically accessible tubulysin precursor from Angiococcus disciformis. Angewandte Chemie (International ed. in English), 48(24), 4422–4425.

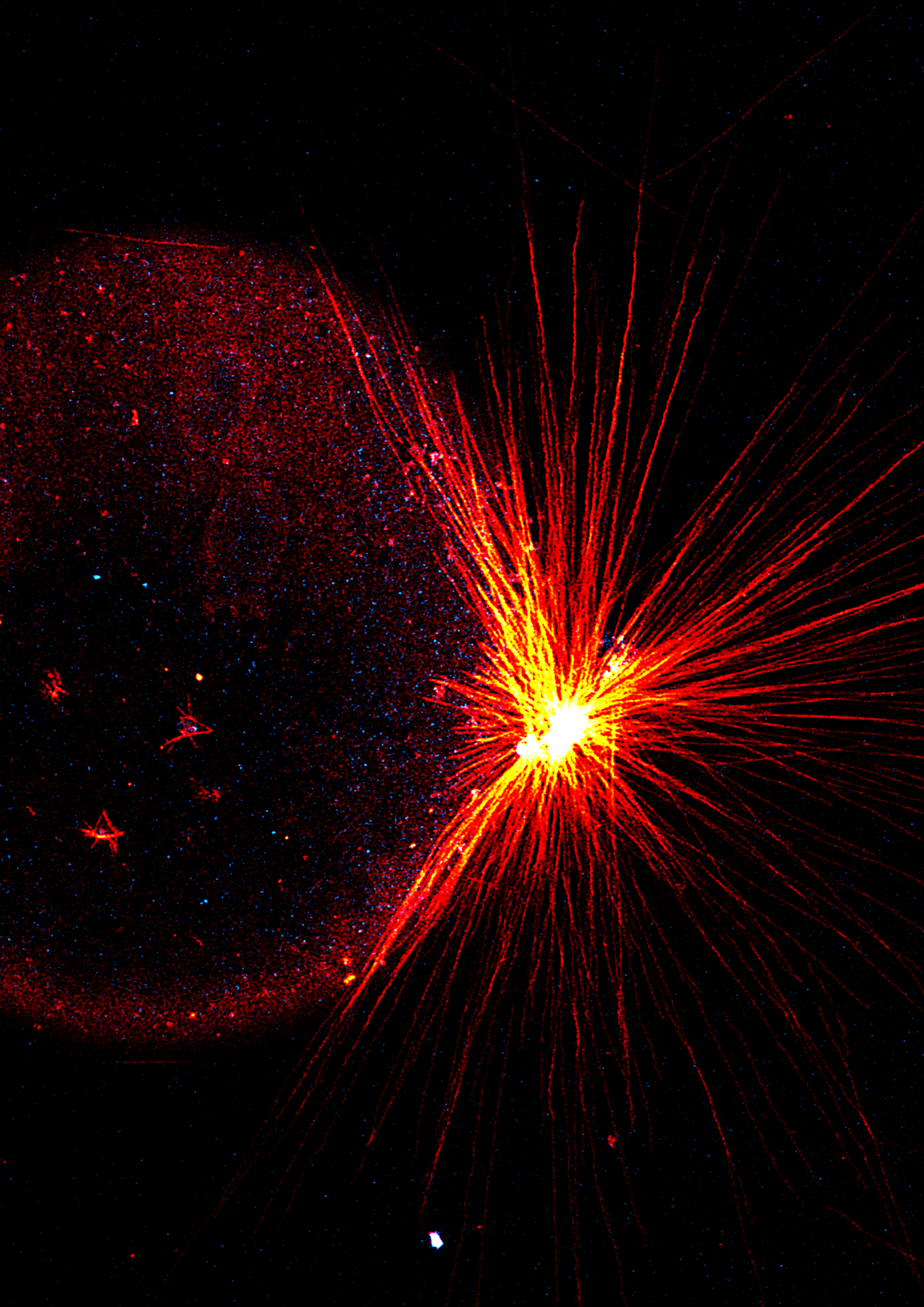

Discussion

Microtubules are inherently metastable polymers whose metastability is reflected in both tip and lattice dynamics. Dynamic instability at the growing tip governs stochastic switching between growth and shrinkage, thereby controlling microtubule length and mass in cells. The dynamic exchange of tubulin subunits along the lattice length enables defect elimination, remodeling in response to external factors and self-repair. Together, the metastable nature of microtubules enables microtubules to be both sensitive to stimuli as well as respond to it. Given their central roles in a multitude of cellular functions and their rigid nature, this dissertation attempted to understand how the metastable nature of microtubules governs their response and adaptation to stress. Further, understanding how microtubule integrity is preserved under stress is essential to decipher how their functions are sustained. In this dissertation, through a combination of inter-related studies, I investigated how mechanical affects microtubule lattice remodeling and dynamic behaviour. In addition, I also showed how perturbations to the microtubule tips by microtubule-targeting agents (MTA's) or drugs (chemical stress) affect microtubule function and consequently have implications on cellular function. Building on my findings, I also explore the nature of inherent lattice dynamics and how external factors like force and post-translational modifications affect microtubule lattice remodeling. Overall, this work provides a unifying framework in which metastability not only functions as a precursor for microtubule dynamic behaviour but also as a tuneable feature that enables mechanoadaptation and functional specialization.

6.1 Mechanically challenging microtubules as in the intracellular environment

Microtubules exist in a mechanically active environment in cells. Despite their high rigidity, microtubules are seen to undergo dynamic deformations in cell, including buckling. This has been attributed predominantly due to the action of microtubule-based molecular motor proteins like kinesin and dynein (Bicek *et al.,* 2009; Pallavacini *et al.*, 2017; Shekhar *et al.*, 2013, Blob *et al.*, 2025). Building on previous studies that show that microtubules self-repair in response to bending by orthogonal fluid flow (Schaedel *et al.*, 2015) as well as by the motile action of unloaded motors (Triclin *et al.*, 2021; Carbo *et al.*, 2022), the first part of my dissertation explored the extent of damage and consequent self-repair in buckling microtubules (wherein microtubules undergo dynamic change in curvature whilst also being subjected to motor forces).

Owing to the complexity of the intracellular environment and the difficulty in separating the influence of the different factors that might contribute to damage in buckling microtubules, I used a combination of *in vitro* reconstitution approaches using purified components with cell-based observations and theoretical simulations. In contrast to previous studies that explored microtubule buckling, I used capped GDP microtubules with the GDP lattice intact, closer to physiological conditions.

In study 1 (Chapter 2, Nandakumar *et al*), I established *in vitro* assays that mimic the different stresses that microtubules are subjected to during buckling in cells. These assays allowed for controlled application of defined mechanical challenges and allowed me to estimate the effect of:

(a) Curvature using static curvature assays wherein microtubules are bent and maintained in this conformation
(b) Motile action of motor proteins by subjecting microtubule to gliding assays
(c) Double anchored assays where microtubules are maintained in a straight conformation but subjected to the pulling action of motors.
(d) Buckling assays wherein microtubules are subjected to a combination of damage due to curvature, motor movement and motor forces.

6.1.1 Kinesin-induced buckling reveals limits of microtubule self-repair

By separating the contribution of different factors in the above study, I found that though curvature, motor movement and forces individually cause damage and tubulin loss, the extent of lattice damage is limited and can largely be balanced by intrinsic self-repair. In contrast, the combination of all three factors during dynamic buckling triggers extensive lattice damage that frequently exceeds microtubule self-repair capabilities leading to breakage particularly at zones of high curvature. Quantification revealed that curvature at point of breakage was three times the average curvature of buckling microtubules, suggesting that curvature may act as an amplifier of motor-induced damage in buckling microtubules (See **Fig 6.1** below).

Since the discovery of microtubule self-repair, it has been widely assumed that this mechanism alone is sufficient to counteract the mechanical stress that microtubules face in cells. My findings challenge this notion and reveal that in situations where microtubules are subjected to continuous dynamic deformations, self-repair mechanisms can be overwhelmed. Consistent with my observations, a recent study reported enhanced bending, buckling, and microtubule fragmentation in cells containing kinesin condensates formed upon overexpression of kinesin-3 (Geng *et al.*, 2025), in line with my observation of catastrophic filament failure at high motor densities.

6.2 Intracellular factors enhance microtubule resilience under mechanical stress

Microtubule breakage is relatively rare in cells (Odde *et al.*, 1999). This implies that there must exist intracellular mechanisms in cells that protect buckling microtubules from breakage and help maintain microtubule integrity. To test this, I performed buckling assays in the presence of cell lysates containing cytosolic components from HEK293 and PtK2 cells and found enhanced microtubule resilience to buckling action of motors in the presence of cell lysates (**Fig 6.1**). Quantifications revealed that in the presence of intracellular factors, microtubules buckle at higher curvatures and are also 1.35- fold softer. My findings suggest that cells may improve microtubule resilience to mechanical stress by possibly recruiting factors that may reduce microtubule stiffness in cells.

This observation therefore raises the possibility that microtubule stiffness in cells may be lower than previously estimated from *in vitro* measurements (Pallavacini *et al.*, 2014; Chakraborty *et al.*, 2020). Reduced stiffness could serve as a protective function by allowing microtubules to be more flexible and resistant to mechanical stress– a form of mechanical compliance that may potentially be actively regulated in cells. Previous studies have implicated that cells may selectively increase microtubule flexibility through recruitment of MAPs like MAP-65-1 that reduce microtubule rigidity (Portran *et al.*, 2013). At present, apart from MAP-65 (bundling protein found in plants), no other MAP has been shown to reduce microtubule stiffness. PTMs like acetylation have been shown to increase microtubule flexibility (Xu *et al.*, 2017), but considering the slow enzymatic rate of the acetylating enzyme αTAT1 (0.4 hr^{-1}; Szyk *et al.*, 2014) and the short timescales of the buckling experiments, it is unlikely that acetylating enzymes contribute to this enhanced resilience.

Identifying the intracellular component(s) that help confer mechanical resilience to microtubules is an important next step in extending the findings of this study, as well as towards exploring how microtubule response is regulated in cells.

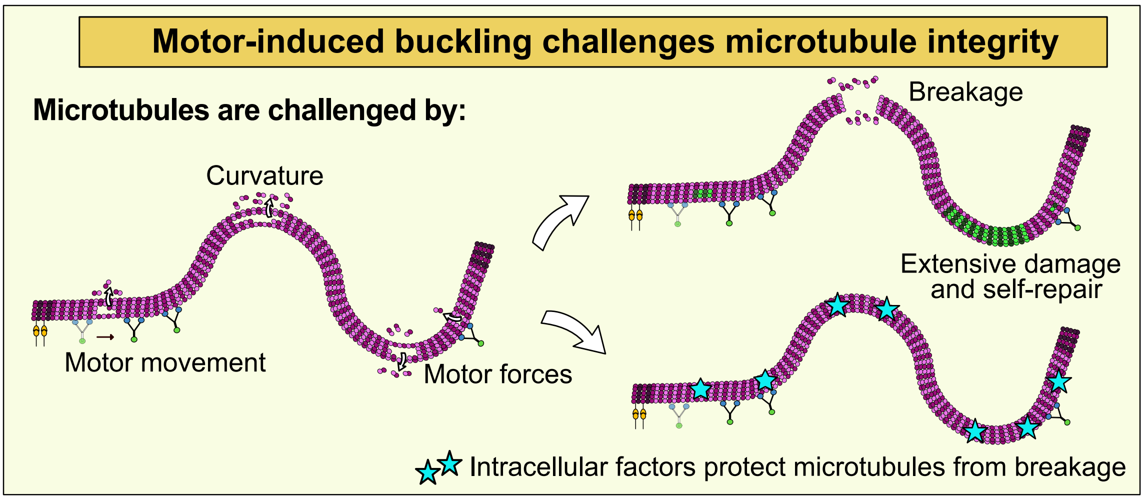

Fig 6.1: Buckling microtubules are challenged by the combination of motor motility, forces and curvature resulting in extensive damage and self-repair or breakage. Intracellular factors protect microtubules and help enhance their survival under sustained deformation

6.3 Differences in tubulin isotypes and PTMs offer an additional layer of regulation to microtubule response to mechanical stress

The tubulin code adds an additional layer of diversity to microtubule composition and thus can modulate the microtubule lattice as well as how microtubules respond to stress. In Chapter 4, I show preliminary results from buckling assays using tubulin purified from HeLa cells that possess differences both in isotypes as well as PTMs when compared to bovine brain tubulin. Microtubules made from HeLa tubulin show enhanced survival under buckling stress, suggesting that the tubulin code may serve as means to regulate microtubule response to stress depending on cellular type and need.

The repertoire of tubulin isotypes and PTMs serves as a great resource for the cell to regulate and (re)organize the intracellular microtubule network locally as an adaptive response to external mechanical stimuli. Modulating the expression of specific tubulin isotypes or PTMs changes the microtubule dynamics and microtubule-associated interaction pathways, thus aiding microtubules in mechanosensing.

In this direction, Torrino *et al.*, 2021 showed that the stiffness of the cell's Extracellular matrix (ECM) modulates glutamylation of microtubules by suppressing microtubule dynamics, promoting microtubule stability, thus influencing changes in cell shape and mechanics. The authors also showed that overexpression of tubulin mutants lacking glutamylation sites decreased microtubule stability and hampered cancer progression. Detyrosination of microtubules and its role in kinesin-1-mediated transport of APC (Adenomatous Polyposis Coli) was reported to be crucial for symmetry breaking and cell migration (Lavrsen *et al.*, 2023).

Recently Viar *et al.*, 2024 used a combination of immunolabeling and Cryo-ET (Cryo-Electron Tomography) studies to show that glycylation and polyglutamylation PTMs in motile cilia give rise to a protofilament-specific pattern (that they term 'Tubulin nano-code') which may directly influence interaction with dynein, and contribute to ciliary beating as well as ciliary function (Viar *et al.*, 2024). Thus, cells may harness the diversity offered by the tubulin code and post-translational modifications to modulate cellular metabolism and the mechanical properties of microtubules.

6.4 Cells may selectively modulate microtubule response to stimuli based on functional needs

My findings from Chapter 2 and 4 suggest the intriguing possibility that cells may fine-tune the mechanical properties of microtubules and their responsiveness to mechanical stimuli based on functional needs. The observations from both studies (Study 1 and Study 4) support the idea that microtubule rigidity, lattice plasticity and responsiveness to mechanical stress can be modulated in a context dependent manner. This raises the possibility that cells actively balance microtubule mechanosensitivity (the ability to detect and respond to forces) with mechanoresilience (capacity to withstand sustained mechanical stress without breakage or failure)(See **Fig 6.2**).

This feature to selectively tune microtubule responsive can result in the estabilishment of specific microtubule subsets in cells. For instance, in primary cilia that function as specialized sensory organelles that detect mechanical cues, microtubules may be more mechanosensitive. Having microtubules that undergo subtle deformation and lattice remodeling would be advantageous to transduce small mechanical stimuli to biochemical signals. In contrast, in motile cilia that undergo continuous bending, microtubules may be more mechano-resilient and flexible in nature to resist damage. In addition to modulating microtubule rigidity by direct recruitment of factors, cells may also modulate microtubule mechanical properties by recruitment of MAPs or enzymes that carry out specific PTMs.

Similar priniciples may also operate in plant cells where cortical microtubule arrays align along the axis of maximal tension and guide cellulose deposition during morphogenesis (Hamant, 2019). These observations suggest that microtubule mechanical properties are adaptable and tailored to specific cellular contexts or scenarios. Future studies aiming to elucidating how cells coordinate microtubule lattice dynamics, stiffness, MAP and tubulin code in specific cell types may reveal how different tissues optimize microtubule function.

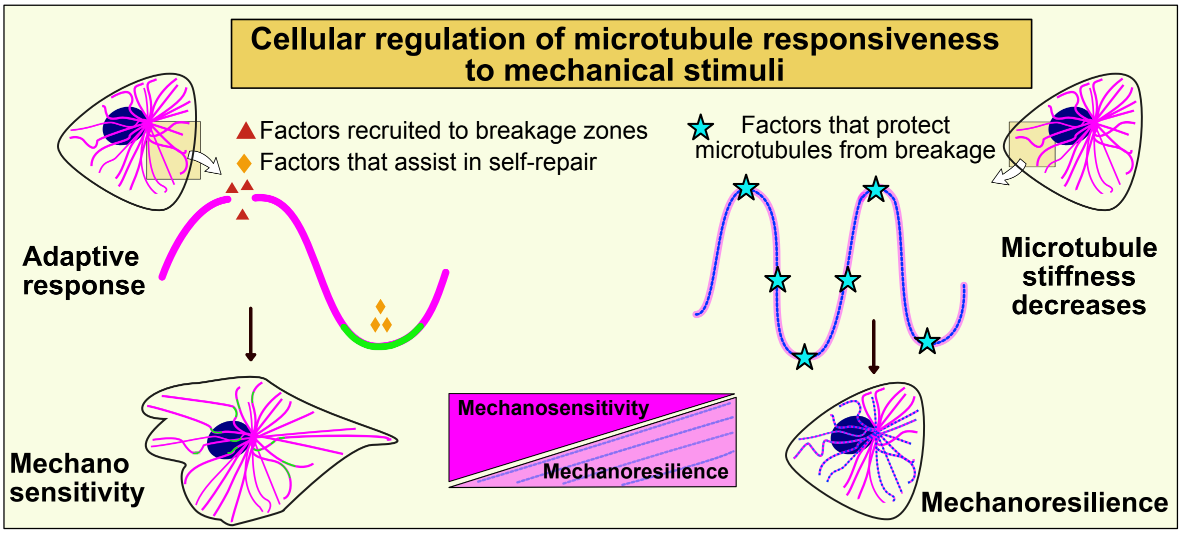

Fig 6.2: Cells may use intracellular factors to regulate microtubule response to mechanical stimuli by factors specifically recruited to microtubule breakage zones and repair sites (mechanosensitivity) and by factors that decrease microtubule stiffness (mechanoresilience).

6.5 Inherent lattice dynamics is mediated by defect propagation and can be modulated by external factors

Inherent lattice dynamics in the absence of external factors is mediated by the heterogenous nature of the microtubule lattice and the presence of structural defects (Schaedel *et al.*, 2019). In study 2 (Chapter 3), I extend observations from earlier studies by investigating the nature and mode of defect propagation using tubulin incorporation as a readout. By developing *in vitro* assays to study the pattern of tubulin incorporation using multiple cycles, I found that defect propagation is continuous and predominantly ballistic in nature. This is further supported by Kinetic Monte Carlo simulations from my collaborators. Using this developed assay as well as using simulations, I then traced the pattern of incorporation in bent microtubules to show that curvature accelerates tubulin loss in vicinity of defects by destabilizing the lateral tubulin dimers near the defect.

Thus, increasing local curvature destabilizes lateral contacts between tubulin dimers, decreasing the lattice anisotropy and promoting defect mobility in the lateral direction, thus leading to increased tubulin turnover across protofilaments. In this way, curvature acts as a key amplifier of microtubule turnover or breakage.

These findings can be extended to further comprehend the findings observed in buckling microtubules. Modelling studies found that the walk of motors alone can enhance lattice plasticity and accelerate tubulin loss and turnover (Lecompte and John., 2022). Combined with my findings in study 1, we can conclude that the enhanced breakage observed in buckling microtubules (**Fig 4** in the manuscript Nandakumar *et al.*) results from tubulin loss induced by motor-motility that is further amplified by curvature. Buckling microtubules are subjected to continuous deformation, which may account for a tubulin loss rate that can no longer be balanced by incorporation of new tubulin subunits, thus resulting in buckling microtubules breaking even in the presence of free tubulin. In this way, curvature acts as a 'final nail in the coffin' in the case of buckling microtubules.

From these findings, I postulate that effectors (such as force, motors, or MAPs) may mediate lattice dynamics by influencing tubulin loss and consequent tubulin turnover by modulating lattice anisotropy (either by stabilization or destabilization of contacts between tubulin dimers). In the cellular context, these mechanisms may underlie how microtubules adapt to cues.

6.6 Perturbation of microtubule dynamics by chemical agents/drugs have cellular level-implications

In addition to mechanical stimuli, microtubules are also frequent targets of chemical perturbations for therapeutic strategies. MTA (microtubule targeting agents or drugs) predominantly work by disrupting microtubule dynamics. In the latter part of my dissertation, I investigated how chemical perturbations caused by the depolymerizing action of the drug- Pretubulysin affects microtubule dynamicity. Along with immune-cell based studies by my collaborators, the study (Study 5, Chapter 5) shows how changes in microtubule mass caused by microtubule depolymerizing drugs like Pretubulysin and Nocodazole enhance actomyosin contractility through the GEFH1-RhoA/ROCK pathway, to result in persistent cell migration of cytotoxic T-lymphocytes. These findings match recent reports by Meiring et al., 2025 showing that binding of taxanes to microtubules triggers expansion of the microtubule lattice, releasing GEF-H1 and inducing RhoA activation to ultimately result in increased actomyosin contractility through the microtubule-GEFH1-RhoA contractility axis.

Structural study on GEF-H1 indicated that the C1-domain of GEF-H1 mediates its interaction with microtubules, with the binding localized to both the intra-dimer interface and inter-protofilament contacts on the microtubule outer surface (Choi *et al.*, 2025). This characteristic binding of GEF-H1 to microtubules may be pivotal to the release/further recruitment of GEF-H1 in response to changes in the microtubule lattice mediated by MAPs, motors or mechanical stress. The study also identified C1 domains in other key signaling proteins central to other signaling pathways like AKAP13 (another Rho-Guanine Exchange Factor), RASSF1A (Hippo pathway), RAF1A (MAPK pathway). The authors accordingly postulate a 'Microtubule Sequestration and Release' (MSR) model wherein in the native state, C1-domain containing signaling molecules remain inactive and bound to microtubules. Changes in microtubule lattice structure and dynamics (depolymerization, alteration of lattice structure by binding of MAPs or post-translational modifications) may then effect the release and activation of these signaling proteins. Re-organization of the microtubule network in response to mechanical stress was also found to result in degradation of AMOT proteins that sequester YAP/TAZ. AMOT proteins may thus serve as a link between microtubule remodeling and the YAP/TAZ mechanosignaling pathway (Vanni *et al.*, 2025).

These studies collectively illustrate that alterations in the microtubule lattice structure as well as dynamics can serve as a trigger for activation of various signaling pathways. Thus, microtubules occupy a central role as molecular transducers of mechanical signals generated by deformation at the plasma membrane, relaying them to downstream signaling pathways that regulate cell morphology and contractility.

6.7 Microtubule lattice as a heterogeneous interface that can remodel and adapt

The microtubule lattice is thus inherently non-uniform and heterogeneous owing to the presence of structural defects and the compositional diversity arising from different tubulin isotypes and PTMs. This heterogeneity causes lattice plasticity by allowing for the incorporation of free tubulin dimers as well as through changes mediated by MAPs binding to the CTTs of modified tubulin. The dynamic nature of the lattice enables microtubules to sense and adapt to effectors (MAPs, motors, force, drugs) through localized lattice remodeling. Such remodeling can trigger downstream signalling pathways or mechano-chemical feedback loops that formulate a broader cellular adaptive response (See **Fig 6.3**). In this way, the metastable nature of microtubules (reflected in tip and lattice dynamics) makes them sensitive to the action of effectors, and their dynamic adaptability helps in cellular mechano-adaptation.

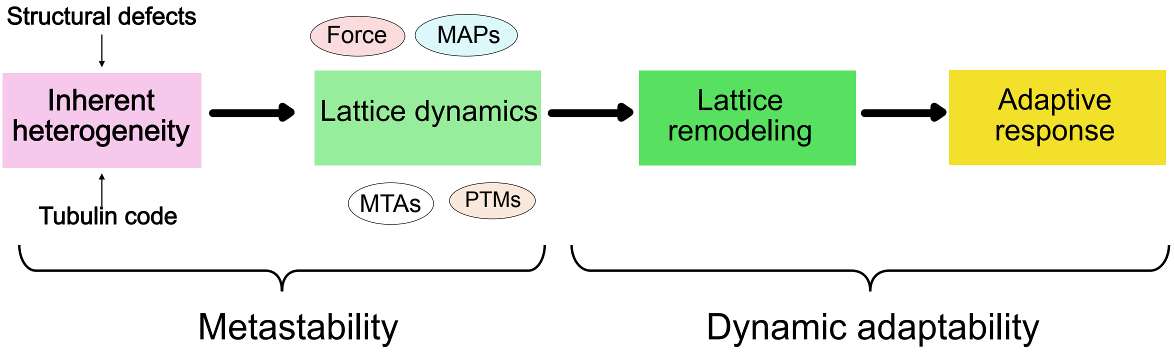

Fig 6.3: Metastable and adaptable nature of microtubules are central to cellular mechanoadaptation.

6.8 Microtubules as proponents of cellular mechanoadaptation

My findings as well as recent evidence increasingly indicate that the force-sensitive nature of the microtubule cytoskeleton helps microtubules serve as a mechanostat for the cell. The dynamic adaptability of the microtubule lattice allows them to translate small mechanical stimuli into biochemical signals that effect cytoskeletal (re)organization and gene expression. This is primarily mediated through a series of changes in microtubule network mechanics, recruitment of MAPs, cytolinkers, crosstalk with other cytoskeletal filaments, thus triggering secondary changes in actomyosin contractility, mechano-signaling, and subsequent cellular mechano-response (**Fig 6.4**). In this way, microtubules effectively orchestrate cellular adaptation to mechanical cues and coordinate important cellular functions. Exploring the molecular mechanisms and force thresholds that trigger lattice remodeling and microtubule-mediated mechanosignaling will be crucial for revealing how cells sense and adapt to mechanical stimuli. Insights in this direction may open new research avenues for targeting microtubule mechanosensitivity for treating cancer and other neurodegenerative diseases.

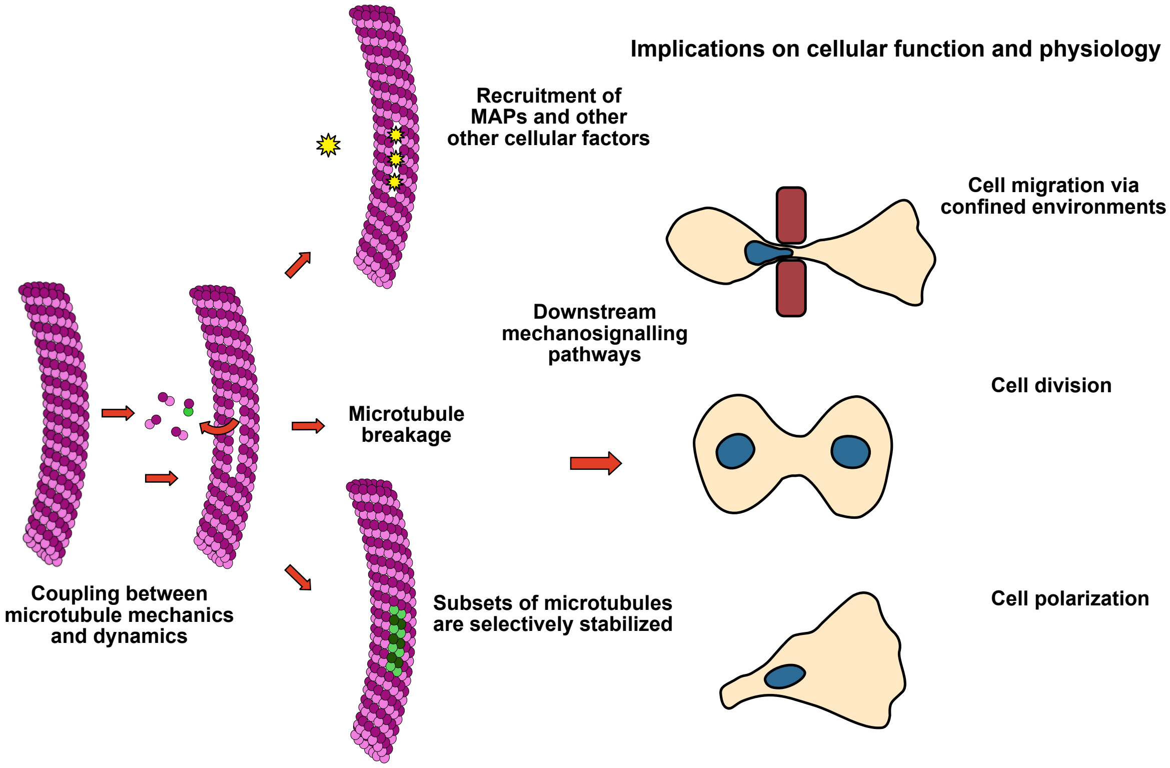

Fig 6.4: Conceptual model of role of microtubules as cellular mechanosensors. The force sensitive nature and dynamically adaptable nature of microtubules make them sensitive to stimuli. Microtubules respond to stimuli through self-repair, recruitment of MAPs and lattice remodeling that triggers downstream signaling pathways thus serving as an allosteric interface for integration of mechanical and biochemical signals.

6.9 Metastability as the basis of mechanoadaptation

Taken together, the studies presented in this dissertation demonstrate that microtubule metastability governs their response and adaptation to mechanical and chemical perturbations. The metastable GDP-lattice sensitizes microtubules to both mechanical and biochemical stimuli. Through quantitative *in vitro* reconstitution assays and cell-based observations, my findings reveal the limits of intrinsic microtubule self-repair and further offer insights into how intracellular factors and the tubulin code help modulate microtubule response.

The heterogenous nature of the microtubule lattice enables continuous tubulin exchange along its length. Mechanical stress like curvature and motile action of motor proteins amplifies local tubulin loss triggering self-repair and in extreme cases, where loss cannot be balanced by self-repair, to filament failure.

Lattice dynamics can also be modulated by external factors like force and MAPs, to effect local lattice remodeling that can be translated to a global cellular level response. Thus, metastability helps microtubules to respond, reorganize and adapt whilst also maintaining structural integrity under physiological stress. Ultimately, metastability functions as a central organizing principle in cells that ensures that microtubules remain both adaptable and resilient in the demanding intracellular environment.

6.10 References (including outlook)

1. Alvarez Viar, G., Klena, N., Martino, F., Nievergelt, A. P., Bolognini, D., Capasso, P., & Pigino, G. (2024). Protofilament-specific nanopatterns of tubulin post-translational modifications regulate the mechanics of ciliary beating. *Current biology : CB*, *34*(19), 4464–4475.e9.
2. Choi, S. R., Blum, T. B., Giono, M., Roy, B., Vakonakis, I., Schmid, D., Oelgarth, N., Ranganathan, A., Gossert, A. D., Shivashankar, G. V., Zippelius, A., & Steinmetz, M. O. (2026). Structural basis of microtubule-mediated signal transduction. Cell, *189*(2), 461–477.e16.
3. Hamant, O., Inoue, D., Bouchez, D. *et al.* (2019) Are microtubules tension sensors?. Nat Commun 10, 2360. https://doi.org/10.1038/s41467-019-10207-y
4. Jijumon, A. S., Bodakuntla, S., Genova, M., Bangera, M., Sackett, V., Besse, L., Maksut, F., Henriot, V., Magiera, M. M., Sirajuddin, M., & Janke, C. (2022). Lysate-based pipeline to characterize microtubule-associated proteins uncovers unique microtubule behaviours. *Nature cell biology*, *24*(2), 253–267.
5. Lecompte, W., & John, K. (2023). Molecular motors enhance microtubule lattice plasticity. *PRX Life*, *1*(1), 013012.
6. López, M., Huber, F., Grigoriev, I. *et al.* Actin–microtubule coordination at growing microtubule ends. Nat Commun 5, 4778 (2014). https://doi.org/10.1038/ncomms5778
7. Novosedlik, S., Reichel, F., van Veldhuisen, T., Li, Y., Wu, H., Janssen, H., Guck, J., & van Hest, J. (2025). Cytoskeleton-functionalized synthetic cells with life-like mechanical features and regulated membrane dynamicity. Nature chemistry, *17*(3), 457.
8. Portran, D., Zoccoler, M., Gaillard, J., Stoppin-Mellet, V., Neumann, E., Arnal, I., Martiel, J. L., & Vantard, M. (2013). MAP65/Ase1 promote microtubule flexibility. *Molecular biology of the cell*, *24*(12), 1964–1973.
9. Vanni, G., Citron, A., Suli, A. *et al.* (2025). Microtubule architecture connects AMOT stability to YAP/TAZ mechanotransduction and Hippo signalling. Nat Cell Biol, 27, 1725–1738. https://doi.org/10.1038/s41556-025-01773-z
10. Vianay, B., Guérin, C., Gressin, L., Orhant-Prioux, M., Blanchoin, L., Théry, M., & Colin, A. (2025). Fabrication of microcompartments with controlled size and shape for encapsulating active matter. Frontiers in cell and developmental biology, 13, 1616089.
11. Xu, Z., Schaedel, L., Portran, D., Aguilar, A., Gaillard, J., Marinkovich, M. P., Théry, M., & Nachury, M. V. (2017). Microtubules acquire resistance from mechanical breakage through intralumenal acetylation. *Science (New York, N.Y.)*, *356*(6335), 328–332.

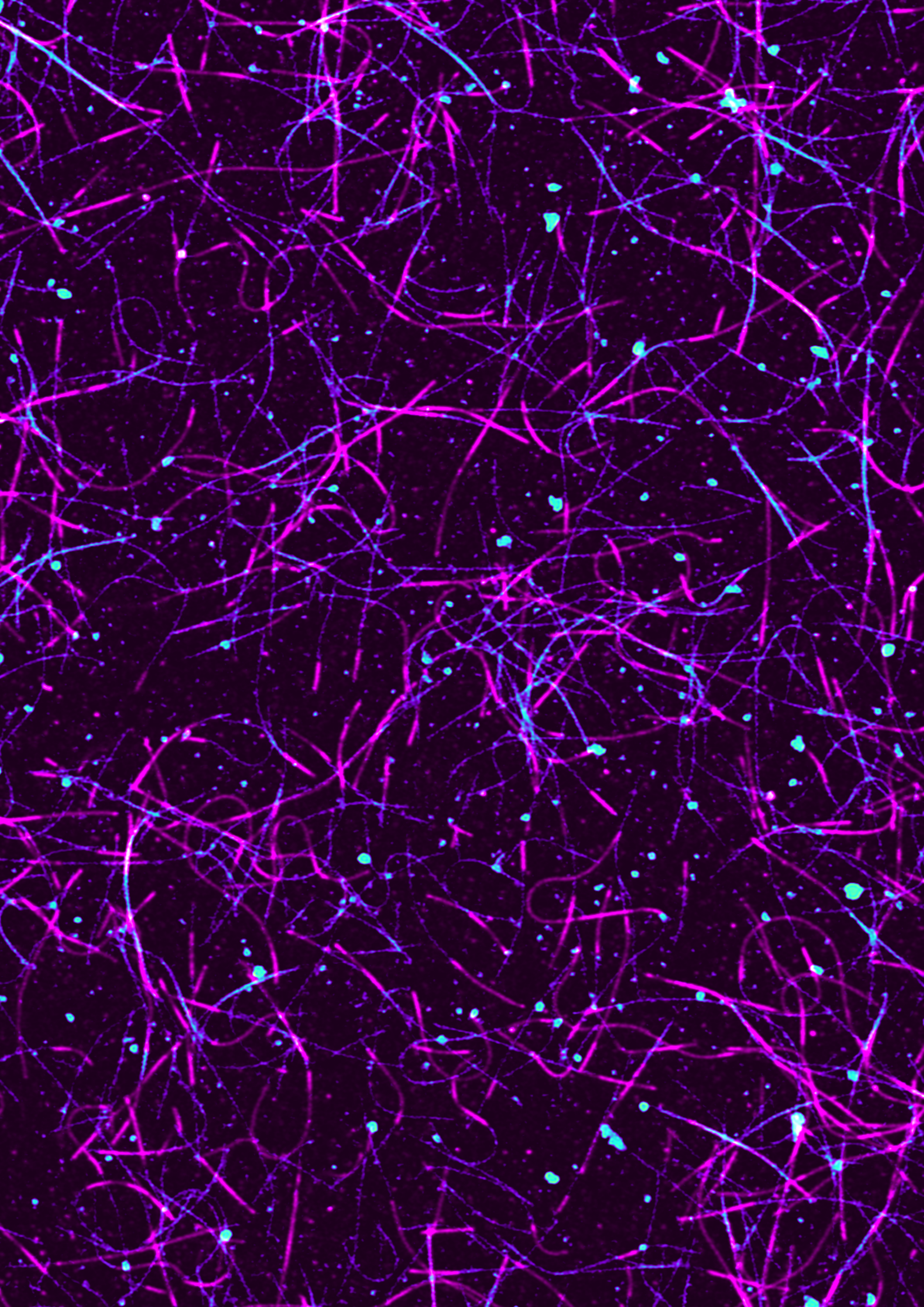

General conclusion and Outlook

The studies undertaken in this dissertation report key insights that are relevant to all facets of the emerging paradigm on the role of microtubules in cellular mechanoadaptation.

Study 1 (Nandakumar *et al.*), provides new insights into how microtubules respond to bending and buckling stress, similar to that what they experience in the intracellular environment. I demonstrate that kinesin-induced buckling can accelerate intrinsic microtubule self-repair and, beyond a threshold, lead to microtubule breakage. Further, the study shows that the presence of intracellular factors boosts microtubule mechano-resilience to buckling-induced damage predominantly by making microtubules less stiff. These findings highlight that **microtubule self-repair alone is insufficient to preserve microtubule integrity** under deformation, suggesting that **additional intracellular or regulatory factors are essential for maintaining microtubule stability**. **The insights from this study have broader implications in cellular contexts wherein microtubules are exposed to continual mechanical deformations (in cilia, neurons) where microtubule integrity is key for function.**

Additionally, the *in vitro* assay setup developed recapitulates intracellular mechanical stress and will serve as a framework for future studies aimed at exploring the role of specific effectors- MAPs, cytolinkers and PTMs. Using this streamlined pipeline of preparing GDP microtubules, bending and buckling assays, one can test the recruitment and mechanoprotective properties of potential microtubule- interacting proteins. In this way, **the developed assay is a great tool for systematic screening of potential candidates for their role in influencing microtubule stability, resilience, as well as lattice remodeling under mechanical stress.** Insights from these studies can then be complemented with cellular and modelling studies to characterize specific interactions and their consequent functional implications. This will help offer more clarity on how local lattice-level interactions translate to global changes in cellular mechanics.

In **study 2** (Chapter 3), I further examine the dynamic nature of the microtubule lattice and show that inherent microtubule plasticity stems from defects or irregularities in the microtubule lattice. By tracking the pattern and evolution of tubulin incorporation over time, my findings extend earlier studies to show that **defect propagation underlies microtubule lattice dynamics**. These observations suggest that defect propagation and consequent tubulin turnover proceed in the longitudinal direction (owing to inherent lattice anisotropy) and is predominantly directional (ballistic) in nature. I then extend these studies and show that curvature and MAPs modulate lattice dynamics by altering the inherent lattice anisotropy (**study 3**). These findings further underscore the plastic nature of the microtubule lattice and how **binding of MAPs and mechanical cues can effect lattice remodeling**.

The tubulin code adds a further layer of heterogeneity to the microtubule lattice, and the role that the tubulin code plays in influencing microtubule response to stress is underexplored. By performing comparative studies using tubulin purified from bovine brains and from HeLa cells (study 4, Chapter 4), I show how **differences in tubulin isotype and PTM patterns can**

markedly influence microtubule response to mechanical stress. These findings highlight an additional facet of regulation of microtubule response in cells.

Finally, Study 5 showcases how **perturbations in microtubule dynamics and mass has cellular-level implications**. Using the microtubule depolymerizing drug-pretubulysin, the study reports that depolymerization of the cellular microtubule network in CTLs can increase actomyosin contractility (via the microtubule-GEF H1-actomyosin contractility axis) and result in CTLs migrating in a faster and more persistent manner. These findings provide further evidence to the **central role microtubules play as mechanosensors that coordinate cytoskeletal remodeling.**

In conclusion, the findings of this dissertation collectively emphasize that the **metastable and dynamically adaptable nature of microtubules enables them to occupy a central role in how cells sense and adapt to mechanical and biochemical cues**. Thus, far from their traditional role as passive, static filaments, the **microtubule lattice acts as a heterogeneous interface that is force-sensitive, can actively undergo remodeling, and adapt to stimuli.**

Outlook and future perspectives:

Despite the multitude of existing studies on microtubule dynamic instability, microtubule-MAP interaction as well as crosstalk between cytoskeletal filaments, our knowledge on how mechanical force influences these interactions remains limited. Addressing this knowledge gap is pivotal to further understand the role of microtubules as cellular mechanosensors.

In this direction, there needs to be a renewed focus on understanding the physiological significance of microtubule interaction studies. The field of cytoskeletal biology is currently fortified with the advent and widespread use of molecular cloning, protein purification, and high-resolution microscopy techniques like MINFLUX, optical trap studies, RNA silencing techniques, and cryo-electron tomography.
It is important that we use insights gained from *in vitro* reconstitution assays and complement these observations with cell-based studies, as well as structural studies like X-ray, cryo-electron microscopy/tomography. This will be essential for correlating insights gained at the molecular scale to physiological contexts.

Some of the possible avenues for future research include:

-Systemic studies of cellular response to mechanical force:
Comprehensive cell-based studies are required to assess changes in microtubule mass, stability, dynamics, PTM, and associated signaling pathways profiles in response to mechanical stress of different types and intensities. Cell stretcher-based studies in combination with high-speed live-cell imaging setups and optogenetic tools for spatio-temporal control -might provide insights into how different microtubule subsets respond to force, as well as quantify physiological thresholds that trigger collapse/breakage.

-**Synthetic and artificial cell-like systems as platforms to assess force balance and biochemical regulation:**

Artificial bottom-up synthetic systems that use minimal components, cell-free extracts, confined to unilamellar lipid vesicles and droplet emulsions, are increasingly used to investigate force generation and biochemical regulation of cytoskeletal networks. These robust systems offer control over boundary conditions, concentrations used, and geometry, enabling measurements of force, deformation, and interactions in a 'cell-like' setup (Novosedlik *et al.*, 2025; Vianay *et al.*, 2025; Colin *et al.*, 2023, Lopez *et al.*, 2014). Combined with optogenetic and light-controlled reactions, these systems offer a powerful tool to investigate how biochemical feedback influences mechanical output (Ahmad *et al.*, 2021). By engineering synthetic scaffolds for controlled interactions between motors, MAPs and cytoskeletal filaments, these systems may reveal key regulating components that can be further validated by cell-based studies. In this way, artificial cell-like systems may be key to bridging minimal reconstitution and cellular complexity.

-**Mechanical and biochemical regulation of both microtubule tip and lattice dynamics** with a focus on the influence of MAPs and motor proteins on lattice remodeling and adaptation. Importance should also be placed on the dynamic nature of these interactions in systems by studying dynamic microtubules, free of stabilizing agents, such that the bond energies and nucleotide state remain unaltered and as close as possible to the cellular environment.

-**Cytoskeletal crosstalk and its implications on network (re)organization:**

Although some cytolinker-mediated and direct interactions are pivotal to mediate crosstalk between cytoskeletal filaments, the mechanical and biochemical basis of their interaction is yet to be uncovered. There exists a need for biochemical studies to estimate the physiological expression levels of cytolinkers in cells, as well as the structural basis of their interaction. Purification of certain MAPs and cytolinkers remains technically challenging. Cell lysate-based *in vitro* reconstitution assays (Jijumon *et al.*, 2022) offer a promising alternative to circumvent this challenge, as well as offer a means to study these interactions in a system that closely mimics that of the intracellular environment.

- **Influence of tubulin code:**

The cell-specific nature of expression, as well as regulation of tubulin isotypes and PTMs, suggests that cells harness the diversity of the tubulin code to achieve specific microtubule-based functions. Research in recent years on the tubulin code, the role of PTMs (particularly in cilia), and the identification of associated enzymes has shown the influence of different PTMs on microtubule dynamics. As proposed by Janke & Magiera, 2020, exploring tubulin PTM-isotype cross-regulation may provide us with clues on how cell-specific isotype expression is in crosstalk with tubulin PTMs as most PTMs target the C-terminal tubulin tails, which are also the most divergent domains of tubulin isotypes.

Identification of interacting proteins and signaling cascades that are involved in the recruitment of tubulin-modifying enzymes would be essential to investigate how PTMs directly influence microtubule mechanics and, consequently, microtubule-based cellular functions. Use of PTM mimetic or deficient mutant cells using CRISPR-mediated knock-in may help assess the functional contribution of specific modifications in the physiological context.

- **From local lattice dynamics to global cellular mechanics:**

A fundamental open question is how local changes in the microtubule lattice- loss of dimers, binding of MAPs or defect propagation translates into changes at the cellular level. Recent evidence also suggests that there exists an allosteric mechanism that may facilitate mechanical information to be transmitted along the microtubule lattice. It may be interesting from both a mechanical and biological standpoint to further track the range and mode of action that enables long-range mechanical coupling in microtubules. This may also provide clues on the cooperative nature of binding of motor proteins, MAPs as well as the effect of microtubule targeting drugs. A key question is to what degree of change in microtubule dynamics or lattice structure is needed to formulate an adaptive response. In the same line of thought, what fraction of local change in microtubule network triggers global change in microtubule network (re)organization ?

-Targeting microtubule mechanosensitivity in cancer and other diseases:

A deeper understanding of the players and mechanisms that modulate microtubule mechanosensitivity and cellular force thresholds may offer new therapeutic implications particularly in cancer and neurodegenerative diseases, wherein cytoskeletal dynamicity and integrity is disrupted.

Annexure 1:

(The following annexure section was taken and rephrased from an initial written report provided by Amir Zablotsky, LiPhy, Grenoble)

Chapter 3: Information on model parameters for coarse grained dimer mechanical model:

Model parameters:

To construct the base dimer, two monomers are placed one on top of the other, so the separation between their centres is equal to σ . Then, the longitudinal and lateral binding sites are placed over the surface of the monomers so that the ground state of an ensemble of dimers is a straight microtubule (MT) with the canonical structure (**Fig. A1a**). To achieve this, lateral binding sites on both sides of the dimer have a slight offset in the dimer's longitudinal direction to reproduce the 3-start helix, and they are positioned forming a slight angle with the dimer centreline to reproduce the 13 protofilament cylindrical shape (**Fig. A1d**).

To induce pre-stress in the lattice, we displace the longitudinal binding sites over the surface of the monomers by performing a rotation of an angle φ on a local coordinate system centred on each monomer, moving them in the direction outwards the centre of the MT (**Fig. A1b**). This reproduces the αβ−tubulin curvature [Gigant *et al.*, 2000; Knossow *et al.*, 2020; Brouhard *et al.*, 2014] responsible for the outwards curling of the protofilaments at the MT tip during depolymerization.

Note that, while the monomers have a repulsive radius σ/2, the binding sites are point particles. The dimers interact through a series of potentials applied to the different bodies. As mentioned before, each dimer is considered as a rigid molecule, so the relative positions of each component within the dimer are fixed, and intradimer interactions are not considered within our model to reduce computational cost.

Volume exclusion between monomers is modelled by a purely repulsive Lennard-Jones potential with cut-off distance equal to σ (**Eq. 1**), so that two monomers repel only as long as they are partially overlapping. The intensity of the repulsion is given by ε, which could be interpreted as a parameter to describe the monomer's stiffness (ε = 0 for non-interacting monomers, ε → ∞ for perfectly rigid monomers).

$$U_{\text{rep}}(r) = \begin{cases} 4\epsilon\left[\left(\frac{\sigma}{r}\right)^{12} - \left(\frac{\sigma}{r}\right)^{6}\right] & \text{if } 0 < r < \sigma \\ 0 \text{ if } r \geq \sigma \end{cases} \qquad (1)$$

Attractive interactions between corresponding binding sites are implemented via soft attractive potentials with an interaction range rc = 0.4 σ [Kononova *et al.*, 2014] and magnitude ΔG < 0 (**Eq. 2**). Lateral binding sites can only interact with other lateral binding sites (either homotypic or heterotypic interactions), and α−monomer longitudinal sites interact exclusively with β−monomer longitudinal sites. Lateral interactions have an intensity of ΔGlat and longitudinal ones have an intensity of ΔGlong (**Fig. A1c**).

$$U_{\mathrm{att}}(r) = \begin{cases} \Delta G \left[1 + \cos\left(\frac{\pi r}{r_c}\right)\right] & \text{if } 0 < r < r_c \\ 0 \text{ if } r \geq r_c \end{cases} \qquad (2)$$

From the attractive potentials we can identify the lattice binding energy (Eq. 3) as the binding energy of a fully surrounded dimer at equilibrium, and the lattice anisotropy (Eq. 4) to quantify the relative strength between the interactions with the longitudinal and lateral dimer neighbours [Biswas *et al.*, 2025; Zablotsky & John, 2025; Cleary *et al.*, 2021]. These quantities, along with the magnitude › of the repulsive potential, are sufficient to characterize a lattice.

$$\Delta G_b = 2\Delta G\text{long} + 4\Delta G\text{lat} \qquad \text{- (3)}$$

-(4)

To study the effects of curvature on the microtubule lattice, we bend the microtubule by applying forces in the longitudinal direction of the straight microtubule axis. To do this, we apply a force of magnitude F to a single dimer close each extreme of the microtubule, in opposite directions (**Fig. A1e**).

Since the scope of this work is to study the lattice properties in statically bent microtubules, we apply the forces until the tips are at the desired distance d and then set both the forces and velocities of the "pulling" dimers to ~0 (we don't impose any condition on their torque, so they can still rotate). After a transient regime, all the dimers in the system accommodate to the configuration that minimizes the energy given the restrictions (fixed tips position, free tips orientation). The resulting equilibrium configuration is the static microtubule with a macroscopic strain $\varepsilon = (d - L_{MT}) = L_{MT}$, where L_{MT} is the length of the microtubule. We can then measure different quantities such as the dimers' position, stress, potential energy, etc.

All simulations are performed using the LAMMPS molecular dynamics package [Thompson *et al.*, 2022]. Tubulin dimers are modelled as rigid bodies using the fix rigid integrator, which maintains the internal geometry of each dimer throughout the simulation. Non-thermal simulations are used to impose controlled bending on the microtubule and analyse the resulting stress distribution along the lattice in the absence of thermal noise. These simulations use a time step of 0.01 in reduced Lennard-Jones units and are evolved deterministically using the velocity-Verlet *al*gorithm to solve the equations of translational and rotational motion. When simulating breakage events, thermal fluctuations are introduced using a Langevin thermostat, which applies stochastic and dissipative forces to each dimer's equations of motion to mimic a constant temperature environment. Unless stated otherwise, the depth of the repulsive potential (Eq. 1) is kept $\varepsilon=1$.

Simulated microtubules, unless stated otherwise, consist of 2600 dimers arranged in a 13-protofilament, 3-start helical configuration ($\simeq$ 1.6 µm in length). We start our simulations with a straight microtubule with perfect lattice (no defects) and carry on the bending procedure to end up with our static, bent microtubule. Then, if desired, we can choose to remove one or more dimers from the lattice to produce dimer-sized vacancies. In that case, we run a series of relaxation time steps for the microtubule to accommodate to the next equilibrium position, given this new lattice configuration. When analysing the stress along the lattice of a microtubule, we measure the stress tensor of each dimer and then use it to compute the signed Von Mises stress, given by the equation below:

$$\sigma_{\mathrm{sVM}} = \mathrm{sgn}\left(\sigma_{\mathrm{Hyd}}\right)\sigma_{\mathrm{VM}} = \mathrm{sgn}\left(\frac{\sigma_1+\sigma_2+\sigma_3}{3}\right)\sqrt{\frac{\left(\sigma_1-\sigma_2\right)^2+\left(\sigma_2-\sigma_3\right)^2+\left(\sigma_3-\sigma_1\right)^2}{2}}$$

This is a scalar magnitude that is a product of Von Misses stress and hydrostatic stress. Hydrostatic stress, also known as mechanical pressure, is positive for the case of tensile stress and negative for the case of compressive stress, and is given by Tr(σ). On the other side, Von Mises stress is a scalar quantity also computed from the principal tensions that is frequently used in material failure theory to predict the conditions under which a solid material will fail under the action of external loads. Therefore, the signed Von Mises stress combines this last magnitude with the information regarding the nature of the stress. All physical quantities are expressed in reduced Lenard-Jones units, in particular energy in terms of ε and distances in terms of σ .

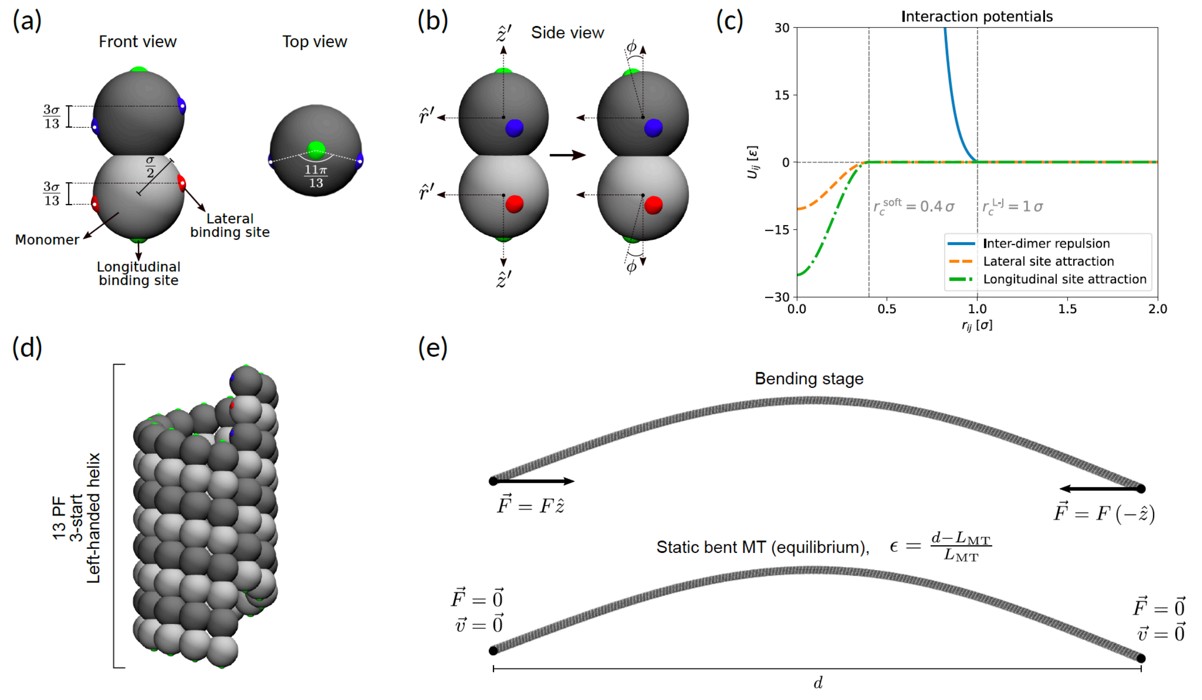

Fig A1: **(a)**: Three-dimensional representation of the dimer model. Each dimer is treated as a rigid body so the relative positions of the monomers and binding sites are fixed. **(b):** Conformational change in the dimer. Longitudinal sites are displaced outwards over the surface of the monomer by an angle φ, which induces protofilament curling. **(c):** Inter-dimer interaction potentials. Repulsion between dimers is modelled as a Lenard-Jones potential with cut-off distance of 1 σ (monomer diameter). Attraction between binding sites, both lateral and longitudinal, is modelled as a soft potential that is minimized when the binding sites overlap and goes to zero when their separation surpasses 0.4 σ. **(d):** Fifty-two dimers arranged in the equilibrium configuration, resulting in a straight canonical structure microtubule. **(e):** Two forces equal in magnitude and opposite in direction are applied to a dimer at each extreme of the microtubule in order to bend it. Once the tips are at the desired distance from each other, they are kept in place by setting the force and velocity to zero, and after a transient regime the microtubule reaches its equilibrium configuration.

References:

Thompson, A. P. *et al.* (2022). LAMMPS - a flexible simulation tool for particle-based materials modelling at the atomic, meso, and continuum scales. Computer Physics Communications 271, 108171 (2022).

Cleary, J. M. & Hancock, W. O. (2021). Molecular mechanisms underlying microtubule growth dynamics. Current Biology 31, R560–R573.

Brouhard, G. J. & Rice, L. M. (2014). The contribution of - tubulin curvature to microtubule dynamics. The Journal of Cell Biology 207, 323–334.

Knossow, M., Campanacci, V., Khodja, L. A. & Gigant, B. (2020). The Mechanism of Tubulin Assembly into Microtubules: Insights from Structural Studies. iScience 23, 101511.

Gigant, B. *et al.* (2000). The 4-A X-ray structure of a tubulin: stathmin-like domain complex. Cell 102, 809– 816.

Kononova, O. *et al.* (2014). Tubulin Bond Energies and Microtubule Biomechanics Determined from Nanoindentation in Silico. Journal of the American Chemical Society 136,17036–17045.

Zablotsky, A. & John, K. The impact of lattice defects on the microtubule shaft and tip dynamics (in preparation).

Biswas, S., Grover, R., Reuther, C., Poojari, C.S., Shaebani, R., **Nandakumar, S.**, Grünewald, M., Zablotsky, A., Hub, J.S., Diez, S., John, K., Schaedel, L. (2025). Tau accelerates tubulin exchange in the microtubule lattice. Nat. Phys. 21, 1616–1628.

Other projects undertaken

In addition to the studies detailed in this dissertation, I was also involved in the following projects during my PhD:

1. Screening of MAPs that play a role in influencing microtubule-vimentin intermediate filament crosstalk

Using the lysate-based pipeline developed by Jijumon *et al.*, 2022, we expressed different MAPs in cells and performed *in vitro* reconstitution assays using purified Vimentin, microtubules and cell lysates containing overexpressed MAPs. Subsequently, we also studied how MAPs affect vimentin network architecture in networks assembled *in vitro*.

2. Investigating the role of ciliary MAPs/MIPs in regulating microtubule dynamics

Using the *in vitro* setup developed in Chapter 2, we are currently investigating the influence of ciliary MAPs/MIPs in regulating microtubule dynamics.

List of publications:

1. **S Nandakumar**, J Bosche, M Wieczorek, C M Albrecht, B König, M Grünewald, L Santen, S Diez, R Shaebani, L Schaedel. Kinesin-1 induced buckling reveals the limits of microtubule self-repair. bioRxiv. Preprint: https://doi.org/10.1101/2025.09.08.672697 **(Study 1)**
2. **S Nandakumar *,** A Zablotsky*, M Wieczorek, Karin John, Laura Schaedel. Curvature accelerates defect-driven tubulin turnover in the microtubule lattice (manuscript in preparation). **(Study 2 &3)**

3. **S Nandakumar*,** D Sreekumar*, L Schaedel. The mechanoadaptive cytoskeleton: emerging role of microtubules (manuscript in preparation). AIP Biophysics Reviews (invited review).

4. M Wieczorek, E Araujo, **S Nandakumar**, M Becker, A Prota, M Grünewald, B König, A Hirsch, R Müller, U Kazmaier, F Lautenschläger, L Schaedel. Mechanistic insights into microtubule depolymerizing drug- Pretubulysin (manuscript in preparation).

5. S Khanfir, A Krishnan, **S Nandakumar**,…...L Schaedel, M Dogterom, C Janke. Selective control of microtubule mechanics by tubulin isotypes and post-translational modifications (manuscript in preparation) **(Study 4).**

6. S Biswas, R Grover, C Reuther, C.S. Poojari, R Shaebani, **S Nandakumar**, M Grünewald, A Zablotsky, J. S Hub, S. Diez, K John, L Schaedel. Tau accelerates tubulin exchange in the microtubule lattice. Nature Phys. 21, 1616–1628 (2025).

7. G Montalvo, R Shaebani, **S Nandakumar,** N Cowley, R Zhao, R Hawkins, M Hoth, M Lauterbach, L Schaedel, B Qu, F Lautenschläger. The mechanism how Pretubulysin-induced microtubule disassembly improves T cell search efficiency. bioRxiv 2025.02.24.639827.Preprint. doi: https://doi.org/10.1101/2025.02.24.639827 **(Study 5)**.

"True knowledge is to be aware of one's ignorance. How much and how painfully do I feel the gaps in my knowledge …there is much that is uncertain and irresolute. It is for this reason that I do not stand still…"   -Rudolf Virchow

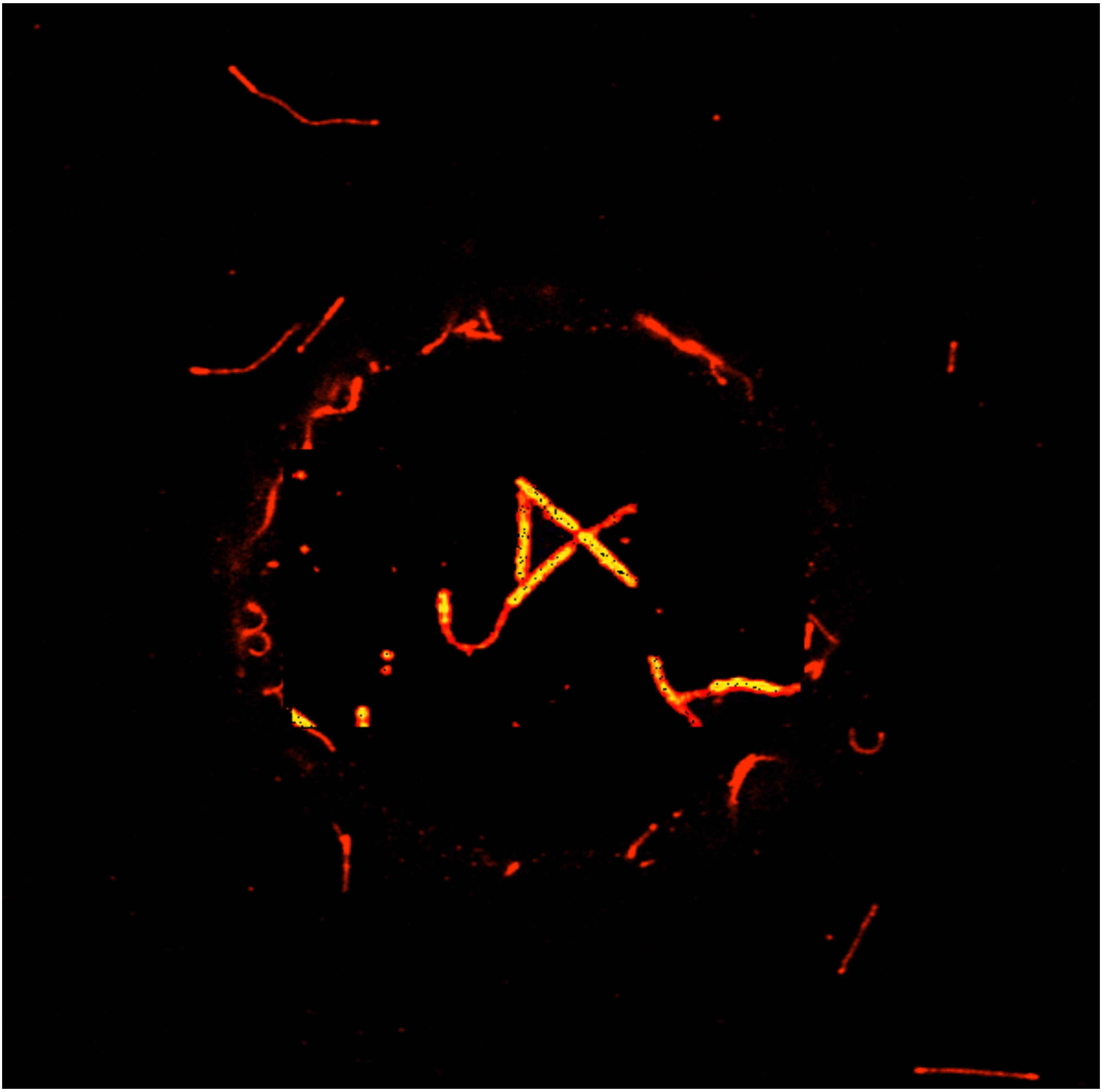

"Enjoy the butterflies,

Enjoy being naive,

Enjoy the nerves,

The pressure,

If you want to stand on the top from day one, then there's nothing else to look forward to. Enjoy the process of making a name for yourself. And meeting some great people along the way. There's a lot of worldly people who you can laugh with, learn from, enjoy some moments with. So, embrace the good ones. Keep trying to build and grow and learn from yourself but don't forget what got you here.

Get after it!"

- Daniel Ricciardo, DR3, 2022

Acknowledgements

Doing a PhD and working in science has been my dream since school and my PhD has been such an incredible and transformative journey. I came to Saarbrücken in 2021, amidst a pandemic, armoured with a fervent passion for biology and here I am 4 years later, with a heart full of ambition, good memories and fortified love for the mysteries of the cytoskeleton. I have many people to thank and a lot to be grateful for.

Thank you, Laura for being an amazing supervisor, for always being there for me- for all the long discussions on science, the fist-bump moments where we shared our common love for the enigma that microtubules are ('microtubules rock!!'). Thank you for being a source of inspiration and knowledge. I am truly grateful for all the words of encouragement, wisdom and your belief in my skill to make microtubules buckle. It has been such a pleasure to watch the lab grow over the last years and I will truly miss discussing science with you.

Thank you, Subham for being my first friend in Saarbrücken, for introducing me to the world of microtubule *in vitro* assays, for all the kinesin-rant filled walks back to Zymma, and the imaging assistance.
I was incredibly lucky to find a great friend and confidant in you, Dyuthi. Thank you for introducing me to the enthralling world of vimentin intermediate filaments. I am so grateful for all your support, friendship and for you being there during my lowest of lows. We have been through it all: admin paperwork, the lysate preps in the snow and when the only good images we had were experiment-fail selfies. Working with you has been amazing. I wish you most and more of everything.

Mona, the tubulin queen, thank you for being a true ray of sunshine and for all the book discussions, warm hugs and the ATP solutions ☺. Thank you, Belinda for all the amazing tubulin, vimentin and for always being patient with me. Steffi, your note welcoming me to Saarbrücken was such a comfort for my anxious soul and I would have been truly lost without your guidance, support and friendly way of reassuring me that I can navigate the tricky waters of all things admin.

To all the amazing students I had the opportunity to work and learn alongside- Miguel, Mirko, Clara and Constantin, it has been incredible watching you all blossom into such talented researchers. Thank you, Mirko, for your friendship, all the code analysis help, Marvel fandom talk, and the joyful conversations on all things under the sun. You are phenomenal and I wish you most and more for your research journey- keep buckling them microtubules ☺. Constantin, you are truly one of a kind-a talented researcher and an amazing friend. Thanks for being my therapist at work, for being as quirky as me, for the

otter GIFs and introducing me to the world of Sleep Token. I will miss our walks with Layla and our fun-filled outings.
Mariana, it was always nice to discuss science with you. Thank you for the Zazu cuddles. Jennifer, it was so fun to bond over our shared love for dogs and music. Thank you, Shaunak for all the cloning and plasmid amplification help. Prajwal, I enjoyed our enlightening discussions on tubulin PTMs, kinesin, and Mr X. Constantin G, it felt so good to finally meet someone who hated weather fluctuations as much as me. Layla, sweet girl, your cuddles and the long summer walks we took are something I will forever treasure. Your calm persona and the cute pet-nudges have brightened many-a-gloomy day. Thank you all for filling my days at AG Aradilla with so much joy and fun. I will miss it all.

I owe a significant part of my research success to Jeremie Gaillard. Thank you, Jeremie for the awesome kinesin that has never failed me and for always being helpful in times of crisis. My time at Grenoble and learning from you will be one of the highlights of my PhD.

They say that the best of talent sparks from the impetus of a great teacher. I owe my love for biology and science to one such guru- Ms Shanthi Santhipalan. I still remember your first class on biomolecules back in 2011 and how I walked out in awe of life and biology. Ma'am, your teachings and words continue to inspire me. I dedicate this thesis and my work in your honour.

To my family away from home- the girls- Dyuthi, Neha and Anjana, I am so glad that we found each other. Our outings and travel adventures are core life memories for me. Sai, our long online conversations on the perils of failed experiments and beyblades will always be special to me. Chirantan, your timely advice on how I should keep believing in my abilities and passion is something I will always remember. Thank you to the nameless strangers who helped in small but meaningful ways: the #150-bus driver who always waited an extra minute and greeted me with a smile, the Chemikalienläger staff who were always extremely patient with me and the staff at Unique Café. I am grateful to my reader community friends for cheering me on during all the tough times. Thank you, Author Dan Garrett, Ms Ann, Lulu, Diana and CrazedCoffeeLady. #TeamRyke forever!

Throughout this journey, there have been three constants that have always been by my side- my mom, Bala and the mellifluous tunes of AR Rahman. Thank you, Amma, for being my everything, for all the sambar analogies and for believing in me more than myself. I couldn't have done this without the support of my family- my parents, my sister Shreyaa, my uncles, and Bala. I love you all. Shreyaa, thank you for being a source of constant support. I love you and I am so proud of all that you have achieved. Bala, thank you for always being my anchor, for being with me through it all- the 3 am phone calls, the lame jokes that never fail to turn tears into smiles and lull the pain away. I am truly blessed to be surrounded by all your love.